DTU Library

An examination of the anti-icing mechanisms of charged polymer coatings

Biro, Robert Andrew

Publication date:
2022

Document Version
Publisher's PDF, also known as Version of record

Link back to DTU Orbit

Citation (APA):
Biro, R. A. (2022). *An examination of the anti-icing mechanisms of charged polymer coatings*. DTU Chemistry.

An examination of the anti-icing mechanisms of charged polymer coatings

Robert A. Biro

PhD Thesis

Abstract

The formation and adhesion of ice onto surfaces is a critical issue towards the continued operation and safety of aircraft, wind turbines, maritime vessels, heat exchangers, power and telecommunications network cables, etc. Combating ice adhesion has historically relied on active methods, through heating, applying freezing point depressants, or most obviously: the mechanical removal of ice itself. Yet, the more passive approach of anti-icing coatings, has attracted significantly attention recently, given the inevitable nature of ice formation. Therefore, this research aims to shed light on the mechanisms of ice adhesion on charged polymer coatings, which have previously been largely inferential. To this end, I have developed a home-built ice adhesion test apparatus to measure the adhesion strength of ice on various surfaces. The design of charged polymer coatings has been a principle component of this research, and its efforts have led to a widely tunable system, to produce surfaces with variable chemical and coating structures.

These abilities have allowed the thorough investigation of ice adhesion onto charged polymer coatings, with variable counterion, polymer charge, and crosslink density. Observed variations in anti-icing behaviour suggested a mechanism based on the physical state of hydration water, which was confirmed using two independent methods: TIR Raman spectroscopy and a combination of ellipsometry and differential scanning calorimetry. Additionally, the magnitude of the ice adhesion strength at low temperatures was found to be correlated to a fraction of "non-freezable" water. Mechanistic insights gained from this research can be used to efficiently design future anti-icing coatings.

Resumé

Dannelsen af is på overflader er et kritisk spørgsmål for den fortsatte drift og sikkerhed af blandt andet fly, vindmøller, maritime fartøjer, varmevekslere og el- og telekommunikationskabler. Afisning af sådanne overflader har historisk set været baseret på aktive metoder, herunder opvarmning, afrensning med frysepunktssænkende midler, eller mest åbenlyst: ved mekanisk fjernelse af is. I senere år har en mere passiv tilgang til anti-icing belægninger dog tiltrukket sig betydelig opmærksomhed på grund af den naturgivne karakter af isdannelse på afkølede overflader. Forskningen præsenteret i denne PhD. afhandling har til formål at kaste lys over mekanismerne bag isadhæsion på ladede polymerbelægninger, hvilket tidligere i vid udstrækning ikke har være tilstrækkeligt underbygget. For at undersøge dette fænomen nærmere har jeg udviklet et hjemmebygget isadhæsionstestapparat til at måle adhæsionsstyrken af is på forskellige overflader. Designet af en række forskellige ladede polymerbelægninger har været en af hovedkomponenterne i forskningen og har resulteret i et justerbart system af polymerer med varierende kemiske egenskaber og overfladestrukturer.

Disse forskellige egenskaber har muliggjort en grundig undersøgelse af isadhæsion på ladede polymerbelægninger med variable modioner, polymerladninger og tværbindingsdensiteter. Observerede variationer i anti-icing adfærd antydede en mekanisme baseret på den fysiske tilstand af hydreringsvand, hvilket blev bekræftet af to af hinanden uafhængige metoder: TIR Raman-spektroskopi og en kombination af ellipsometri og differentiel scanningskalorimetri. Derudover blev vedhæftningsstyrken af is ved lave temperaturer korreleret til at være en mængde af "ikke-fryseligt" vand. De mekanistiske indsigter som er opnået ved de her beskrevne studier kan I fremtiden bruges til effektivt at designe nye anti-icing belægninger.

Acknowledgments

This path to this thesis has been an incredible challenging and rewarding adventure that I could not have accomplished without the numerous people that have helped and supported me along the way. I first must thank my supervisor, Esben Thormann, for his extraordinary guidance and support. I'm grateful for the opportunity that you afforded me, and your continued optimism and interest in the project has been beyond inspiring. I have truly appreciated all of our discussions and feedback, both on a scientific and personal level, which I will take with me into the future. I must also thank Professor Eric Tyrode for his invaluable teachings, experience, and help during my external stay at KTH. Your passion and excitement have made my time in Stockholm a warm one to look back on. I had the privilege of working with some of most wonderful colleagues at DTU or KTH, especially at the Group of Polymers and Functional Interfaces (GPFI). Whether it be the far-too-frequent-coffee-breaks, scientific discussions, or lunch-time jokes, it has been a great environment to have been a part of, and I appreciate all of the time we have spent together.

On a more personal level, from the welcoming energy of the entire danish ultimate frisbee community, to the close friendships that have grown since I first landed in Denmark, I am thankful for your constant encouragement and benevolence. I must also thank my family, both here and at home, for their enduring care, patience, and love. And to you, Line, thank you for holding my hand and heart along this journey.

Publications

Appended Publications/Manuscripts

(1) Understanding the ion-specific anti-polyelectrolyte effect on the swelling behavior of polyzwitterionic layers
Frederik Hegaard, <u>Robert A. Biro</u>, Koosha Ehtiati, and Esben Thormann
Submitted

(2) Reducing ice adhesion to polyelectrolyte surfaces by counterion mediated nonfrozen hydration water
<u>Robert A. Biro</u>, Eric C. Tyrode, Esben Thormann
In preparation

(3) Ice adhesion to cationic, anionic, zwitterionic, and non-ionic polymer surfaces: on the understanding of the role of hydration water
<u>Robert A. Biro</u>, Esben Thormann
In preparation

Not included Publications/Manuscripts

(1) Fibrin formation and fractal organization at cationic, anionic, and zwitterionic polymer coated interfaces
Achebe N. O. Nzulumike, <u>Robert A. Biro</u>, Esben Thormann
Submitted

Contents

Chapter 1

Introduction

Icing is the formation and adhesion of ice onto surfaces. Adhered ice can cause a plethora of safety concerns and operational difficulties for aircraft, wind turbines, transmission lines, heat exchangers, etc. ultimately leading to their inactivity.[1–5] As an example, ice adhered to aircraft can significantly increase its mass, as well as introduce rough features, both of which may impact aircraft performance.[6] Additionally, frozen debris may break-off and cause damage to the aircraft's control surfaces or engines.[7] For said reasons, de-icing, the active removal of ice from these surfaces has become a staple in cold-climate aviation, as the issue of safety is paramount. Active mechanical removal or spraying of hot de-icing fluids over all surfaces of the aircraft is but a temporary solution that must be reapplied or repeated from time to time. Yet, anti-icing surfaces, materials resistant to icing, whether through minimizing ice adhesion strength, reducing ice growth, or preventing the nucleation of supercooled water droplets, are considerably attractive due to their passive nature, ideally requiring little to no upkeep.[8–10]

Considerable research has seen the development of numerous of anti-icing surfaces, often falling into one of three classes: hydrophobic surfaces, slippery liquid-infused porous surfaces, or hydrophilic surfaces, each attempting to thwart the problem of icing.[11] Particularly, with regards to ice adhesion to hydrophilic surfaces, reasoning towards the mechanism of anti-icing properties remains largely inferential. Therefore in the aim of designing more effective anti-icing surfaces, it is important to gain insights and develop an understanding in the mechanism of ice adhesion to hydrophilic surfaces. To this end, my work discussed in this thesis, has resulted in three manuscripts: first delving into the swelling behaviour of charged hydrophilic polymer films, then attempting to provide a more mechanistic understanding of ice adhesion on charged polymer surfaces in the remaining two.

Background information pertinent to the understanding of this work is presented in Chap-

ter 2. Here, insights into the mechanisms of ice adhesion on bare, hydrophobic, slippery-liquid-infused infused, and hydrophilic surfaces are presented. Next, the synthesis of charged polymer systems and coating formation is discussed, after which their characteristic properties are examined, all laying the groundwork to design and investigate novel anti-icing coatings.

Chapter 3 provides details regarding the synthetic techniques used to produce charged polymer coatings. Additional background information regarding their characterization is also introduced where deemed necessary. The design of a development of a home-built ice adhesion apparatus is discussed at length in Chapter 4, and was key in later investigations.

The design of synthesis of charged polymer coatings (as mentioned before) was not uncomplicated. Chapter 5 reviews my own efforts to produce stable charged polymer coatings and the successful design of the coating system used in later investigations. It is here that the I present the results of a study on the characteristic swelling behaviour of the polyelectrolyte and zwitterionic polymer coatings.

Studies on the anti-icing performance of charged polymer coatings, specifically with regards to ice adhesion strength are presented in the Chapter 6. Results of counterion-specific ice adhesion experiments suggests mechanisms at play that are previously unproven. Using two independent characterisation techniques, a novel mechanistic understanding of ice adhesion on polyelectrolyte surfaces is presented. Following this, the effect of coating structure with regards to charge identity and crosslink density on ice adhesion, was investigated. The results afforded from these two studies provide significant mechanistic insights into the anti-icing properties of charged polymer surfaces. These are summarized in a conclusion in Chapter 7, along with new perspectives for future investigations.

Chapter 2

Background

This chapter provides the background information necessary to understand ice adhesion to polymer coatings; pertinent information towards mechanism of ice adhesion, anti-icing coatings, charged polymer systems for coating applications, and characteristic properties of these polymers are described.

2.1 Ice adhesion

The formation and adhesion of ice onto surfaces is a critical challenge, bringing significant economic, energy, and safety concerns in many facets of today's society.[12] Whether on aircraft, power transmission lines, vehicles, or wind turbines, the hostility and persistence of icing problems is one that warrants a combative attitude to solve, through either active or passive strategies.

Active strategies often rely on a combination of thermal, chemical, and or mechanical methods to remove ice, and generally solve the problem in the short term. Ice on wind-turbine blades and the leading edge of aircraft wings can be removed by heating the surfaces, requiring significant energy supplies.[4, 13] Ice accreted on maritime vessels often must be physically removed and puts the crew in significant danger.[2] And perhaps most familiarly, adhered snow and ice on waiting planes (and wind turbines) must be actively removed through by spraying hot de-icing fluid.[14, 15] Yet all of these active solutions focus on the short-term and are only applied when necessary.

However, passive strategies towards anti-icing focus on creating a functional surface, by inhibiting ice nucleation, preventing ice propagation, or lowering the ice adhesion force.[16–18] Significant focus has already been brought regarding the nucleation and propagation of ice, yet it believed that ice will form and grow on any surface eventually.[9, 19–21]

Therefore, I focus solely on reducing the adhesion force between ice and a surface, relying on the chemistry of surface. Ice adhesion to surfaces is broken down into 4 classifications and examined further below: ice adhesion on (i) bare substrates, (ii) hydrophobic coatings, (iii) slippery liquid-infused porous surfaces, and (iv) hydrophilic coatings.

2.1.1   Ice adhesion on bare substrates

The adhesion of ice onto bare neat surfaces is not as simple as once thought. It was first postulated by Faraday that a state of water, between solid ice and liquid water may exist, and that nearly a century later its effects would be shown through tensile adhesion strength of ice on surface - going from adhesive breakage at high (yet still below 0 °C) temperatures and transitioning into cohesive breakage at sufficiently cool temperatures.[22, 23] In more modern experiments, Jellinek proposed the existence of a quasi-liquid layer (QLL) (sometimes also referred to as a premolten layer or liquid-like layer) between ice and a substrate responsible the linearly increasing ice adhesion strength on bare substrates.[24] Yet only in the past 3 decades has this state of water between solid and liquid that seemingly lubricates the interface between bulk ice and a solid substrate, been proven. Evidence provided from ellipsometry, X-ray reflectivity, VSFS, TIR-Raman spectroscopy, and NMR experiments have all helped provide direct evidence towards the existence of a QLL.[25–30]
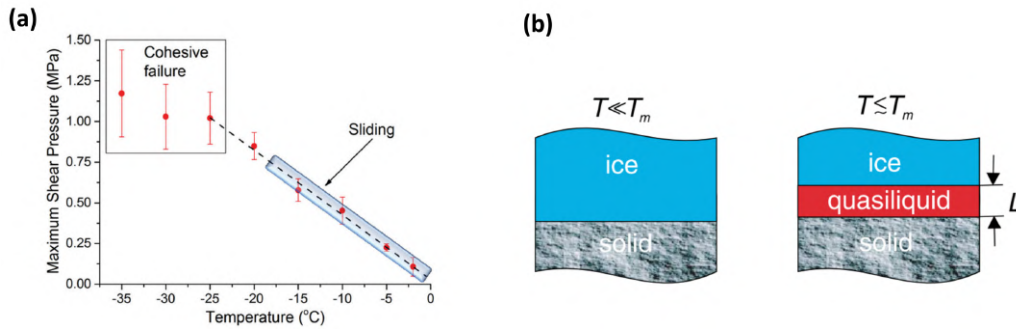
Figure 2.1: (a)Temperature dependent ice adhesion strength on a silica interface. Reprinted with permission[29]. (b) Schematic of temperature dependent interfacial melting of ice on a homogeneous solid substrate. Reprinted with permission[27]

Picking out two of these studies, one based on ice adhesion strength with corresponding TIR Raman spectroscopy and the other on X-ray reflectivity measurements, one can better understand the nature of the QLL and its affect on ice adhesion on bare substrates, i.e. silica.[27, 29] Figure 2.1a details the temperature dependent ice adhesion strength (here called maximum shear adhesion pressure) of ice on ultra-smooth silica samples. Starting at temperatures close to 0 °C and decreasing through -20 °C, a linearly increasing ice adhesion strength was observed, and could be characterized as adhesive failure, although at temperatures greater than -15 °C, a seemingly rare behaviour of sliding was reported.[23, 24] At temperature below -20 °C, a larger and constant ice adhesion strength representing

a cohesive failure at the interface was observed, evident by the remaining fragments of ice left on the silica surface. Illustrated by Figure 2.1b, one can imagine that the ice adhesion strength on solid silica surface would be lower given the existence of a QLL that promotes sliding, in comparison to its absence in which ice would be free to mechanically interlock with the substrate. Therefore the thickness of the QLL may play a role in the ice adhesion strength in this temperature regime (0 to -20 °C). Attempted observations of a presumptive QLL at the interface through TIR Raman spectroscopy failed due to its inherently small thickness or lack of distinguishing spectral characteristics, although more NMR and VSFS experiments yielded more fruitful results towards the existence of a QLL above approximately -25 °C.

These observations are bolstered by an earlier X-ray reflectivity experiment that directly probed a silica-ice interface.[27]. Here, reflectivity curves of the interface were analysed and associated density profiles were deduced, revealing the existence of a QLL between from 0 to -17 °C via its characteristic density (Figure 2.2). But perhaps of most value, was the observed temperature dependent thickness of the QLL that linearly increased from 0.8 nm at -14.7 °C, to 5.5 nm at -0.036 °C. Connecting this to previously discussed ice adhesion measurements, it is simple to see the linearly increasing ice adhesion strength must be related to the thickness of an interfacial QLL, such that a higher temperatures exists a thicker QLL that is more apt at promoting sliding leading to intrinsically low ice adhesion strengths. [24, 29] Lower temperatures gives rise to a thinner QLL that intrinsically will have lower molecular mobility, ultimately leading to greater values of ice adhesion strength. And finally, once the roughness of the surface has overtaken the thickness of the QLL, its contribution is presumed to be non-existent, and the ice adhesion strength is governed by the mechanical interlocking and adhesion forces between ice and silica, as is demonstrated by the cohesive failure of ice on a smooth bare silica surface below -20 °C.

2.1.2 Hydrophobic coatings

In addition to measurements of ice adhesion strength on silica, Jellinek identically conducted experiments of ice adhesion strength on polystyrene (PS) and poly(methyl methacrylate) (PMMA) surfaces.[24] In this first finding of adhesive strength of ice vs. temperature on a smooth hydrophobic surface, a linear increase in ice adhesion strength as a function of temperature was observed. As the behaviour was nearly identical to the aforementioned experiments on silica, it suggests that the mechanism that denotes ice adhesion behaviour must also be QLL. However, although the overall temperature dependence in ice adhesion behaviour could be reconciled by the existence and eventual diminishing of a QLL, the differences in the magnitude of ice adhesion strength, such that PMMA films had slightly higher adhesion strengths than PS, could not.

Interestingly, theoretical predictions on the adhesion of ice on a given surface describe the
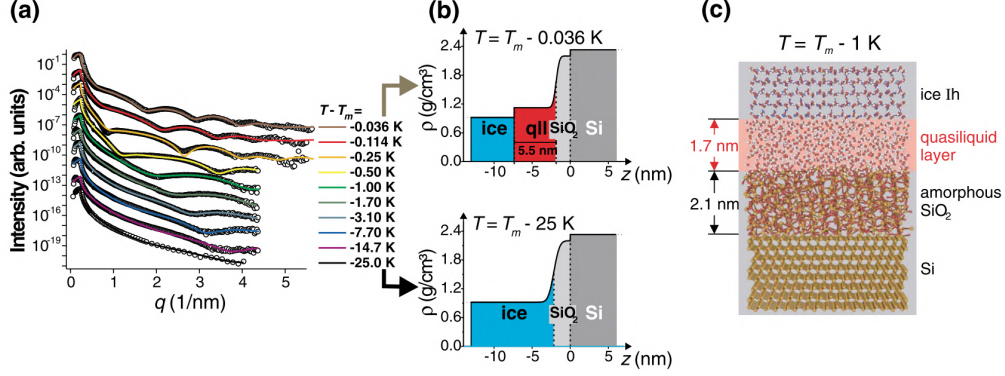
Figure 2.2: Reprinted with permission[27] (a) Reflectivity curves of the ice-SiO$_2$ interface at temperatures ranging from T = T$_m$ -0.036 K to T = T$_m$ - 25 K. (b) $\rho(z)$ across the interface displaying existence of a quasi-liquid layer (QLL) at temperature near the melting point (T =T$_m$ -0.036 K), and a lack of QLL at T = T$_m$ - 25 K. (c) A real space model of ice-SiO$_2$ interface associated with T = T$_m$ - 1 K.

work of adhesion between ice (i) and and a solid (s) to be a function of the respective surface energies and the energy required to break the bond between them (Equation 2.1). Through estimations of the various surface energies listed in Equations number the thermodynamic work of adhesion can be approximated as function of the contact angle and the surface energy of ice/water (Equation 2.2).[12, 31] Accordingly, the work of adhesion is minimized as the contact angle between the surface and water approaches 180 °, thus describing an theoretical framework for the ice adhesion strength based on water wettability. As a result, studies on the ice adhesion strength on surfaces with varying contact angles have been undertaken, some of which have present a correlation of reduced ice adhesion on surfaces with high contact angles.[7, 32, 33] However, this trend is by no means universal and significant scatter has been observed between supposedly alike samples.

$$W_a = \gamma_{surface} + \gamma_{ice} - \gamma_{surface-ice} \tag{2.1}$$

$$W_a = \gamma_w(1 + cos(\theta)) \tag{2.2}$$

$$W_p = \gamma_{ice}(1 + cos(\theta_{rec})) \tag{2.3}$$

An in-depth discussion concluded that the wettability of a surface cannot be adequately described through a single static contact angle, and that an improved definition of surface
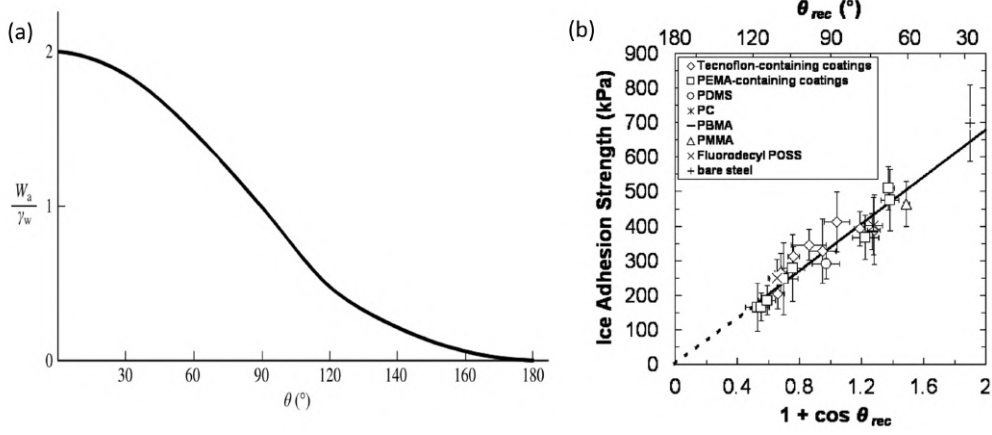
Figure 2.3: (a) Thermodynamic work of ice adhesion scaled with surface energy of water versus the water contact angle (Θ). Reprinted with permission [12]. (b) Average strength of ice adhesion measured at -10 ℃ of various surfaces against a scaled receding contact angle parameter. Reprinted with permission [33]

wettability can be based on dynamic contact angle experiments. As such the practical work of adhesion for removing a liquid from a solid surface was attempted to be correlated to the ice adhesion strength on those surfaces. Although previous studies ventured to correlate ice adhesion strength with various parameters such as equilibrium work of adhesion, practical work of adhesion, and liquid drop roll-off angle, all to varying degrees of success, these trends were again not universal. Eventually, Meuler et al. firmly established a strong correlation between ice adhesion strength and the practical work of adhesion scaling parameter for liquid water on a solid surface $[1 + cos(\theta_{rec})]$(Equation 2.3 and Figure 2.3).[33] Interestingly, the study and described trend does not outwardly communicate the mechanism of adhesion, although it is believed that the existence of a QLL on most of these surfaces is likely. Yet the findings concur with the previous theoretical framework, although with some deviation, such that maximizing the receding contact angle of a water drop will give a surface with favourable (low) ice adhesion strength.

Building on this relationships, Meuler et al. measured the ice adhesion strength on fluorodecyl polyhedral oligomeric silsequioxane (fluorodecyl POSS) / PMMA coatings that, when measured, exhibited a adhesion strength of $\sim$ 150 kPa, corresponding to a high receding contact angle of $\sim$ 117 °.[33] Above this angle, they postulated that the formulation of durable smooth hydrophobic surfaces would yield considerably higher ice adhesion strengths, as it had already been discovered that increasing surface texture and roughness of like polymer coatings increased the adhesion strength of ice due to increase surface area and mechanical interlocking between ice and the substrate.[34–37] Additionally, the surface texture of hydrophobic coatings seemingly changed given successive and continuing tests leading to increased ice adhesion strength, in stark contrast to the hydrophilic polymer coatings to-be-discussed.

Follow-up investigations on this finding, attempting to disect the relationship between surface wettability to ice adhesion strength, found that superhydrophobic surfaces may not be ideal as low ice adhesion surfaces.[38, 39] And upon closer examination, surface roughness was determined to be a key player in the resulting ice adhesion strengths. For (super)hydrophobic surfaces, water wets the surface by the Cassie-Baxter state, on top of any surface textures, trapping air between the droplet and the surface.[40, 41] When the temperature of the drop is lowered, the air condensates water onto the surface imparting more hydrophilic properties. This allows for easier wetting of the drop into the surface texture, thereby increasing the surface area between ice and the substrate, but most importantly, increasing the mechanical interlock between ice and the surface significantly. As a result (super)hydrophobic surfaces may sometimes have significant ice adhesion strengths due to their surface texture.[38] And despite procedures to produce smooth hydrophobic coatings, the surface texture invariably increases over repeated icing/deicing tests.[42]

2.1.3   SLIPS

One method of eliminating any significant surface texture is by employing a coating completely infused with liquid, ascribing a nearly-perfectly smooth liquid surface that dramatically reduces the adhesion strength of ice; classified as slippery liquid-infused porous surfaces (SLIPS).[43, 44] In general, the flat liquid interface of SLIPS does not allow water droplets to easily settle or reducing the amount of freezing on sub-zero surfaces.[45] Inevitably though, ice will form on the surface, and the lubricating properties of the infused present at the interface can be used to effortlessly remove ice.[11]

Wong et al. designed and prepared a micro/nanoporous substrate infused with a liquid that gave a smooth and defect-free surface.[46] Additionally they outlined that the lubricating liquid must preferentially wet the substrate over water/ice, and that the lubricating liquid must be immiscible with the any contacting liquid/solid. As such, the SLIPS fabricated were based on a polyfluoroalkylsilane network infused with a low-surface-tension perfluorinated liquids, forming a slippery and uniform surface that is immiscible with aqueous and hydrocarbon phases. Liquid repellency of the fluorous-phase SLIPS was exceptional, and ice was similarly discarded solely by discarding the substrate, as seen in Figure 2.4.

Rationally, the strong repellent properties of SLIPS can be tuned by changing the infused liquid used to lubricate the interface, and when explored by Ozbay et al. the ice adhesion strength on SLIPS was found to be dependent on the hydrophobicity of the infused liquid.[47] In contrast to ice adhesion on hydrophobic coatings/surfaces, generally, hydrophilic liquids provided the greatest reduction in the adhesion strength of ice when compared to the bare filter paper. Ethylene glycol, formaldehyde, and glycerine liquid gave incredibly low ice adhesion strengths ($\sim$16 kPa), while more more hydrophobic oils
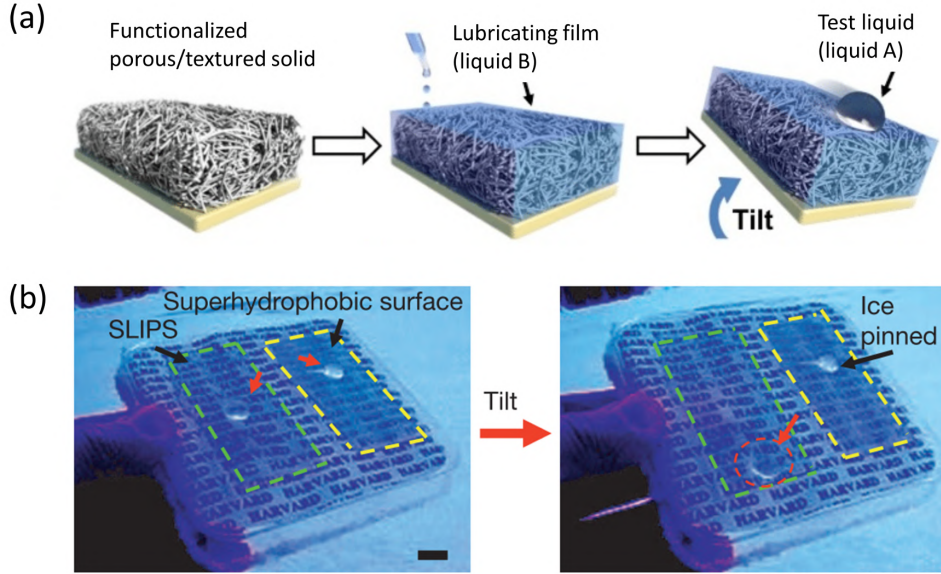
Figure 2.4: (a) Illustration of SLIPS and repellent coatings by infusing a lubricating liquid. Reprinted with permission [46] (b)Ice repellent properties of SLIPS compared to a superhydrophobic surface visualized. Reprinted with permission [46].

and polyolefins resulted in greater adhesion ($\sim$120 kPa). Yet some perfluorinated liquids, again, provided exceptionally low ice adhesion strengths on par with the hydrophilic liquids, despite being hydrophobic fluorinated aliphatics. It is thought that the liquid state of all these liquids at sub-zero temperatures is what gives SLIPS advantageous anti-icing properties, due to their ability to weaken the interaction between ice and the solid substrate by lubricating and wetting the interface.[48]

One shortcoming of using a liquid to infuse a porous surface for anti-icing, is that any hydrophilic liquid will eventually be diluted with water over successive icing/deicing and be consumed, requiring replenishment. More hydrophobic alternatives, such as silicon oil were thought to give greater longevity as they would not be so easily wicked by water. Although rationally sound, even silicon oil infused porous surfaces, which had initially low ice adhesion strengths, were eventually in need of replenishment as ice adhesion strengths rose dramatically from $\sim$10 kPa to $\sim$100 kPa over the course of approximately 45 icing/deicing cycles.[49] Although incredible longevity was achieved, the steady rise in ice adhesion strength necessitated repair and replenishment, which after completed returned the favourable anti-icing properties. The rise in adhesion strength was characteristic in the consumption of the infused silicon oil lubricant, that over the course of 45 cycles gradually exposed ice droplets to a greater portion of porous surface without lubricant, giving rise to greater ice-surface interactions. Additionally, over multiple repair and replenishment cycles, the initial ice adhesion and contact-angle could not be re-established (Figure 2.5).
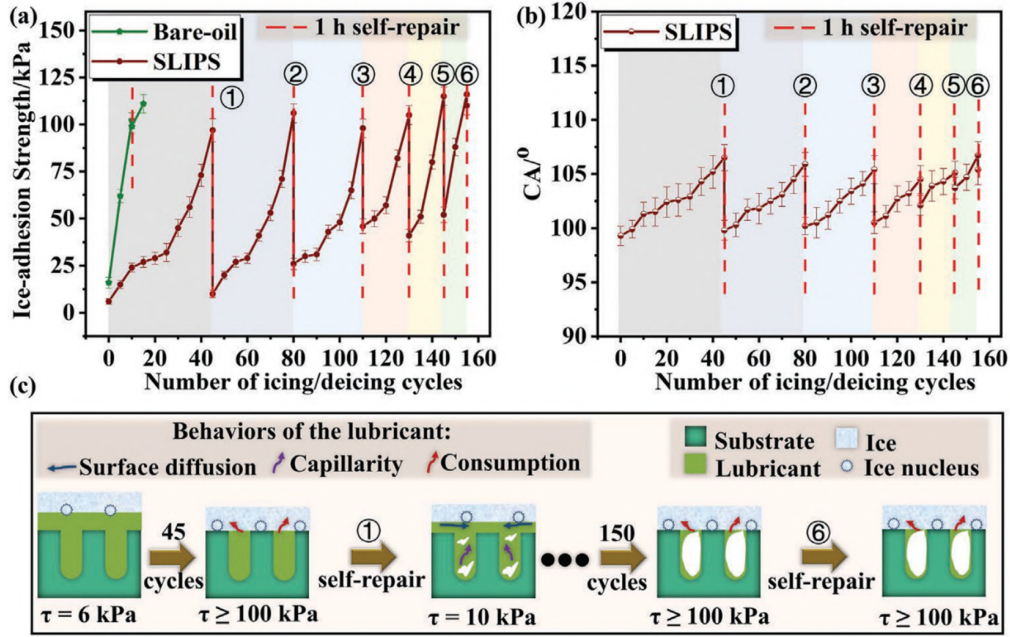
Figure 2.5: (a) Ice adhesion strength over many icing/deicing cycles. (b) Contact ange of water on SLIPS over the course numerous icing/deicing cycles. (c) Schematic mechanism of the icing-repairing-degradation process. Reprinted with permission [49].

2.1.4   Ice adhesion to hydrophilic polymer coatings

Rather than using an expendable and finite amount of a liquid to infuse the surface, water, which is in abundant supply, has the potential to impart similarly beneficial anti-icing properties. It is postulated that by using hydrophilic and hygroscopic polymers to form a coating, the resulting water absorption that comes from water droplets, bulk ice, or the moisture in the surrounding atmosphere, imparts the coating with advantageously low ice adhesion strengths through a aqueous lubricating layer, similar to how on bare and smooth hydrophobic surfaces a quasi-liquid layer bestows a decrease in ice adhesion strength when present.

Inspired by this, a microporous poly(acrylic acid) (PAA) network was grafted from a functionalized silicon wafer, with surface area fraction ranging from $\phi = 0.05 - 1.00$.[50] Investigating the ice adhesion strength on the coating versus the surface area fraction of hygroscopic PAA, it was found that ice adhesion strength was constant between at $\phi < 0.2$, as the swollen PAA and its embedded water provided a continuous aqueous lubricating layer. At $\phi > 0.2$, the ice adhesion strength grew linearly and significantly, and was explained due to the lower surface coverage imparting a non-continuous and less effective aqueous lubricating layer (Figure 2.6a). Additionally, at a single phase fraction, ice adhesion strength was observed to be temperature dependent: remaining constant ($\sim$65 kPa) until -25 °C, and then sharply increasing to another plateau ($\sim$1100 kPa) by

-30 °C. This novel behaviour, the sudden and steep increase in ice adhesion strength at -25 °C, was attributed to the phase transition of the aqueous lubricating layer from liquid to ice (Figure 2.6b).
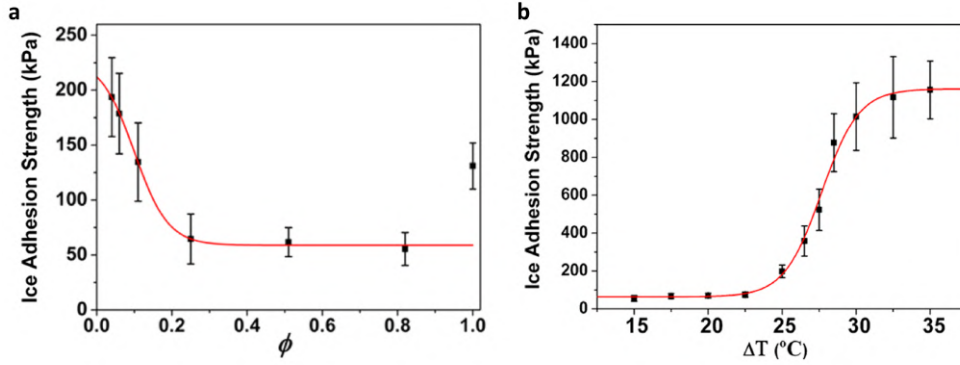
Figure 2.6: (a) Ice adhesion strength versus the volume fraction of hydrophilic polymer on microporous array. (b) Temperature dependent ice adhesion strength on a self-lubricating liquid layer. Reprinted with permission [50].

Following up on this work, Dou et al. prepared a series of polyurethanes with varying amounts of hydrophilic dimethylolpropionic acid (DMPA) that when cast and thermally cured onto a aluminium substrate, also provided exceptional anti-icing properties.[51] The highest performing coating, displayed similar temperature dependent ice adhesion behaviour to work accomplished by Chen et al.; an unchanging ice adhesion strength (27 kPa) was observed between -15 and -53 °C, followed by a steep increase in ice adhesion strength from -53 to -60 °C, after which a second plateau in ice adhesion strength (700 kPa) is reached.[51] Rationally, a similar conclusion was reached, the behaviour being justified by the hydrophilic and ionic DMPA component that strongly binds water and forms a aqueous lubricating layer that at approximately -55 °C, transitions from liquid to ice, resulting in an increase in ice adhesion strength.

Later, Chen et al. used mussel-inspired surface chemistry to produce anti-icing coatings, first by synthesizing PAA-dopamine (PAA-DA) conjugates with varying functionality of dopamine, and then crosslinking with sodium periodate onto a substrate, giving a crosslinked PAA-DA coating(Figure 2.7a).[52] Subsequent measurements of ice adhesion strength on these surface-attached PAA-DA hydrogels showed a decrease in ice adhesion strength as dopamine content increases, although this relationship is only valid to a certain degree (Figure 2.7b). This was explained by the varying dopamine content in the PAA-DA conjugate and therefore crosslink density, such that a PAA-DA conjugate with greater dopamine functionality will give way to a more crosslinked network. This in turn, is known to affect the fractions and amounts of "non-freezable" and freezable water absorbed in the coating, as well as the freezing temperature of the freezable water.[53–55]
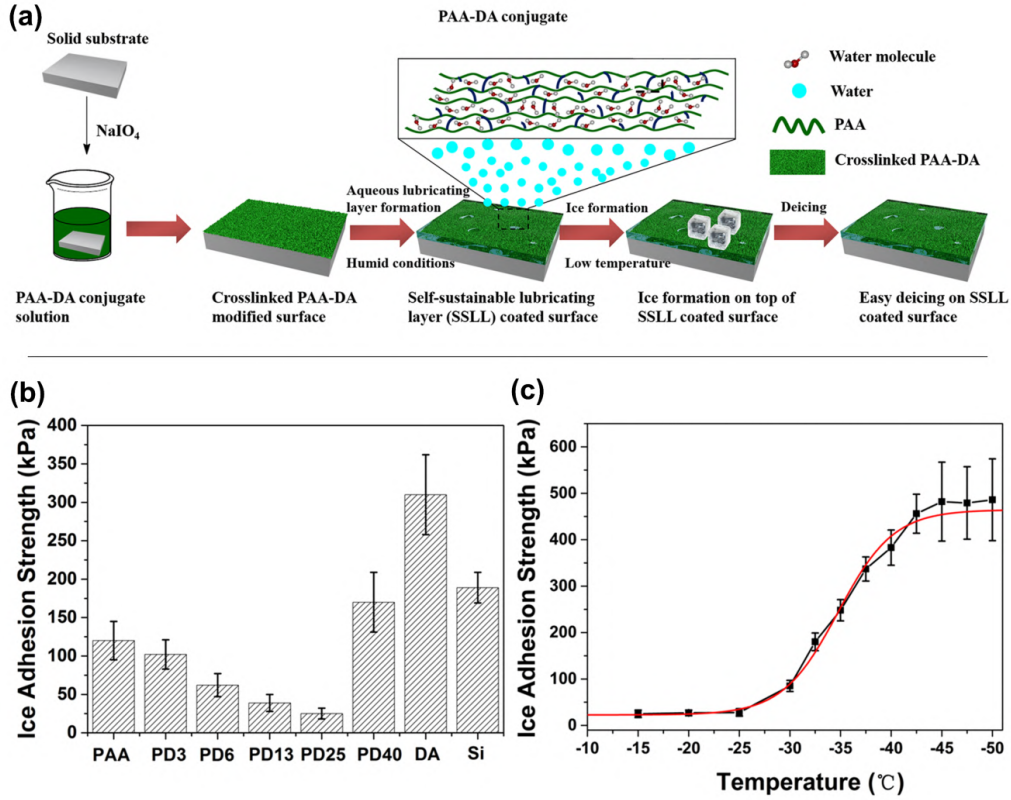
Figure 2.7: (a) Schematic representation of the synthesis of PAA-DA surfaces, and its interactions with water leading to low ice adhesion (b) Ice adhesion strength at -15 °C, as a function of percentage of dopamine. (c) Temperature dependent ice adhesion strength from -15 °C to -50 °C, of PD25, exhibiting a self-sustainable lubricating layer. Adapted and reprinted with permission [52].

The observed crosslink density dependent ice adhesion behaviour observed here was explained in part to the decreasing fraction of freezable water, as well as its freezing point, such that a greater of liquid water in the coating would impart a lower ice adhesion strength.

Additionally, ice adhesion strength measurements over a wide-range of temperatures on a single coating again uncovered a temperature-dependent relationship that bears a striking resemblance to previous work.[50, 51] Here, a first plateau (~25 kPa) lasting down to -25 °C, then a more gradual increase in ice adhesion strength between -25 and -42 °C, and finally a second plateau (~500 kPa) was observed (Figure 2.7c). Chen et al. discuss these details through the lens of an aqueous lubricating layer, such that when the freezable water is liquid it promotes an aqueous lubricating layer at the coating-ice interface that lowers the ice adhesion strength, and when frozen there is a lack of liquid water to lubricate the

interface, ultimately leading to an increase in ice adhesion strength.

This design focus towards producing coatings that promote and support interfacial non-frozen water was also accomplished by incorporating various PDMS-PEG copolymers into a precursor PDMS.[56] Ice adhesion strength was significantly reduced ($\sim$120 kPa) compared to a standard hydrophobic PDMS film ($\sim$320 kPa), despite only film containing only 1 wt.% of the PDMS-PEG copolymer. It is believe that the PEG components can preferentially migrate towards the surface, segregating to form a more hydrophilic surface that can form hydrogen bonds with water at the interface. As a result, the strong hydrogen bonds between PEG and the interfacial water molecules allows them to remain liquid at temperatures below the freezing temperature of bulk water, and serves as a lubricating layer to reduce the ice adhesion strength on the surface. Interestingly, the study describes the interfacial nonfrozen water as a quasi-liquid layer (QLL), as opposed to an aqueous lubricating layer, making a clear distinction that water molecules in the QLL have a lower configurational entropy due to their comparatively high order (Figure 2.8). This should lead to increase in viscosity, and was confirmed by performing ^{1}H T_2 relaxation NMR measurements.
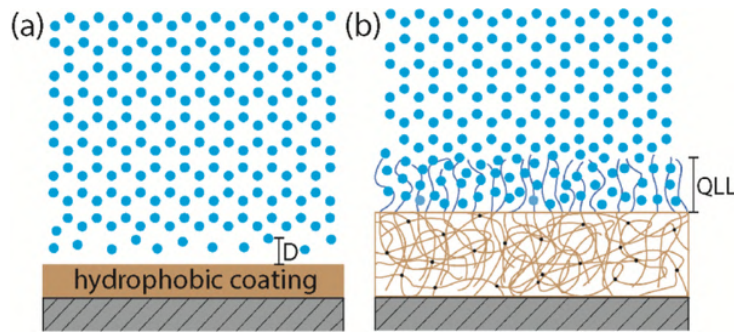
Figure 2.8: (a) Proposed mechanism on ice adhesion on a hydrophobic coating. D representing the water depletion layer leading to a QLL. (b) Proposed mechanism of a larger nonfrozen QLL on PDMS-PEG surfaces leading to reduced ice adhesion strengths. Reprinted with permission [56].

Chernyy et al. demonstrated the feasibility of a superhydrophilic polyelectrolyte brush coatings for anti-icing applications as well, interpreting the ice adhesion strength data through the lens of a quasi-liquid layer.[57] Here, surface grafted charged polymer brushes were grown on silicon substrates, with strong anionic (R-SO$_3^-$), weak anionic (R-CO$_2^-$), or strong cationic (R-N(CH$_3$)$_3^+$), polymer bound moieties. Simple counterion exchange allowed for a considerable profile of various polyelectrolyte brushes and their properties to be explored. The observed ice adhesion strengths for all the brushes were greater at lower temperatures (-18 °C) than higher temperatures (-10 or -5 °C). This temperature dependence implied that interfacial melting of ice was the mechanism, similar to the previously observed X-ray reflectivity experiments. Succinctly, a temperature dependent QLL is believed to exist and lubricate the ice-coating substrate.

Interestingly, highly hydrating counterions, smaller structure-making ions with high charge density that enhance the degree of hydrogen bonding between water molecules, led to a significant reduction in ice adhesion strength when compared to an bare glass substrate. Weakly hydrating ions on the other hand, larger structure-breaking ions with low charge density that disrupt the hydrogen bonding network between water molecules, did not affect the ice adhesion strength. This suggests that counterions able to promote greater hydrogen bonding between water molecules can better contribute to the formation of a QLL, and reduce the ice adhesion strength. This basis comes to play an important role in later investigations, attempting to aptly describe the counterion dependent ice adhesion strength.

The nature of the charges in the polyelectrolyte was another factor investigated in the study. Strong (anionic, $R\text{-}SO_3^-$) polyelectrolyte brushes were found to lead to lower ice adhesion strength in comparison to their weak ($R\text{-}CO_2^-$) counterparts. This contrast was rationalized through XPS analysis, revealing that a sizeable fraction of the counterions in weak polyelectrolyte brushes were washed out and the carboxylate functionalities protonated by water upon hydration. As a result, far fewer ions interact with the interfacial ice water leading to a less thick and therefore less effective QLL at subzero temperatures. Yet, no distinctive anti-icing behaviour between strong anionic and strong cationic polyelectrolyte brshes was observed.

This was probed in depth in a similarly designed system, comparing the ice adhesion strength on strong cationic, strong anionic, and zwitterionic polymer brushes.[58] Despite all displaying remarkably low ice adhesion strengths, zwitterionic brushes exhibited the most favourable anti-icing performance, followed by strong cationic, and then strong anionic brushes. Rather than focusing on the role of counterions (or lack of such in zwitterionic systems), water in the charged polymers was investigated using differential scanning calorimetry (DSC) and FTIR spectroscopy.[58–60] Upon analysis of each characterization, the zwitterionic system was found to contain far more "non-freezable" water than both the strong cationic and anionic coatings, correlating to observed ice adhesion. Liang et al. suggest that this correlation is brought by the proportion of "non-freezable" water that supports a self-lubricating water layer to reduce ice adhesion. However, unfavourable durability this system was observed, as ice adhesion strengths steadily increased for all compositions over the course of multiple cycles.

Although research of ice adhesion on hydrophilic polymer coatings is young, the shear number and depth of investigations into their anti-icing properties, either by means of exploiting an aqueous lubricating layer or nonfrozen hydration water, is significant towards the future applicability. However, questions remain as to how to best balance the chemistry and coating structure to produce a dependable and enduring system with remarkably low ice adhesion strength.

2.2 Charged polymer systems

Charged polymers are characterized by the incorporation of ionizable or ionized units into a classical polymer chain or network.[61] In the case of charged polymers with ionizable (electrolyte) units, depending on the surrounding environment, the opposite charges may dissociate with one remaining bound to the polymer chain and the other released into the volume surrounding the polymer (although still a finite distance between the polymer and the counterion exists).[62, 63] On the other hand, these units may be undissociated, where the two opposing charges maintain a small charge separation and create an ion pair. In either case, or a melding of both, the polymer chain and its respective counterions always appear charge neutral. Coming from the incorporation of electrolytes into the polymer, these charged polymers are accordingly classified as polyelectrolytes.

Polyelectrolytes can be categorized as either cationic or anionic, depending on the charge of ionizable monomer. Additionally, the behaviour of the charges in water can be used to divide them into strong polyelectrolytes and weak polyelectrolytes. Whereas strong polyelectrolytes fully dissociate when placed in water, weak polyelectrolytes may not as the degree of dissociation in the ion pair relies heavily on the pH value of the aqueous solution.[64–66]

Other classes of charged polymer systems exist (polyampholytes, and pseduo-polyelectrolytes), but most relevant to this discussion is zwitterionic polymers, with repeat units that each consist of both a positive and a negative charge, covalently bound to a polymer chain. Unlike polyelectrolytes, zwitterionic polymers possess no counterions, remaining charge neutral in each incorporated monomer unit and therefore throughout the polymer.

In both polyelectrolytes and zwitterionic polymers, these nature of the charges and the resulting polymer structures endue unique and specific properties, useful in a variety of applications.

Although they have considerable potential in various applications, synthesis of polyelectrolytes and zwitterionic polymers for coatings (or any other use-case) is often complicated by problematic monomer solubility and interfering interactions with the chosen polymerization method. Additionally, the preparation of polymer coatings provides yet another barrier to overcome, although a wide variety of chemistries and techniques are available and reviewed in a later section.

2.2.1 Synthesis of polyelectrolytes and zwitterionic polymers

Independent of their chemical structure, there are generally two strategies leading towards the successful synthesis of polyelectrolytes and zwitterionic polymers. Firstly, is through the polymerization of electrolytic/charged monomers, often through chain-growth polymerization that leads to compositionally well-defined polymers. Through this approach,

the chain length, composition, architecture, and morphological structure can all be controlled, all by tuning the polymerization method and conditions. In fact, polyelectrolytes and zwitterionic polymers) have been synthesised through free-radical and numerous other controlled reversible-deactivation radical polymerization techniques, and will be discussed in the following passages. The other pathway leading towards polyelectrolytes and zwitterionic polymers is through the post-polymerization modification of uncharged neutral polymer, discussed immediately below. Although this approach can be advantageous in the synthesis of block copolymers and circumvents the occasionally meticulous synthesis of the underlying electrolytic monomer, it may suffer in terms of functionality if the reactions towards post-polymerization modification are incomplete.

The post-polymerization modification of an uncharged neutral polymer into a polyelectrolyte or zwitterionic polymer will have the same chemical structure of those prepared through a direct polymerization (discussed in the following section). This strategy allows for the functionalization of a polymer with predefined architecture, monomer composition, and degree of polymerization, whereby tuning any or all of these defined characteristics of the precursor polymer can give a wide-variety of polyelectrolyte or zwitterionic polymer compositions. As an example, poly(p-chloromethylstyrene) (PCMS) was successfully synthesized by RAFT, giving a product with a defined molecular weight and narrow polydispersity.[67] Subsequently, the quaternization of PCMS units with excess N-butylimidazole was accomplished and found to be quantitative with regards to functionalization, as evident by ^{1}H-NMR data. Identical quaternizations have been replicated on block copolymers, to create a diblock product that self-assembles into micelles.[68]

Lastly, the qualities demonstrated by solution-based techniques also extends to producing stimuli-responsive polyelectrolyte brushes.[69] Surface-initiated atom-transfer radical polymerization (SI-ATRP) of 2-(dimethylamino)ethyl methacrylate (DMAEMA) and subsequent quaternization with various alkyl bromides gave strong polyelectrolyte brushes with varying degrees of hydrophobicity based on the grafting density and alkyl chain length.[70] Given the breadth of copolymerizations and architectures, a wide-range of charged polymer products are possible, although depending on reaction conditions and polymer composition, it may be more advantageous to approach the synthesis of polyelectrolytes and zwitterionic polymers through a direct polymerization of charged monomers.

Free-radical polymerization (FRP) of charged monomers offers the most simple and straightforward method of synthesizing any quantity of polyelectrolyte or zwitterionic polymer. This popularity lies in-part due to the resilient nature of radical polymerization towards impurities, moisture, and many functional groups.[71] However, the preparation of charged monomers often leads to products containing impurities and it is well-known that these monomers/ionic-liquids are exceptional solvent. Additionally, FPR offers the simplest form of radical polymerization - where the polymerization of acrylate, acrylamide, methacrylate, methacrylamide, vinyl charged monomers is all possible. Furthermore,

most applications do not require the controlled molecular weight and narrow polydispersity afforded by controlled methods, however many academic studies of polyelectrolytes and zwitterionic polymers use controlled radical polymerization techniques to produce a specifically desired product.

Perhaps the most controlled of these techniques, is atom transfer radical polymerization (ATRP). Although some experiments have successfully prepared polyelectrolytes through ATRP, it is mostly avoided for the direct polymerization of charged monomers as considerable and detrimental interactions are found to take place between the copper cation and charged monomer species through ion-exchange, ultimately leading to a far less controlled polymerization process. This issue can be partially circumvented by using the activator regeneration by electron transfer (ARGET) ATRP method, in which reducing agents such as phenols, ascorbic acid, hydrazine, etc., can only react with copper. In addition, due to the regenerative nature of copper catalyst in ARGET ATRP, copper concentrations can be substantially lower and therefore will have minimal interactions with charged monomer. One concern to note is that the choice of counterion in an electrolyte monomer is very important for any successful ATRP leading towards a polyelectrolyte: such that strongly coordinating ions (e.g., Cl$^-$) should be avoided, and noncoordinating ions (e.g., Tf$_2$N$^-$) should be favoured. Disparagingly, the ATRP of zwitterionic monomers is equally complicated by ionic interactions with the copper, and may also be more limited as these monomers are often exclusively soluble in aqueous solutions that usually induce the deactivation of the copper catalyst causing a loss of control. All in all, successful syntheses of polyelectrolyte and zwitterionic polymers are not facile and require extensive optimization to return a desired charged polymer.

Nitroxide mediated polymerization (NMP) avoids many of the challenges faced when conducting ATRP of charged monomers. Tailoring of the nitroxide allows for controlled homopolymerization (and sometimes copolymerization) of styrenics, acrylamides, dienes, and methacrylates, however the monomer compatibility is still limited.[72] As it stands, the synthesis of polyelectrolytes or zwitterionic polymers is not overly new, as styrenesulfonic acid sodium salt (SSNa) was shown to be prepared by NMP using TEMPO.[73]. Although polymerizations of polyelectrolytes has been shown to be successful, there is an apparent lack of maturity regarding the synthesis of polyelectrolytes through this method.[36, 74] In addition to the limited monomer classes that can be prepared, polymerization by NMP must be of high purity and degassed significantly to achieve a significantly well-controlled product, but the undeveloped nature of the technique is also likely due to the more attractive and robust nature of other reversible-deactivation radical polymerization techniques.

Lastly, one particular type of controlled radical polymerization is reversible addition-fragmentation chain-transfer, better known as RAFT polymerization, has been used more extensively in the synthesis of polyelectrolytes. Arguably the most versatile controlled

radical polymerization technique, it's characteristic versatility stems from its use of a tailorable chain-transfer agent (CTA) that relies on the degenerative transfer of radicals from an equilibrium of active and dormant species.[75] Figure 2.9 illustrates the proposed mechanism of RAFT polymerization, in which (I) a radical is generated and (II) reacts with a monomer commencing the growth of a polymer chain. A (III) RAFT pre-equilibrium is set in which a polymeric radical reacts with the CTA (commonly known as RAFT agent) to form a RAFT radical adduct or radical species, that can (IV) re-initiate with another monomer species, starting an an active chain. (V) The RAFT equilibrium, is a process of rapid interchange in which radicals are shared (ideally equally) causing chains to have equal opportunities for growth and low polydispersity, before they are ultimately (VI) terminated by bi-radical termination.
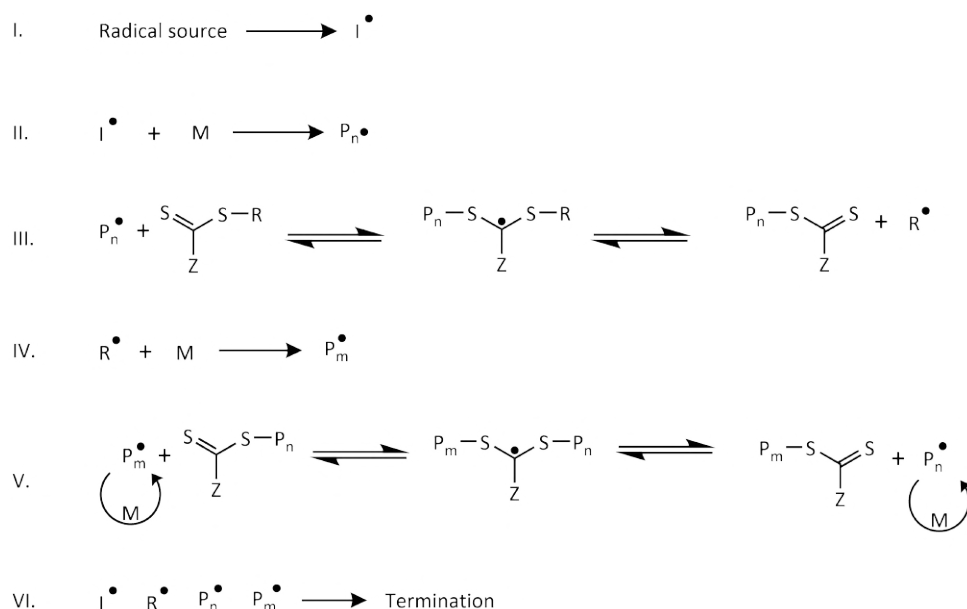
Figure 2.9: Schematic representation of RAFT polymerization. (I) initiation/activation of a radical species. (II) Propogation. (III) Reversible chain transfer pre-equlibrium (IV) Re-initiation (V) RAFT main equilibrium (VI) Termination. Adapted and reprinted with permission [75].

Based on the CTA/RAFT agent selected, mainly the substituent R and Z groups that will impact the reactivity of the $C = S$ bond, a wide-range of conditions and monomer classes can be polymerized with high control.[76] As an example, dithiobenzoates are prone to hydrolysis, while trithiobenzoates are far more hydrolytically stable. However, robustness to moisture is but one category that the chemical structure of a RAFT agent affects, as transfer constants, temperature stability, and most notably: monomer compatibility are all affected. Dithiocarbamates are very useful in the polymerization of vinyl esters and vinyl amides, while styreneics and methacrylates are often best controlled dithiobenzoates or trithiocarbonates.[75] Given varying monomer compatibilities and hydrolytic stabilities,

the choice of RAFT agent is perhaps the most important consideration in the synthesis of polyelectrolytes and zwitterionic polymers.

In the first publication introducing RAFT as a novel polymerization method, the process was successfully used to prepare PMMA, PDMAEMA, PBA, PS, and most notably PSSNa homopolymers through a variety of RAFT agents and initiators, all while maintaining a narrow polydispersity over a wide-range of molecular weights.[77] Further research into the polymerization technique found that the thiocarbonyls of (many) RAFT agents are exceptionally tolerant to water, allowing for aqueous polymerizations of charged monomers. Additionally, although RAFT is stable with regards to acidic media and degrades when exposed to base, it is extraordinarily tolerant of charged electrolyte monomers. [78, 79] In fact, polymerizations of charged monomers, whether cationic, anionic, or zwitterionic have become routine, and rather focus has been shifted to the self-assembly behaviour and applications of these polymers.[80–82]

That being said, examples of successful RAFT polymerization of polyelectrolytes are abundant, and are quickly summarized here to provide context and precedent for routes chosen in our study. Poly(DMAEMA-*co*-FMA)-*b*-polyelectrolytes were synthesized via RAFT polymerization for antifogging coating applications.[83] Cationic, anionic, and zwitterionic methacrylate based monomers were block copolymerized in aqueous isopropyl alcohol solutions, all successfully, and then covalently bound to a substrate through a UV-cured semi-interpenetrating network to be tested. Random copolymerizations of styrene and a cationic styrene-based monomer have been conducted as well in DMF, and shown minimal compositional drift upon polymerization.[84] Another attractive facet of RAFT polymerization is its specificity towards reacting mainly with the polymerizable units, often vinyl, (meth)acrylates, (meth)acrylamides, styrenics, etc., and inertness towards other functional groups, such as epoxides, thiols, alcohols, allyl, nitriles, and more. Thus in principle, it is possible to produce reactive polymers without any post-polymerization modification; a useful feature for coatings and single chain nanoparticles.

As result of the reasons outlined, RAFT polymerization is seen as the most attractive route towards the synthesis of functional charged polymers, and was ultimately chosen as the polymerization method towards polyelectrolytes and zwitterionic polymers as presented in later studies.

2.2.2   Coating formation

The formation of strong and durable polymer coatings is critical towards the functionality of the material, therefore the design and engineering of their surface attachment can be regarded as equally as significant to its desired application. Here, we provide a brief overview of mechanisms available for coating-formation/surface attachment, and provide brief considerations regarding their compatibility with charged polymers.

In line with the scope of this section, methods of deposition will not be covered in great detail, rather shortly in the following sentences. On an industrial scale, roll-to-roll coating processes (including slot-die, dip, extrusion, and hot-melt coating) or spray coating are some of the most common to prepare thin polymer films. Meanwhile, fundamental studies in research laboratories often rely on smaller-scale processes such as spin-coating or dip-coating to prepare uniform polymer films of a desired thickness. Therefore, when discussing the following chemistries, it should be noted that all employ one of these two coating methods.

Many fundamental studies, such as those of layer-by-layer (Lbl) or even hydrophobic polymer systems rely on the physical bonding (electrostatic, hydrogen bonding, or hydrophobic interactions). These forces have been proven to be stable enough to prevent their removal from a substrate, under hydration, despite no covalent attachment, however charged polymers and their hydrophilic nature can be easily removed. LbL assemblies also require many cyclic steps, realistically limiting their eventual thickness.[85, 86] Meanwhile, polymer brushes, polymer chains covalently grafted to a substrate, have been extensively explored even in charged polymer systems.[58, 87] Yet despite the promising observations, one apparent shortcoming here is their scalability, as nearly all brushes produced have been restricted to a few hundred nanometers.[88] Additional concerns here also lie in synthetic approaches to grafting (grafting-to or grafting-from) as well as the polymer brush density, both of which conceivably could affect functionality.

Moving away from these methods, it is also possible to create polymer coatings by covalently bonding (crosslinking) the polymer chains to one-another and the substrate, the latter can typically be accomplished using a functionalized silane (e.g. a polymerizable unit).[89] Concurrently, a solution of various monomers, some with multiple polymerizable groups, and an initiator is prepared. Once the solution is cast on the now-functionalized substrate, the film can be cured to create a three-dimensional polymer network.[90–92]

Additionally, the solution can contain already synthesized polymers that also bear polymerizable units (achievable through post-polymerization modification), also resulting in a surface attached polymer network.[93] However, post-polymerization modifications of charged polymers are often complicated by their solubility. Nevertheless, a solution of prefabricated polymer, monomers, and initiator can also create a stable coating and characterized as a semi-interpenetrating polymer network. In principle the linear prefabricated polymers can be separated from the network, yet in practice, chain entanglements and interactions prevent this.

Complications in the post-polymerization modifications of charged polymer systems are mainly based on solubility and interfering reactions. However, one option is to directly prepare functional charged polymers. Benzophenone, carbene insertion, nitrene generation, trialkoxysilane, thiol-ene, and catechols, have all successfully been incorporated and

used in charge poylmer systems, and thus present a base to explore.[93]

Benzophenone is a type II photoinitiator that when exposed to UV-light forms radicals, abstracting a nearby labile hydrogen atom and inserting a new carbon-carbon or carbon-nitrogen bond. Therefore, when covalently bound to a polymerizable group it can act as a pendant UV crosslinker; numerous studies have shown this possible in uncharged polymer systems. Koc et al. demonstrated the feasibility of preparing zwitterionic polymer coatings by exploiting the capabilities of the benzophenone randomly incorporated in the polymer chain.[94] Once cast onto prepared substrates and subsequently cured, the films were found to be smooth and hydrolytically stable.

Trialkoxysilanes represent an interesting case in potential crosslinking technologies. Herein lies the potential for a universal mechanism of crosslinking: between the polymer chains themselves and to the substrate. In addition, no additives or initiators would need to be added to a cast solution; rather, the cast film would only need to accommodate the hydrolysis of the trialkoxysilanes to silanols, and condensation generating crosslinks. Hydrolysis could be achieved by permitting a cast (hygroscopic) film to remain uncovered in a humid atmosphere, and the following condensation step driven by thermal curing in an oven. However, the advantages of hydrolytically sensitive crosslinking is also the primary challenge that some must overcome. The preparation of polyelectrolytes and zwitterionic polymers nearly always includes water due to their hygroscobicity. However, for the polymerization of trialkoxysilanes, all water must be removed and the product stored in a dry environment before it is cast, a thus a significant challenge in charged polymer films. Nevertheless, hydrophilic and even charged polymer coatings have been formed, although all necessitating the use of completely dry solvents.[95–97]

Thiols and alkene's react via radical addition or catalysed Michael's additions, both of which produce thioethers in high yields. A commonly employed type of "Click" chemistry, polythiols or polyenes could be mixed with multifunctional alkenes or thiols respectively, and cured to form a crosslinked product. This has mainly been accomplished by first preparing a polymer with pendant allyl functionality, predominantly through the controlled copolymerization of allyl methacrylate.[90] Upon mixing in a solution of multifunctional thiol (e.g. dithiothreitol), casting on a thiol or -ene modified surface, and either through thermal or UV curing, one can prepare a surface-attached charged polymer films. Protocols similar to the one above have been used to actively make charged polymer films with nearly any desired thickness.[98, 99] However one challenge envisioned in this approach is controlled copolymerization of allyl methacrylate, particular the competing solubiliities of charged monomers and allyl methacrylate.

In all though, there are a significant number of strategies towards preparing surface-attached stable charged polymer coatings. Rather than exploring routes of post-polymerization modifications to prepare a more functional polymer, various chemistries, such as the ones

outlined above, can be prepared and incorporated during the polymerization of charged monomers. These chemistries can be used to attach films to the surface, as well as crosslink them through themselves, ultimately delivering a stable and durable polymer coating.

2.3   Properties of charged polymers

2.3.1   Ion-pairing

Polyelectrolytes, as previously introduced, are polymers that incorporate ionizable units, whose behaviour is dependent on the surrounding environment and the ion-pair themselves. Commonly, every charge, positive or negative, on the polymer chain is balanced by oppositely charged counterions. This electrostatic effect mainly describes the total amount of counterions balancing against a charged polymer.[63] In addition to electrostatic interactions, counterions can have non-electrostatic (dispersion) interactions with the charges on the polymer. These non-electrostatic interactions are ion-specific, such that tuning of either ion (counterion or polyelectrolyte) will lead to different degrees of ion association (Figure 2.10).[100, 101] Strong interactions between the polymer and the counterion will lead to the formation of an ion-pair, whereas weaker interactions tend to be more dissociated resulting in specific-ion effects.
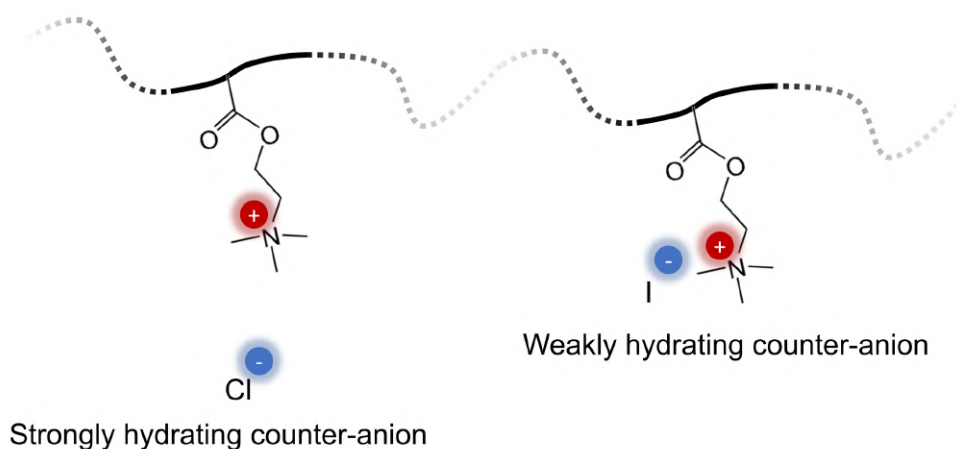
Figure 2.10: Schematic illustration of cationic polyelectrolyte charges interacting with (left) Cl⁻, a strongly hydrating counterion, and (right) I⁻, a weakly hydrating counterion, leading to variations in ion-pair. Here it is illustrated in an ideal state, such that strongly hydrating counterions will have greater degrees of dissociation when compared to weakly hydrated counterions

Such specific-ion effects are frequently discussed by the Hofmeister series, originally a ordering of an ion's ability to stabilize protein solutions.[102, 103] Over the years this classification has been extensively studies, and ion properties such as size, hydration abil-

ity, polarizability, and effect on water structure, have been generalized (Figure 2.11).[104] Typically, anions have greater effects than cations, and smaller more-charge -dense ions will lead to greater hydration and coordination with water than larger less-charge-dense ions. In consideration to ion-pair formation in polyelectrolytes, it has been seen that weakly hydrated ions generally have a greater ability to ion pair over that of highly hydrated ions. In aqueous polymer films, the effects of this ion pairing have been visualized in terms of wettability, lubrication, heterogeneous ice nucleation, and of course: swelling.[19, 87, 105–109]
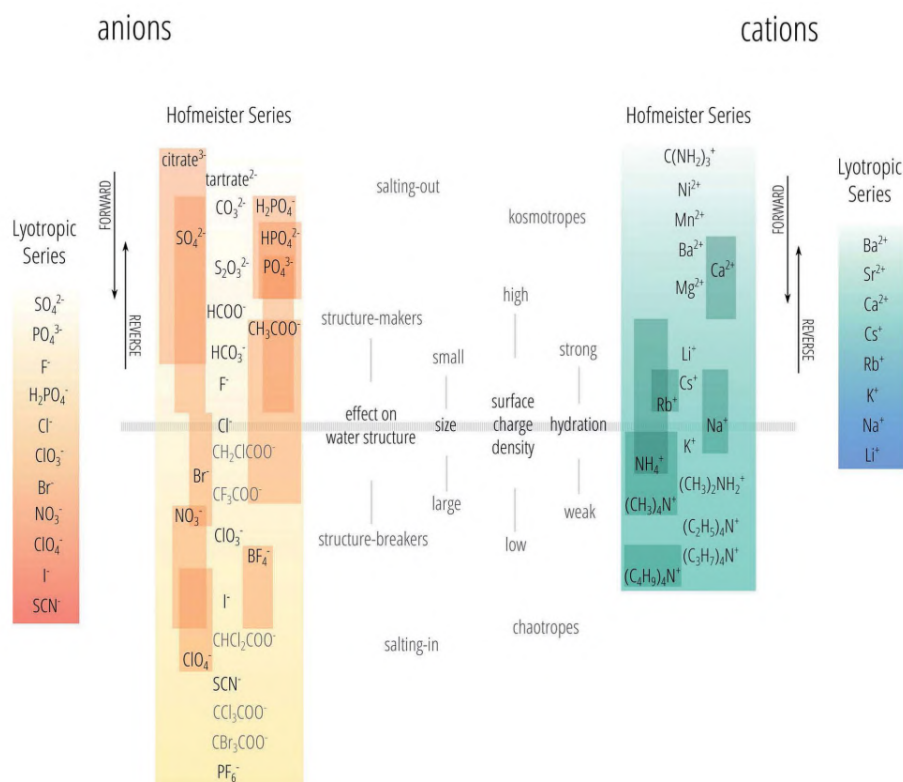
Figure 2.11: The hofmeister series and lyotropic series of ions in water. These ions are plotted against a variety of properties that they have been shown to exhibit, such as effect on water structure, size, surface charge density, and hydration. Reprinted with permission [104].

Separately, zwitterionic polymers are charge neutral and possess no dissociable counterions, as both positive and negative charged are covalently bonded to each monomer. This can lead to a plethora of intra- and inter-chain interactions, as zwitterionic functionalities can still electrostatically associate, despite the charge neutrality (Figure 2.12b in aqueous solution, before the addition dissolved electrolytes).[110, 111] Furthermore, the behaviour of the zwitterionic polymers (with regards to swelling, stiffness, surface lubrication, etc.) can be loosely predicted by the aforementioned Hofmeister series, as the nature of the cationic and anionic groups and their spacing affect the zwitterionic pair.[112–114] As

an example, poly(sulfobetaine)s display significant electrolyte-sensitive behaviour, while poly(carboxybetaine)s,, poly(phosphorylcholine)s, and poly(choline phosphate)s have display a more muted behaviour.[115–117]

2.3.2   Swelling behaviour of charged polymer coatings

Specific-ion effects are sometimes visualized by the swelling of charged polymer films Polyelectrolytes coatings, (whether in crosslinked coatings or polymer brushes) swell due to the osmotic pressure of the counterions and non-electrostatic effects. [87] Exploring further, the osmotic pressure of the counterions stems directly from the concentration gradient between the counterions in the film vs. the surrounding medium. While the total number of counterions within a polymer film is governed by the electrostatic effects, the fraction of smotically active counterions is dependent on the ability of the counterion and polyelectrolyte to form an ion pair. Thus, it is only rational that in a system with a constant polyelectrolyte chain, different counterion will form ion pairs to different degrees, resulting in different osmotic pressures and swelling behaviour.[118–121]

Additionally, polyelectrolyte coatings are known to be salt-responsive; when exposed to low salt concentrations coatings swell based on the ion-osmotic effect, while at high salt concentrations non-electrostatic effects dominate and the coating collapses. This phenomenon is known as the "polyelectrolyte effect" (Figure 2.12a).

Zwitterionic polymers have no counterions and therefore swelling in aqueous environments cannot be osmotically driven. Their swellling is far more dependent on chemistries involved; for example, in H_2O, poly(sulfobetaines) will self-aggregate, while poly(phosphorylcholines) will dissolve or swell completely.[122–124] Bringing back focus to poly(sulfobetaines), a reversed ionic strength dependence is seen, in that high concentrations of aqueous salt solutions bring about greater swelling, commonly referred to as the "anti-polyelectrolyte effect" (Figure 2.12b).[112, 115, 117, 125] Here, the characteristically strong self-association present in poly(sulfobetaines) is screened more as aqueous electrolyte concentrations increase, breaking apart self-associations and allowing greater polymer mobility. Additionally, increasing the distance between cationic and anionic moieties, commonly referred to as carbon-spacer-length (CSL), had no affect at low and high salt concentrations. Rather longer CSLs in poly(sulfobetaines) increased the coating's ionic strength sensitivity greatly.[112, 126]

2.3.3   Freezing point depression in aqueous charged polymer systems

Freezing point depression is perhaps the most well-known anti-icing strategies. In some cold climates, rock salt (mostly NaCl) is used to to melt snow or ice on roads, depressing the freezing point of the mixture by lowering the chemical potential of the once pure

(a) Polyelectrolyte effect
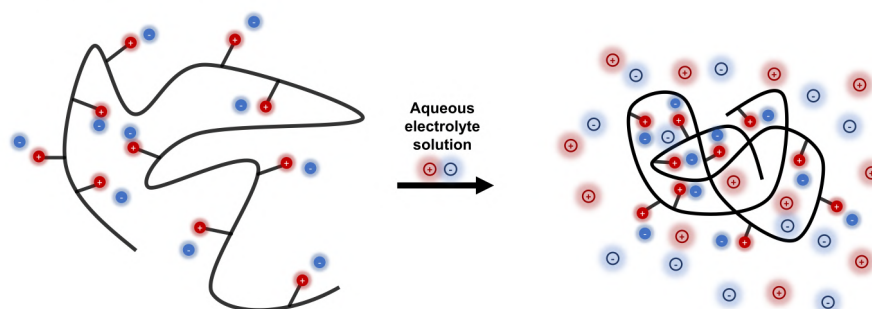
(b) Anti-polyelectrolyte effect
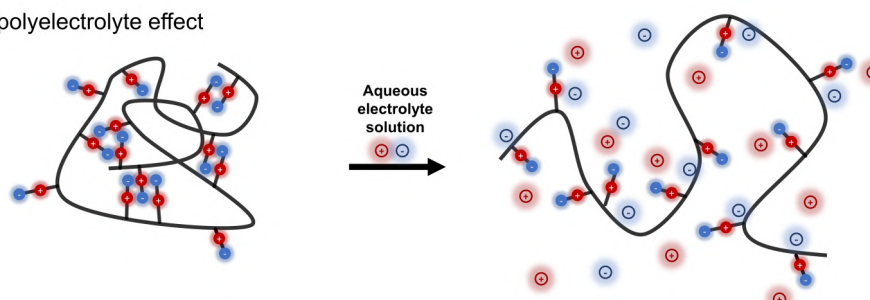
Figure 2.12: (a) The polyelectrolyte effect, showing the collapse of a cationic polyelectrolyte due to the addition of an aqueous electrolyte solution that changes the osmotic pressure difference between the polyelectrolyte and in the surrounding environment. (b) The anti-polyelectrolyte effect, displaying the result of a zwitterionic polymers expansion due the screening of charges that releases the effective physical crosslinks caused by the aggregation of zwitterionic moieties.

solvent, in this case: water. Likewise, ground de-icing of aircraft takes advantage of this phenomenon as propylene glycol or ethylene glycol solutions are sprayed onto the aircraft, where once diluted, the aqueous solution now freezes at a temperature far below the freezing point of either pure component. The theory and corresponding experiments regarding of freezing point depression in aqueous solutions of small molecules has been well laid out. In ideal and dilute conditions: the magnitude that a solutions freezing point is lowered is proportional to the amount of substance dissolved (Equation 2.4). (Inversely, this relationship can be used to determine the molar mass of the particular solute, yet only under ideal and dilute conditions). However, this method fails to account for dependence in solute association, ionic nature, partial dissociation, solubility, and effects of solute on the solvent. Using activities and activity coefficients, one can account for these deviations from ideal behaviour (Equation 2.5).

Yet, when the molar mass of the solute becomes sufficiently large, accurately calculating the freezing point depression becomes more complicated. For an aqueous polymer solution, the activity of the solvent can be given by the Flory-Huggins expression (Equation

2.6). Under dilute conditions, and when chains are longer, the expression is simplified, (Equation 2.7) whereby the term ($1x$), describing the ratio of molar volumes between polymer and solvent, converges to 0. In the two former equations presented here, χ, the Flory-Huggins interaction parameter, is introduced, and represents a dimensionless thermodynamic parameter that is characteristic of the polymer-solvent pair. Whilst not covered more here, the definition of this parameter implies a temperature dependence and experiments have shown a concentration dependence as well, although the latter is seemingly codependent on solvent quality.[127]

Despite, the laid out theory, calculations of freezing point depression for aqueous charged polymeric systems are scarce in the literature, unlike that of small-molecules. One of these studies, coincidently studying anti-icing coatings and previously discussed, attempts to rationalize the existence of an aqueous lubricating layer supplied by liquid hydration water in the PAA-DA coating. Figure 2.13 (using Equation 2.7) shows that the water can remain in a liquid state far below 0 °C, and increasing the crosslinking (and therefore reducing the volume fraction of water) will progressively depress the freezing temperature further. Similar studies, although not explicitly stated, come to the same conclusion; their results supporting the rationale that a phase transition in the hydration water, will lead to a phase transition in the lubricating layer.[50, 51, 128]

$$\Delta T_m = i \cdot K_b \cdot m \tag{2.4}$$

$$\left[\frac{1}{T_m} - \frac{1}{T_m^0}\right] = \frac{-R}{\Delta H_f} \cdot ln(a_1) \tag{2.5}$$

$$\left[\frac{1}{T_m} - \frac{1}{T_m^0}\right] = \frac{-R}{\Delta H_f} \cdot \left[ln(\phi_1) + \left(1 - \left(\frac{1}{x}\right)\right) \cdot \phi_2 + \chi_{12} \cdot \phi_2^2\right] \tag{2.6}$$

$$\left[\frac{1}{T_m} - \frac{1}{T_m^0}\right] = \frac{-R}{\Delta H_f} \cdot \left[ln(\phi_1) + \phi_2 + \chi_{12} \cdot \phi_2^2\right] \tag{2.7}$$

Zwitterionic coatings may also exhibit significant freezing point depression, owing to their inherently strong interactions with water. Using DSC, Tao et al. showed that zwitterionic polymers had such effect when combined with water, with the water exhibiting various degrees of freezing point depression at different water contents.[129] Water affected by the polymer to significantly, displayed a lower freezing point at low water contents, and higher water contents in more dilute polymer-water mixtures. Additionally, water was also observed in a 'free' state, with slightly weaker interactions resulting in lower mag-
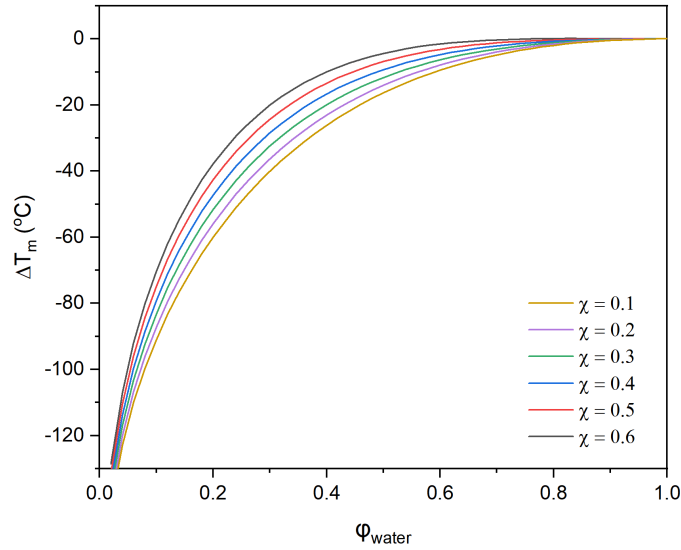
Figure 2.13: Inspired by [52], Theoretical calculations based on 2.7 versus the volume fraction of water in the system. These calculations show only slight dependence on the value of the Flory Huggins interaction parameters.

nitudes of freezing point depression, yet all near 0 °C. Lastly, water was observed in a "non-freezable" state, defined as water that does not crystallize at exceedingly low temperatures, in this paper -50 °C), but often defined as unfreezing through -80 °C to -100 °C.[55, 59, 60, 130–133]. Here, the amount of "non-freezable" water is unchanging despite increases in total water content, signifying that a threshold of this state of water has been reached, consistent with previous DSC studies of uncharged aqueous polymer solutions. Increasing crosslinker showed slight decreases in the mass of "non-freezable" water, and was attributed to the overall reduction of zwitterionic groups in the loading of polymer.

As previously discussed, Liang et. al. compared the ice adhesion strength of strong cationic, strong anionic, and zwitterionic polymer brushes, and explained the adhesion results through arguments on the proportion of "non-freezable" water, such that greater proportions of "non-freezable" water results in less strong ice adhesion.[58] DSC traces displayed all three states of water previously introduced: free, freezable, and "non-freezable". At high water contents, significant free water melting at 0 °C was observed, and freezable water affected by freezing point depression was seen to melt at temperatures ranging from -40 °C to -50 °C. However, in each system, it was demonstrated that a significant amounts of "non-freezable" water exists, and was maximized in zwitterionic polymers.

As to what makes this water "non-freezable" is complex discussion, as it is often attributed to different effects or a combination of them.[55, 59] Here, we aim to introduce the most commonly discussed reasons, as a more in depth discussion on this topic is beyond the

scope of relevant background information.

Some have postulated that "non-freezable" water is caused by the the confinement of water clusters by polymer chains.[134–136] Others have reasoned its existence to strong interactions of water molecules with polar groups of hydrophilic polymers.[114, 137–139]. Conversely, explanations regarding kinetic factors have also been put forward as explanations, proposing that "non-freezable" water contents are irrespective of the strength of polymer-water interactions and rather are dependent on the polymer glass transition.[140, 141]

No matter the root cause(s) of "non-freezable" water, the depression of waters' freezing point into either a freezable or "non-freezable" state is an unique property of in some aqueous polymer systems. Principally, charged polymers have been to have the greatest potential to affect water and depress its freezing point, these materials are ideal candidates to be explored as anti-icing materials.

2.4 Problem definition

The adhesion of ice onto any surfaces is an issue that has been investigated for decades. Attempts at mitigating ice formation (through either delaying the nucleation of ice or its propagation) have been overshadowed by the end-result that ice will inevitably form and adhere on surfaces. Therefore, to minimize the adhesion of ice, passive anti-icing surfaces with a variety of different properties have been investigated. Based on the early rationality that hydrophobicity would also correlate to icephobicity, hydrophobic surfaces have been well-studies in the literature. However, many of these surfaces do not have icephobic behaviour or display the necessary longevity due to gradually degrading/increasing surface texture. SLIPS seemingly rectify these issues, but present their own complications in longevity, requiring maintenance to return favourable anti-icing properties.

Meanwhile, more recent literature has presented encouraging signs regarding the adhesion of ice to hydrophilic polymer coatings, postulating the existence of lubricating layers, and nonfrozen interfacial water. Introducing charged moieties into the coating structure has also seemingly provide advantageous anti-icing properties, due to greater polymer-solvent (here water) interactions. However, despite the promise, an understanding as to the mechanim(s) at play remains elusive.

In this PhD thesis, I seek to gain a mechanistic understanding of ice adhesion on charged polymer coatings in order to design and formulate more effective anti-icing solutions. First, in an aim to examine the adhesion of ice to any surface, I will develop a home-built test apparatus to which I can compare the measured adhesion strength to literature. This requires a in-depth knowledge of previously testing methods to acknowledge the considerations taken, followed by the design and construction of my own home-built ice adhesion test apparatus. Secondly, I aim to produce stable surface-attached polymer hydrogel coatings, with a broad tailorability, through which changes in polymer composition will affect the resulting properties of the coating. Finally, I aim to decipher the effects of various polymer and coating properties with regards to ice adhesion. More specifically, I aim to analyse the ice adhesion on charge polymer coatings with varying counterion, polymer charge identity, or crosslink density and draw correlations in order to resolve the mechanisms of ice adhesion.

Chapter 3

Materials and methods

This section is a detailed summary of the main synthesis and characterization techniques used during this project and parts of included directly in Manuscript 1, Manuscript 2, and Manuscript 3. Where deemed necessary, background information is introduced.

3.1 Reagents

2-(methacryloyloxy)ethyl trimethylammonium solution (METAC, 75wt.% in H_2O, Sigma-Aldrich), n-butyl methacrylate (n-BMA, 99%, Sigma-Aldrich), allyl methacrylate (AMA, 98%, Sigma-Aldrich), and 2-dimethylamino methacrylate (DMAEMA, 98%, Sigma-Aldrich) were all passed through a column of basic activate aluminium oxide (Brockmann I, Sigma-Aldrich) before use. 3-sulfopropyl methacrylate potassium salt (98%, Sigma-Aldrich), 1,4-butane sultone ($\geq$99%, Sigma-Aldrich), 4-cyano-4- [(dodecylsulfanylthiocarbonyl)sulfanyl] pentanoic acid (CDPA, 97%, Sigma-Aldrich), 4,4-azobis(4-cyanvaleric acid) (ACVA, $\geq$98%, Sigma-Aldrich), 1,3,5-Trioxane ($\geq$99%, Sigma-Aldrich), 3-mercaptopropyl trimethoxysilane (3-MPTMS, 95%, Sigma-Aldrich), $1H$,$1H$,$2H$,$2H$- perfluorooctyltriethoxysilane (98% , Sigma-Aldrich), pentaerythritol tetrakis (3-mercaptopropionate) (PETMP, $\geq$95%, Sigma-Aldrich), toluene ($\geq$99.8%, VWR Chemicals BDH), acetonitrile ($\geq$99.9%, VWR Chemicals BDH), dichloromethane (100%, VWR Chemicals BDH), dimethylformamide ($\geq$99.9%, VWR Chemicals BDH), diethyl ether ($\geq$99.9%, VWR chemicals BDH) 2,2,2-trifluoroethanol (TFE, gqe99%, Sigma-Aldrich), chromosulfuric acid (Merck), sodium fluoride ($\geq$99%, Sigma-Aldrich), sodium fluoride ($\geq$99.99%, Sigma-Aldrich), potassium chloride (99-100.5%, Sigma-Aldrich), sodium chloride ($\geq$99.999%, Sigma-Aldrich), sodium bromide ($\geq$99%, Sigma-Aldrich), sodium bromide ($\geq$99.99%, Sigma-Aldrich), potassium iodide ($\geq$99.5%, Sigma-Aldrich), potassium iodide ($\geq$99.99%, Sigma-Aldrich), sodium thiocyanate ($\geq$98%, Sigma-Aldrich), and sodium thiocyanate ($\geq$99.99%, Sigma-Aldrich), were all used as received. All water used was passed through a Sartorius Arium Pro ultrapure water system

or an equivalent Millipore Integral 15 filtration unit (resistivity of 18.2 MΩ cm).

3.2 Polymer Synthesis

RAFT polymerization was selected as it is a robust and convenient method to produce polyelectrolytes and zwitterionic polymers. Design choices for the production of coatings (to be discussed in greater detail in Chapter 5, also pointed towards RAFT as a ideal polymerization technique, as it could support water as a co-solvent, did not evidently react with allyl functionality of a co-monomer, and could co-polymerize three monomers without significant compositional drift.

3.2.1 Synthesis of cationic polyelectrolytes

A 50mL, round-bottomed flask containing METAC (75 wt.% in H_2O, 1.996 mL, 1.654 g, 7.963 mmol), n-BMA (3.295 mL, 2.944 g, 20.7 mmol), AMA (0.428 mL, 0.402 g, 3.186 mmol), 4-cyano-4-[(dodecylsulfanylthiocarbonyl)sulfanyl] pentanoic acid (63.47 mg, 0.157 mmol), ACVA (4.41 mg, 0.0157 mmol), DMF (9.30 mL), H_2O (2.32 mL), and 1,3,5-trioxane as internal standard (∼50 mg), was sparged with N_2 for approximately 30 min. The flask was kept under an inert nitrogen atmosphere and subsequently lowered into a pre-heated 70 °C oil bath and monitored via ^{1}H-NMR until completion. The solution was removed from heat, exposed to atmosphere, and precipitated into a large excess of cold stirred diethyl ether, then collected and dried under vacuum at 30 °C overnight. The afforded polymer, poly(METAC-co-BMA-co-AMA)$_{25/70/10}$ was characterized by ^{1}H-NMR and confirmed to have approximately 25 mole percent METAC and 10 mole percent AMA functionalities.

Analogous polymerizations were made containing 5 and 15 mole percent AMA, and 70 and 60 mole percent BMA respectively, to maintain the targeted 25 mole percent METAC functionality while increasing the functionality of AMA. Polymers made with 5, 10, or 15 mole percent AMA were labeled as such and given the monikers Poly-Cat-L, Poly-Cat-M, and Poly-Cat-H, respectively (*L M*, and *H* being representative of the *low, medium,* and *high* mole fraction AMA incorporated).

Figure 3.1: Schematic of cationic polyelectrolyte synthesis by RAFT polymerization in which the target compositions are x_{METAC}=0.25, and x_{AMA}=0.05, 0.10, or 0.15

3.2.2 Synthesis of anionic polyelectrolytes

SPMA-K (1.886 g, 7.502 mmol), n-BMA (3.103 mL, 2.774 g, 19.5 mmol), AMA (0.404 mL, 0.379 g, 3.000 mmol), 4-cyano-4-[(dodecylsulfanylthiocarbonyl)sulfanyl] pentanoic acid (59.84 mg, 0.148 mmol), ACVA (4.15 mg, 0.0148 mmol), DMF (8.11 mL), H_2O (2.69 mL), and 1,3,5-trioxane as internal standard ($\sim$50 mg) was added to a 50 mL round-bottomed flask. The solution was stirred and sparged with N_2 for approximately 30 min before the flask was placed into a pre-heated 70 °C oil bath while maintaining an inert atmosphere by purging with nitrogen. The polymerization was monitored by ^{1}H-NMR until completion, then removed from heat, exposed to atmosphere, and precipitated into a large excess of cold stirred isopropanol. The polymer was collected by vacuum filtration and redissolved in a minimal volume of DMF/H_2O (10 mL, 8 mL DMF and 2 mL H_2O before being precipitated once more into cold stirred diethyl ether. Upon collection by vacuum filtration, the resulting polymer was dried overnight in a vacuum over at 30 °C overnight. The afforded polymer, poly(METAC-co-BMA-co-AMA)$_{25/65/10}$ was characterized by ^{1}H-NMR and confirmed to have approximately 25 mole percent METAC and 10 mole percent AMA functionalities.

Corresponding polymerizations of anionic polyelectrolytes containing 5 and 15 mole percent AMA, and 70 and 60 mole percent BMA respectively, were also synthesized. The polymers were denominated Poly-An-L, Poly-An-M, and Poly-An-H, based on 5, 10, or 15 mole percent AMA respectively, in a similar fashion to the previously mentioned cationic polyelectrolytes.
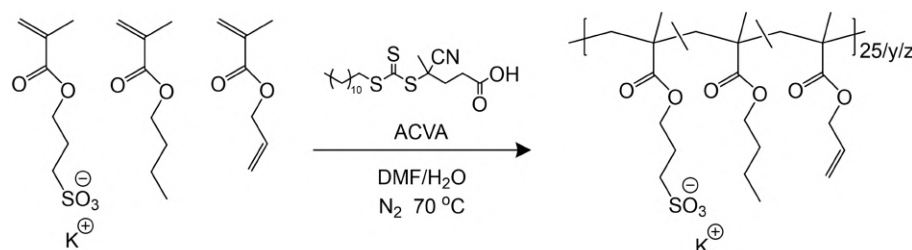
Figure 3.2: Schematic of anionic polyelectrolyte synthesis by RAFT polymerization in which the target compositions are x_{SPMAK}=0.25, and x_{AMA}=0.05, 0.10, or 0.15

3.2.3 Synthesis of zwitterionic polymers

3-(N-2- methacryloyloxyethyl-N,N-dimethyl) ammonatobutanesulfonate (MABS) zwitterionic monomer was prepared beforehand accordingly.[142]

Zwitterionomer MABS (2.056 g, 7.007 mmol), n-BMA (2.900 mL, 2.591 g, 18.22 mmol), AMA (0.377 mL, 0.354 g, 2.803 mmol), 4-cyano-4-[(dodecylsulfanylthiocarbonyl)sulfanyl] pentanoic acid (55.94 mg, 0.139 mmol), ACVA (3.88 mg, 0.0139 mmol), TFE (10.09 mL), and 1,3,5-trioxane as internal standard ($\sim$50 mg) was added to a 50 mL round-bottom

flask containing a teflon-coated magnetic stir bar. The solution was sparged with N_2 while stirring for approximately 30 min, after which it was placed into a 70 °C oil bath, and monitored by ^{1}H-NMR. Once complete, the solution was precipitated into a large excess of cold stirred diethyl ether, collected by vacuum filtration and dissolved once more into a small amount of lightly heated TFE ($\sim$15 mL), and precipitated once more into diethyl ether. before being collected by vacuum filtration. The product was dried overnight at 30 °C before being characterized by ^{1}H-NMR, which confirmed the molar percentage of each monomer into the polymer was accurate to the targeted functionality ($\sim$ 25 mole percent MABS, and 10 mole percent AMA).

Likewise to cationic and anionic polyelectrolytes, a total of 3 polymerizations were completed to afford zwitterionic polymers each with 25 mole percent zwitterionic functionality, but with 5, 10, or 15 mole percent AMA (and 70, 65, and 60 mole percent BMA respectively). In line with cationic and anionic polyelectrolytes, these products were identified as Poly-Zwitt-L, Poly-Zwitt-M and Poly-Zwitt-H, based on the level of AMA functionality.
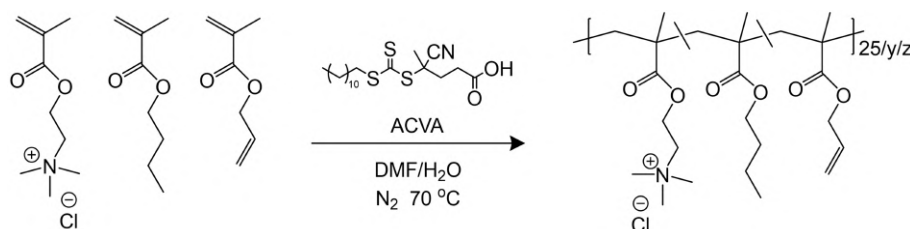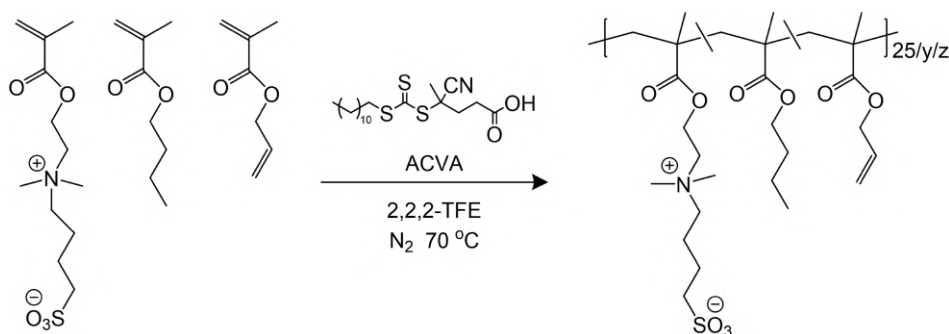

Figure 3.3: Schematic of zwitterionic polymer synthesis by RAFT polymerization in which the target compositions are x_{MABS}=0.25, and x_{AMA}=0.05, 0.10, or 0.15

3.2.4 Synthesis of nonionic polymers

BMA (1.0187 mL, 0.910 g, 6.401 mmol), AMA (0.0956 mL, 0.0897 g, 0.711 mmol), 4-cyano-4-[(dodecylsulfanylthiocarbonyl)sulfanyl] pentanoic acid (14.15 mg, 35.1 µmol), ACVA (0.98 mg, 3.51 µmol),DMF (2.56 mL) and 1,3,5-trioxane as internal standard ($\sim$10 mg) was added to a 25 mL round bottom flask. After sparging with N_2 for 30 min, the flask was placed into a 70 °oil bath and monitored by ^{1}H-NMR until completion, before being precipitated directly into an excess of cold methanol. The polymer was collected by vacuum filtration and driend overnight at 30 °C before characterization by ^{1}-NMR to confirm the targetted content of AMA in the copolymer ($\sim$10 mole percent).

Additionally, polymerization with 5 and 15 mole percent were completed, with the remainder of the polymer being composed of BMA. In accordance with the targeted content of AMA, the polymers were labelled Poly-Non-L, Poly-Non-M, and Poly-Non-H.
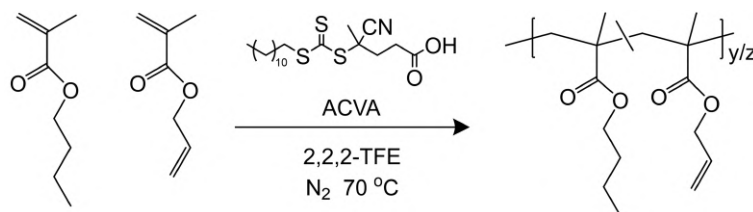
Figure 3.4: Schematic of non-ionic polyBMA-*co*-AMA polymers, in which x_{AMA} =0.05, 0.10, or 0.15

3.3 Preparation of coatings

In order form stable coatings, the prepared polymers must be surface-attached, that is covalently bound to the underlying substrate. Furthermore, as a route to the goal of thin-film hydrogels, crosslinking of the polymer film was necessary. Therefore, rather than having two separate methods, one for surface attachment and the other for crosslinking, a single thiol-ene cure was selected to accomplish both tasks and prepare a surface-attached thin-film hydrogel. Therefore, thiol-functionalized surfaces were required, and spin-coating was used to consistently produce coatings of a desired thickness. Following this, coatings were cured (by thermal radical initiation of the thiol-ene reaction) in order prepare a homogeneous and smooth surface.

3.3.1 Surface functionalization of substrates

Thermally oxidized silicon wafers ($\sim$19 mm x $\sim$19 mm) were rinsed with acetone, ethanol, and milli-Q water twice before a treatment with H_2O plasma at 500 mTorr for 180 sec. Following this, the substrates were then submerged into a lightly stirred solution of 3-MPTMS in toluene (20 vol.%) at room temperature for 3 h. The wafers were then dried under a dry stream of nitrogen and thermally cured at 130 ℃ for 2 h to induce the dehydration condensation of the silane on to the substrates. Similarly, a slightly altered procedure was used for the functionalization of silica hemisphere, whereby they were initially cleaned using lightly heated chromosulfuric acid and then washed thoroughly with milli-Q water before plasma treatment.

3.3.2 Spin coating and curing

A previously synthesized polymer was dissovled in TFE (1.25 wt./vol. %) with an equimolar amount of ACVA and PETMP, with respect to the AMA content of the polymer. This solution was vigorously stirred for at least 30 minutes before passing through a 0.22 µm filter. $\sim$225 µL of this solution was then spin-coated onto the prepared substrates (2000 rpm for 40 sec) after which the coatings were placed in a 90 ℃ oven for 2 h to induce radical generation and thiol-ene click chemistry. The coatings were washed with excess

water to remove any unattached material and dried under a dry nitrogen stream before use. For the silica hemispheres, an identical procedure was used with the exception that only 60 µL of solution was added onto the flat-side of the hemisphere for spin coating, corresponding to the decrease in surface area.

Although UV-curing was possible and was successful in preparing surface-attached hydrogels, a noticeably higher roughness was observed when compared to coatings that had been thermally cured.

3.3.3 Counterion exchange

In order to exchange the counterions of the coatings, the coatings were placed in a home-built sample holder and submerged in a stirred 100 mM solution of sodium or potassium salt accompanying the preferred counterion. The coatings were stirred for 30 min after which they were rinsed with excess water and dried under nitrogen.

3.4 Characterization

A variety of characterization were used during the project, including NMR and AFM, however, here the focus is solely on the main techniques used in the project of ice adhesion strength measurements, TIR Raman spectroscopy, and ellipsometry.

3.4.1 Ice adhesion strength measurements

Background

As this technique was home-built and is a major part of my work, background information regarding its design, construction, and validation will be discussed in *Chapter 4*.

Experimental details

A home-built shear adhesion apparatus was used to measure the ice adhesion strength of the samples. A pneumatic piston (MQQTB16-50D, SMC Corp.) with a load cell (8413-5050, 50N, Blichfeld) attached to a plastic pushing rod, was used to push an ice-filled Teflon cuvette (pre-treated with $1H,1H,2H,2H$ - perfluorooctyltriethoxysilane). The pushing force was controlled using a pressure regulator (ARX20-F01, SMC Corp) set to 3.0 bar, with an adjustable flow restriction valve (AS1002F, SMC Corp.) set to 10mL min-1. A cork-insulated stainless-steel chamber with square indents (20 mm x 20 mm x 0.5 mm) in which the coatings were placed and secured to the stage, was temperature controlled by a recirculating chiller (AD15R-30, 462-0230, VWR) flowing cooled fluid through a connected baseplate. Ice/coating samples were prepared by first placing the Teflon cuvettes into a home-built cuvette holder functioning as a weighted alignment piece, then inserting the holder into the pre-cooled chamber, and filling each cuvette with

degassed pure water (0.7 mL). The samples were frozen at -20 °C for 1 h, before the measurement temperature was set and allowed to equilibrate for 1 h more.

3.4.2 TIR Raman spectroscopy

Background

Raman spectroscopy is an established non-invasive and non-destructive technique to characterize many types of samples. However, its sensitivity is limited when attempting to characterize thin films and monolayers, until the development of surface-enhanced Raman scattering (SERS). The development of TIR Raman stalled with the growth of SERS, despite Iwamoto et al. was demonstrating the ability to record the spectra of a thin polystyrene film without any signal of the underlying substrate or surface enhancement.[143] However, TIR Raman maintains the advantage of versitility, and can be applied to a wide variety of systems without the restrictions imposed by SERS.[144]
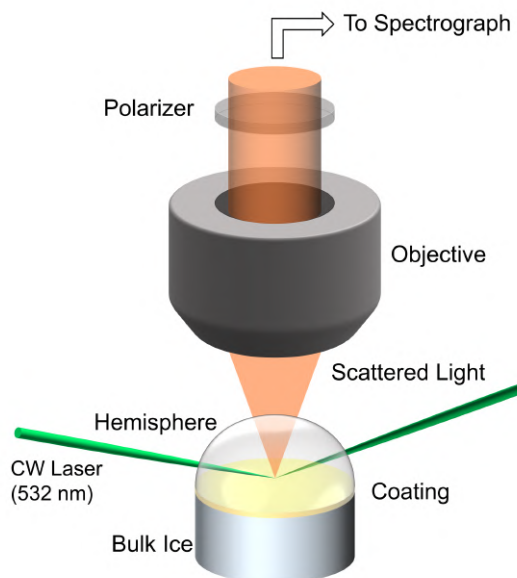
Figure 3.5: Diagram of TIR Raman setup, in which (S or P) polarized incident light is focused onto a bottom surface of the hemisphere where the polymer coating is. Raman scattered light is emitted and collected by an objective of an optical microscope before passing through another polarizer (x or y) before being sent to the spectrograph. Figure is redrawn and adapted with permissions [145]

In a typical TIR Raman setup (Figure 3.5), a beam of light from an excitation source is aimed at a hemisphere sample at a specific angle of incidence (AOI), and is focused on the flat-side of the hemisphere - where the sample is located. The Raman scattered is emitted and collected by an objective, passed through more optics (polarizers and filters), and sent to a spectrograph. Based on the AOI of the incident light, the penetration depth

of the evanescent wave into the sample changes, whereby angles above a critical angle (based on the refractive index of the two materials) will be completely reflected (TIR). Simply put, as angle of incidence increases, the penetration depth of the evanescent wave decreases, and the Raman scattered light is dominated by an decreasingly thin layer of the sample. In the setup used, a sufficiently large angle of incidence was employed, ensuring a TIR Raman response of the molecular vibrations only in the coating (Figure 3.6).
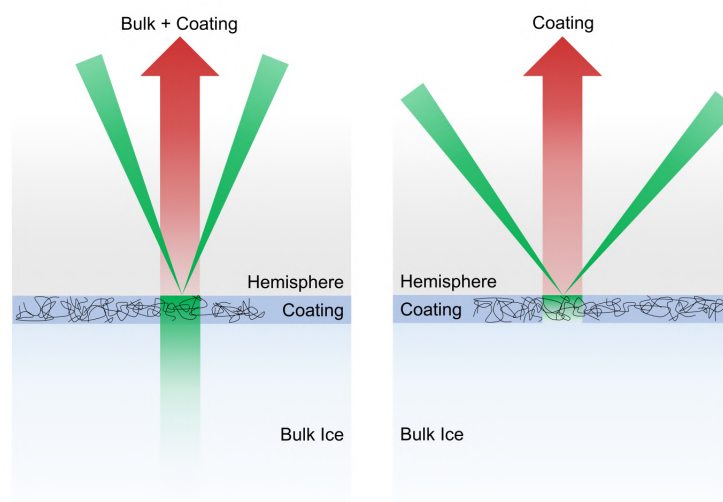
Figure 3.6: Cross-sectional illustration of (left) incident light focused on the hemisphere-coating interface that penetrates through the coating and into the bulk ice, leading to Raman signal from both the coating and the bulk ice. (right) Higher AOI incident light is focused onto the hemisphere-coating interface, the penetration depth of which is below that of the thickness of the coating. Therefore Raman signal should only come from the molecules of the coating and its hydration water.

Experimental details

A home-built spectrometer has been described in detail previously and was used for all experiments(Figure 3.5).[28] A 532 nm CW laser (20 mW) was used as an excitation source and focused onto a coated silica hemisphere sample held in a custom sample holder used for all *in-situ* freezing experiments and described in more detail here.[29] A stainless-steel body circulated cooling fluid at a desired temperature, set by a recirculating chiller (Julabo FP-50 ME) and monitored by an embedded thermocouple placed in close proximity to the silica-ice interface. The sample was fit by placing the coated silica hemisphere (radius = 5 mm) on top of a Viton O-ring and sealed using two homemade clamps made of high

thermal conductivity polymer (CoolPoly-E5101, Cool Polymers/Celeanese, RI, USA) that were screwed into the stainless steel cell body. A very weak laminar flow of dry cold air was established with two plastic tubes placed near the sample in order to purge any condenstation on the hemisphere during freezing experiments that would impair the path of the excitation source or Raman scattered light.
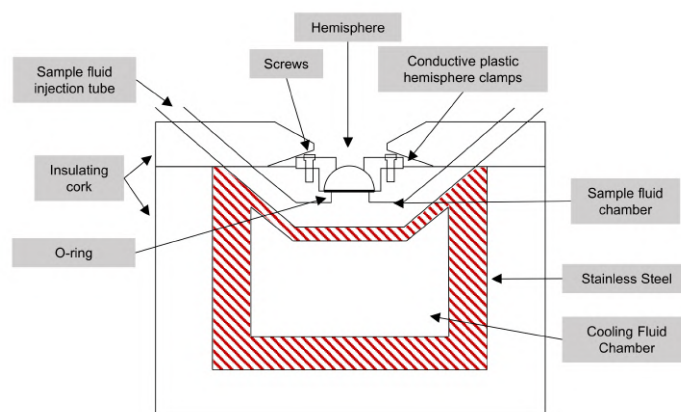
Figure 3.7: Cross-sectional illustration showing the intricate design of a custom-built ice-cell/sample holder, allowing for considerable control of the temperature of ice and hemisphere, and interfaces.

Degassed ultrapure water was carefully introduced into the sample fluid cell, filling the chamber in its entirety. Yet, as the volume expansion of freezing water into ice would break the cell if in a completely closed system, it was necessary to carefully introduce an air-bubble into the sample fluid chamber. In order to be analogous to our ice adhesion measurements and ensure that bulk ice is frozen onto the coating, the entire freezing process was conducted upside-down, ensuring this and that the air-bubble would not be at the sample interface. Then, identically to ice adhesion measurements, the sample was frozen at 20 °C for a minium of 1 h, before being orientated correctly and placed in the Raman spectroscopy setup. The temperature was subsequently lowered to -35 °C (temperature of the thermocouple at the silica-ice interface) and incrementally increased through to -0.7 °C. The sample was allowed to equilibrate for at least 15 min before spectra were collected at each temperature.
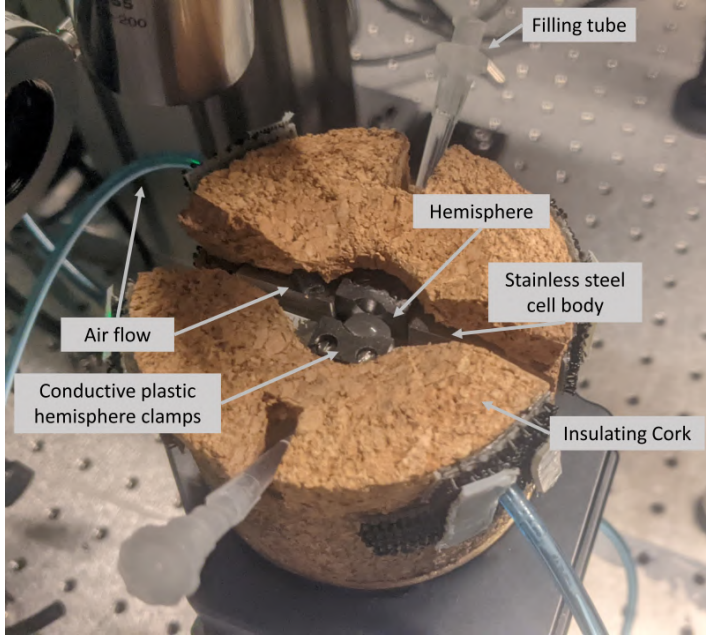
Figure 3.8: Frozen set-up of custom built ice-cell. Air flow tubes can be seen supplying a weak laminar flow of cool dry air to the surface of the hemisphere in an attempt to wick away any condensation on the surface of the hemisphere. Filling tubes are more clearly seen, where various fluids can be inserted into the chamber, yet here only water is added in the chamber, leading to ice.

Figure 3.9: Frozen set-up of custom built ice-cell. Air flow tubes can be seen supplying a weak laminar flow of cool dry air to the surface of the hemisphere in an attempt to wick away any condensation on the surface of the hemisphere. Filling tubes are more clearly seen, where various fluids can be inserted into the chamber, yet here only water is added in the chamber, leading to ice.

The Raman scattered light was collected by an ultra-long working distance objective (M-Plan Apo 50X, NA 0.55, Mititoyo, Japan) attached to a microscope (Zeiss, Germany) and directed into a combined spectrometer and CCD camera (Shamrock 303i, Newton DU940N-BV, Andor, Ireland). The penetration depth of the evanescent wave into the sample was controlled through the angle of incidence of the beam into the sample. Using polarization optics (Thorlabs, USA) set in the beam path, spectra were collected using s-polarized incident light and y-polarized scattered light, unless otherwise stated.

The design of the ice cell was such that counterion exchange could easily be accomplished without removing the hemisphere. Similar to the silicon-wafer based coatings, a 100 mM salt solution with the desired counterion was prepared after which the sample fluid chamber was filled with said solution and left undisturbed for 20 min. The solution was then drained, and more fresh salt solution was introduced and left to rest for another 20 min. After the second washing with the chosen salt solution, the chamber was drained and a minimum of 100 mL degassed ultra water was passed through to wash the cell chamber before freezing measurements.

The presented spectra have been smoothed using a running average over five data points, baseline subtracted, and finally normalized to the highest intensity peak. To quantify any observed phase transition of hydration water in the coating, a three-component linear combination model was used (Equation 3.1), consisting of a polymer component (X), a frozen-ice component (B), and a liquid-water component (C). S represents the model spectrum, Ref_A, Ref_B and Ref_C are given reference spectra (of polymer, ice, and water, respectively), and X, Y and Z are calculated coefficients.

$$S = (X \cdot Ref_A) + (Y \cdot Ref_B) + (Z \cdot Ref_C) \tag{3.1}$$
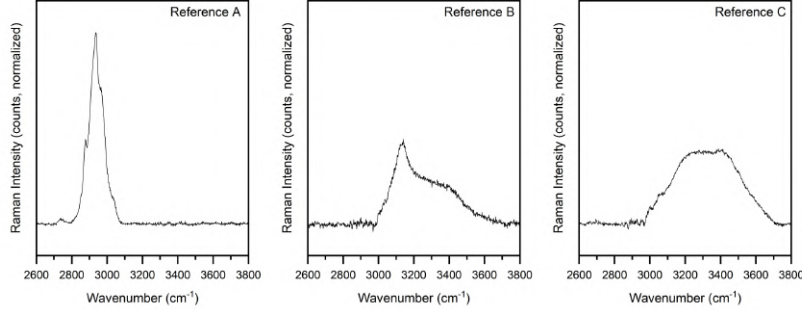
Figure 3.10: Reference spectra of (left) Ref_A, displaying the spectrum of of Cat-M-(Cl⁻) at -20 ℃, (middle) Ref_B of frozen ice in the coating at -35 ℃ without contributions of the polymer, and (right) Ref_C showing liquid water hydrating the coating at -0.7 ℃.

The reference spectra produced are critical to correctly quantify each system. The reference spectrum of the polymer, Ref_A, was produced by taking a spectrum of Cat-M-(Cl⁻), at -20 ℃, and then creating a baseline over any remaining signal over 3080 cm⁻¹, that would pertain to significant signal from H_2O. Suitable references of frozen-ice and liquid-water components were produced using spectra collected at -35 ℃ and -0.7 ℃ respectively. For both of these, the aforementioned polymer component (Ref_A) was scaled with regards to peak height and subtracted from the spectrum collected at -35 ℃, giving Ref_B and Ref_C, corresponding to ice and liquid water.

By combining the reference spectra (Figure 3.10), an accurate model of the spectra at any temperature could be verified. Figure 3.11 displays collected spectra at various temperatures overlaid with our model outlined in Equation 3.1. Undoubtedly, the linear combination of these three reference spectra can be used to describe any of the spectra. Therefore, by gathering the coefficient (X, Y and Z), relating to the scaling of the reference spectra, one can determine the phase fraction of the liquid water or ice in a particular spectrum. Equations 3.2 and 3.3 were used to calculate the ice and liquid water phase fractions for a sample as a frunction of temperature, independent of polymer.
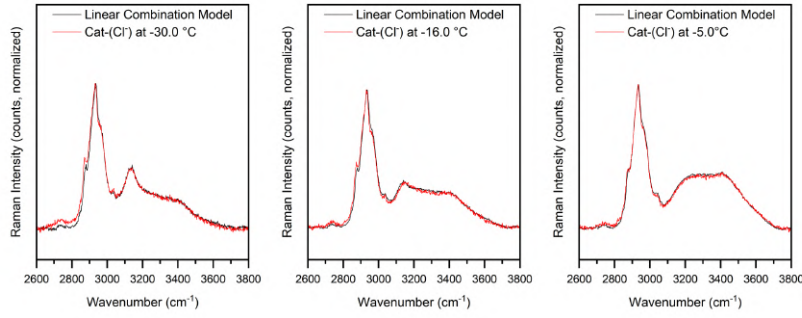
Figure 3.11: Fittings of TIR Raman data at (left) -30 °C, (middle) -16.0 °C, and (right) -5.0 °C using Equation 3.1. As can be observed, the data can be fit well by the simple three-component linear combination model.

$$Frozen - phase - fraction(f_{ice}) = \frac{\frac{Y}{X}}{\frac{Y}{X} + \frac{Z}{X}} \tag{3.2}$$

$$Liquid - phase - fraction(f_{water}) = \frac{\frac{Z}{X}}{\frac{Y}{X} + \frac{Z}{X}} \tag{3.3}$$

3.4.3 Differential scanning calorimetry

Background

Differential scanning calorimetry (DSC) is a commonly used tool to characterize the phase transition of polymers, solutions, and mixtures. The underlying principle of the technique is when a phase transition occurs in a sample, more or less heat flow will be required in comparison to a reference to keep both the sample and reference at the same temperature.[146] The DSC measures both these heat flows as a function of temperature (or time), and records the difference, producing a DSC thermogram (Figure 3.12). Sometimes, phase transitions will be exothermic and release heat into the system, such as condensation or freezing. In an opposite fashion, endothermic transitions can also occur, where the system consumes heat during a transitions, as in melting. Not only are the temperatures at

which phase transition occur, but the amount of heat required or released in the phase transition can be of great use.
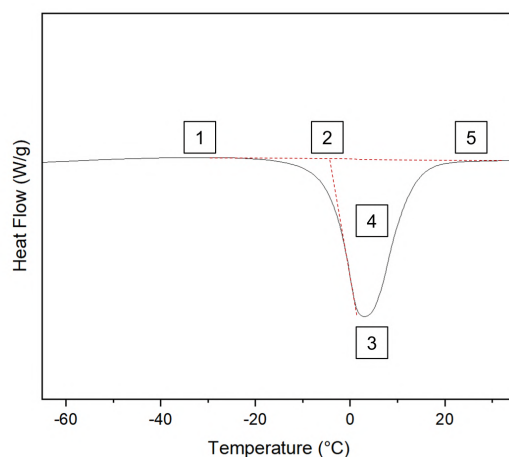
Figure 3.12: Representative thermogram of melting transition with various important points labelled: (1) the pre-transition baseline (2) onset melting temperature (3) peak melting temperature (4) area of melting endotherm and (5) post transition baseline.

In the to-be-described experiment(s), DSC was used solely to characterize the melting phase transition of a polymer-water mixture. Here, the onset melting temperatures, T_m, were recorded, in addition to the enthalpy of fusion, ΔH_f. While the T_m is valuable in determining the magnitude of freezing point depression, the ΔH_f is necessary to determine the "non-freezable" water content. This can be accomplished by comparing the recorded ΔH_f of the sample and comparing it to the hypothetically ideal ΔH_f of the sample, in which all the water in the sample undergoes a phase transition. Assuming that the recorded $\Delta H_f \leq \Delta H_{f\,ideal}$, then the "missing" enthalpy is described as belonging to water termed as "non-freezable".

Experimental details

In an effort to determine the states of water in aqueous polymer systems, differential scanning calorimetry (DSC) was used. To this end, a TA Instruments Q200 DSC with RCS 90 (TA Instruments - Waters LLC, USA) was used. A determined amount of polymer, e.g. Poly-Cat-M-(Cl⁻),and water corresponding to a wide range of mass fractions of water (w_{H_2O} = 0.09 - 0.8) was hermitcally sealed in aluminum pans (Tzero Pans and Tzero Hermetic Lids TA Instruments - Waters LLC, USA) and left to equilibrate over 48 h at room temperature. The sealed pans were cooled from 25 ℃ to -90 ℃, held for 10 min, then heated to 40 ℃ at a rate of 5 ℃ min⁻¹.

Data was analysed by Universal Analysis software, and onset melting points, T_m's were assigned. The enthalpy of fusion was calculated by integrating the area of the endother-

mic phase transition, giving the amount of freezable water in the sample (Equation 3.4). "Non-freezable" water content was calculated by determining the difference between the expected melting transition enthalpy if all water in the sample is freezable, and the measured enthalpy (as stated before and in Equation 3.5).

$$m_{\text{H}_2\text{O freezable}} = \frac{\Delta H_f}{334 mJ/mg} \qquad (3.4)$$

$$m_{\text{H}_2\text{O "non-freezable"}} = m_{\text{H}_2\text{O total}} - m_{\text{H}_2\text{O freezable}} \qquad (3.5)$$

3.4.4 Ellipsometry

Background

Spectroscopic ellipsometry is a non-destructive optical technique widely used to characterize thin-films, particularly thickness, roughness, and its optical properties. Simply put, ellipsometry measures the change in polarization of light as it interacts/reflects off a sample.[147] Figure 3.13 depicts this in greater detail; a light is emitted and passed through a polariser where it is typically linearly polarized, meaning the s-polarized and p-polarized light are in-phase. Upon reflection from a sample, the polarizations of the light are out-of-phase and the polarization state is denoted as "elliptic."[148] The change in polarization state, from linear to elliptic is measured by a second polariser coupled to a detector. It is this change in polarisation, commonly described by the reflection coefficients ratio of the polarized light, and is a complex function of wavelength, optical parameters of the substrate, the film, surrounding environment, and angle of incidence (Equation 3.6).[147]
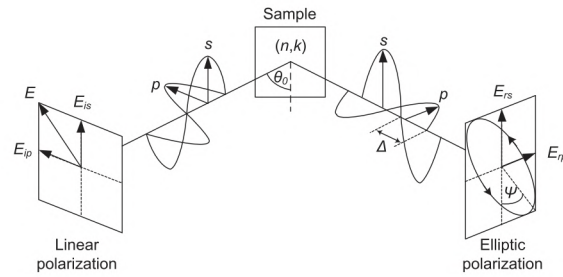
Figure 3.13: Schematic illustration of the ellipsometry measurement principle. Reprinted with permission from [148] based on an adapted figure taken with permissions [149].

$$\rho = \frac{r_p}{r_s} = \rho(\theta_i, \lambda, n_{\text{substrate}}, n_{\text{environment}}, n_{\text{sample}}, k_{\text{sample}}, d_{\text{sample}}) = tan(\Psi)exp(i\Delta) \qquad (3.6)$$

Experimental details

A variable angle spectroscopic ellipsometer (M-2000, J.A. Woollam Co., USA) using CompleteEASE software (JA Woolam Co., USA) was employed to determine the thickness of the polyelectrolyte coatings. The presented data is a result of three identically prepared samples that were used for both dry and hydrated measurements in order to demonstrate the reproducibility of both sample preparation and the measurement technique.The dry measurements were conducted over a wavelength of 250 – 1000 nm at five angles of incidence (55°, 60°, 65°, 70°, and 75°), by placing the coating onto the sample stage at room temperature, where a steady stream of nitrogen was used to resolve any other ambient factors e.g., humidity. The Ψ and Δ data collected was modelled using a three-layer system composed of a silica substrate, a silicon dioxide layer (100 nm in thickness), and a final empirical Cauchy model that is used to describe the polymer coating. The film was assumed to be homogeneous and transparent, with no adsorption ($k = 0$), therefore the refractive index could be simply described by Equation 3.7.[150]

$$n(\lambda) = A + B/\lambda^2 \tag{3.7}$$

$$0 = f_w \frac{n_w^2 - n^2}{n_w^2 + 2n^2} + (1 - f_w) \frac{n_p^2 - n^2}{n_p^2 + 2n^2} \tag{3.8}$$

To determine the hydrated thickness of the coatings, a standard liquid cell (5mL Heat Liquid Cell) was set to 25 °C and used to collect the Ψ and Δ data at an angle of incidence of 75°over a wavelength of 250 – 1000nm. In this setup, water was flowed into the cell, and the samples left to equilibrate for at least 20 min before measurement. While the silica and silicon dioxide layers of the model used remained, the thickness of the hydrated polymer film was determined using a two-component layer consisting of the dry polymer (with fitted A and B parameters given by dry measurements) and water. By fitting according to the Bruggeman Effective Medium Approximation (BEMA) model (Equation 3.8, both the hydrated film thickness and volume fraction of water in the coating could be estimated.[151]

Chapter 4

Development of ice adhesion apparatus

In order to qualitatively and quantitatively describe the anti-icing behaviour, more specifically, the adhesion strength of ice to a surface, it was necessary to design and construct an ice adhesion test apparatus. The following outlines the basic test methods that have been previously explored, considerations to be made both when measure the adhesion strength of ice to materials and in the design of the test rig, the design and construction of a home-built ice adhesion test apparatus, and its validation through a comparison of reference values. The end result of this work, is the ability to measure the temperature dependent ice adhesion strength on a variety of surfaces.

In this chapter, key aspects (and figures) of the ice adhesion apparatus are presented in Manuscript 2, and used extensively in Manuscripts 2 and 3, as will be discussed in Chapter 6.

4.1   Ice adhesion test methods

From the available literature on the measurement of ice adhesion strength to surfaces, it is clear that there is no general agreement about reference value, and the standardization of testing methods, although proposed, is not generally implemented.[152–154] As the number institutions, facilities, and research groups studying the adhesion of ice to surfaces has historically been few and far between, there has been little to no commercial options to purchase complete and dedicated set-ups measuring ice adhesion strength. As a result, each individual group must develop its own custom set up, invariably leading to a wide-variety of testing methods, with adhesion strength values that span three orders of magnitude.[155, 156] Although the set-ups may drastically differ between one another,

overall, the majority of ice adhesion testing methods can be categorized into three groups as illustrated in Figure 4.1: (a) centrifugal adhesion tests, (b) tensile adhesion tests, and (c) shear adhesion tests.
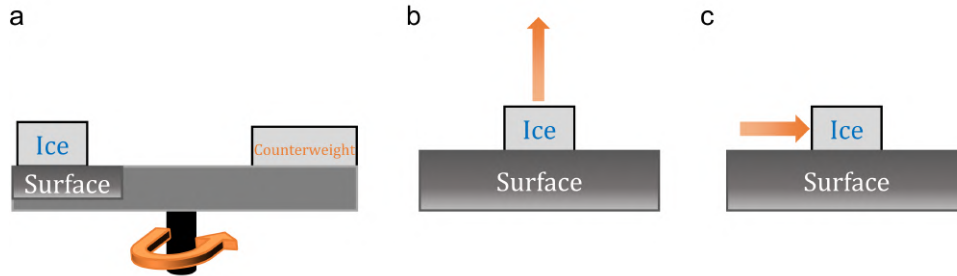
Figure 4.1: Graphical illustration of (a) centrifugal adhesion testing (b) tensile adhesion test and (c) shear adhesion testing. Adapted and redrawn with permissions [156]

The centrifugal adhesion test (CAT) is use centripetal forces to shear ice on surface. Ice frozen to a surface is secured on a rotating beam with attached counterweight (Figure 4.1a). By controlling the acceleration and speed of the centrifuge, linearly increasing centrifugal shear forces can be applied at the ice/surface interface until it detaches.[157] CAT has been shown to be one of the most repeatable testing methods, with standard deviations consistently below 15% of the reported values, if not less.[156] Without a wind-tunnel, this testing method is seemingly the next-best option to simulate the real-world de-icing environments commonly encountered by aerofoil surfaces (i.e. airplane wings and wind turbine blades). The ability to test different types of ice and compare the adhesion of bulk water ice (the most common where water is set into a mold and frozen) and precipitation ice (coming from the impact of supercooled water droplets on surface) must also not be understated, as in most practical applications precipitation ice is more realistic than bulk water ice.[155] However, some disadvantages to using CAT are that this type of measurement does not easily allow for the failure mode to be determined, and necessitates the use of detectors/sensors to discern the rotation speed at which ice was detached.

Whereas CAT applies a force in-line with the interface, tensile adhesion tests apply a force perpendicular from the interface, as seen in Figure 4.1b. This testing method is less common than CAT or shear-adhesion testing, but is still necessary to determine the tensile adhesion strength of ice, as other methods are unable. Nonetheless, reported values for the tensile adhesion of ice to a surface are slightly greater than those reported by shear methods (e.g. CAT or shear adhesion tests), yet with greater error.[23, 24, 158, 159] This can be the result of a combination of factors, such as the pull-off speed or misalignments between the applied force and interface.[160] The latter possibility is more consequential and presents a greater challenge in tensile adhesion testing in applying a uniform tensile stress to a perpendicular interface, where any small errors in alignment can cause significant local stresses that will likely yield less-than-expected adhesion strengths.[153]

Lastly, the most popular method is shear adhesion testing whereby a force is applied to ice that is frozen onto a surface, parallel to the surface/ice interface. The resulting ice adhesion strength is then defined as the peak value, and generally synonymous with the force at which the stationary ice block detaches. With shear testing, there are multiple modes through which the ice adhesion strength can be determined regarding both the orientation of the surface and adhered ice (vertical or horizontal), and whether to pull or push, the adhered ice from the surface. Given the variety, it is no surprise that there are numerous designs for shear adhesion test apparatuses in the literature.[155, 161] Yet given the number of different designs, it becomes difficult to compare reported ice adhesion values between them given the multitude of factors that may be differ between them that are known to affect the resulting ice adhesion strength on a surface, for example, temperature, sample size, and speed of the pushing force, orientation, and more.[162, 163] Even factors as simple as the distance of the pushing force probe (or string) to the surface have been found to drastically affect the reported values.[164]
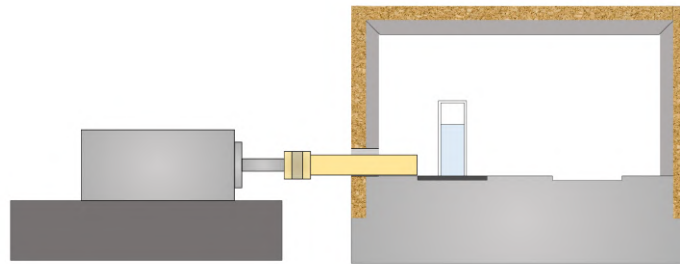
Figure 4.2: Basic cross-sectional schematic of a home-built shear ice adhesion test apparatus

Therefore, to compare ice adhesion strength values reported by different groups, it is best to design and build a test apparatus as similar as possible to the literature source. In place of this, one can also draw comparisons if the values ice adhesion strength of a reference sample are similar. To this end, it was my aim to design, construct, and validate a shear adhesion test apparatus, capable of measuring the adhesion strength of ice to a wide range of surfaces..

Considerations for the development of a shear-adhesion test apparatus

As alluded to in the previous section, when designing a shear-adhesion test apparatus, there are a multitude of factors to consider that may ultimately affect the ice adhesion strength. Here, I based my design and test-rig off of detailed descriptions in works by Meuler et al., Chen et al., Liljeblad et al., and Liang et. al., taking note on a variety of

factors they have reported.[29, 33, 56, 58] Figure 4.2 displays a rough schematic of the designed ice adhesion test apparatus. Critically, the ice adhesion strength on bare silicon wafers was found to be the same by three of the four groups under similar conditions, despite slight variations in their design. Taking inspiration from these groups then, the freezing time of the ice on the sample was decided to be at least 1 h. To reduce or eliminate any sudden stress concentrations on the ice, the distance of the probe to the surface was to be minimized, an the impact speed of the probe to the ice-containing cuvette was also reduced.

4.2   Design, construction, and validation of in-house ice adhesion test apparatus

The design and construction of the ice adhesion test apparatus is reviewed below and is discussed in Manuscript 2. Additionally, this apparatus was used extensively in Manuscripts 2 and 3 to measure the adhesion strength of ice to charged polymer surfaces.
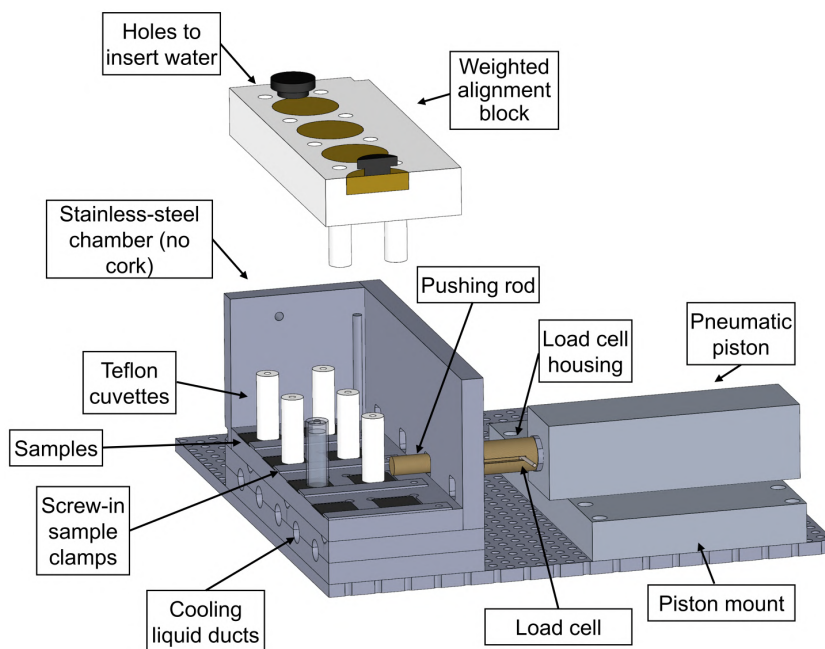
Figure 4.3: Detailed illustration of home-built shear ice adhesion test apparatus. A pneumatic piston is mounted onto perforated metal surface, and used to push a rod that applies a linearly increasing force onto the ice-containing Teflon cuvettes. The force is measured using a load-cell/force sensor placed in a custom housing. Temperature control of the test chamber was critical, therefore stainless steel was used and wrapped in a thick layer of cork (not seen), and cooling liquid was passed through ducts below the samples to chill the entire chamber to a desired temperature

Expanding on Figure 4.2, Figure 4.3 presents a more detailed cutaway diagram of the constructed test-rig. The overall apparatus is contained on a levelled perforated stainless-steel sheet, to which a stainless steel chamber, and two piston mounts (placed on opposite sides of the chamber), are secured. Temperature control is afforded by continuously flowing cooling liquid (65 wt.% ethylene glycol in water) through a recirculating chiller and into snaking duct-work in the bottom of the stainless steel chamber, directly below the samples. Importantly, to reduce the amount of condensation on the exterior of the chamber, and provide insulation (putting less strain on the recirculating chiller), a thick layer of cork surrounded the chamber, as seen in Figure 4.4.

Initially, it was thought that environmental/atmospheric conditions, such as humidity, might play a role in the adhesion strength. Therefore the ability to control the atmosphere of the chamber, in particular, the temperature and humidity, was also designed in mind. By bubbling cooled dry air through cooled aqueous glycerol solutions, we were able to vary the humidity to within ~10% of targeted value, however, temperature control of the atmosphere was made more challenging. Eventually, humidity control of the box was abandoned altogether as at low temperatures (e.g. -20 °C), the amount of water in the atmosphere is effectively negligible, being one order of magnitude below the amount of atmosphere at room temperature (approximately 20 °C). However, in-place, a weak stream of cool dry air was run through the chamber (entering in a perforated metal tube and exiting at the top of chamber through a small hole) in order to remove residual moisture that may condense during cooling the process.
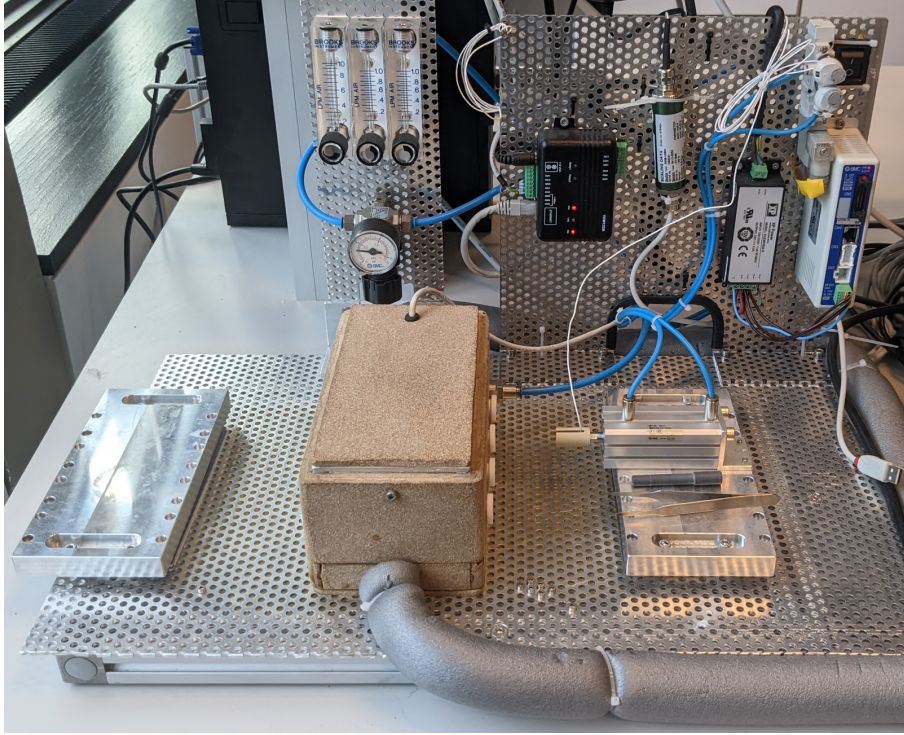
Figure 4.4: Overall home-built ice adhesion setup. Piston mounts are seen on either side of the test chamber, anda pneumatic piston with force sensor is mounted onto the blocks for stability.

Samples to be evaluated were placed in any of the eight indents, measuring 20 mm x 20 mm 0.5 mm. In order to minimize any torque or movement of the samples, screw-in sample clamps were placed on the top edge of all samples, that once fastened, secured the samples in the indents. Cylindrical cuvettes were used to freeze ice onto the samples, which were made with Teflon and modified to reduce their surface energy and water wettability, aiming to stop any leaks or interactions with the samples being tested. This was accomplished in a the following procedure that takes inspiration from both Meuler et al. and Liang et al. First, the open side of the cuvettes were polished with 1200 grit sandpaper, then the cuvettes were plasma cleaned, and treated with $1H,1H,2H,2H$-perfluorooctyltriethoxysilane vapour.[33, 58]
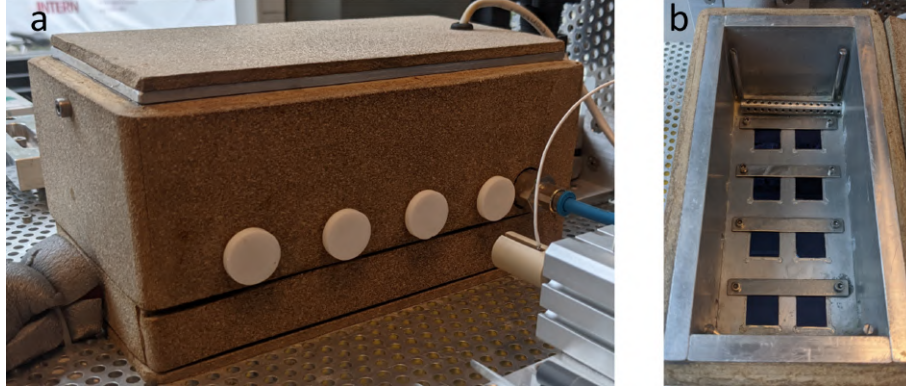
Figure 4.5: (a)Exterior of temperature controlled ice adhesion test chamber. Note the presence of Teflon plugs used to seal the interior environment when measurements are not ongoing (b) Interior of ice adhesion test chamber with silicon-wafer based samples placed in the eight available indents and fastened with sample clamps.
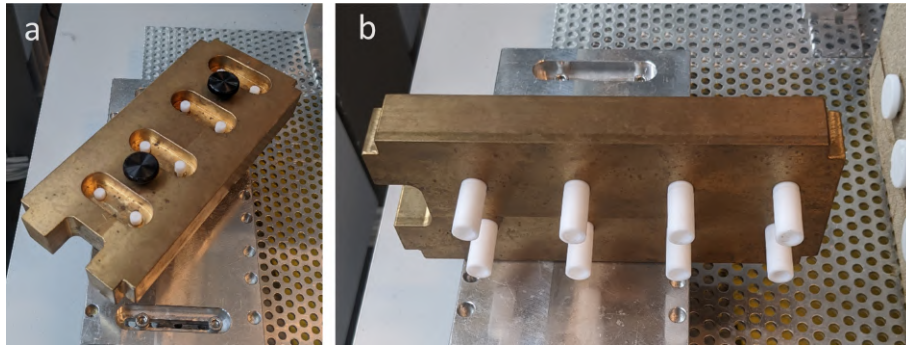
Figure 4.6: (a) Top-view of weighted cuvette alignment block (made of brass) with teflon cuvette plugs keeping the cuvettes in-place while loading into the chamber. (b) bottom-view of Teflon cuvettes placed in weighted cuvette alignment block.

In order to freeze ice onto a sample surface, forming bulk ice, liquid water had to be added from top of the precisely placed cuvettes. The correct placement of the cuvettes was crucial in the eventual step of applying a force to the ice cylinders, as misalignment would cause local stresses rather than a uniform stress across the interface. Therefore, a home-built weighted alignment block (made of brass) was used to repeatedly place the cuvettes in the ideal location(Figure 4.6a). To keep cuvettes in the alignment block, the top of the cuvettes were snugly fit into notches in the bottom of the brass alignment block, and fixed into place using Teflon stoppers through holes in the block. Once secured, the assembly of block and cuvettes could be added directly to the chamber, a snapshot is of this is presented in Figure 4.7, after which the Teflon stoppers were removed, exposing holes in the top of cuvettes. This allowed the cuvettes to be filled with chilled degassed

Milli-Q water while weighed down, preventing the leaking of cuvettes. The freezing process was ubiquitously set, with water being added onto samples at -20 ℃, and left to freeze for a minimum of 1 hour. Following this, the weighted alignment block was then carefully removed, leaving the Teflon-containing frozen ice cylinders on the samples. Following this, the target temperature at which to measure the ice adhesion strength was set on the chiller and the samples were heated/cooled and left to equilibrate for at least another hour.
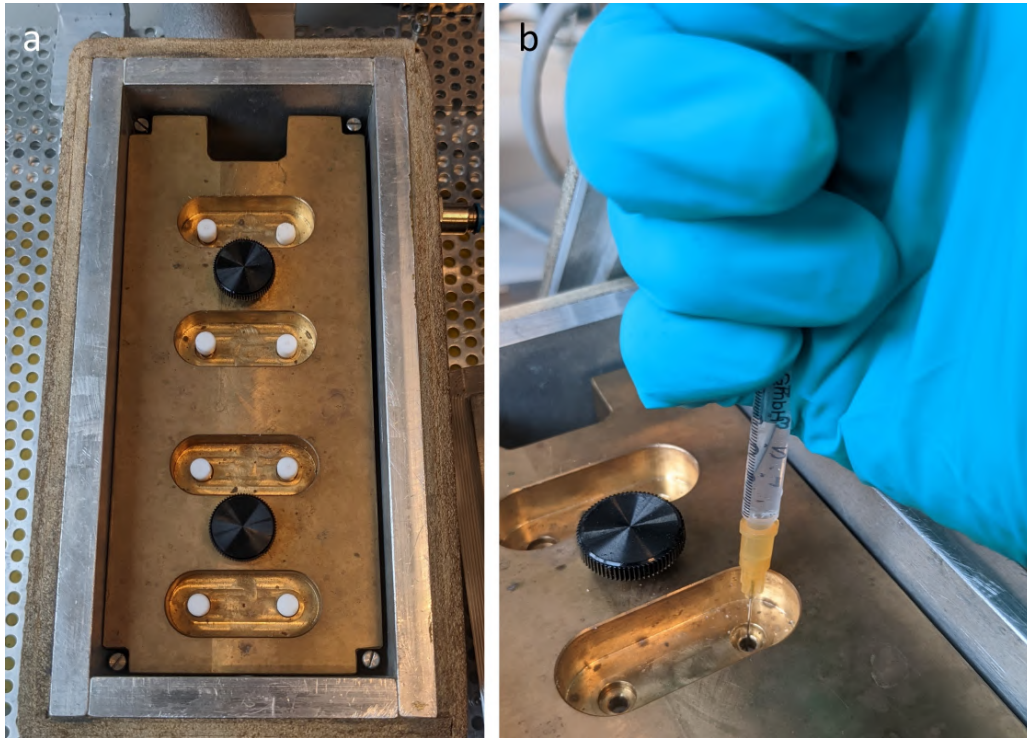
Figure 4.7: (a) Weighted cuvette alignment block placed in chamber. (b) After removal of Teflon cuvette plugs, chilled water is added to the cuvettes.

The pushing of the adhered ice cylinder was accomplished using a custom-shaped polycarbonate probe/pushing-rod. This fit snugly into a load-cell housing that screwed into the top of a pneumatic piston. Teflon plugs were accordingly removed from the exterior of the ice adhesion chamber allowing for the pushing rod to be placed, and measurements undertaken without significantly comprising the controlled environment that would come from opening the lid of the chamber. The pneumatic piston and pushing-rod assembly was then placed in the requisite position on a piston mount and secured by two bolts, after which a controlled flow of pressurized air was introduced, slowly propelling the probe towards the sample. This process, in which the probe approaches the sample, and makes contact, and applies a force, is depicted in Figure 4.8. The distance between the bottom of the probe and the sample was ideally minimal, and could be controlled by adjusting

the height of the piston mount with thin spacers. As the probe slowly contacted the sample, the flow of pressurized air continued, leading to a linearly increasing applied force. Concurrent with all other ice adhesion test methods, the peak force recorded by the load cell, coincides with the force at which ice detaches from the surface, and is divided by the surface area of the ice/surface interface, converting it to ice adhesion strength.[33, 157]
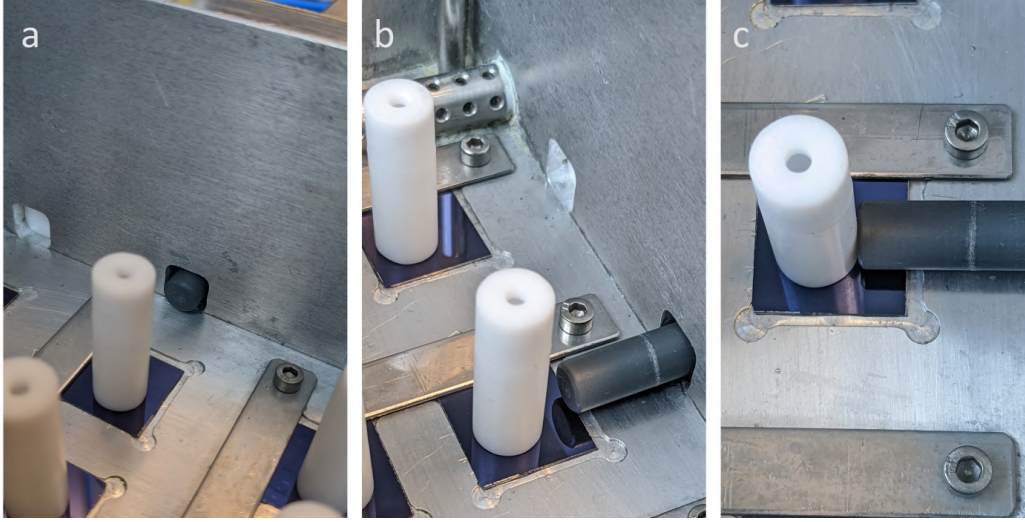
Figure 4.8: (a) Approach of ice adhesion pushing rod into the chamber. (b) Approach of pushing rod to ice-containing Teflon ice cylinder. (c) Application of force by pushing rod/pneumatic piston on an adhered ice cylinder.

A total of eight ice adhesion strength measurements could be run over a single freezing cycle. This was made possible by being able to precisely place the pneumatic piston assembly in front of each specified target ice cylinder. After all measurements were completed, it was possible to reset the chamber at near-ambient conditions, before the whole freezing and measurement process are undertaken again.

Validation of ice adhesion test apparatus and measurements

A key aspect of the design of the ice adhesion test apparatus presented here is to be able to compare to previously reported values on standard or common surfaces. Meuler et al. has published values of the ice adhesion strength of 22 surfaces, including common/standard surfaces such as steel, PMMA, PC.[33] Additionally, Chen et al. has reported values on 17 surfaces, such as on silicon, which can be compared to earlier ice adhesion strength investigations on bare substrates or hydrophobic surfaces. Therefore, the temperature dependent ice adhesion strength was measured and is displayed below in Figure 4.9. Here, the adhesion strength of silicon is found to linearly increase with decreasing temperatures, indicative of a gradually decreasing QLL. Not only does the temperature-dependent behaviour match, but the values of adhesion strength are close (within 15%) of previously

reported values, bringing greater assurance to the validity of the presented ice adhesion strengths.

Furthermore, the temperature dependent ice adhesion strength of smooth crosslinked PBMA coatings was measured (in a study to be summarized in Chapter 6, and presented in Manuscript 3), giving another point to draw comparison to the literature. Values reported by Chen et al. at -15 ℃ are in the same range as the values presented here, and although not exact, it my belief that these differences are tolerable. The temperature-dependent behaviour is similar to that seen on bare silicon, and suggests that similar mechanism is at play. This behaviour is unseen on PBMA samples thus far, with only Jellenik reporting similar behaviour on smooth polystyrene coatings.[23, 165] .
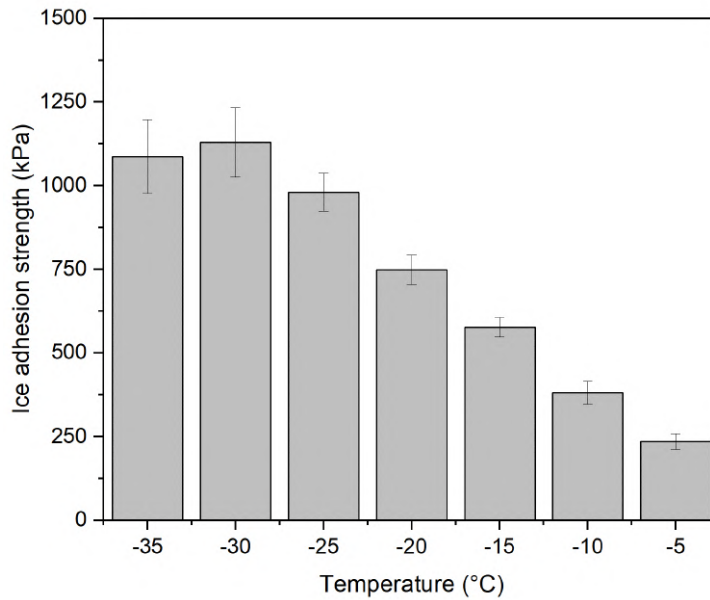
Figure 4.9: Temperature dependent shear ice adhesion strength of bare clean silicon wafers measured using the home-built ice adhesion test apparatus introduced in this chapter. Values are an average of at least three measurements, with accompanying standard deviations additionally plotted.

Chapter 5

Design and synthesis of charged polymer coatings

5.1 Efforts towards charged polymer coatings

Of the various chemistries that have been researched in polymer coatings for anti-icing applications (hydrophobic, SLIPS, hydrophilic), it is believed that mechanism of ice adhesion on hydrophilic charged polymer coatings is not yet fully understood, and considerable optimization is left-out to be explored. Water molecules can interact more intimately with hydrophilic polymers, so much so that coordinated water in surface-attached hydrogels may remain liquid through low temperatures due to freezing point depression.[51, 52, 56, 129] The enhanced ability of polyelectrolytes to strongly coordinate water through electrostatically enhanced hydrogen bonding, and their adaptability through either counterion exchange or varying the nature of the charge, has proven quite favourable anti-icing behaviour.[57, 58] Though the breadth of literature has often focused on affecting the interfacial behaviour causing a reduction in ice adhesion strength (developing explanations through terms such as aqueous lubricating layer, quasi-liquid layer, and liquid-like layer), little attention has been paid towards developing the relevance of coating composition, and its relationship with the imparted hydration water, and the resulting ice adhesion strength.

In order to prepare charged polymer coatings for anti-icing applications, and more importantly draw comparisions between their exhibited properties, certain design requirements must be met. The coatings must be robust towards the shear-stresses of de-icing, preferably over multiple cycles. Additionally, previous research revealed that coatings must be as smooth as possible, as increasing roughness not only leads to greater ice adhesion strengths but a faster decline in its performance.[37, 42] Learning from SLIPS, the coat-

ings must not rely on any external lubricants, and must only rely on the water inherently on and or in the polymer coating.[49] Therefore the coating must also be hydrolytically stable, and not change over time in water. The structure of the coatings must also be able to be varied through either straightforward and congruent changes in the polymer chemistry, counterion exchange, or the coating/curing method.

To this end, surface-attached thin-film hydrogels and the techniques used to prepare them, were focused on to develop a meet the requirements for the production of robust and stable charged polymer coatings. Here, the architecture of these thin-film hydrogels is inspired from their macroscopic counterparts: employing a *cure* that introduces covalent bonds and crosslinks, and forming a polymer network. Typically this is done through UV, thermal, or by an additive that drives the crosslinking reaction. To prepare surface-attached thin films on various substrates, dip coating and spin-coating are typically used in laboratory settings. In order to minimize the amount material necessary for application process of the coating, as well as to both tailor the thickness and minimize the roughness of the coatings, it was decided to spin-coat the charged polymers. Yet, this step, in conjunction with previous polymer synthesis steps can be complicated by the usually low solubility of charged polymers in conventional solvents.

Some hydrogels are often prepared with multifunctional polymerizable monomers, such as ethylene-glycol dimethacrylate (EGDMA) or divinylbenzene (DVB).[166, 167] However, the polymerization of these will inevitably yield to a cross-linked gel, which is not capable of being spin-coated. However, in place of this, one can prepare a polymer with pendant polymerizable units that, upon curing, crosslink the polymer into a gel.[168] One option that was shortly explored as a possible crosslinking chemistry was the copolymerization of methacrylic acid (MAA) into the polyelectrolyte, followed by the esterification with 2-hydroxyethyl methacrylate (HEMA), or vice versa where HEMA is copolymerized and the esterification is completed with MAA afterwards.[169, 170] Although the copolymerization of either monomer with a polymerizable electrolyte (cationic or anionic) was completed in a controlled manner, the solubility of the resulting polymer into a suitable solvent for an efficient esterification was complicated. First, any alcohols (e.g. EtOH, IPA, TFE) would directly compete in the esterification with HEMA. Second, H_2O could not be used as the reaction is reversible, whereby hydrolysis could break the formed ester to form the alcohol and carboxylic acid. And third, although eventually a DCM-soluble copolymer was produced whereby a Steglich esterification using DCC and DMAP could be attempted. However, once isolated, it was found that this reaction was slow and had low yields, even after 48 h. Given all of these barriers, the esterification of MAA or HEMA to form a polymer with a pendant polymerizable methacrylate was not explored further. Additionally, other pathways towards a charged polymer with a pendant polymerizable crosslinker were also explored, however these were not deeply explored due to the percieved and found difficulties in copolymerization and constraints towards solvent and reagents.[84]

An alternative method towards surface-attached hydrogels is through the use of photo-crosslinkable monomer, such as a benzophenone-functionalized methacrylate. This has been accomplished in a multitude of previous reports where after coating a polymer onto a surface, the benzophenone moiety can be excited by near-UV or UV irradiation, photo-reacting and producing surface-attached polymer networks and hydrogels.[94, 171, 172] Briefly, upon the absorption of a photon, an electron is excited to the to the antibonding π^*-orbital of the carbonyl group, which then undergoes an intersystem crossing into a triplet state to form a diradical with one unpaired electron on the oxygen, and another one on the former carbonyl carbon. The oxygen-based radical can now interact with any C-H σ-bonds of neighboring molecules by abstracting a hydrogen atom and forming an OH bond, creating another carbon-based radical on the neighboring molecule that can combine with the radical on the former carbonyl carbon forming a new covalent carbon-carbon bond acting as a crosslink between the two molecules.[173]

Rationally, it was attempted to explore this possibility given the breadth of possibilities and the attractiveness of the system - whereby a polymerizable unit can then be directly crosslinked with no modifications or additives. However, this process was toilsome, as the benzophenone-functionalized methacrylates are inherently hydrophobic and insoluble in the polar solvents commonly used in the polymerization of electrolytes. This was eventually overcome using an EtOH/H$_2$O or MeOH/H$_2$O solution, for copolymerization with METAC and SPMA-K respectively. However, the corresponding polymers exhibited a lower than expected content of benzophenone-functionalized methacrylate. Despite this, the polymers were cast onto silicon wafers by spin-coating and attempted to be cured by UV-irradiation. However, upon washing, the crosslinking was found to be unsuccessful as the polymers dissolved completely. It was reasoned that this occured either due to low benzophenone functionality, or an incorrect UV curing method (time, distance from sample, wavelength and intensity of UV light).[174] Attempts to gain higher amounts of benzophenone-functionality into the polymer were successful to a certain degree, however, no matter the changes in UV-cure, the coating was easily washed off the substrate. Although this may still have been a result of low benzophenone functionality, it is also likely that the pendant benzophenone had no suitable reaction partner, therefore any excitation would eventually return to its original ground state rather than going towards a desired crosslink.[175] More exploration into the topic was not undertaken, and other crosslinking chemistries were investigated instead.

5.2   Thiol-ene click chemistry for polymer coatings

Key aspects of the results of polymer synthesis and the coating process gave surfaces that were used in all the attached works, and are therefore included in Manuscript 1, Manuscript 2, and Manuscript 3.

The method of utilizing thiol-ene click chemistry to prepare surface-attached hydrogels was attempted due to the potential to either UV or thermally cure the spin-coated films through the quick and high-yielding nature of the thiol-ene reaction. To this end, the goal was to synthesize a polymer with -ene functionality, then for spin-coating, mixing in multifunctional thiols and radical initiators that could be cured to produce a surface-attached hydrogel, as done in previous works (Figure 5.1).[90, 176]

Furthermore, the insights gained through the previous failures on both monomer solubility and polymer solubility, was directed towards finding a suitable polymerization solvent for all monomers and polymers: both for the polymerization and spin-coating. To dissolve and spin-coat the cationic and anionic polyelectrolytes and zwitterionic polymers from either ethanol or TFE, it was found that a high content of BMA, at least 50 mole percent was needed. Additionally, rather than attempting a post-polymerization modification of the polymer where yields could affect the amount of functionality, it was decided that polymerization of an -ene methacrylate (i.e AMA) with BMA and an electrolyte could be done through RAFT polymerization.[129, 177, 178] The chain-transfer agent (RAFT agent) used was particularly well suited for the polymerization of methacrylates, and similar to comparable studies that copolymerized a given methacrylate and AMA without inducing any gelation. The aforementioned procedures (see Chapter 3) detail the successful synthesis of polymers with varying AMA functionality, and the following paragraphs quickly describe the polymerization and coating processes, ultimately leading to a suitably stable and highly variable system to produce charged polymer coatings.

Rather than stay near the threshold BMA content to maintain polymer solubility, a higher content was targeted where 75 mol.% of the polymers would be non-ionic (BMA + AMA), with the charged monomers making up the remaining 25 mol.%. Yet it remained a challenge to find a suitable solvent that balances the hydrophobic nature of BMA and AMA with the hydrophilic nature of any charged monomer. Numerous combinations were attempted, but in the end, cationic and anionic polyelectrolytes were synthesized in DMF/H_2O 4:1 vol./vol./), zwitterionic polymers in TFE, and non-ionic polymers in DMF. These solvents allowed for the respective polymerizations to be conducted to high conversation and with a high degree of control.

Once precipitated and isolated, all charged polymers were found to be soluble in TFE, a favourable solvent for spin-coating onto the thiol-functionalized silicon substrates. The introduction of PETMP and ACVA to a mixture was necessary to produce surface-

Figure 5.1: Schematic illustration of the coating process, where charged polymers are dissoved in TFE (non-ionic polymers in DMF) and spin coated onto a prefunctionalized silicon wafer with equimolar amounts of PETMP and ACVA with regards to AMA content in the polymer. The cast films are then thermally cured by the thiol-ene reaction to give a crosslinked (and surface-attached) polymer coating.

attached thin-film of approximately 100 nm. Here, an equimolar amount of PETMP and ACVA with respect to targeted allyl functionality in the polymer was dissolved in a 1.25 wt./vol.% polymer solution. Spin-coating the solutions onto the thiol-functionalized silicon substrates, followed by curing at 90 °C for 120 min., resulting in cured polymer coatings that when washed excessively with water, remained present.

This coating design ultimately yielded the ability to tailor the charged nature of the coating, by selecting either a cationic, anionic, zwitterionic, or non-ionic methacrylate monomer for the initial polymerization. Further customization of the counterions in cationic or anionic poylelectrolytes can also be done. Additionally, through the incorporation of varying fractions of AMA in the polymerization, the resulting crosslink density of the coatings can be easily adjusted (Figure 5.2).
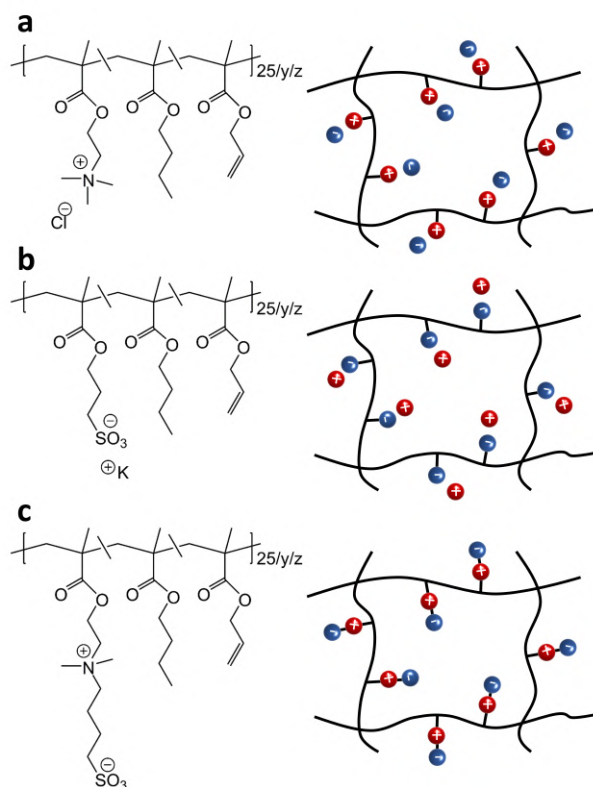
Figure 5.2: Illustration of (a) cationic polyelectrolytes and charge structure of coatings with mobile counter-anions (b) anionic polyelectrolytes and charge structure of coatings with mobile counter-cations (c) the chemical and charge structure of coatings made of zwitterionic polymers, with both positive and negative charged functionalities covalently bound to the polymer chain.

5.3   Ionic-strength dependent swelling of charged polymer coatings

Manuscript 1

It is well known that hydrophilic polymer coatings inherently swell, however the swelling behaviour of charged polymers is unique. The previously discussed coatings structure and method in Figure 5.1 allowed a study towards better understanding the swelling behaviour of charged polymers in different electrolyte solutions of various concentrations. This study was conducted on coatings that I produced, as it is my main and major contribution to the work. However, as my charged polymer coatings are to be used in anti-icing applications where they are hydrated (i.e. swollen), their behaviour in pure water (in the osmotic regime) is of clear importance. Below we briefly summarize the work, as presented in

Manuscript 1.

5.3.1 Polyelectrolyte effect in cationic and anionic polymer films

First of all, it is important to discern why polyelectrolytes swell in aqueous solutions. Simply put, polyelectrolyte coatings swell due to a combination of the osmotic pressure gradient of the counterions and various non-electrostatic effects. In water, the swelling of polyelectrolytes is controlled primary by the osmotic pressure of the counterions in the film.[179, 180] In salt solutions, the previous statement is valid up until 10 - 100 mM, after which point the polyelectrolyte is 'salted' and collapses.[181, 182] Here, the osmotic pressure of the film decreases steadily, and non-electrostatic effects dominate.[70, 87] This phenomenon is known commonly as the polyelectrolyte effect, occurs in all polyelectrolyte films, regardless of crosslink density, as shown in Figure 5.3. Not surprisingly, the addition of more crosslink limits the swelling of a polyelectrolyte through increased contributions to entropic elasticity, as chain stretching is more restricted.[183]

In cationic polyelectrolyte films, the swelling behaviour was seen to be solely counterion dependent (Figure 5.4). In the osmotic regime, the swelling of a low crosslink density polyelectrolyte coating with chloride counterions was 2.4x its original dry thickness, while its thiocynanate analogue was limited to a swelling ratio 1.6. However, these swelling ratios converge at high ionic strength, in the salted regime. This forms the basis to conclude a counterion specific osmotic pressure, in which the greater ability of counterions to form ion-pairs with the polymer-bound charge trends results in a more osmotically passive system. This phenomenon will revisited later, as it is critical to the anti-icing properties of investigated polyelectrolyte surfaces (Chapter 6). Comparing to the swelling of anionic polyelectrolyte films, shown in Figure 5.5, no counterion or co-ion effects are seen. This is suggested to due to a lack of ion-pairing regarding cationic counterions and anionic films, and can be rationalized through comparing the polarizability of cationic and anionic counterions.[100, 102]
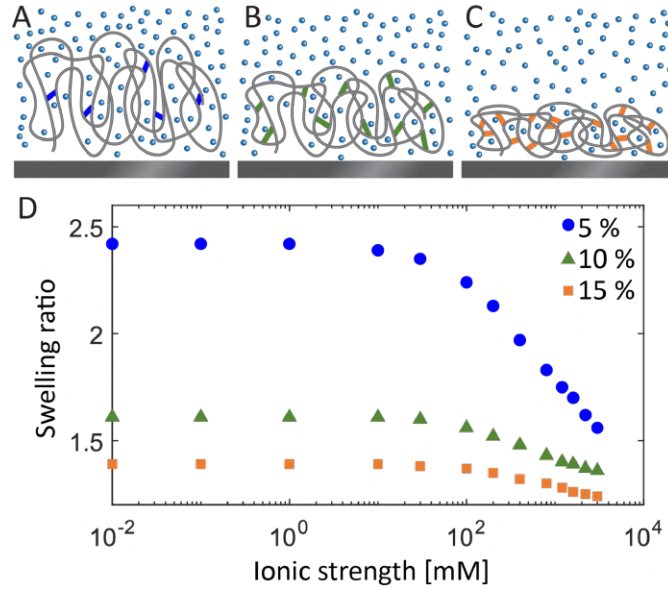
Figure 5.3: Illustration of effect of crosslinking on thin cationic coatings at (a) low (b) medium and (c) high crosslinking densities. (d) The swelling ratio is plotted against the ionic strength of the solution showing that no matter crosslinking density, the polyelectrolyte effect takes place as the coating passes from the osmotic regime into a salted regime.
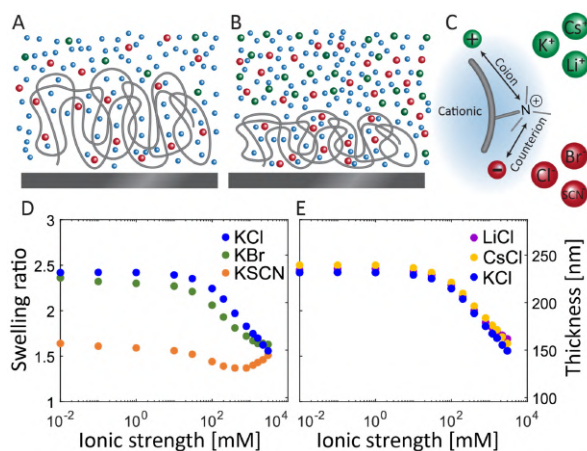
Figure 5.4: Illustration of cationic polyelectrolye coating swelling in the (a) osmotic regime and (b) salted regime. (c) Interaction of cationic moeities with counterions and co-ions. Polyelectrolyte effect as a function of (d) counter-anions, and (e) co-cations.
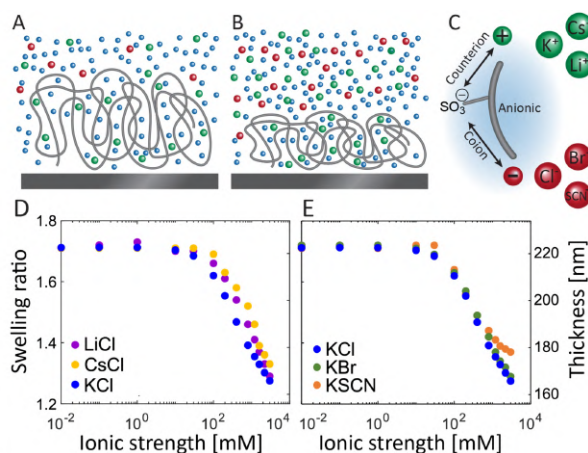
Figure 5.5: Illustration of anionic polyelectrolye coating swelling in the (a) osmotic regime and (b) salted regime. (c) Interaction of anionic moeities with counterions and co-ions. Polyelectrolyte effect as a function of (d) counter-cations, and (e) co-anions.

5.3.2 Anti-polyelectrolyte effect in zwitterionic polymer films

Meanwhile the swelling of zwitterionic polymer films is characteristically different due to the nature of both cationic and anionic charged moieties being covalently bonded to the same monomer unit. Here, an anti-polyelectrolyte effect is observed, in which films are collapsed in water and low ionic strength aqueous electrolyte solutions, and then swell drastically at high ionic strengths (Figure 5.6).[184] To explain behaviour in the low ionic strength regime; there are no mobile counterions in the film and therefore no osmotic pressure gradient, therefore non-electrostatic effects and the only source of drawing-water into the coating. Furthermore, in addition to the covalent crosslinks in the coating, sulfobetaines are known to aggregate, and are here envisioned as physical crosslinks. As ionic strength increases into the salted regime, the paired charges holding together these physical crosslinks are screened, unrestricting the swelling of the film.[185]

Although this general behaviour was observed no matter the nature of the electrolyte solution added, anion-specific effects could be discerned; such that greater interactions between the anions and tethered quaternary alkyl ammonium led to greater dissociation of the physical sulfobetaine crosslinks, increasing the film's swelling. However, not cation-specific swelling was seen, and is again justified by a lack of ion pairing.
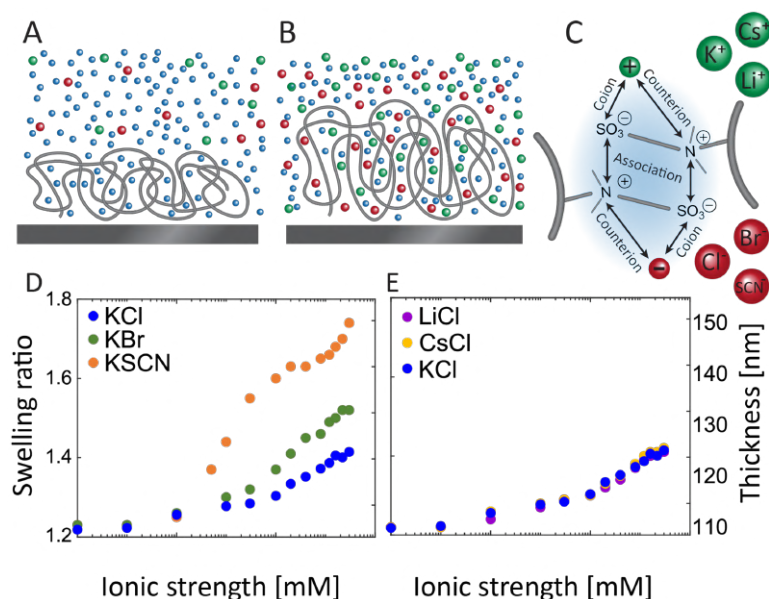
Figure 5.6: Illustration of the swelling behaviour of zwitterionic polymer coatings in (a) low ionic strength solutions and (b) high ionic strength solutions. (c) Possible interactions between coions and counterions in the zwitterionic coating. Anti-polyelectrolyte effect as a function of varying (d) anions and (e) cations in electrolyte solutions

Overall, the ionic-strength dependent swelling of cationic, anionic, and zwitterionic polymer coatings was studied here, and is significant to understanding the swelling behaviour of the coatings later investigated in Chapter 6. In low ionic strength solutions, the swelling of polyelectrolytes is expansive due primarily to osmotic pressure difference between the surrounding environment and the polyelectrolyte-counterion pair. Exhibited here, one can clearly denote the counterion dependent swelling response, such that less hydrating counterions form stronger ion pairs, leading to decreased swelling. Zwitterionic systems swell far less in low ionic strength solutions, mostly due to the lack of any osmotic pressure difference. This can lead to much a concentration of charges than compared to a completely swollen polyelectrolyte coating, which we will later see affects the anti-icing properties of polymer coatings.

Chapter 6

Principles and performance of anti-icing charged polymer coatings

6.1 Counterion-specific ice adhesion strength on cationic polyelectrolyte coatings

Manuscript 2

The first part presented here is a study on the counterion dependent ice adhesion strength on cationic polyelectrolyte coatings (design and synthesis previously described in Chapter 5.2). Based on the temperature-dependent behaviour, a phase transition in the coating's hydration water was theorized. In order to its legitimacy, two independent and novel methods were used to validate the presence of both a phase transition and "non-freezable" water, in the coating's hydration water, on the way rationalizing the counterion-specific behaviour in ice adhesion. The results and explanations summarized here are presented in Manuscript 2.

For the cationic coatings reported, RAFT polymerization was successfully used to synthesize a random copolymer of poly(METAC-*co*-BMA-*co*-AMA) with a 25 mol.% electrolyte METAC and 10 mol.% AMA incorporated. In order to investigate only the nature of the counter, and its dependence on ice adhesion strength, all coatings used in the following discussion are based on this polymer, and are labelled as either Cat-(X^-), where X^- denotes the counterion to METAC in the polymer coating, or just with the anion identify itself. Ice adhesion strength measurements were conducted in five degree intervals, from -5 °C to -35 °C on Cat-(X^-) with varying counterion identity: F^-, Cl^-, Br^-, I^-, SCN^-, and are shown in Figure 6.1.
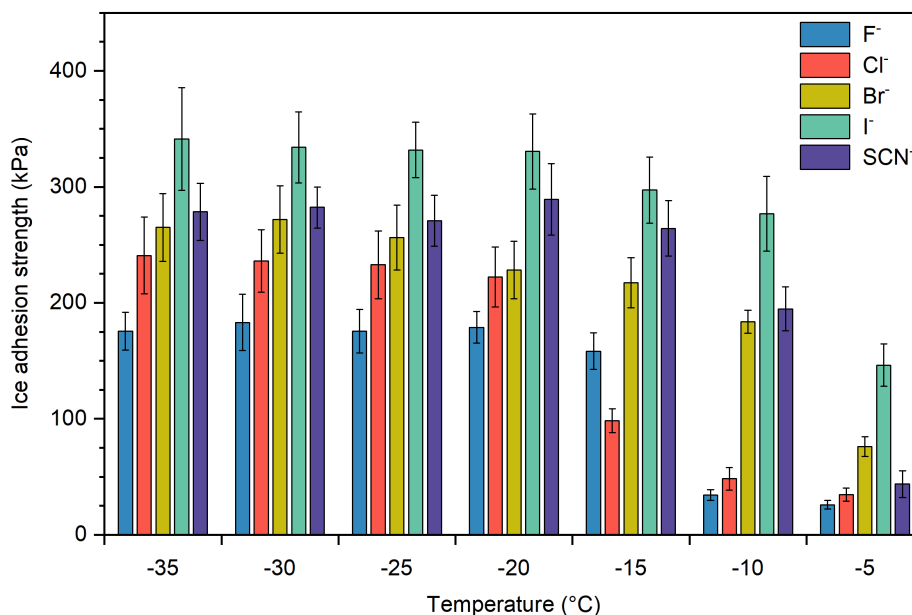
Figure 6.1: Temperature dependent shear ice adhesion strength on cationic polyelectrolyte coatings with varying counterions, measured in at least triplicates

Focusing on Cat-(F⁻), the ice adhesion strength is very low (≤ 50 kPa) from -5 through to -10 ℃. After which, the adhesion strength is seen to suddenly and steeply increase to $\sim$170 kPa and is seemingly constant through to -35 ℃. Similar behaviour in Cat-(Cl⁻), where the jump occurs at $\sim$ -15 ℃, lower than Cat-(F⁻), and in the remaining samples at higher temperatures. Significantly, the low temperature ice adhesion strength after this 'jump' was seen to vary widely and appears to be a function of the counterion, Cat-(F⁻) demonstrating the lowest plateau strength, and Cat-(I⁻) the largest plateau strength.

Based on these results, it was my goal to rationalize the nature of the sudden jumps, the counterion-dependent temperature of the jumps, and the resulting level of ice adhesion strength at low temperatures.

It is well known that hydrophilic polymer coatings will naturally hydrate with water, and swell, and has been discussed in a previous section in relation to Manuscript 1. It is my belief here that the physical state of the hydration water is important to the hydration water, such that the ice adhesion strength on hydrated polymer surfaces is intrinsically low - as ice adhesion on liquid and liquid-like interfaces benefits from much greater molecular mobility and a lack of any mechanical interlocking between the ice and surface. The antipode of this effect would be a completely frozen ice-coating interface with no lubrication and much greater mechanical interlocking, leading to a distinct increase in

ice adhesion strength. Linking these two states is a sharp phase transition of the hydration water in the coating, from liquid water to ice.

6.1.1 Detecting the phase transition of hydration water by TIR Raman Spectroscopy

This investigation necessitated the use of a technique capable of detecting changes in the hydrogen-bonding environment of water molecules, as well as focus on a plane/scale consistent in the same range of the thickness of the swollen coatings ($\sim$100-200 nm). This was found in TIR Raman Spectroscopy, in a custom-built specially-designed setup that allowed for the spectroscopy of the coatings in an identical environment to the undergone ice adhesion measurements (described in detail in Chapter 3).[29]

First, based on the angle of incidence of the incident light, one can probe to different penetration depths of the coatings, ranging from many microns to less than 100nm.[145] In order to be certain that the collected Raman spectra were composed of solely of the polymer coating and its hydration water, without any contributions of bulk ice, the angle of incidence was varied on Cat-(Cl$^-$), resulting in Figure 6.2.

Not surprisingly, at the lowest angle of incidence where the penetration depth of excitiation is on the micron scale, bulk ice, characterized by the peak at $\sim$3140 cm^{-1}, is seen to dominate, additionally overlapping with a region ascribed to various stretching modes of C-H of the polymer. However, as the angle of incidence is increased the penetration depth of the evanescent wave correspondingly decreases. It can be seen that at high angles of incidence, the bulk ice contributions disappear completely, and rather liquid water (centered at $\sim$ 3250 cm^{-1} in the polymer coating is seen, and confers that a high angle of incidence should be targeted for the investigation.
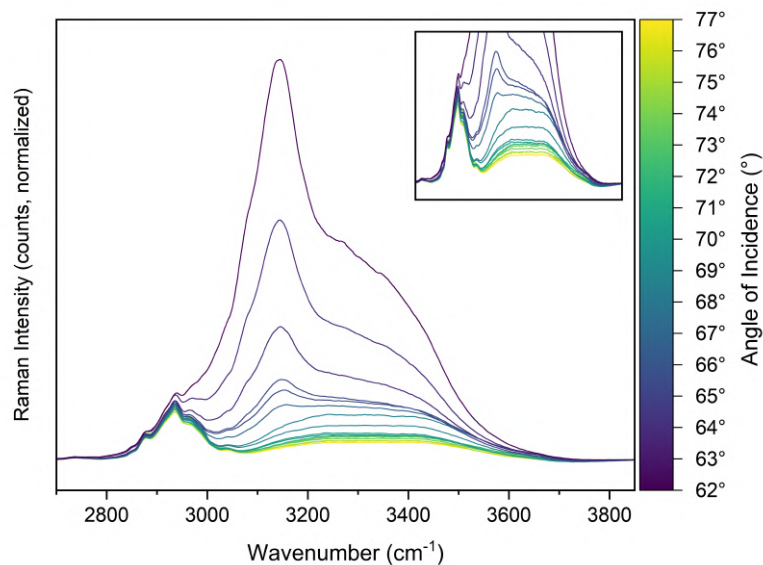
Figure 6.2: TIR Raman spectra of Cat-(Cl$^-$) at -10 °C with varying angles of incidence (AOI). Lesser AOIs result in greater penetration depth into the bulk ice, whereas AOIs nearing 77°approach a steady penetration depth that observes the coating and its hydration water. Spectra have been normalized to the corresponding polymer peak at ~1450 cm^{-1} due to increasing high contributions of ice into the bulk spectra that add to the intensity of polymer peaks at ~2930 cm^{-1}.

TIR Raman spectra were then collected at temperature ranging from -0.7 °to -35 °C , are presented Figure 6.3, and offers clear spectroscopic evidence of a phase transition from ice to liquid water in the hydrated coating. In Cat-($^-$), seen in Figure 6.3b, no characteristic ice domains can be identified from -0.7 °C to - 13 °C, rather displaying liquid hydration water in the coating.[186, 187] The presence of liquid water at sub-zero temperatures, is believed to be the result of polymer-induced freezing point depression, and will be discussed in a later section. A phase transition from liquid water to ice is distinctly visible from -14 °C to -16.5 °C, as the peak of ice begins to dominate over that of liquid water. Lastly, from -17 °C to -35 °C, the spectra describe a polymer coating with frozen hydration water.
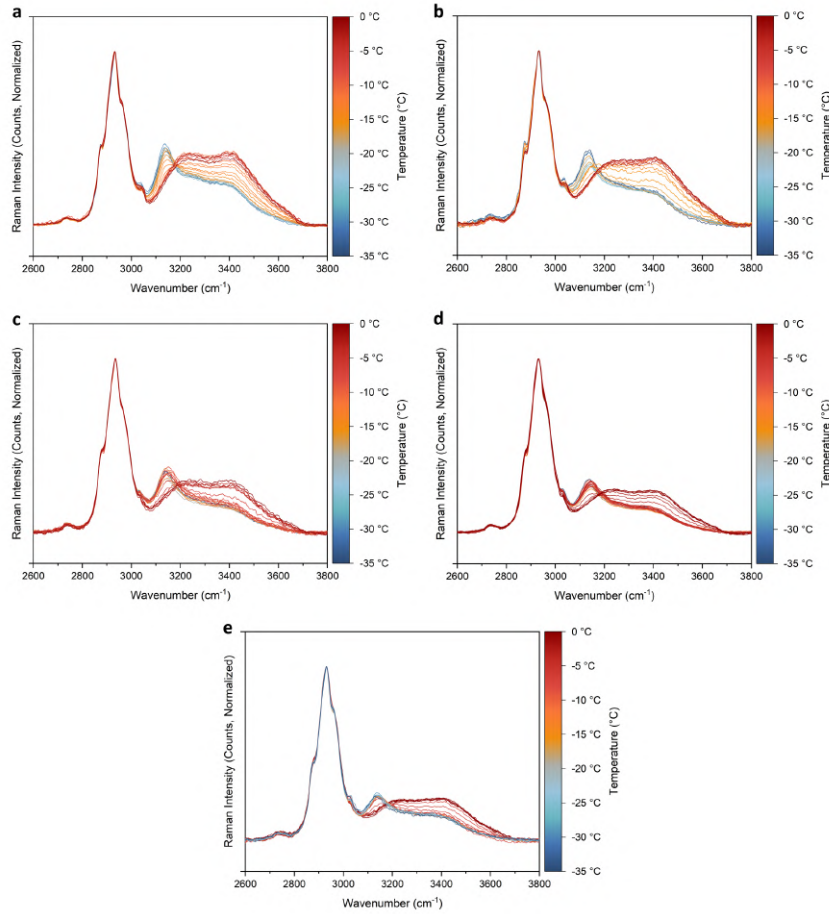
Figure 6.3: Compiled temperature dependent TIR Raman spectra of (a) Cat-(F⁻), (b) Cat-(Cl⁻), (c) Cat-(Br⁻), (d) Cat-(I⁻), and (e) Cat-(SCN⁻), displaying the phase transition of hydration water from ice to liquid water at varying temperatures. Spectra have been normalized to a polymer peak at ∼2930 cm⁻¹, as there are no observed contributions from bulk ice beyond the coating.

Although a qualitative analysis of the TIR Raman spectra displayed evidence of a phase transition, the results were quantified to give resulting ice/frozen fractions of the water in the film as a function of temperature. This was accomplished by modelling the acquired data with a linear combination of generated reference spectra of the polymer, liquid water, and ice, from which ice/frozen fraction in all spectra could be determined.Accordingly, water in the Cat-(SCN-), Cat-(Br-) and Cat-(I-) coatings were observed to undergo phase transitions at approximately -6.1 °C, -5.9 °C and -3.2 °C respectively, whilst freezing point of water in the Cat-(Cl-) and Cat-(F-) coatings were observed at lower temperatures: approximately -15.8 °C and -13.5 °C, respectively. Overlaying the ice adhesion data and frozen fraction of hydration water in the coating, gave Figure 6.4, where the location of the freezing transitions of the hydration water in the coatings are nearly perfectly aligned

with the jumps in in ice adhesion strength.
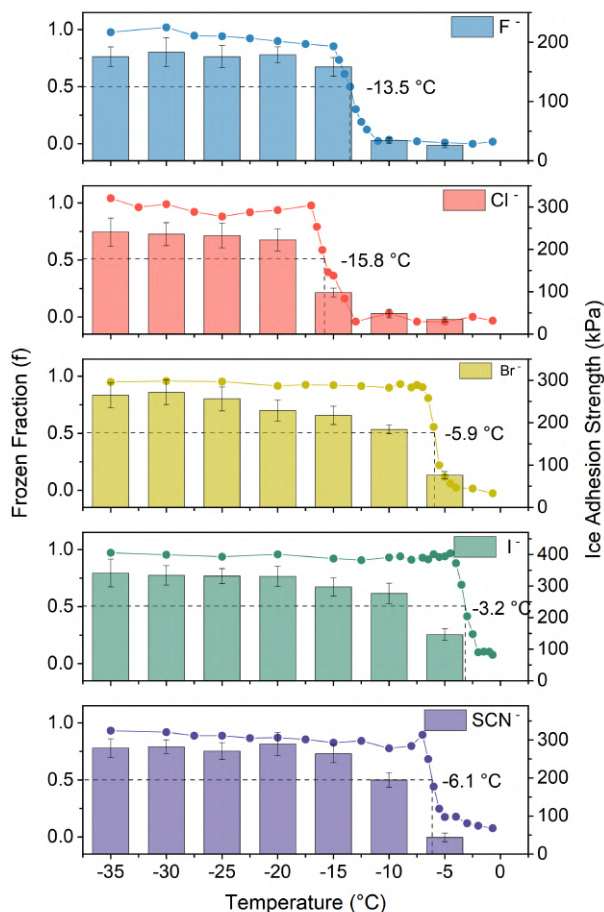
Figure 6.4: Quantified phase transition of hydration water by fitting of TIR Raman data to a three-component linear combination model, corresponding to the shear ice adhesion strength of cationic polyelectrolyte coatings with varying counterions.

6.1.2 Polymer-induced freezing point depressions of hydration water

The aligned behaviour of the jump in ice adhesion strength and the proven phase transition brings forth a discussion as to the specific temperature of the aforementioned 'jump' and its dependence on the counterion. It is the hypothesis here that freezing point depression is a result of the activity of the counterion, which correspondingly depends on the fraction of mobile ions and the counterion dependent swelling of the coatings. However, polyelectrolyte swelling is known to be affected by identity of the counterion.[70,

87, 188] Therefore, independent measures of both swelling and the fraction of mobile ions (ion-mobility) is needed to understand if the different phase transition temperatures in the coatings can be linked to different counterion activities.
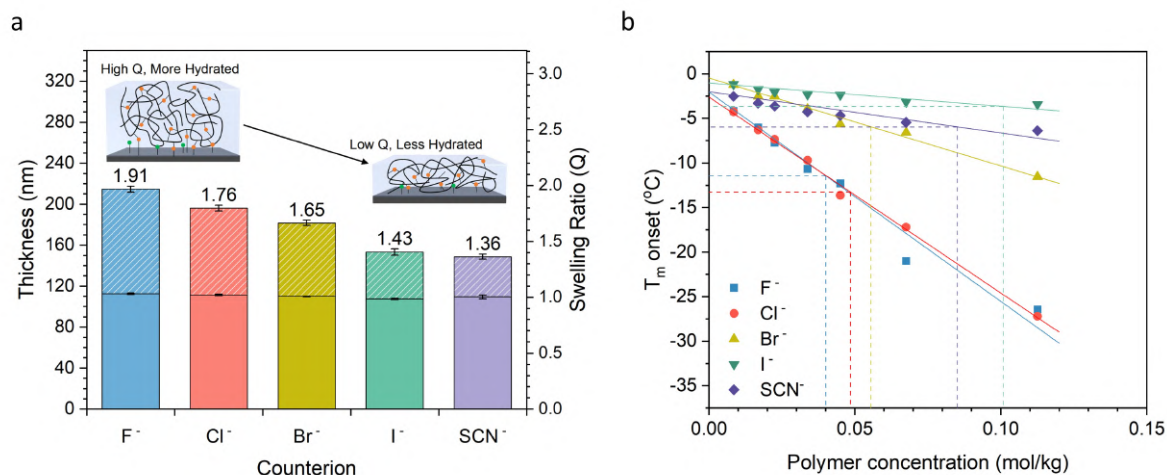
Figure 6.5: (a) Dry (solid) and hydrated (striped) thicknesses of cationic polyelectrolyte coating with varying counterions measured by ellipsometry. Labelled values display the swelling ratio of the coating in water. All reported values are the average of measurements on at least three samples. (b) Variation of freezing point depression, as quantified by onset melting temperature (°C), with polyelectrolyte concentration (mol/kg) in DSC samples for the five different counterions. Linear fits have been added to each data set. Corresponding drop lines were used to independently estimate the freezing phase transition temperature of the hydration water in the coatings, and are plotted at the concentration of polymer in each polymer coating

First, the counterion-specific swelling of the cationic polymer coatings was measured by ellipsometry (Figure 6.5a). Cat-(F^-) was seen to swell to maximum of 1.91 its dry thickness, while in contrast, Cat-(SCN^-) returns a swelling ratio of 1.36. From previous studies has been shown that the swelling of a polyelectrolyte in water is due to a combination of the ion osmotic effect and various non-electrostatic effects. As such, Cat-(F) swells due to a combination higher osmotic pressure and the greater hydration of the mobile fluoride anions, while conversely, the more intimate ion pairing in Cat-(SCN) results in a decreased osmotic pressure, all the while the hydration of free thiocyanate ions requires less water.

While ellipsometry provides a measure of counterion-specific swelling, differential scanning calorimetry can be used to study the counterion mobility through a measure of freezing point depression (Figure 6.5b). Here binary mixtures of uncrosslinked Cat-(X^-) polymer and water with mass fraction ranging from 0.09 to 0.8 were measured by DSC, and shown

to exhibit a single phase transition of the water melting. As expected, increasing polymer concentration yielded a larger freezing point depression, no matter the identify of the counterion.[127, 189, 190] Yet most interestingly, the $T_{m\ onset}$ between the counterions was found to vary significantly, and were ranked as F⁻ ≈ Cl⁻ < Br⁻ < SCN⁻ < I⁻. This implies that fluoride and chloride counterions have the least tendency to form ions pair with the cationic coating and thus have the highest fraction of mobile counterions, while iodide has the highest tendency to form ion pairs and thus lowest fraction of mobile counterions

Combining the results from ellipsometry and differential scanning calorimetry (DSC) allows one to discuss to the counterion-specific phase transition temperature of the coatings hydration water. As determined by freezing-point depression experiments, fluoride and chloride have nearly identical fractions of mobile counterions, yet different swelling behaviours are observed. It is to be expected then that the more concentrated coated yields the larger freezing point depression, and is neatly observed by the drop-lines in Figure 6.5b, and are estimates of the phase transition temperature of the hydration water in the coatings. The temperature dependent jumps in the other coatings can explained in a similar manner.

6.1.3 Effect of "non-freezable" water on ice adhesion

Lastly, it was an aim of the study to rationalize differences in low temperature ice adhesion strength (here defined as temperatures sufficiently low in which the hydration water is frozen, e.g. -30 °C). Beyond the definite evidence of a single phase transition occurring in the binary polymer-water system, analysis of DSC measurements revealed the presence of "non-freezable" water, defined here as the difference between the expected value of the enthalpic melting transition (assuming all water was frozen) and the measured magnitude of the phase transition.

The existence of "nonfreezable" water, which supposedly is a result of strong interactions between some water molecules and the polyelectrolyte chains and counterions, has previously been observed in DSC experiments, however, its presence is not visible in the TIR Raman data at low temperatures, and is therefore believed to be different than bulk liquid water.[58, 60, 129, 191] Rather its presence could be related to size of crystalline domains and the interfacial environment between them, such that greater "non-freezable" water should soften the coatings and reduce the adhesion strength of ice. Notably, this expectation is true, and can be visualized in Figure 6.6b. This comparison, exemplifies the significance the ion pair strength, where counterions with lower tendency to form ion pairs, promote greater amounts of strong interactions with water, and thus higher fractions of "non-freezable" water.
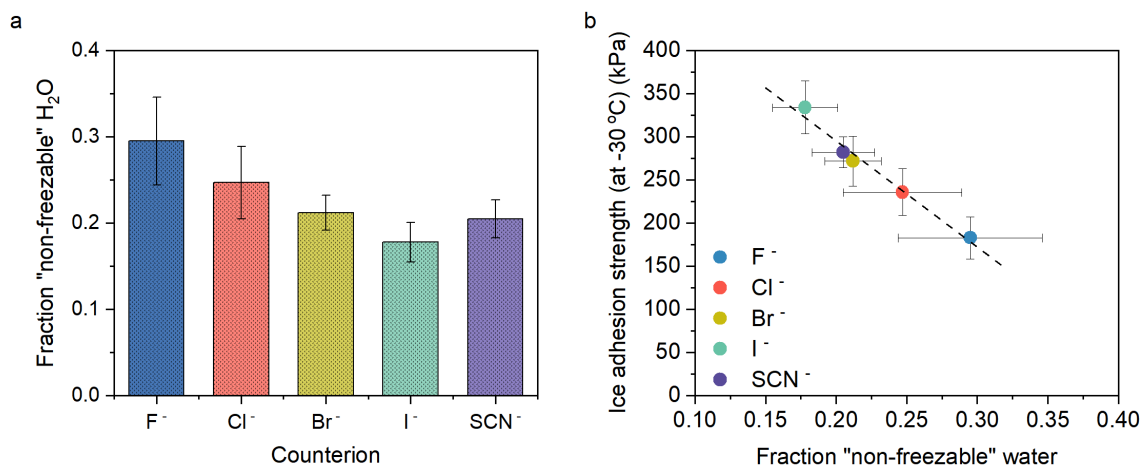
Figure 6.6: (a) Fraction of "non-freezable" water with respect to total hydration water in each polyelectrolyte coating with different counterions. (b) Correlation between ice adhesion strength at -30 ℃ and the fraction of "non-freezable" water present in each coating.

6.2 Hydration water's role in the adhesion of ice to charged polymer coatings

Manuscript 3

Based on the preceding work, it only rational to expect that more drastic tuning of the coatings structure will result in more varied ice adhesion behaviour (Manuscript 2 included work on this subject with regards to crosslinked cationic coatings). In pursuit of this, the temperature dependent ice adhesion behaviour on charged polymers was analysed with respect to both the charge identity of the coated polymer (cationic, anionic, zwitterionic, or non-ionic) and the crosslink density of the cured thin-film. Results of this and subsequent analysis through a combination of and ellipsometry (outlined above and in Manuscript 2) show that changes charge identity and crosslink density drastically affect the phase transition temperature of hydration water in the coating. Furthermore, the nature of the polymer-bound charge was ultimately the source of low-temperature ice adhesion behaviour, correlating the fraction of "non-freezable" water to the adhesion strength of ice. Altogether, this represents the main body of work presented in Manuscript 3, and is described below.

Effect of polymer charge on ice adhesion

As a base, coatings with variable charge identity (cationic, anionic, zwitterionic, and non-ionic) and crosslink density (low, medium, and high) were prepared. Measures of ice adhesion strength were then investigated using the previous described home-built shear ice adhesion apparatus, at 5 °C intervals, from -5 °C to -35 °C. First, it was a main goal to garner an understanding of effect of the polymer charge identity on ice adhesion, and is presented in Figure 6.7a. Here, temperature dependent ice adhesion behaviour can be seen in each of the coatings. Non-M, a non hydrated hydrophobic coating made from crosslinked pBMA, showed a linear increase in ice adhesion strength to ∼500 kPa, at which cohesive failure was observed. Meanwhile, in cationic and anionic polyelectrolyte coatings Cat-M and An-M, the ice adhesion strength was first very low through temperatures of -10 °C, followed by a sudden jump in the ice adhesion strength near -15 °C, after which a constant ice adhesion strength was observed, where adhesive failure of the coating-ice interface was observed. Zwitterionic coatings followed this trend, however, the low temperature ice adhesion strength was noticeably lower (∼150 kPa).

Effect of coating crosslink density on ice adhesion

Noticeably, in figures 6.7b-d, the ice adhesion strength of cationic, anionic, and zwitterionic polymer coatings with low (L), medium (M) and high (H) crosslink densities is presented. In similar fashion to the effect of polymer charge in ice adhesion, the behaviour of each coating over the range of temperatures was such that at temperatures near 0 °C,

the ice adhesion was low (60 kPa $\leq$), after which at approximate temperature, the ice adhesion strength suddenly increased, after which the adhesion strength was constant over the rest of the range. Most interestingly, a crosslink density dependent relationship is observed here, such that less densely crosslinked coatings appear to have this 'jump' in ice adhesion strength at higher temperatures when compared to the more tightly crosslinked coatings which can undergo jumps below -20 °C. Taking anionic coatings as an example: An-L was seen to have a steep increase at approximately -7.5 °C, (between -5 °C and -10 °C), An-M at -15 °C, and An-H at approximately -25 °C. Additionally, although the crosslink density was seen to effect the temperature of these 'jumps' in ice adhesion strength, low temperature ice adhesion strengths were unchanging and indistinguishable between coatings with identical polymer charges, but variable crosslink density.
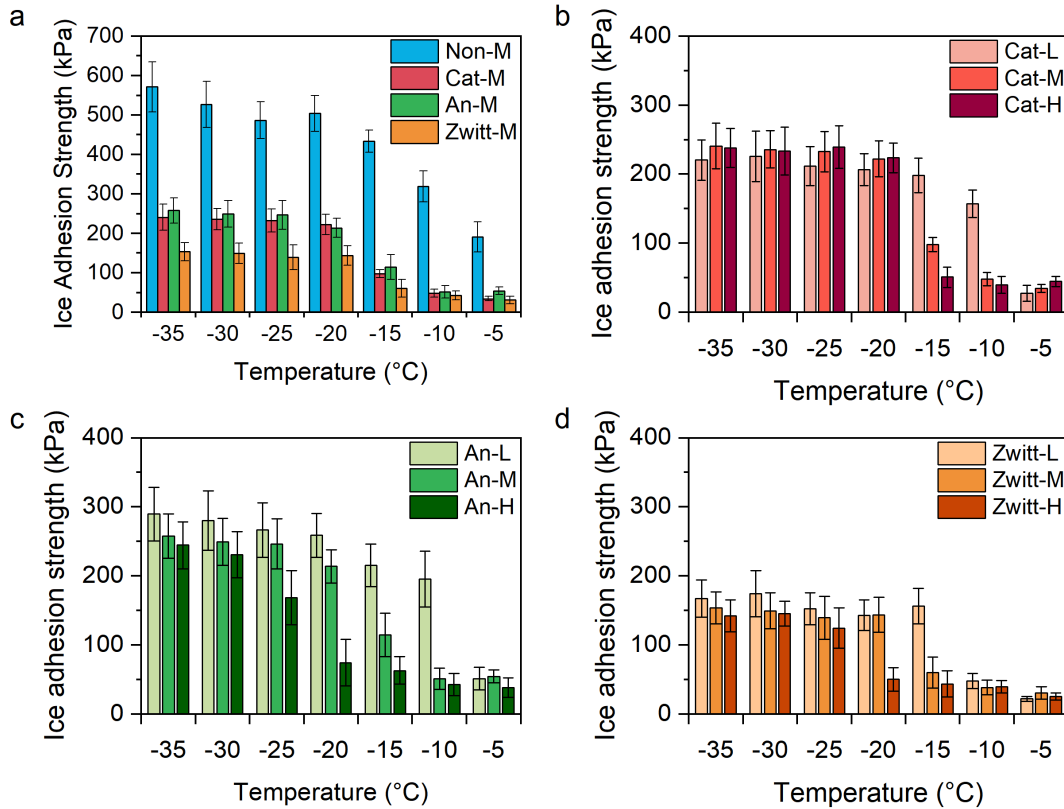
Figure 6.7: (a) Temperature dependent shear ice adhesion strength on cationic, anionic, zwitterionic, and non-ionic polymer coatings of medium crosslink density. Shear ice adhesion strength measurements for (b) cationic, (c) anionic, and (d) zwitterionic polymer coatings with low (L), medium (M) and high (H) crosslink densities are also shown. Plotted values are an average of a minimum of three measurements with corresponding standard deviation.

6.2.1 Mechanism of ice adhesion to charged polymer coatings

From these measurements, it is clear that a difference in ice adhesion mechanism exists between the non-ionic polymer and the charged polymers (Cat, An, and Zwitt). The behaviuor of Non-M resembled the behaviour of ice adhesion on bare or hydrophobic surfaces, where the a linear increase in ice adhesion strength is rationalized by the diminishing presence of a quasi-liquid layer (QLL) that when present, prevent mechanical interlocking between ice and substrate. However, at low temperatures, here observed to be between -15 °C and -20 °C, the QLL is no longer present and the adhesion strength of ice to surface is then defined as the strength necessary to break mechanical interlocking between ice and surface (adhesive failure), or rather the ice itself (cohesive failure).[29, 33, 56]

In contrast to this, the ice adhesion behaviour exhibited by the charged polymer coatings was suggestive towards a phase transition in the coatings hydration water. Identical to the behaviour presented in Manuscript 2, this would propose that ice adhesion on a coatings with liquid hydration water would be inherently low due to its softer nature and lack of mechanical interlocking between ice and the surface. Following, a sharp freezing phase transition would then occur in the hydration water, leading to greater ice adhesion strengths.[51, 52] However this phase transition would not be able to explain the distinct differences in low temperature ice adhesion strength observed.

6.2.2 Effects of charged polymer coatings on swelling and freezing point depression

Effect of polymer charge on swelling

In order to confirm that a phase transition in the hydration water of the coating is indeed responsible for increases seen in ice adhesion strength, a method combining ellipsometry and DSC was used, previously mentioned above in relation to Manuscript 2. Here, ellipsometry measurements on the charged polymer coatings were used to determine the fractions and concentrations of water in the hydrated films, as plotted in Figure 6.8. Between a singular crosslink density, similar swelling is observed between cationic and anionic polyelectrolyte coatings, reporting nearly identical ϕ_{H_2O} values. On the other hand, the swelling of zwitterionic coatings was comparably low. Observed differences in swelling were explained by the fact that polyelectrolyte swelling in water is primarily based on the ion-osmotic effect in partnership with non-electrostatic effects, the latter of which are responsible for hydration of the zwitterionic system as no ion-induced osmotic pressure exists.[70, 87, 180, 192]

Effect of coating crosslink density on swelling

Unsurprisingly, the crosslink density of the coatings plays a significant role in the amount of water of that can be accommodated in the coating. Whereas An-L reported a ϕ_{H_2O} = 0.63, increasing the crosslink density resulted in progressively less water uptake, with ϕ_{H_2O} = 0.44 for An-M and ϕ_{H_2O} = 0.26 for An-H. Increasing crosslink density increases the restrictive elastic force of the crosslinks, therefore leading to decreased swelling in the osmotic regime, as seen here in pure H_2O.
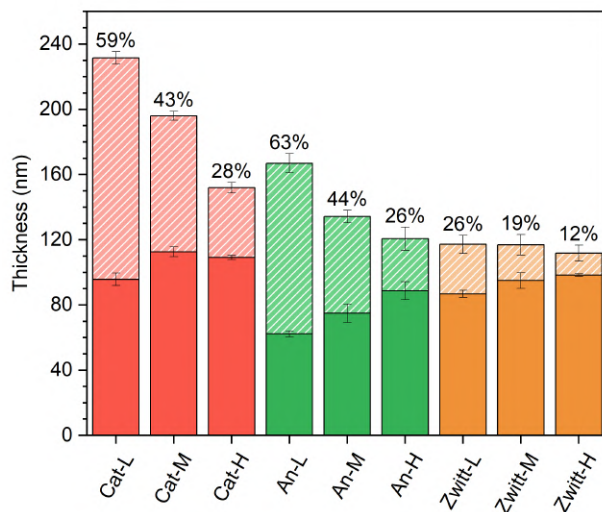
Figure 6.8: Swelling behaviour of variably charged and crosslinked polymer coatings, as measured by ellipsometry. Dry (solid) and hydrated measurements (striped), as well as the labelled percentages corresponding to the volume fraction fraction of water in each polymer coating, ϕ_{H_2O}, are a average of at least three measurements, with the corresponding standard deviations attached.

Effect of polymer charge on freezing point depression

Meanwhile DSC allowed for $T_{m\ onset}$ of binary polymer water samples to be determined, with the intention of providing greater understanding to the concentration dependence of freezing point depression in aqueous charged polymer systems. Figure 6.9a compares the polymer concentration dependent freezing point depression. Here it can be gleamed from the slope of the linear trend that cationic and anionic polyelectrolyte systems cause nearly indistinguishable freezing point depressions, while the zwitterionic system displays a more muted colligative effect. Freezing point depression in these systems stems from the polymer chemistry and concentration of mobile counterions.

Here it is argued that due to their hydrophilic nature, the effect of polymer chemistry is minimal and any differences in freezing point depression must be a function of concentra-

tion of mobile counterions.[189] Based on this argument, cationic and anionic polyelectrolyte have an equally indistinguishable concentration of mobile counterions, contributing to freezing point depression whereas the zwitterionic polymer does not, hence the reduction in freezing point depression at equal polymer concentrations.

Effect of crosslink density on freezing point depression

Figures 6.9b-6.9d, provides further evidence to the notion that changes in polymer chemistry do not significantly affect the freezing point depression, as the trend lines are all seen to overlap, regardless of crosslink density/AMA content.
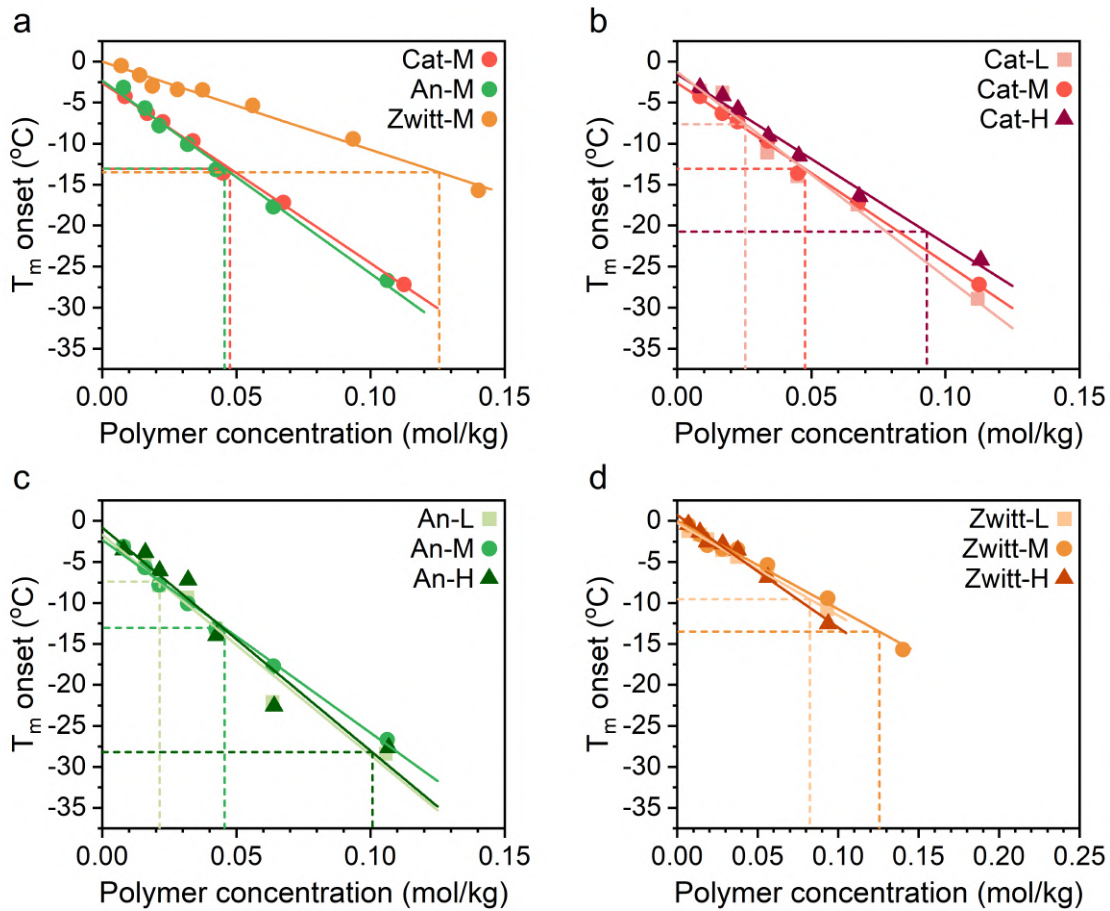
Figure 6.9: Variation in freezing point depression, measured by onset melting temperature (°C) in binary polymer-water mixtures by DSC versus polymer concentration (mol/kg) for (a) variously charged polymers with medium crosslink density, and (b) cationic, (c) anionic, and (d) zwitterionic polymer coatings with low (L), medium (M) and high (H) crosslink densities. To each set, linear fit, and drop lines corresponding to the concentration of polymer in each coating are used to estimate the phase transition temperature of hydration water in the coating, have been added.

6.2.3 Estimating the phase transition temperature of hydration water in charged polymer coatings

Effect of polymer charge on phase transition of coating hydration water

Finally, plotting the onset melting temperatures against polymer concentration (obtained DSC) and then adding drop-lines at the specific points denoting the polymer concentraiton in the films, accurate estimations of the phase transition temperature in the polymer coating can be made. Unsurprisingly, due to aligned swelling and freezing point depression behaviours, Cat-M and An-M are estimated to undergo a phase transition of hydration water in the coating at the same temperature. Coincidentally, Zwitt-M, despite the reduced effect on depressing the freezing point of water, is expected to have a similar phase transition temperature, as the polymer concentration is higher (a result of its lower swelling degree).

Effect of coating crosslink density on phase transition of coating hydration water

Comparing coatings between their respective crosslink density, estimations of freezing point depression are again seen, where given the same effect on freezing point depression, it is expected that a more crosslinked coating will yield a lower estimated phase transition temperature. This is seen when comparing all estimates, here focusing on zwitterionic as an example. Zwitt-L exhibits the greatest swelling, and therefore has the lowest polymer concentration, leading to an estimate of -9.5 ℃, while the moderate swelling of Zwitt-M returns a -13.5 ℃ estimate, and Zwitt-H with the greatest polymer concentration (lowest swelling) providing an extraordinary low estimate of -28.3 ℃.

Correlation to 'jump' in ice adhesion strength

Plotting the temperature of the observed jump in ice adhesion strength against the estimated freezing phase transition temperature of hydration water in the coating (Figure 6.10), provides a good correlation and therefore solid evidence as to the mechanism of temperature-dependent ice adhesion on charged polymer coatings. Additionally, it provides backing as to the accuracy of the method towards estimating the phase transition temperature of the hydration water in the coating. Yet, here it is noted that this accuracy fades slightly with the highly crosslinked coatings. This may be due to the greater error in accurately measuring the freezing point depression at exact yet high polymer concentrations, which would play a sufficient role in affecting the estimates. However, conceivably, inaccuracies in swelling measurements (or polymer density measures) may also lead to slightly erroneous estimates.
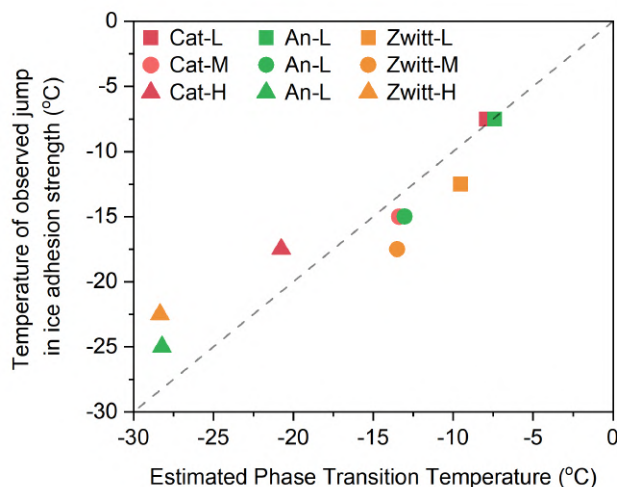
Figure 6.10: Plot of estimated phase transition tempertaure (calculated by ellipsometry and DSC), against the temperature of the observed jump in ice adhesion strength in the polymer coating. The added dashed line, maintains a slope of 1, and depicts where the observed and estimated phase transition temperature are equal.

6.2.4   Correlating low temperature ice adhesion to "nonfreezable" water in the hydration layer

Although the freezing phase transition of hydration water in the coating can rationalize the 'jump' in ice adhesion strength observed, it cannot explain the solely polymer charge dependent nature of low temperature ice adhesion strength. Rather, based our earlier observations above and outlined in Manuscript 2, disparities in low temperature ice adhesion strength can be correlated to the fraction of "non-freezable" hydration water. Therefore a corresponding analysis of the previously gathered DSC data allows us to plot the fraction of "non-freezable" water with regards to each polymer, and against ice adhesion strength.
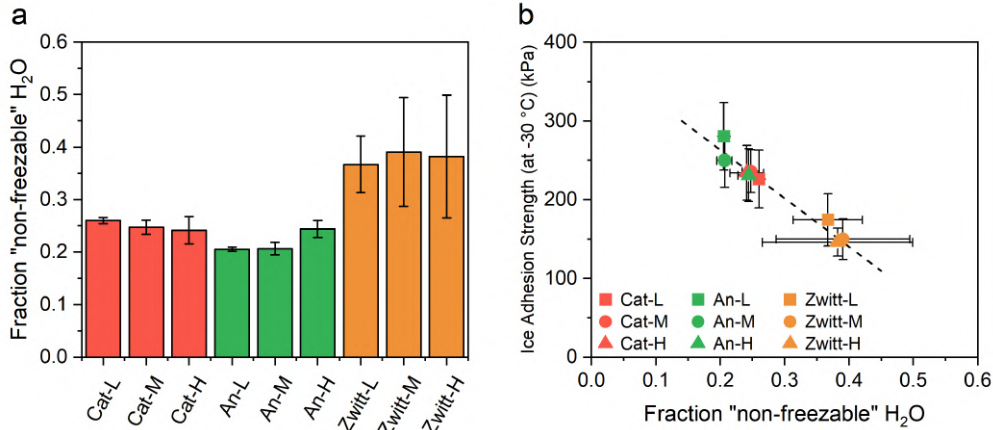
Figure 6.11: (a) Fraction of "non-freezable" water with respect total hydration water in each polymer coating. (b) Correlation between ice adhesion strength at -30 °C, and the fraction of "non-freezable" water. A dashed linear trend line is added as a guide to the eye.

As can be seen in Figure 6.11a, the fraction of "non-freezable" water between coatings of identical polymer charge can be ranked as the following: cationic ≈ anionic ≥ zwitterionic. It is proposed that the greater fraction of "non-freezable" water in zwitterionic coatings is a result of their unique chemical structure. Due to the covalently bound nature of both cationic and anionic charges, a strong dipole between the charges is formed, that when combined with the inherent electrostatic effects, is postulated to have greater and stronger interactions with water.[20, 58, 129]

When plotted against ice adhesion strength (Figure 6.11b, one can observe a clear correlation between the ice adhesion strength and fraction of "non-freezable" water. Yet, analogously, it is stated here that "non-freezable" water should not be looked at as a non-frozen bulk water in the coating, but rather is a measure of different from bulk ice the the system is. It may be envisioned that this is related to the size of crystalline domains and the interfaces that separate them, such that greater "non-freezable water" is correlated to smaller crystalline domains and is expected to give greater coating mobility.

Chapter 7

Conclusions and Perspectives

7.1 Conclusions

Previous findings in this area have shown the incredible promise that lies in low ice adhesion surfaces based on hydrophilic or charged polymer surfaces, however, the mechanisms as to which these anti-icing coatings act to promote low ice adhesion has largely been inferential. Therefore, this overarching study has been to focused on revealing these mechanisms, specifically on charged polymer coatings, and highlighting the tunability of various aspects of charged polymer coatings (i.e. counterion, polymer charge, crosslink density) in pursuance of more effective anti-icing solutions.

To investigate the adhesion strength of ice to various surfaces over a wide-range of temperatures, an ice adhesion test apparatus was developed, mimicking ideal icing conditions of the freezing of bulk ice onto a surface. The design of the apparatus was important as to minimize erroneous ice adhesion measurements through localized shear stresses, such that pushing probe height was minimized yet importantly kept constant, probe speed was minimized, and a linearly increasing force was applied onto the sample. Although not perfect, the development of this ice adhesion test apparatus has been critical in accurately measuring the adhesion strength of ice to surfaces commonly used literature, such as a bare silicon or PBMA.

The preparation of charged polymer coatings with desired tunability in counterion, polymer charge, and crosslink density, was a more challenging endeavour. Furthermore, early on in the project, it was my aim to produce a polymer that could be cured without additives (e.g. radicial initiators, crosslinkers) from ideally the same solvent, however these prerequisites made the preparation even more daunting. Efforts towards coatings with variable crosslink density were a main issue, first attempting to produce polymers with

pendant polymerizable functionalities, before moving towards UV-curable system based on the incorporation of benzophenone moieties to the polymer. Unfortunately neither of these systems were adequate in producing a suitably 'crosslinkable' polymer, and therefore attention was shifted towards thiol-ene click chemistry for polymer coatings. By incorporating allyl methacrylate crosslinker into the polymer via RAFT polymerization, one could create pendant crosslinkable functionalities. However, in order to sure of adequate crosslinking between the chains, the alkene functionalities were reacted with added tetra-functional thiols to form thioether crosslinks between the surface and polymer chains, and the polymer chains themselves. By spin-coating coating polymers with various charged monomer and allyl methacrylate composition, a structure was produced through which the following investigations could be based on.

Measures of ice adhesion strength on cationic polymer coatings with varying counterions presented both temperature and counterion dependence, suggesting a mechanism based on the physical state of hydration water. To better resolve this behaviour and proposed mechanism, TIR Raman spectroscopy was used to accurately probe the hydration water of the coating. Results of this characterization provide clear evidence of a freezing phase transition of the hydration water in charge polymer coatings. Independently, data from ellipsometry and DSC rationalized the counterion-dependent freezing phase transition, such that the strength of the ion pair (i.e. the degree to which they are dissociated) will affect swelling and freezing point depression of the polymer. Furthermore, partnering these two measurements, gave a separate technique to estimate the phase transition temperature of the hydration water in the polymer coating, matching the measures garnered by TIR Raman. Yet this mechanism could not explain disparities of low temperature ice adhesion strength, rather, correlating with the presence of "non-freezable" water was uncovered by our earlier DSC experiments, and believed to be related to how different from bulk ice the system is.

Focused on the prospect of further improving the anti-icing properties, polymer coatings with variously charged functionalities were investigated. In a similar manner to tuning the counterions in cationic coatings, the type of charge on the polymer had a considerable effect on both the swelling and the polymer-induced freezing point depression of water. The presence of dissociated counterions in polyelectrolytes manifested into greater swelling and freezing point depressions over that of zwitterionic polymers. Yet, the less swollen nature zwitterionic polymer coatings gives a concentrated polymer solution that in-practice resulted in an equal freezing point depression of the hydration water. Lastly, the greater fraction of "non-freezable" water in zwitterionic polymer coatings was found to reduce the low temperature ice adhesion strength, and was concluded to be the result of stronger polymer-water interactions with zwitterions over polyelectrolytes. Additional tuning in the crosslink density of these variably charged polymers led to a broad range of freezing phase transitions of hydration water, where more tightly networked coatings result in more concentrated polymer solutions with lower freezing phase transitions. However,

the fraction of "non-freezable" water was unchanging, explaining the indistinguishable nature of ice adhesion on coatings with variable crosslink density.

These investigations have conclusively provided evidence towards the freezing phase transition of hydration water and presence of "non-freezable water" in charged polymer coatings. By modifying the chemical and coating structure, these effects can tuned to provide more efficient anti-icing coatings.

7.2   Perspectives

Although this thesis has brought a mechanistic understanding of ice adhesion on hydrophilic charged polymer coatings - there still lie questions regarding how to further tune coatings, developing more realistic measurements of ice adhesion, and what impacts these potential studies may have on continued research towards efficient anti-icing coatings.

One feature that had the ability to be tuned in our developed coating technology was the concentration of charged functionalities in the polymer. Here it would be interesting to see the effect that the incorporation of greater amounts of charged monomers into a polymer chain would have on ice adhesion. In previous experiments, only 25 mol.% of monomers were charged. However, it would be expected given a 40 or 50 mol.% composition, that there may be considerable changes in absolute ice adhesion strength, temperature of the phase transition of a coating's hydration water, and fractions of "non-freezable" water. Additionally, explaining these effects may be a more complex task, as in polyelectrolytes, it could be expected that a lesser fraction of counterions are dissociated due to the high crowding of charges; current understanding postulated fluoride and chloride ions are completely dissociated given a METAC incorporation of only 25 mol.% , yet given much higher METAC monomer functionalitiy into a polymer (e.g. 50-95 percent mol.%), this dissociation might sway. In zwitterionic polymers system with greater zwitterionic functionality, this may also lead to greater zwitterionic associations, with unknown consequences towards ice adhesion. Moreover, this work found the fraction of "non-freezable" water was found to be high in zwitterionic systems, however changing the chemical and charge structure of these zwitterionic functionalites may unlock new potential, further increasing this beneficial anti-icing property.

Yet despite these possible investigations, one research area that is seemingly underdeveloped is the nature of realistic ice adhesion to coatings. Here, thick protective coatings, such as those on the exteriors of aircraft and wind turbines today, could be produced, incorporating some of developments that this thesis has brought to light. Rather than thickness being measured in 100-200 nm scale, exterior coats would be on the order of 50 - 500 μm, and may present effects or complications previously unseen in this work. Yet there still lies intreestingly potential to develop a coating with low ice adhesion properties

such that the force of gravity or light wind could effectively remove ice from the surfaces. Bringing in a further facet of realism, the difference in type of ice on the ice adhesion strength to thick coatings could be investigated. Whereas bulk ice is the freezing of liquid water into a clear and more homogeous solid structure, rime ice, the freezing of super-cooled water droplets to surfaces, may be more realistic type of icing for applications with aircraft or wind turbines. However investigating the adhesion strength of rime, or even frost ice, snow, or a mixture of these, in a realistic setting is inherently challenging.

Bibliography

(1) Parent, O.; Ilinca, A. Anti-icing and de-icing techniques for wind turbines: Critical review. *Cold Reg. Sci. Technol.* **2011**, *65*, 88–96.

(2) Ryerson, C. C. Ice protection of offshore platforms. *Cold Reg. Sci. Technol.* **2011**, *65*, 97–110.

(3) Farzaneh, M., *Atmospheric Icing of Power*, 2008; Vol. 84, p 381.

(4) Farzaneh, M.; Ryerson, C. C. Anti-icing and deicing techniques. *Cold Reg. Sci. Technol.* **2011**, *65*, 1–4.

(5) Dalili, N.; Edrisy, A.; Carriveau, R. A review of surface engineering issues critical to wind turbine performance. *Renew. Sustain. Energy Rev.* **2009**, *13*, 428–438.

(6) Wu, Z.; Wang, Q. In *Ice Adhes. Mech. Meas. Mitig.* 2020, pp 567–606.

(7) Dotan, A.; Dodiuk, H.; Laforte, C.; Kenig, S. The relationship between water wetting and ice adhesion. *J. Adhes. Sci. Technol.* **2009**, *23*, 1907–1915.

(8) Wang, T.; Zheng, Y.; Raji, A. R. O.; Li, Y.; Sikkema, W. K.; Tour, J. M. Passive Anti-Icing and Active Deicing Films. *ACS Appl. Mater. Interfaces* **2016**, *8*, 14169–14173.

(9) Zhuo, Y.; Chen, J.; Xiao, S.; Li, T.; Wang, F.; He, J.; Zhang, Z. Gels as emerging anti-icing materials: A mini review. *Mater. Horizons* **2021**, *8*, 3266–3280.

(10) Golovin, K.; Kobaku, S. P.; Lee, D. H.; DiLoreto, E. T.; Mabry, J. M.; Tuteja, A. Designing durable icephobic surfaces. *Sci. Adv.* **2016**, *2*, DOI: `10.1126/sciadv.1501496`.

(11) He, Z.; Zhuo, Y.; Zhang, Z.; He, J. Design of icephobic surfaces by lowering ice adhesion strength: A mini review. *Coatings* **2021**, *11*, 1–26.

(12) Makkonen, L. Ice adhesion - Theory, measurements and countermeasures. *J. Adhes. Sci. Technol.* **2012**, *26*, 413–445.

(13) Gao, L.; Hu, H. Wind turbine icing characteristics and icing-induced power losses to utility-scale wind turbines. *Proc. Natl. Acad. Sci. U. S. A.* **2021**, *118*, 4–6.

(14) Libisch, B.; French, H. K.; Hartnik, T.; Anton, A.; Biró, B. Laboratory-scale evaluation of a combined soil amendment for the enhanced biodegradation of propylene glycol-based aircraft de-icing fluids. *Environ. Technol.* **2012**, *33*, 717–724.

(15) Ma, H.; Ma, H.; Yu, H.; Da, B.; Gong, W.; Zhang, N. The physical properties of organic aircraft deicers under low temperature. *Cold Reg. Sci. Technol.* **2022**, *196*, DOI: `10.1016/j.coldregions.2021.103471`.

(16) Wang, F.; Zhuo, Y.; He, Z.; Xiao, S.; He, J.; Zhang, Z. Dynamic Anti-Icing Surfaces (DAIS). *Adv. Sci.* **2021**, *8*, 1–26.

(17) Kenzhebayeva, A.; Bakbolat, B.; Sultanov, F.; Daulbayev, C.; Mansurov, Z. A mini-review on recent developments in anti-icing methods. *Polymers (Basel).* **2021**, *13*, DOI: `10.3390/polym13234149`.

(18) Liu, Y.; Hu, H. In *Ice Adhes. Mech. Meas. Mitig.* 2020, pp 547–575.

(19) He, Z.; Xie, W. J.; Liu, Z.; Liu, G.; Wang, Z.; Gao, Y. Q.; Wang, J. Tuning ice nucleation with counterions on polyelectrolyte brush surfaces. *Sci. Adv.* **2016**, *2*, DOI: `10.1126/sciadv.1600345`.

(20) Huang, B.; Jiang, S.; Diao, Y.; Liu, X.; Liu, W.; Chen, J.; Yang, H. Hydrogels as durable anti-icing coatings inhibit and delay ice nucleation. *Molecules* **2020**, *25*, DOI: `10.3390/molecules25153378`.

(21) He, Z.; Wu, C.; Hua, M.; Wu, S.; Wu, D.; Zhu, X.; Wang, J.; He, X. Bioinspired Multifunctional Anti-icing Hydrogel. *Matter* **2020**, *2*, 723–734.

(22) Faraday, M. Note on Regelation. **1860**, 440–450.

(23) H.H.G.Jellinek Ice Adhesion. *Can. J. Phys.* **1962**, *40*, 1294–1309.

(24) Jellinek, H. H. Adhesive properties of ice. *J. Colloid Sci.* **1959**, *14*, 268–280.

(25) Furukawa, Y.; Ishikawa, I. Direct evidence for melting transition at interface between ice crystal and glass substrate. *J. Cryst. Growth* **1993**, *128*, 1137–1142.

(26) Final, I. Extrinsic Premelting at. **1994**, 8096–8100.

(27) Engemann, S.; Reichert, H.; Dosch, H.; Bilgram, J.; Honkimäki, V.; Snigirev, A. Interfacial melting of ice in contact With SiO2. *Phys. Rev. Lett.* **2004**, *92*, 2–5.

(28) Tyrode, E.; Liljeblad, J. F. Water structure next to ordered and disordered hydrophobic silane monolayers: A vibrational sum frequency spectroscopy study. *J. Phys. Chem. C* **2013**, *117*, 1780–1790.

(29) Liljeblad, J. F. D.; Furó, I.; Tyrode, E. C. The premolten layer of ice next to a hydrophilic solid surface: correlating adhesion with molecular properties. *Phys. Chem. Chem. Phys.* **2017**, *19*, 305–317.

(30) Ishizaki, T; Marauyama, M; Furukawa, Y; Dash, J. Premelting of ice in porous silica glass T. *J. Cryst. Growth* **1996**, *163*, 455–460.

(31) Makkonen, L. Surface melting of ice. *J. Phys. Chem. B* **1997**, *101*, 6196–6200.

(32) Petrenko, V. F.; Peng, S. Reduction of ice adhesion to metal by using self-assembling monolayers (SAMs). *Can. J. Phys.* **2003**, *81*, 387–393.

(33) Meuler, A. J.; Smith, J. D.; Varanasi, K. K.; Mabry, J. M.; McKinley, G. H.; Cohen, R. E. Relationships between water wettability and ice adhesion. *ACS Appl. Mater. Interfaces* **2010**, *2*, 3100–3110.

(34) Susoff, M.; Siegmann, K.; Pfaffenroth, C.; Hirayama, M. Evaluation of icephobic coatings - Screening of different coatings and influence of roughness. *Appl. Surf. Sci.* **2013**, *282*, 870–879.

(35) Hassan, M. F.; Lee, H. P.; Lim, S. P. The variation of ice adhesion strength with substrate surface roughness. *Meas. Sci. Technol.* **2010**, *21*, DOI: `10.1088/0957-0233/21/7/075701`.

(36) Sood, R.; Obadia, M. M.; Mudraboyina, B. P.; Zhang, B.; Serghei, A.; Bernard, J.; Drockenmuller, E. 1,2,3-Triazolium-based poly(acrylate ionic liquid)s. *Polymer (Guildf).* **2014**, *55*, 3314–3319.

(37) Kreder, M. J.; Alvarenga, J.; Kim, P.; Aizenberg, J. Design of anti-icing surfaces: Smooth, textured or slippery? *Nat. Rev. Mater.* **2016**, *1*, DOI: `10.1038/natrevmats.2015.3`.

(38) Jung, S.; Dorrestijn, M.; Raps, D.; Das, A.; Megaridis, C. M.; Poulikakos, D. Are superhydrophobic surfaces best for icephobicity? *Langmuir* **2011**, *27*, 3059–3066.

(39) Chen, J.; Liu, J.; He, M.; Li, K.; Cui, D.; Zhang, Q.; Zeng, X.; Zhang, Y.; Wang, J.; Song, Y. Superhydrophobic surfaces cannot reduce ice adhesion. *Appl. Phys. Lett.* **2012**, *101*, 95–98.

(40) Menini, R.; Farzaneh, M. Advanced icephobic coatings. *J. Adhes. Sci. Technol.* **2011**, *25*, 971–992.

(41) Cassie, A. Contact Angles. *Discuss. Faraday Soc.* **1948**, *3*, 11–16.

(42) Kulinich, S. A.; Farhadi, S.; Nose, K.; Du, X. W. Superhydrophobic surfaces: Are they really ice-repellent? *Langmuir* **2011**, *27*, 25–29.

(43) Sojoudi, H.; Wang, M.; Boscher, N. D.; McKinley, G. H.; Gleason, K. K. Durable and scalable icephobic surfaces: Similarities and distinctions from superhydrophobic surfaces. *Soft Matter* **2016**, *12*, 1938–1963.

(44) Kim, P.; Wong, T. S.; Alvarenga, J.; Kreder, M. J.; Adorno-Martinez, W. E.; Aizenberg, J. Liquid-infused nanostructured surfaces with extreme anti-ice and anti-frost performance. *ACS Nano* **2012**, *6*, 6569–6577.

(45) Wilson, P. W.; Lu, W.; Xu, H.; Kim, P.; Kreder, M. J.; Alvarenga, J.; Aizenberg, J. Inhibition of ice nucleation by slippery liquid-infused porous surfaces (SLIPS). *Phys. Chem. Chem. Phys.* **2013**, *15*, 581–585.

(46) Wong, T. S.; Kang, S. H.; Tang, S. K.; Smythe, E. J.; Hatton, B. D.; Grinthal, A.; Aizenberg, J. Bioinspired self-repairing slippery surfaces with pressure-stable omniphobicity. *Nature* **2011**, *477*, 443–447.

(47) Ozbay, S.; Yuceel, C.; Erbil, H. Y. Improved Icephobic Properties on Surfaces with a Hydrophilic Lubricating Liquid. *ACS Appl. Mater. Interfaces* **2015**, *7*, 22067–22077.

(48) Liang, Z. H.; Wu, S. L.; Liu, C.; Yang, H. C.; Darling, S. B.; Xu, Z. K. When SLIPS meets TIPS: An endogenous lubricant-infused surface by taking the diluent as the lubricant. *Chem. Eng. J.* **2021**, *425*, 130600.

(49) Yuan, Y.; Xiang, H.; Liu, G.; Wang, L.; Liu, H.; Liao, R. Self-Repairing Performance of Slippery Liquid Infused Porous Surfaces for Durable Anti-Icing. *Adv. Mater. Interfaces* **2022**, *9*, 1–10.

(50) Chen, J.; Dou, R.; Cui, D.; Zhang, Q.; Zhang, Y.; Xu, F.; Zhou, X.; Wang, J.; Song, Y.; Jiang, L. Robust prototypical anti-icing coatings with a self-lubricating

liquid water layer between ice and substrate. *ACS Appl. Mater. Interfaces* **2013**, *5*, 4026–4030.

(51) Dou, R.; Chen, J.; Zhang, Y.; Wang, X.; Cui, D.; Song, Y.; Jiang, L.; Wang, J. Anti-icing coating with an aqueous lubricating layer. *ACS Appl. Mater. Interfaces* **2014**, *6*, 6998–7003.

(52) Chen, J.; Li, K.; Wu, S.; Liu, J.; Liu, K.; Fan, Q. Durable Anti-Icing Coatings Based on Self-Sustainable Lubricating Layer. *ACS Omega* **2017**, *2*, 2047–2054.

(53) Okoroafor, E. U.; Newborough, M.; Highgate, D. Effects of thermal cycling on the crystallization characteristics of water within crosslinked hydro-active polymeric structures. *J. Phys. D. Appl. Phys.* **1998**, *31*, 3130–3138.

(54) Faroongsarng, D.; Sukonrat, P. Thermal behavior of water in the selected starch- and cellulose-based polymeric hydrogels. *Int. J. Pharm.* **2008**, *352*, 152–158.

(55) Liu, W. G.; Yao, K. D. What causes the unfrozen water in polymers: Hydrogen bonds between water and polymer chains? *Polymer (Guildf).* **2001**, *42*, 3943–3947.

(56) Chen, D.; Gelenter, M. D.; Hong, M.; Cohen, R. E.; McKinley, G. H. Icephobic surfaces induced by interfacial nonfrozen water. *ACS Appl. Mater. Interfaces* **2017**, *9*, 4202–4214.

(57) Chernyy, S.; Järn, M.; Shimizu, K.; Swerin, A.; Pedersen, S. U.; Daasbjerg, K.; Makkonen, L.; Claesson, P.; Iruthayaraj, J. Superhydrophilic polyelectrolyte brush layers with imparted anti-icing properties: Effect of counter ions. *ACS Appl. Mater. Interfaces* **2014**, *6*, 6487–6496.

(58) Liang, B.; Zhang, G.; Zhong, Z.; Huang, Y.; Su, Z. Superhydrophilic Anti-Icing Coatings Based on Polyzwitterion Brushes. *Langmuir* **2019**, *35*, 1294–1301.

(59) Ping, Z. H.; Nguyen, Q. T.; Chen, S. M.; Zhou, J. Q.; Ding, Y. D. States of water in different hydrophilic polymers - DSC and FTIR studies. *Polymer (Guildf).* **2001**, *42*, 8461–8467.

(60) Guan, L.; Xu, H.; Huang, D. The investigation on states of water in different hydrophilic polymers by DSC and FTIR. *J. Polym. Res.* **2011**, *18*, 681–689.

(61) Mecerreyes, D. Polymeric ionic liquids: Broadening the properties and applications of polyelectrolytes. *Prog. Polym. Sci.* **2011**, *36*, 1629–1648.

(62) Higaki, Y.; Inutsuka, Y.; Ono, H.; Yamada, N. L.; Ikemoto, Y.; Takahara, A. Counteranion-Specific Hydration States of Cationic Polyelectrolyte Brushes. *Ind. Eng. Chem. Res.* **2018**, *57*, 5268–5275.

(63) Manning, G. S. Counterion Binding in Polyelectrolyte Theory. *Acc. Chem. Res.* **1979**, *12*, 443–449.

(64) Willott, J. D.; Murdoch, T. J.; Humphreys, B. A.; Edmondson, S.; Wanless, E. J.; Webber, G. B. Anion-specific effects on the behavior of pH-sensitive polybasic brushes. *Langmuir* **2015**, *31*, 3707–3717.

(65) Sanjuan, S.; Perrin, P.; Pantoustier, N.; Tran, Y. Synthesis and swelling behavior of pH-responsive polybase brushes. *Langmuir* **2007**, *23*, 5769–5778.

(66) Zhang, J.; Kou, R.; Liu, G. Effect of Salt Concentration on the pH Responses of Strong and Weak Polyelectrolyte Brushes. *Langmuir* **2017**, *33*, 6838–6845.

(67) Tang, H.; Tang, J.; Ding, S.; Radosz, M.; Shen, Y. Atom transfer radical polymerization of styrenic ionic liquid monomers and carbon dioxide absorption of the polymerized ionic liquids. *J. Polym. Sci. Part A Polym. Chem.* **2005**, *43*, 1432–1443.

(68) Stancik, C. M.; Lavoie, A. R.; Schütz, J.; Achurra, P. A.; Lindner, P.; Gast, A. P.; Waymouth, R. M. Micelles of imidazolium-functionalized polystyrene diblock copolymers investigated with neutron and light scattering. *Langmuir* **2004**, *20*, 596–605.

(69) Galvin, C. J.; Genzer, J. Applications of surface-grafted macromolecules derived from post-polymerization modification reactions. *Prog. Polym. Sci.* **2012**, *37*, 871–906.

(70) Ehtiati, K.; Z. Moghaddam, S.; Daugaard, A. E.; Thormann, E. Crucial Nonelectrostatic Effects on Polyelectrolyte Brush Behavior. *Macromolecules* **2021**, *54*, 3388–3394.

(71) Yuan, J.; Antonietti, M. Poly(ionic liquid)s: Polymers expanding classical property profiles. *Polymer (Guildf).* **2011**, *52*, 1469–1482.

(72) Lamontagne, H. R.; Lessard, B. H. Nitroxide-Mediated Polymerization: A Versatile Tool for the Engineering of Next Generation Materials. *ACS Appl. Polym. Mater.* **2020**, *2*, 5327–5344.

(73) Keoshkerian, B.; Georges, M. K.; Boils-Boissier, D. Living Free-Radical Aqueous Polymerization. *Macromolecules* **1995**, *28*, 6381–6382.

(74) Bouchet, R.; Maria, S.; Meziane, R.; Aboulaich, A.; Lienafa, L.; Bonnet, J.-p.; Phan, T.; Bertin, D.; Gigmes, D.; Devaux, D.; Denoyel, R.; Armand, M. Efficient electrolytes for lithium-metal batteries. *Nat. Mater.* **2013**, *12*, 1–6.

(75) Perrier, S. 50th Anniversary Perspective: RAFT Polymerization - A User Guide. *Macromolecules* **2017**, *50*, 7433–7447.

(76) Moad, G.; Rizzardo, E.; Thang, S. H. Radical addition-fragmentation chemistry in polymer synthesis. *Polymer (Guildf).* **2008**, *49*, 1079–1131.

(77) Chiefari, J.; Chong, Y. K. B.; Ercole, F.; Krstina, J.; Jeffery, J.; Le, T. P. T.; Mayadunne, R. T. A.; Meijs, G. F.; Moad, C. L.; Moad, G.; Rizzardo, E.; Thang, S. H.; South, C. Living Free-Radical Polymerization by Reversible Addition - Fragmentation Chain Transfer : The RAFT Process We wish to report a new living free-radical polymer- ization of exceptional effectiveness and versatility . 1 The living character is conferred by. **1998**, *9297*, 5559–5562.

(78) Baussard, J. F.; Habib-Jiwan, J. L.; Laschewsky, A.; Mertoglu, M.; Storsberg, J. New chain transfer agents for reversible addition-fragmentation chain transfer (RAFT) polymerisation in aqueous solution. *Polymer (Guildf).* **2004**, *45*, 3615–3626.

(79) Cao, X.; An, Z. RAFT synthesis in water of cationic polyelectrolytes with tunable UCST. *Macromol. Rapid Commun.* **2015**, *36*, 2107–2110.

(80) D'Agosto, F.; Rieger, J.; Lansalot, M. RAFT-Mediated Polymerization-Induced Self-Assembly. *Angew. Chemie - Int. Ed.* **2020**, *59*, 8368–8392.

(81) Doncom, K. E.; Willcock, H.; O'Reilly, R. K. The direct synthesis of sulfobetaine-containing amphiphilic block copolymers and their self-assembly behavior. *Eur. Polym. J.* **2017**, *87*, 497–507.

(82) Das, D.; Gerboth, D.; Postma, A.; Srinivasan, S.; Kern, H.; Chen, J.; Ratner, D. M.; Stayton, P. S.; Convertine, A. J. Synthesis of zwitterionic, hydrophobic, and amphiphilic polymers: Via RAFT polymerization induced self-assembly (PISA) in acetic acid. *Polym. Chem.* **2016**, *7*, 6133–6143.

(83) Bai, S.; Li, X.; Zhang, R.; Li, C.; Zhu, K.; Sun, P.; Zhao, Y.; Ren, L.; Yuan, X. Enhancing antifogging/frost-resisting performances of amphiphilic coatings via cationic, zwitterionic or anionic polyelectrolytes. *Chem. Eng. J.* **2019**, *357*, 667–677.

(84) Lyon, C. K.; Hill, E. O.; Berda, E. B. Zipping polymers into nanoparticles via intrachain alternating radical copolymerization. *Macromol. Chem. Phys.* **2016**, *217*, 501–508.

(85) Jiang, T.; Zajforoushan Moghaddam, S.; Thormann, E. PPEGMEMA-based cationic copolymers designed for layer-by-layer assembly. *RSC Adv.* **2019**, *9*, 26915–26926.

(86) Jiang, T.; Moghaddam, S. Z.; Thormann, E. A single-component, cross-linked, and surface-grafted polyelectrolyte film fabricated by the layer-by-layer assembly method. *Polymer (Guildf).* **2020**, *200*, 122524.

(87) Ehtiati, K.; Moghaddam, S. Z.; Klok, H.-a.; Daugaard, A. E.; Thormann, E. Speci fi c Counterion E ff ects on the Swelling Behavior of Strong Polyelectrolyte Brushes. **2022**, DOI: 10.1021/acs.macromol.2c00411.

(88) Buhl, K. B.; Agergaard, A. H.; Lillethorup, M.; Nikolajsen, J. P.; Pedersen, S. U.; Daasbjerg, K. Polymer brush coating and adhesion technology at scale. *Polymers (Basel).* **2020**, *12*, 1–15.

(89) Lyu, Z.; An, Q.; Qin, P.; Li, W.; Wang, X. Preparation and characterization of POSS-containing poly(perfluoropolyether)methacrylate hybrid copolymer and its superhydrophobic coating performance. *RSC Adv.* **2019**, *9*, 4765–4770.

(90) Chollet, B.; Li, M.; Martwong, E.; Bresson, B.; Fretigny, C.; Tabeling, P.; Tran, Y. Multiscale Surface-Attached Hydrogel Thin Films with Tailored Architecture. *ACS Appl. Mater. Interfaces* **2016**, *8*, 11729–11738.

(91) Chollet, B.; D'Eramo, L.; Martwong, E.; Li, M.; Macron, J.; Mai, T. Q.; Tabeling, P.; Tran, Y. Tailoring Patterns of Surface-Attached Multiresponsive Polymer Networks. *ACS Appl. Mater. Interfaces* **2016**, *8*, 24870–24879.

(92) D'eramo, L.; Chollet, B.; Leman, M.; Martwong, E.; Li, M.; Geisler, H.; Dupire, J.; Kerdraon, M.; Vergne, C.; Monti, F.; Tran, Y.; Tabeling, P. Microfluidic actuators based on temperature-responsive hydrogels. *Microsystems Nanoeng.* **2018**, *4*, 1–7.

(93) Seidi, F.; Zhao, W. F.; Xiao, H. N.; Jin, Y. C.; Saeb, M. R.; Zhao, C. S. Advanced Surfaces by Anchoring Thin Hydrogel Layers of Functional Polymers. *Chinese J. Polym. Sci. (English Ed.* **2021**, *39*, 14–34.

(94) Koc, J.; Schönemann, E.; Amuthalingam, A.; Clarke, J.; Finlay, J. A.; Clare, A. S.; Laschewsky, A.; Rosenhahn, A. Low-Fouling Thin Hydrogel Coatings Made of Photo-Cross-Linked Polyzwitterions. *Langmuir* **2019**, *35*, 1552–1562.

(95) Dong, H.; Ye, P.; Zhong, M.; Pietrasik, J.; Drumright, R.; Matyjaszewski, K. Superhydrophilic surfaces via polymer-SiO2 nanocomposites. *Langmuir* **2010**, *26*, 15567–15573.

(96) Jon, S.; Seong, J.; Khademhosseini, A.; Tran, T. N. T.; Laibinis, P. E.; Langer, R. Construction of Nonbiofouling Surfaces by Polymeric Self-Assembled Monolayers. *Langmuir* **2003**, *19*, 9989–9993.

(97) Colak, S.; Tew, G. N. Dual-functional ROMP-based betaines: Effect of hydrophilicity and backbone structure on nonfouling properties. *Langmuir* **2012**, *28*, 666–675.

(98) Wang, C.; Ma, C.; Mu, C.; Lin, W. A novel approach for synthesis of zwitterionic polyurethane coating with protein resistance. *Langmuir* **2014**, *30*, 12860–12867.

(99) Dai, J.; Zhao, H.; Lin, X.; Liu, S.; Liu, Y.; Liu, X.; Fei, T.; Zhang, T. Ultrafast Response Polyelectrolyte Humidity Sensor for Respiration Monitoring. *ACS Appl. Mater. Interfaces* **2019**, DOI: `10.1021/acsami.8b18904`.

(100) Salis, A.; Ninham, B. W. Models and mechanisms of Hofmeister effects in electrolyte solutions, and colloid and protein systems revisited. *Chem. Soc. Rev.* **2014**, *43*, 7358–7377.

(101) Kou, R.; Zhang, J.; Chen, Z.; Liu, G. Counterion Specificity of Polyelectrolyte Brushes: Role of Specific Ion-Pairing Interactions. *ChemPhysChem* **2018**, *19*, 1404–1413.

(102) Kunz, W.; Lo Nostro, P.; Ninham, B. W. The present state of affairs with Hofmeister effects. *Curr. Opin. Colloid Interface Sci.* **2004**, *9*, 1–18.

(103) Kunz, W.; Henle, J.; Ninham, B. W. 'Zur Lehre von der Wirkung der Salze' (about the science of the effect of salts): Franz Hofmeister's historical papers. *Curr. Opin. Colloid Interface Sci.* **2004**, *9*, 19–37.

(104) Mazzini, V.; Craig, V. S. What is the fundamental ion-specific series for anions and cations? Ion specificity in standard partial molar volumes of electrolytes and electrostriction in water and non-aqueous solvents. *Chem. Sci.* **2017**, *8*, 7052–7065.

(105) Wei, Q.; Cai, M.; Zhou, F.; Liu, W. Dramatically tuning friction using responsive polyelectrolyte brushes. *Macromolecules* **2013**, *46*, 9368–9379.

(106) Farhan, T.; Azzaroni, O.; Huck, W. T. AFM study of cationically charged polymer brushes: Switching between soft and hard matter. *Soft Matter* **2005**, *1*, 66–68.

(107) Azzaroni, O.; Moya, S.; Farhan, T.; Brown, A. A.; Huck, W. T. Switching the properties of polyelectrolyte brushes via "hydrophobic collapse". *Macromolecules* **2005**, *38*, 10192–10199.

(108) Azzaroni, O.; Brown, A. A.; Huck, W. T. Tunable wettability by clicking counterions into polyelectrolyte brushes. *Adv. Mater.* **2007**, *19*, 151–154.

(109) Moghaddam, S. Z.; Thormann, E. The Hofmeister series: Specific ion effects in aqueous polymer solutions. *J. Colloid Interface Sci.* **2019**, *555*, 615–635.

(110)   Schlenoff, J. B. Zwitteration: Coating surfaces with zwitterionic functionality to reduce nonspecific adsorption. *Langmuir* **2014**, *30*, 9625–9636.

(111)   Schulz, D. N.; Peiffer, D. G.; Agarwal, P. K.; Larabee, J.; Kaladas, J. J.; Soni, L.; Handwerker, B.; Garner, R. T. Phase behaviour and solution properties of sulphobetaine polymers. *Polymer (Guildf).* **1986**, *27*, 1734–1742.

(112)   Xiao, S.; Zhang, Y.; Shen, M.; Chen, F.; Fan, P.; Zhong, M.; Ren, B.; Yang, J.; Zheng, J. Structural Dependence of Salt-Responsive Polyzwitterionic Brushes with an Anti-Polyelectrolyte Effect. *Langmuir* **2018**, *34*, 97–105.

(113)   Wang, T.; Kou, R.; Liu, H.; Liu, L.; Zhang, G.; Liu, G. Anion Specificity of Polyzwitterionic Brushes with Different Carbon Spacer Lengths and Its Application for Controlling Protein Adsorption. *Langmuir* **2016**, *32*, 2698–2707.

(114)   Erfani, A.; Seaberg, J.; Aichele, C. P.; Ramsey, J. D. Interactions between Biomolecules and Zwitterionic Moieties: A Review. *Biomacromolecules* **2020**, *21*, 2557–2573.

(115)   Wang, F.; Yang, J.; Zhao, J. Understanding anti-polyelectrolyte behavior of a well-defined polyzwitterion at the single-chain level. *Polym. Int.* **2015**, *64*, 999–1005.

(116)   Petroff, M. G.; Garcia, E. A.; Herrera-Alonso, M.; Bevan, M. A. Ionic Strength-Dependent Interactions and Dimensions of Adsorbed Zwitterionic Copolymers. *Langmuir* **2019**, *35*, 4976–4985.

(117)   Higaki, Y.; Kobayashi, M.; Takahara, A. Hydration State Variation of Polyzwitterion Brushes through Interplay with Ions. *Langmuir* **2020**, *36*, 9015–9024.

(118)   Kunz, W.; Belloni, L.; Bernard, O.; Ninham, B. W. Osmotic coefficients and surface tensions of aqueous electrolyte solutions: Role of dispersion forces. *J. Phys. Chem. B* **2004**, *108*, 2398–2404.

(119)   Parsons, D. F.; Boström, M.; Nostro, P. L.; Ninham, B. W. Hofmeister effects: Interplay of hydration, nonelectrostatic potentials, and ion size. *Phys. Chem. Chem. Phys.* **2011**, *13*, 12352–12367.

(120)   Duignan, T. T.; Parsons, D. F.; Ninham, B. W. Collins's rule, Hofmeister effects and ionic dispersion interactions. *Chem. Phys. Lett.* **2014**, *608*, 55–59.

(121)   Van Der Vegt, N. F.; Haldrup, K.; Roke, S.; Zheng, J.; Lund, M.; Bakker, H. J. Water-Mediated Ion Pairing: Occurrence and Relevance. *Chem. Rev.* **2016**, *116*, 7626–7641.

(122)   Monroy Soto, V.; Galin, J. Poly(sulphopropylbeatines): Dilute Solution Properties. *Polymer (Guildf).* **1984**, *25*, 254–262.

(123)   Cheng, N.; Brown, A. A.; Azzaroni, O.; Huck, W. T. Thickness-dependent properties of polyzwitterionic brushes. *Macromolecules* **2008**, *41*, 6317–6321.

(124)   Matsuda, Y.; Kobayashi, M.; Annaka, M.; Ishihara, K.; Takahara, A. Dimensions of a free linear polymer and polymer immobilized on silica nanoparticles of a zwitterionic polymer in aqueous solutions with various ionic strengths. *Langmuir* **2008**, *24*, 8772–8778.

(125) Wang, T.; Wang, X.; Long, Y.; Liu, G.; Zhang, G. Ion-specific conformational behavior of polyzwitterionic brushes: Exploiting it for protein adsorption/desorption control. *Langmuir* **2013**, *29*, 6588–6596.

(126) Higaki, Y.; Inutsuka, Y.; Sakamaki, T.; Terayama, Y.; Takenaka, A.; Higaki, K.; Yamada, N. L.; Moriwaki, T.; Ikemoto, Y.; Takahara, A. Effect of Charged Group Spacer Length on Hydration State in Zwitterionic Poly(sulfobetaine) Brushes. *Langmuir* **2017**, *33*, 8404–8412.

(127) Kawai, T. Freezing point depression of polymer solutions and gels. *J. Polym. Sci.* **1958**, *32*, 425–444.

(128) Chen, J.; Luo, Z.; Fan, Q.; Lv, J.; Wang, J. Anti-Ice coating inspired by ice skating. *Small* **2014**, *10*, 4693–4699.

(129) Tao, C.; Bai, S.; Li, X.; Li, C.; Ren, L.; Zhao, Y.; Yuan, X. Formation of zwitterionic coatings with an aqueous lubricating layer for antifogging/anti-icing applications. *Prog. Org. Coatings* **2018**, *115*, 56–64.

(130) Higuchi, A.; Iijima, T. D.s.c. investigation of the states of water in poly(vinyl alcohol-co-itaconic acid) membranes. *Polymer (Guildf).* **1985**, *26*, 1833–1837.

(131) Zhang, W. Z.; Satoh, M.; Komiyama, J. A differential scanning calorimetry study of the states of water in swollen poly(vinyl alcohol) membranes containing non-volatile additives. *J. Memb. Sci.* **1989**, *42*, 303–314.

(132) Li, W.; Xue, F.; Cheng, R. States of water in partially swollen poly(vinyl alcohol) hydrogels. *Polymer (Guildf).* **2005**, *46*, 12026–12031.

(133) Morisaku, T.; Watanabe, J.; Konno, T.; Takai, M.; Ishihara, K. Hydration of phosphorylcholine groups attached to highly swollen polymer hydrogels studied by thermal analysis. *Polymer (Guildf).* **2008**, *49*, 4652–4657.

(134) Cuperus, F. P.; Bargeman, D.; Smolders, C. A. Critical points in the analysis of membrane pore structures by thermoporometry. *J. Memb. Sci.* **1992**, *66*, 45–53.

(135) Arndt, K. F.; Zander, P. Characterization of polymer networks by measurements of the freezing point depression. *Colloid Polym. Sci.* **1990**, *268*, 806–813.

(136) Gun'ko, V. M.; Savina, I. N.; Mikhalovsky, S. V. Properties of water bound in hydrogels. *Gels* **2017**, *3*, DOI: 10.3390/gels3040037.

(137) Scherer, J. R.; Bailey, G. F.; Kint, S.; Young, R.; Malladi, D. P.; Bolton, B. Water in polymer membranes. 4. Raman scattering from cellulose acetate films. *J. Phys. Chem.* **1985**, *89*, 312–319.

(138) Filho, G. R.; Bueno, W. A. Water state of Cuprophan (hemodialysis membrane). *J. Memb. Sci.* **1992**, *74*, 19–27.

(139) Kardela, J. H.; Millichamp, I. S.; Ferguson, J.; Parry, A. L.; Reynolds, K. J.; Aldred, N.; Clare, A. S. Nonfreezable Water and Polymer Swelling Control the Marine Antifouling Performance of Polymers with Limited Hydrophilic Content. *ACS Appl. Mater. Interfaces* **2019**, *11*, 29477–29489.

(140) Roorda, W Do hydrogels contain different classes of water? *J. Biomater. Sci. Polym. Ed.* **1994**, *5*, 383–395.

(141)   Kocherbitov, V. The nature of nonfreezing water in carbohydrate polymers. *Carbohydr. Polym.* **2016**, *150*, 353–358.

(142)   Gauthier, M.; Carrozzella, T.; Penlidis, A. Sulfobetaine zwitterionomers based on n-Butyl acrylate and 2-ethoxyethyl acrylate: Monomer synthesis and copolymerization behavior. *J. Polym. Sci. Part A Polym. Chem.* **2002**, *40*, 511–523.

(143)   Ikeshoji, T.; Ono, Y.; Mizuno, T. index. This equation is the effective thickness 6 for bulk. *Appl. Opt.* **1973**, *12*, 2236–2237.

(144)   Woods, D. A.; Bain, C. D. Total internal reflection Raman spectroscopy. *Analyst* **2012**, *137*, 35–48.

(145)   Tyrode, E.; Rutland, M. W.; Bain, C. D. Adsorption of CTAB on hydrophilic silica studied by linear and nonlinear optical spectroscopy. *J. Am. Chem. Soc.* **2008**, *130*, 17434–17445.

(146)   Skoog, D.; Holler, F.; Niemann, T, *Principles of Instrumental Analysis (5th edition)*; Saunders: New York, 1998, pp 805–808.

(147)   Woollam, J. A.; Snyder, P. G.; Rost, M. C. Variable angle spectroscopic ellipsometry: A non-destructive characterization technique for ultrathin and multilayer materials. *Thin Solid Films* **1988**, *166*, 317–323.

(148)   Ogieglo, W.; Wormeester, H.; Eichhorn, K. J.; Wessling, M.; Benes, N. E. In situ ellipsometry studies on swelling of thin polymer films: A review. *Prog. Polym. Sci.* **2015**, *42*, 42–78.

(149)   Fujiwara, H. Spectroscopic Ellipsometry: Principles and Applications. *Spectrosc. Ellipsom. Princ. Appl.* **2007**, 1–369.

(150)   Woollam, J. A.; Johs, B. D.; Herzinger, C. M.; Hilfiker, J. N.; Synowicki, R. A.; Bungay, C. L. Overview of variable-angle spectroscopic ellipsometry (VASE): I. Basic theory and typical applications. *Opt. Metrol. A Crit. Rev.* **1999**, *10294*, 1029402.

(151)   Aspnes, D. E.; Theeten, J. B.; Hottier, F. Investigation of effective-medium models of microscopic surface roughness by spectroscopic ellipsometry. *Phys. Rev. B* **1979**, *20*, 3292–3302.

(152)   Sayward, J. M. *Seeking low ice adhesion - Special Report*; tech. rep. Tech Rep. 00197109; U.S. Army Cold Regions Resarch and Engineering Laboratory, 1979, pp 1–88.

(153)   Kasaai, M. R.; Farzaneh, M. In *Proc. Int. Conf. Offshore Mech. Arct. Eng. - OMAE*, 2004; Vol. 3, pp 919–926.

(154)   Rønneberg, S.; He, J.; Zhang, Z. In *Int. Work. Atmos. Icing Struct. (IWAIS), Reykjavik, Icel.* 2019, pp 1–5.

(155)   Work, A.; Lian, Y. A critical review of the measurement of ice adhesion to solid substrates. *Prog. Aerosp. Sci.* **2018**, *98*, 1–26.

(156)   Rønneberg, S.; Zhuo, Y.; Laforte, C.; He, J.; Zhang, Z. Interlaboratory study of ice adhesion using different techniques. *Coatings* **2019**, *9*, 1–12.

(157)   Hakimian, A.; Nazifi, S.; Ghasemi, H. In *Ice Adhes. Mech. Meas. Mitig.* 2020, pp 217–236.

(158) Rothrock, A.; Selden, R. *Adhesion of ice in its relation to the de-icing of airplanes*; tech. rep.; Langley Memorial Aeronautical Laboratory, 1939.

(159) Petrenko, V.; Whitworth, R., *Physics of Ice*; Oxford University Press: 1999.

(160) Mirshahidi, K.; Alasvand Zarasvand, K.; Luo, W.; Golovin, K. A high throughput tensile ice adhesion measurement system. *HardwareX* **2020**, *8*, e00146.

(161) Bleszynski, M.; Clark, E. Current Ice Adhesion Testing Methods and the Need for a Standard: A Concise Review. *Standards* **2021**, *1*, 117–133.

(162) Wang, C.; Gupta, M. C.; Yeong, Y. H.; Wynne, K. J. Recent advances in applied polymer science. *J. Appl. Polym. Sci.* **2018**, *135*, 45734–45741.

(163) Schulz, M.; Sinapius, M. Evaluation of Different Ice Adhesion Tests for Mechanical Deicing Systems. *SAE Tech. Pap.* **2015**, *2015-June*, DOI: `10.4271/2015-01-2135`.

(164) Wang, C.; Zhang, W.; Siva, A.; Tiea, D.; Wynne, K. J. Laboratory test for ice adhesion strength using commercial instrumentation. *Langmuir* **2014**, *30*, 540–547.

(165) Jellinek, H. H. Liquid-like (transition) layer on ice. *J. Colloid Interface Sci.* **1967**, *25*, 192–205.

(166) Bai, S.; Li, X.; Zhang, R.; Li, C.; Zhu, K.; Sun, P.; Zhao, Y.; Ren, L.; Yuan, X. Enhancing antifogging/frost-resisting performances of amphiphilic coatings via cationic, zwitterionic or anionic polyelectrolytes. *Chem. Eng. J.* **2019**, *357*, 667–677.

(167) Hrib, J.; Krumbholcova, E. C.; Duskova-Smrckova, M.; Hobzova, R.; Sirc, J.; Hruby, M.; Michalek, J.; Hodan, J.; Lesny, P.; Smucler, R. Hydrogel tissue expanders for stomatology. Part II. Poly(styrene-maleic anhydride) hydrogels. *Polymers (Basel).* **2019**, *11*, DOI: `10.3390/polym11071087`.

(168) Lyon, C. K.; Prasher, A.; Hanlon, A. M.; Tuten, B. T.; Tooley, C. A.; Frank, P. G.; Berda, E. B. A brief user's guide to single-chain nanoparticles. *Polym. Chem.* **2015**, *6*, 181–197.

(169) Bera, R.; Dey, A.; Datta Sarma, A.; Chakrabarty, D. Synthesis and characterization of acrylic acid-2-hydroxyethyl methacrylate IPN hydrogels. *RSC Adv.* **2015**, *5*, 75870–75880.

(170) Mahkam, M.; Assadi, M.; Mohammadzadeh, R. Synthesis and characterization of crosslinked polyacrylates containing cubane and silyl groups. *Macromol. Res.* **2006**, *14*, 34–37.

(171) Leigh, B. L.; Cheng, E.; Xu, L.; Derk, A.; Hansen, M. R.; Guymon, C. A. Antifouling Photograftable Zwitterionic Coatings on PDMS Substrates. *Langmuir* **2019**, *35*, 1100–1110.

(172) Schuh, K.; Prucker, O.; Rühe, J. Tailor-made polymer multilayers. *Adv. Funct. Mater.* **2013**, *23*, 6019–6023.

(173) Prucker, O.; Naumann, C. A.; Rühe, J.; Knoll, W.; Frank, C. W. Photochemical attachment of polymer films to solid surfaces via monolayers of benzophenone derivatives. *J. Am. Chem. Soc.* **1999**, *121*, 8766–8770.

(174) Körner, M.; Prucker, O.; Rühe, J. Kinetics of the Generation of Surface-Attached Polymer Networks through C, H-Insertion Reactions. *Macromolecules* **2016**, *49*, 2438–2447.

(175) Becker, G.; Deng, Z.; Zober, M.; Wagner, M.; Lienkamp, K.; Wurm, F. R. Surface-attached poly(phosphoester)-hydrogels with benzophenone groups. *Polym. Chem.* **2018**, *9*, 315–326.

(176) Li, M; Bresson, B; Cousin, F; Fretigny, C; Tran, Y Submicrometric Films of Surface-Attached Polymer Network with Temperature-Responsive Properties. *Langmuir* **2015**, *31*, 11516–11524.

(177) Martwong, E.; Tran, Y. Lower Critical Solution Temperature Phase Transition of Poly(PEGMA) Hydrogel Thin Films. *Langmuir* **2021**, *37*, 8585–8593.

(178) Wang, H.; Zhang, C.; Wang, J.; Feng, X.; He, C. Dual-mode antifouling ability of thiol-ene amphiphilic conetworks: Minimally adhesive coatings via the surface zwitterionization. *ACS Sustain. Chem. Eng.* **2016**, *4*, 3803–3811.

(179) Borisov, O. V.; Zhulina, E. B.; Birshtein, T. M. Diagram of the States of a Grafted Polyelectrolyte Layer. *Macromolecules* **1994**, *27*, 4795–4803.

(180) Pincus, P. Colloid Stabilization with Grafted Polyelectrolytes. *Macromolecules* **1991**, *24*, 2912–2919.

(181) Israëls, R.; Leermakers, F. A.; Fleer, G. J.; Zhulina, E. B. Charged Polymeric Brushes: Structure and Scaling Relations. *Macromolecules* **1994**, *27*, 3249–3261.

(182) Dobrynin, A. V.; Rubinstein, M. Theory of polyelectrolytes in solutions and at surfaces. *Prog. Polym. Sci.* **2005**, *30*, 1049–1118.

(183) Rumyantsev, A. M.; Pan, A.; Ghosh Roy, S.; De, P.; Kramarenko, E. Y. Polyelectrolyte Gel Swelling and Conductivity vs Counterion Type, Cross-Linking Density, and Solvent Polarity. *Macromolecules* **2016**, *49*, 6630–6643.

(184) Kumar, R.; Fredrickson, G. H. Theory of polyzwitterion conformations. *J. Chem. Phys.* **2009**, *131*, DOI: 10.1063/1.3216107.

(185) Georgiev, G. S.; Kamenska, E. B.; Vassileva, E. D.; Kamenova, I. P.; Georgieva, V. T.; Iliev, S. B.; Ivanov, I. A. Self-assembly, antipolyelectrolyte effect, nonbiofouling properties of polyzwitterions. *Biomacromolecules* **2006**, *7*, 1329–1334.

(186) Duričković, I.; Claverie, R.; Bourson, P.; Marchetti, M.; Chassot, J. M.; Fontana, M. D. Water-ice phase transition probed by Raman spectroscopy. *J. Raman Spectrosc.* **2011**, *42*, 1408–1412.

(187) Xue, X.; He, Z. Z.; Liu, J. Detection of water-ice phase transition based on Raman spectrum. *J. Raman Spectrosc.* **2013**, *44*, 1045–1048.

(188) Rumyantsev, A. M.; Pan, A.; Ghosh Roy, S.; De, P.; Kramarenko, E. Y. Polyelectrolyte Gel Swelling and Conductivity vs Counterion Type, Cross-Linking Density, and Solvent Polarity. *Macromolecules* **2016**, *49*, 6630–6643.

(189) Wang, S. C.; Wang, C. K.; Chang, F. M.; Tsao, H. K. Second virial coefficients of poly(ethylene glycol) in aqueous solutions at freezing point. *Macromolecules* **2002**, *35*, 9551–9555.

(190)   Solms, D. J.; Rijke, A. M. Anomalous freezing behavior of polymer gels and solu-
         tions. *J. Phys. Chem.* **1971**, *75*, 2623–2631.

(191)   Fushimi, H.; Ando, I.; Iijima, T. States of water in cationically charged poly(vinyl
         alcohol) membranes. *Polymer (Guildf).* **1991**, *32*, 241–248.

(192)   De Gennes, P. G. Conformations of Polymers Attached to an Interface. *Macro-
         molecules* **1980**, *13*, 1069–1075.

Manuscripts

(1) Understanding the ion-specific anti-polyelectrolyte effect on the swelling behavior of polyzwitterionic layers
Frederik Hegaard, <u>Robert A. Biro</u>, Koosha Ehtiati, and Esben Thormann
Submitted

(2) Reducing ice adhesion to polyelectrolyte surfaces by counterion mediated nonfrozen hydration water
<u>Robert A. Biro</u>, Eric C. Tyrode, Esben Thormann
In preparation

(3) Ice adhesion to cationic, anionic, zwitterionic, and non-ionic polymer surfaces: on the understanding of the role of hydration water
<u>Robert A. Biro</u>, Esben Thormann
In preparation

Manuscript 1

Ion-specific antipolyelectrolyte effect on the swelling behavior of polyzwitterionic layers

Frederik Hegaard, Robert Biro, Koosha Ehtiati and Esben Thormann*

Department of Chemistry, Technical University of Denmark, 2800 Kgs. Lyngby, Denmark.

ABSTRACT In this study, we systematically investigate the interactions between mobile ions generated from added salts and immobile charges within a sulfobetaine-based polyzwitterionic film in the presence of five salts (KCl, KBr, KSCN, LiCl, and CsCl). The sulfobetaine groups contain quaternary alkyl ammonium and sulfonate groups, giving the positive and negative charges. The swelling of the zwitterionic film in the presence of different salts is compared with the swelling behavior of a polycationic or polyanionic film containing the same charged groups. For such a comparative study, we design crosslinked terpolymer films with similar thicknesses, crosslink densities, and charge fractions, but with varying charged moieties. While the addition of salt in general leads to a collapse of both cationic and anionic films, the presence of specific types of mobile anions (Cl^-, Br^-, and SCN^-) considerably influences the swelling behavior of polycationic films. We attribute this observation to a different degree of ion-pair formations between the different types of anionic counterions and the immobile cationic quaternary alkyl ammonium groups in the films where highly polarizable counterions such as SCN^- lead to a high degree of ion pairing and less polarizable counterions, such as Cl^-, cause a low degree of ion pairing. Conversely, we do not observe any substantial effect of varying the type of cationic counterions (K^+, Li^+, and Cs^+), which we assign to the lack of ion pairing between the weakly polarizable cations and the immobile anionic sulfonate groups in the films. Further, we observe that the zwitterionic films swell with increasing ionic strength and the degree of swelling is anion dependent, which is in agreement with previous reports on the "antipolyelectrolyte" effect. Herein, we explain this ion-specific swelling behavior with the different cation and anion abilities to form ion pairs with quaternary alkyl ammonium and sulfonate in the sulfobetaine groups.

Introduction

Polyzwitterions are polymers containing functional groups, which carry both positive and negative charges. In their simplest form, as seen for polymers containing, e.g., phosphorylcholine or sulfobetaine groups, each chain carries an equal number of positive and negative charges and is therefore overall electrically neutral. This overall electrically neutrality will provide such polymers with unique hydration and swelling properties compared with uncharged polymers or polyelectrolytes that carry an overall positive or negative charge. Polyzwitterions also provide several interesting properties that make them interesting when used in films and coatings, e.g., antifouling applications and in aqueous lubricating systems.[1–6] One of the unique properties of some polyzwitterionic films is the so-called "antipolyelectrolyte effect," which refers to the aqueous swelling behavior of polyzwitterionic films in response to changes in the ionic strength. As implied by the term, the antipolyelectrolyte effect means that the swelling response is opposite to the response of the polyanionic or polycationic films. More specifically, polyzwitterionic films often swell with increasing ionic strength, whereas polyanionic or polycationic films collapse with increasing ionic strength.[7–10]

At low ionic strength, owing to the strong dipole–dipole pairing of zwitterionic groups on either the same polymer chain or on neighboring chains, the polyzwitterionic films are normally found in a collapsed state. Therefore, a zwitterionic film comprises a tight bond network with a high number of interchain and intrachain physical crosslinks, resulting in a low ability of the film to swell even if the polymers are hydrophilic. However, the dipole–dipole interactions are disrupted and the film is able to swell when the ionic strength is increased. As discussed by Wang et al., this disruption can occur either in a symmetric manner, where both internal ions in the zwitterionic ion pair are similarly affected by the increasing ionic strength (e.g., by electrostatic screening), or in an asymmetric manner, where the positive and the negative charges in the zwitterionic group are differently affected by the external salt (e.g., through the chemisorption of mobile ions).[11–13]

To further explain the molecular mechanisms of the "antipolyelectrolyte effect," it is interesting to mention that the swelling induced by increasing ionic strength has been found to be strongly dependent on the type of the added salt.[14,15] Most experimental studies have focused on varying the anions of the added salt, [7,8,16–18] for which parallels have been drawn to the Hofmeister series,

where varying the type of anions has been shown to have a crucial effect on the solution behavior of both charged and uncharged macromolecules.[19–23] This is, for example, the case for several studies of polymer films containing sulfobetaine groups, where the exact degree of swelling with increasing ionic strength has been shown to be strongly dependent on the specific type of anions. However, the fact that the swelling behavior is ion type-dependent shows that the electrostatic screening of the dipole–dipole interactions cannot be the only reason for swelling. Yet, a full molecular understanding of the "antipolyelectrolyte effect" is still lacking, especially, when it comes to how specific types of ions affect the swelling behavior. To this end, we believe that comparing this swelling behavior with the swelling behavior of structurally simpler cationic and anionic analogs is the key to understanding the complex swelling behavior of polyzwitterionic films.

For polycationic and polyanionic films, the swelling behavior is caused by a balance between counterion-induced osmotic pressure, polymer–polymer and polymer–solvent nonelectrostatic interactions, and chain entropic elasticity.[24–27] The response of the polycationic and polyanionic films to changes in ionic strength is derived from the variation in the counterion-induced osmotic pressure. This arises from the excess counterion concentration within the film compared with the concentration in the bulk solution, which is required to compensate the charges on the polyelectrolyte chains and causes swelling of the film at low salt concentrations. This swelling regime is known as the osmotic regime. With increasing ionic strength of the medium, the difference between the ion concentration inside and outside the film decreases; thus, the osmotic pressure decreases and the film collapses accordingly in the so-called salted regime. Finally, when the salt concentration reaches a high level, the osmotic pressure is supposedly no longer effective for the swelling of the film and the film enters a regime with a low, ionic strength-independent thickness, known as the quasineutral regime.[24,28–30]

The specific ion type can affect the counterion-induced osmotic pressure and polymer–solvent nonelectrostatic interactions. However, these effects are different depending on whether the ion is a counterion or a coion. Even when the salt concentration in bulk is low, the counterions inside the polymer film are always present in a high amount, and are therefore always affecting the film. According to the Boltzmann distribution caused by the chemical potential difference, the coion concentration inside the film is considerably lower than that in the bulk.[31]

In the present study, we aim to decouple the interactions between mobile ions generated from the added salt and two immobile charges in the zwitterionic group. This was achieved first by studying the specific ion and ionic strength–dependent swelling behavior of polycationic films containing positively charged quaternary alkyl ammonium groups and polyanionic films containing negatively charged sulfonate groups. These films' swelling behavior was directly compared with the swelling behavior of polyzwitterionic films containing sulfobetaine groups that are zwitterionic owing to a combination of quaternary alkyl ammonium and sulfonate groups. Thus, we were able to study the effects of different counterions and coions on the quaternary alkyl ammonium and the sulfonate groups, separately, and use this knowledge to predict how different mobile cations and anions would interact with the positive and negative charges in the zwitterionic groups.

Experimental Section

Chemicals

[2-(methacryloyloxy)ethyl]trimethylammonium chloride (METAC, 75 wt.% in H_2O), 3-sulfopropyl methacrylate potassium (SPMAK, 98%), 2-(dimethylamino)ethyl methacrylate (98%), 1,4-butane sultone (BS, ≥99%), 4-cyano-4-[(dodecylsulfanylthiocarbonyl)sulfanyl] pentanoic acid (CDPA, 97%), allyl methacrylate (AMA, 98%), *n*-butyl methacrylate (*n*-BMA, 99%), 3-mercaptopropyl trimethoxysilane (MPTMS, 95%), 2,2,2-trifluoroethanol (TFE, ≥99%), pentaerythritol tetrakis(3-mercaptopropionate) (PETMP, ≥95%), 4,4′-azobis(4-cyanovaleric acid) (ACVA, ≥98%), potassium chloride (KCl, 99.5%), potassium thiocyanate (KSCN, 99%), potassium bromide (KBr, 99%), lithium chloride (LiCl, 99%), and cesium chloride (CsCl, 98%) were purchased from Sigma-Aldrich Denmark. *N,N*-Dimethylformamide (≥99.9%), diethyl ether (≥99.9), toluene (≥99.8), and acetonitrile (≥99.9) were received from VWR Chemicals BDH and passed through activated basic aluminum oxide (Brockman I, Sigma-Aldrich) before use to remove any inhibitors. Zwitterionic monomer *N*-(2-methacryloylxyethyl)-*N,N*-diemthylammonium butanesulfonate (MABS) was prepared beforehand using the procedure reported in a previous study.[32] Ultrapure water (Sartorius Arium Pro; 18.2 MΩ·cm) was used for preparing aqueous salt solutions.

Polymer films

Polymer films were produced through a stepwise process: reversible addition–fragmentation chain-transfer (RAFT) polymerization, surface functionalization of the substrate, and then spin coating and curing.

First, charged terpolymers were synthesized using RAFT polymerization by incorporating 25 mol.% of charged monomer (METAC, SPMAK, or MABS) and varying amounts of AMA and n-BMA (corresponding to the targeted AMA composition and eventual film crosslink density). CDPA and ACVA were added in a 200:1:0.1 molar ratio (monomer:CDPA:ACVA). Cationic and anionic polyelectrolytes were synthesized using METAC and SPMAK, as the charged monomers, in a 2.5-M monomer solution in 4:1 N,N-dimethylformamide/H_2O. Accordingly, zwitterionic polymers were synthesized using MABS and polymerized in TFE (2.5 M with respect to the monomers). AMA contents were selected as 5, 10, or 15 mol.%, equating to n-BMA contents of 70, 65, or 60 mol.%, respectively, which corresponded to the eventual crosslink density of the polymer films. Ultimately, the total monomer concentration was 2.5 M, and the solution was degassed by sparging with N_2 for 30 min after which the temperature was raised to 70 °C, initiating polymerization. The polymerization was conducted under N_2 atmosphere and monitored via ^{1}H-NMR until completion. Then, the reaction was precipitated in cold-stirred diethyl ether. Once collected via vacuum filtration, the product was dried overnight at 30 °C in a vacuum oven and characterized using ^{1}H-NMR, which confirmed the approximate composition of the polymer.

Silicon wafers were used as the substrate for the films, which needed to be functionalized before grafting the film. The wafers were rinsed with water, ethanol, and acetone, then dried under a N_2 stream, and cleaned using plasma for 180 s under a 500-mTorr water-vapor atmosphere. Then the wafers were submerged in a 15-vol.% MPTMS toluene solution and stirred at room temperature (~23-°C). After 3 h, the functionalized wafers were removed from the solution, dried under an N_2 stream, and placed in a 130-°C vacuum oven to induce silanization.

The polymer solution was spin coated onto the functionalized wafer and anchored via thermally initiated crosslinking. First, an ~1 wt.% polymer in TFE solution was prepared, and tetrafunctional thiol PETMP and a radical initiator ACVA was added. PETMP (though tetrafunctional) was loaded at a 1:1 molar ratio to that of the -ene- functionality of the polymer. After stirring for 30 min, the solution was spin coated onto the previously prepared thiol-functionalized silicon wafer

(2000 rpm for 40 s) before being placed in a 90-°C oven for 2 h to induce a thermally initiated thiol–ene crosslinking reaction. The wafers were then removed from the oven and cooled to room temperature. Then they were washed twice with an excess of water to remove any unattached materials and then dried under N_2 atmosphere.

Ellipsometry

The thicknesses of the films were measured using an ellipsometer (J. A. Woollam, M-2000) equipped with a liquid cell. The measurements were conducted with a fixed angle of incidence of 75° and at wavelengths of 250–1000 nm. The measurements were analyzed using the instrument's software, CompleteEase, where the sample was described with a model containing multiple layers. The model was created with Si as the substrate, a 1 nm–thick Si–SiO$_2$ transition layer, a 100 nm–thick SiO$_2$ layer, a uniform polymer film without absorption of light, and finally ambient conditions matching the refractive index of the solvent. The properties of the polymer film were described using a Cauchy model with the form $n(\lambda) = A + B/\lambda^2$ where n and λ are the refractive index and the wavelength, respectively, and A and B are fitting parameters. The fitting parameters for the film were *A* and *B* from the Cauchy model and the thickness of the polymer film. The refractive index of the salt solution changed with the concentration and type of the salt, which was adjusted accordingly in the model. See supporting information Section S1 for details on the procedure of performing the measurements and the optical model.

Results and Discussion

In this study, we have used random terpolymers comprising three repeating units: a noncharged unit (*n*-butyl methacrylate), a crosslinkable unit (allyl methacrylate), and a charged unit (Figure 1). While the fraction of the charged units was kept constant (25 mol.%) for all polymer films, the fraction of crosslinkable units was systematically varied between 5, 10, and 15 mol.% to obtain polymer films with various crosslink densities. Three types of charged units were chosen: either a positively charged unit (METAC), a negatively charged unit (SPMAK), or a zwitterionic unit (MABS) (Figure 1). With such molecular designs, we were able to first systematically vary the crosslink density for the polyelectrolyte systems while keeping the charge fraction constant. Second, we were able to compare the swelling behavior of the polycationic, polyanionic, and polyzwitterionic films, which have the same fraction of charged units, similar crosslink density

(controlled via the fraction of crosslinkable units), and controlled nonelectrostatic interactions arising from the fraction of noncharged units. Dry-film thicknesses determined using the ellipsometry and topographical information from AFM images of the prepared polymer films are provided in Supporting Information Section S2.
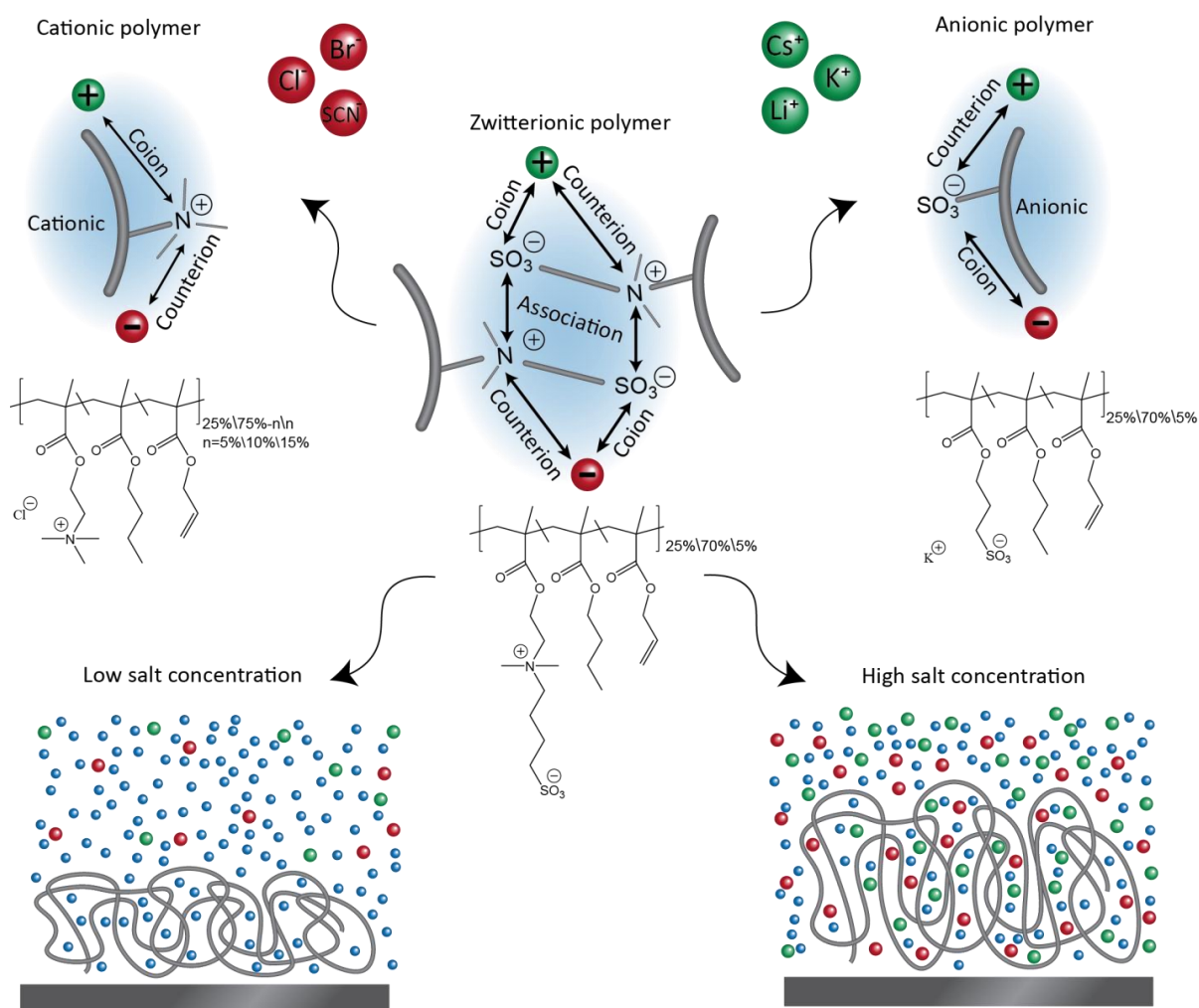
Figure 1. Schematic of the investigated systems and relevant ionic interactions. Three random terpolymers with cationic, anionic, and zwitterionic groups were used to prepare surface grafted, crosslinked polymer films. Swelling behavior was investigated as a function of the concentration of added salts (KCl, KBr, KSCN, LiCl, and CsCl), corresponding to three different anions and three different cations. Then, the different cations and anions worked as counterions, coions, or both, depending on the ionic nature of the polymers.

Next, we investigated the swelling behavior of the systems: polycationic, polyanionic, and polyzwitterionic films. For this, we first considered the effect of the ionic strength on the swelling behavior of the polymer films in the presence of KCl and then determined how this response is affected by the type of counterions and coions. To later provide a detailed discussion of the polyzwitterionic films based on these understandings, we studied the polycationic and polyanionic films to investigate the interactions between the mobile ions and the immobile charged groups in the films

Effects of ionic strength and crosslink density on polycationic films

For the polycationic films with different crosslink densities, the absolute thicknesses of the hydrated films and the swelling ratios (relative to the dry-film thickness) are plotted in Figure 2 as a function of KCl concentration. The overall swelling behavior of the polycationic film follows the typical behavior of strong polyelectrolyte films with respect to ionic strength.[10,25,33] We observed that this film exhibited a high and constant thickness at low salt concentrations, from 0.01 to 10 mM, which corresponds to the osmotic regime, where the counterion-induced osmotic pressure caused considerable swelling of the film.[29,30,34] From ~10–30 mM, the salted regime started, where a decline in swelling was observed because the osmotic pressure difference decreased due to the addition of external salts. In addition to the osmotic and salted regimes, a quasineutral regime is sometimes observed for polyelectrolyte films at very-high salt concentrations, depending on the films properties.[25,35,36] In the current case, this regime is, however, not manifested below 3 M KCl.
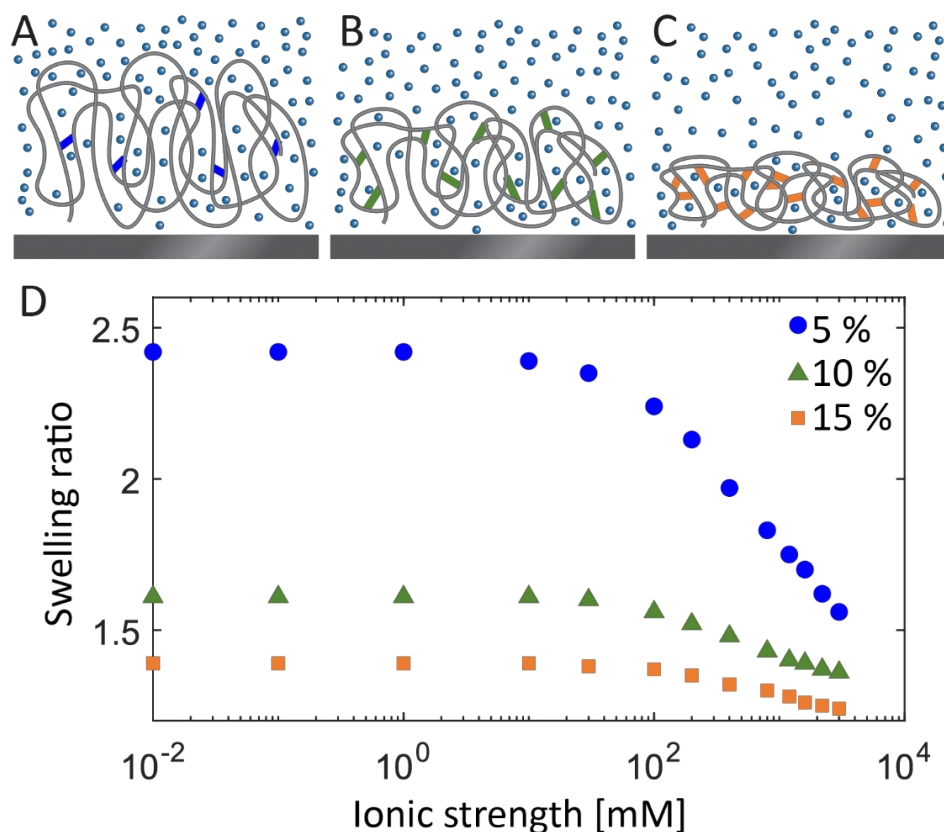
Figure 2. Illustration of the crosslinking effect for (A) low, (B) intermediate, and (C) high crosslinking degrees. (D) Swelling ratios of hydrated polycationic films (hydrated-film thickness compared with dry-film thickness, see Supporting Information S2 for dry-film thicknesses) as a function of KCl concentration for films with either 5, 10, or 15 mol.% of the crosslinked monomer.

Films of different degrees of crosslinking but with the same charge density were investigated to show how the degree of crosslinking can influence the swelling behavior. As shown in Figure 2, all the three films qualitatively followed the same trends with an osmotic regime in the first part (constant thickness) and a salted regime in the last part (declining thickness). However, with increased crosslink density, chain stretching became restricted; thus, the swelling decreased in the osmotic regime. This observation is not surprising; however, it is important for the interpretation of the zwitterionic films' swelling, where it is expected that dipole–dipole intrachain and interchain bonds will also limit the swelling due to a similar effect (although the effect is caused by a different type of crosslinking).

Specific ion effects on polycationic films

Five monovalent salts KCl, KBr, KSCN, LiCl, and CsCl were chosen to demonstrate how swelling of the polycationic film depends on the specific types of ions. Here, it is possible to systematically vary either the coions or the counterions.

Figure 3. Illustration of polycationic film swelling when hydrated in (A) low and (B) high salt concentrations. (C) Role of ions when interacting with the charged quaternary alkyl ammonium groups (of polymers) as either cationic coions or anionic counterions. Ellipsometry-based thickness of the polycationic film as a function of salt concentration in the presence of (D) either potassium salts with various anionic counterions or (E) chloride salts with various cationic coions.

Figure 3D shows the effect of different anions (counterions) on the swelling behavior of the polycationic film with a low crosslink density (5 mol.% of the crosslinker monomer) while keeping the cation (coion) unchanged as K^+. Here, where the thickness of the films follows the trend $Cl^- > Br^- > SCN^-$ at low salt concentrations, in the osmotic regime, the anionic counterions considerably affect the swelling of the film. However, the thicknesses converge to an approximately similar level at high salt concentrations. This difference in the osmotic regime indicates a lower counterion-induced osmotic pressure in the case of SCN^- compared to other ions. Counterion-

specific behavior has previously been observed in other cationic films, and here, it has been explained by the effect of specific types of counterions on the counterion-induced osmotic pressure and the polymer–polymer and polymer–solvent nonelectrostatic interactions.[10,25,37–39] Thus, we have linked the trend of thickness at low ionic strength to the ability of anionic counterions to form ion pairs with the quaternary alkyl ammonium groups on the polyelectrolyte chains, and thus, become osmotically passive. To this end, based on our results, it is expected that the degree of ion-pair formation follows the trend $SCN^- > Br^- > Cl^-$, which agrees with previous reports.[40,41] Beside this overall behavior, the film with SCN^- as counterions started to swell with increasing salt concentration, from approximately 800 mM. At such high ionic strength, the counterion-induced osmotic pressure declined and the swelling was thus attributed to the effect of SCN^- on the nonelectrostatic polymer–solvent interactions. This effect could thus be similar to the "salting-in" effect of SCN^- observed for many noncharged polymers at high salt concentrations.[19,42–45]

Figure 3E shows the effect of the cations (coions) on the swelling behavior of polycationic films, while the anion (counterion) was kept as Cl^-. In contrast to the drastic variations observed with varying anionic counterions, different cationic coions afforded an almost identical swelling behavior, both with respect to the overall trend (first an osmotic regime and then a salted regime) and the absolute thicknesses. However, at the highest salt concentrations (>1 M) a weak specific cationic coion effect was observed, and we assigned this weak effect to the influence of ions on the polymer–solvent nonelectrostatic interactions (Hofmeister effects).

To investigate the effect of crosslink density on the ion-specific response of the polycationic films, measurements on polycationic films with 10 and 15 mol.% crosslinking monomers have been conducted using the same salts specified in Figure 3 (see Supporting Information Section S3). The thickness of the hydrated films showed a similar trend with the variation of anionic counterions, as observed for the low-crosslink polycationic film ($Cl^- > Br^- > SCN^-$). Similarly, the variation of cationic coions afforded almost identical swelling behavior for each film with fixed crosslink density. However, with increasing crosslink density, the overall swelling of the films and their response to specific anionic counterion effects became less pronounced.

Most relevantly, while the cationic coions only begin to show small variations at very-high salt concentrations, these variations in coions and counterions show how the anionic counterions

considerably affect the swelling at very-low salt concentrations. This agrees well with the idea that the anionic counterions are present inside the film in high concentrations at all times and affect the ion osmotic pressure. However, the concentration of cationic coions inside the film is lower than the concentration in bulk; thus, their effect on the film is negligible in this concentration range.

As demonstrated here, anions can interact and form ion pairs with the quaternary alkyl ammonium groups on the polycationic chain. Therefore, it is expected that in a polyzwitterionic system with the same cationic groups, these anions (Cl^-, Br^- and SCN^-) will compete with the sulfonate groups to bind with the quaternary alkyl ammonium groups. Such a competition in ion-pair formation and the resulting anion-specific behavior of polyzwitterionic systems are discussed later.

Specific ion effects on polyanionic films

Next, we investigated the swelling behavior of polyanionic films that were designed with similar physical properties (charge density and crosslink density) but with a sulfonate side group to develop negative charges on the chain. This makes it possible to investigate the effect of the same five salts used on the polycationic film, but this time, with the reversed roles of coions and counterions (Figure 4).
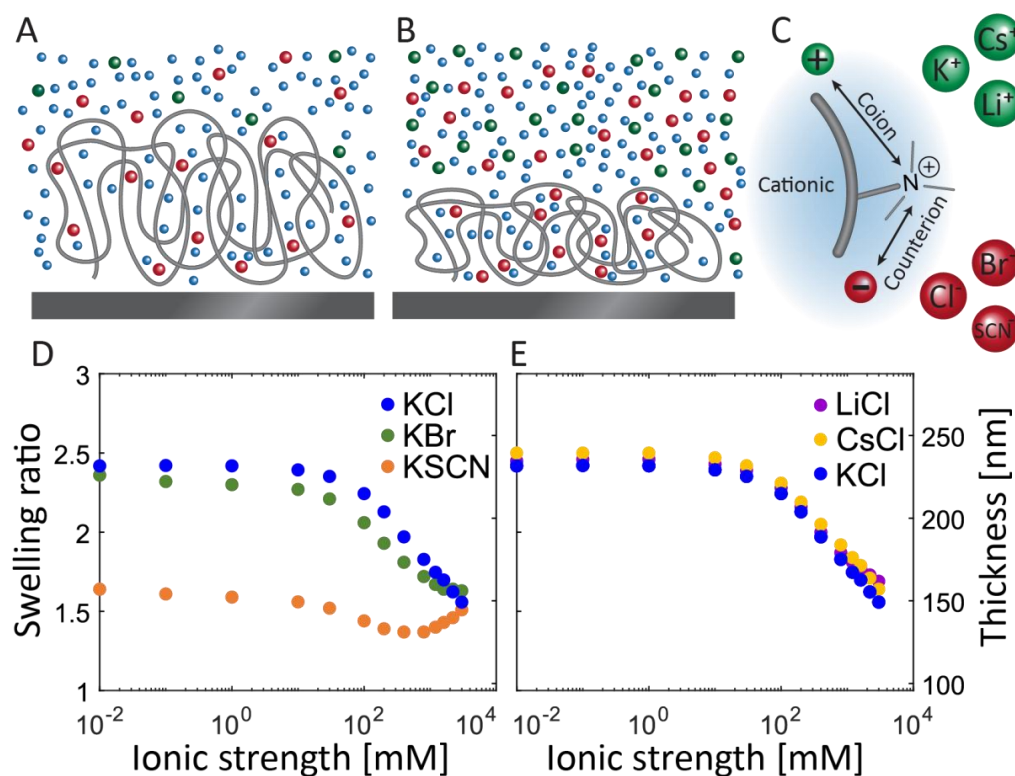
Figure 4. Illustration of polyanionic film swelling when hydrated in (A) low and (B) high salt concentrations. (C) Role of ions when interacting with the charged sulfonated groups (of polymers) as either anionic coions or cationic counterions (C). Ellipsometry-based thickness of the polyanionic film as a function of salt concentration in the presence of (D) either chloride salts with various cationic counterions or (E) potassium salts with various anionic coions.

By comparing Cs^+, K^+, and Li^+, the effect of cations (counterions) on the swelling behavior of the polyanionic film was investigated (Figure 4D). A typical swelling behavior was observed for all the cases with an osmotic regime at low salt concentration, up to ~10–30 mM, followed by a salted regime with a further increase in the salt concentration. However, the variation of the type of cationic counterions showed an insignificant influence on the swelling behavior of the polyanionic film in the osmotic regime because the thickness of the films with various cationic counterions exhibited similar thicknesses at low ionic strength. This indicates that the counterion-induced osmotic pressure is not affected by the type of cationic counterions. This can be explained by a similar degree of ion-pair formation (or no ion pairing) between the sulfonate groups in the film and these mobile cationic counterions. This is in contrast to the observed effect of the anionic

counterions on the polycationic film where we observed various degrees of ion pairs with the quaternary alkyl ammonium groups in the films. To understand and explain this difference, focus should be placed on the mechanism through which ion pairs are formed. Ion-pair formation has been suggested to be correlated with the polarizability of the ions in the pair in such a manner that highly polarizable ions tend to interact stronger with the (also highly polarizable) quaternary ammonium groups and thus form a larger number of ion pairs compared to weakly polarizable ions with sulfonate groups.[10,46,47] In our current study, the polarizability of the mobile anions ranged between 3.5 and 7.0 $Å^3$, while the polarizability of the mobile cations was much lower (0–2 $Å^3$).[48] To this end, we suggest that although the cations used here have different polarizabilities, they are all so low that the ion-pair formation in those cases is negligible (i.e., no ion pairing). Thus, the anion-specific swelling on the polycationic film is associated with higher polarizabilities of some anions, which leads to different degrees of ion-pair formation with the quaternary alkyl ammonium groups. It is worth mentioning that formation of ion pairs is of course dependent on the polarizability of both charged moieties. Thus, while in our system containing sulfonate groups we observed similar counterion-induced osmotic pressure for Cs^+, K^+, and Li^+ as the counterion, the same counterions might result in different counterion-induced osmotic pressure in a polyanionic film with differently charged moieties (see Supporting Information Section S4 for a more detailed discussion).

In Figure 4E, the effect of changing the type of anion (coion) is shown to have an insignificant effect on the swelling of the films at low to medium ionic strength (up to around 400 mM). However, it is observed that the film with SCN^- as the counterion collapses less than those with Cl^- and Br^- as counterions, at higher concentrations of salts. Although the local salt concentrations in the films are not identical in the two situations, this observation is in line with the previously discussed behavior of SCN^- in the polycationic film at high ionic strength.

Here it was demonstrated that various cations have an insignificant ion-pair interaction with the sulfonate groups, in contrast to the various interactions of anions with quaternary alkyl ammonium groups. For the sulfobetaine, we can expect an asymmetric ion association for some types of added salts where mobile anions can form ion pairs with the positively charged quaternary alkyl ammoniums, while mobile and osmotically active cations balance the negatively charged sulfonates.

Specific ion effects on polyzwitterionic films

We next turned the focus to the swelling behavior of the sulfobetaine-based polyzwitterionic film, which contains a quaternary alkyl ammonium and a sulfonate group in each zwitterionic unit. The thickness of the polyzwitterionic film as a function of the ionic strength of the salts with systematic variations of cations and anions is shown in Figure 5.
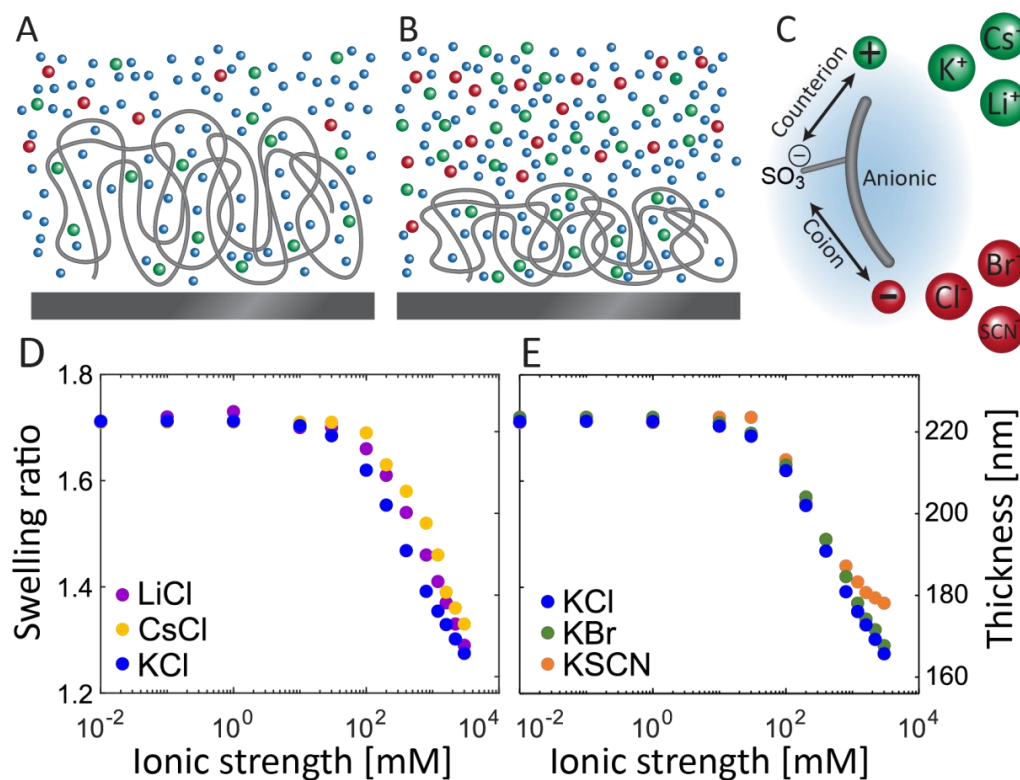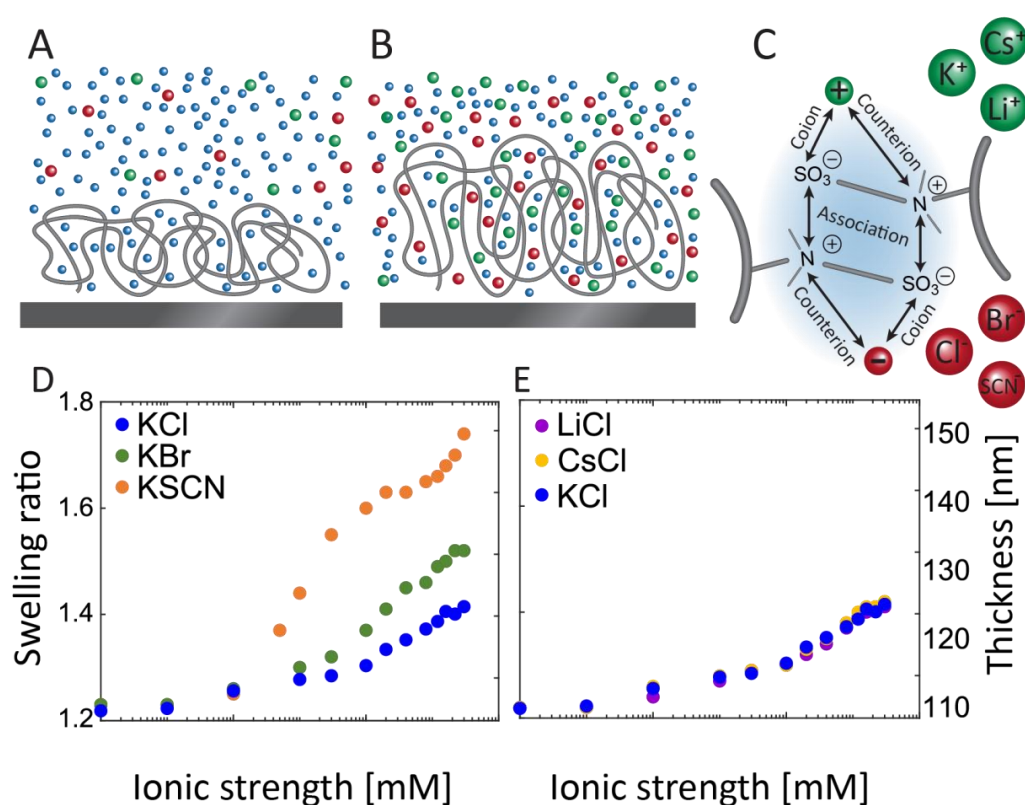

Figure 5. Illustration of polyzwitterionic film swelling when hydrated in (A) low and (B) high salt concentrations. (C) Role of ions when interacting with the charged groups (of polymers) as either coions or counterions (C). Ellipsometry-based thickness of the polyzwitterionic film as a function of salt concentration in the presence of (D) either potassium salts with various anions or (E) chloride salts with various cations.

Starting with the effect of varying the anions, Figure 5D shows the swelling behavior of the polyzwitterionic film in the presence of KCl, KBr, and KSCN. For all three cases, the film was found in a collapsed state at a low salt concentration up to around 1 mM followed by an increase in thickness with a further increase in salt concentration. Secondly, it was observed that the

swelling behavior of the polyzwitterionic film is strongly anion dependent. The film undergoes the most pronounced swelling in the presence of SCN^-, while in the presence of Br^- swelling occurs to a lower extent, and the least pronounced swelling is found in the case of Cl^-. Contrary to this observed effect of different anions, the swelling behavior of the polyzwitterionic film is shown, in Figure 5B, to be independent of the type of cation.

The swelling of polyzwitterionic films with the addition of salt is commonly referred to as the "antipolyelectrolyte" effect and is attributed to the dissociation of intrachain and interchain dipole–dipole bonds between the zwitterionic groups. The electrostatic interactions between the two groups are screened upon increasing medium ionic strength, whereby these groups can undergo dissociation. However, the fact that this behavior depends on the ion type demonstrates that an electrostatic effect cannot solely explain the behavior. In particular, the specific interactions between the salt ions and the immobile ions should be considered. We can implement the learnings from the cationic and anionic systems, to explain this behavior.

In the case of interactions between the mobile anions and the sulfonate group in the anionic film, we observed no significant influence of anionic coions on the swelling behavior of films except for very-high concentrations of SCN^-, where a change in nonelectrostatic interactions was observed (the coion effect in the polyanionic film, Figure 4E). On the other hand, we concluded that the interactions between the anions and the quaternary alkyl ammonium groups in the cationic film could be ranked based on their tendency to form ion pairs with the trend $SCN^- > Br^- > Cl^-$ (the counterion effect in the polycationic film, Figure 3D). This was also the trend of swelling observed in the polyzwitterionic film, indicating that the stronger the interaction of the anions with the quaternary alkyl ammonium groups, the higher degree of dissociation of the intrachain and interchain bonds, and thus the higher swelling of the film.

Regarding the effect of cations (Figure 5E), we observed, on the other hand, no significant interaction between the cations and the immobile groups, neither in the case of the polycationic film where the cations are coions nor in the case of polyanionic films where the cations are counterions. The cations did not form strong ion pairs with the sulfonate groups, in contrast to the case of anions in a polycationic film. We, therefore, suggest that this also can explain why the type of cations does not influence the swelling behavior of the polyzwitterionic systems.

16

By systematically comparing specific cation and anion effects on quaternary alkyl ammonium groups and sulfonate groups, we have now demonstrated that the swelling of the polyzwitterionic films is enhanced by ions that can strongly interact with one of the charges in the zwitterionic groups (in our case, anions pairing with the quaternary alkyl ammonium groups). We can also speculate about how this dissociation induced swelling of the polyzwitterionic film. At low ionic strength, the polyzwitterionic film was found in a collapsed state due to the formation of intrachain and interchain dipole–dipole bonds. These bonds between the chains act as physical crosslinks that limited swelling of the film, similar to the case observed with varying chemical crosslinks (Figure 2 and Supporting Information Section S3). With increasing ionic strength in the medium, more ions enter the polyzwitterionic film. This phenomenon first screens the electrostatic interactions between the quaternary alkyl ammonium groups and the sulfonate groups. Second, ions with strong interactions with one of the charged moieties (e.g., SCN^- and quaternary alkyl ammonium groups) break the bond between the sulfonate and quaternary alkyl ammonium groups to bind to the favored site. Because of this dissociation, the film swells due to a combination of two effects. First, breaking the interchain bonds yields a lower degree of ionic crosslinking, which allows increased swelling. Second, when SCN^- binds to a quaternary alkyl ammonium group, it is required by electroneutrality that an oppositely charged ion (for example K^+) enters the film to compensate the charge on the sulfonate group. Because K^+ is mobile and osmotically active (as demonstrated in the case of polyanionic film), it can induce an osmotic pressure, which further increases the swelling of the film (similar to the case of the polyanionic film).

Conclusions

We have systematically studied the effect of interactions between mobile ions and immobile charges in polycationic and polyanionic films to understand the swelling behavior of polyzwitterionic films with similar charged moieties. We observed that the change in the type of cation did not considerably influence the swelling of the films, neither when acting as coions in the polycationic film nor when acting as counterions in the polyanionic film. Changing the type of anion had an insignificant effect on the swelling of the films when the anions acted as coions in the polyanionic film but exhibited a considerable effect when they acted as counterions in the polycationic film. The counterion-specific effect in the polycationic films is explained by different abilities of anions to form ion pairs with the quaternary alkyl ammonium groups.

For the polyzwitterionic film, we observed increased swelling with increasing ionic strength in accordance with the so-called "antipolyelectrolyte effect," and the magnitude of the swelling was found to be to be strongly affected by the anion types following the order $SCN^- > Br^- > Cl^-$, while it did not depend on the type of cations. By studying all the possible interactions between the mobile ions and immobile charges on the polyzwitterionic chain, we proposed that the antipolyelectrolyte effect is a complicated swelling mechanism related to the electrostatic and nonelectrostatic ion-specific interactions. Dissociation of the intrachain and interchain bonds was derived via electrostatic screening and enhanced by specific ion-pair interactions, in cases where ions from the salt could strongly bind to one of the immobile charged groups. In addition, as another result of dissociation, the osmotic pressure of mobile counterions (which are present to compensate the charge of the immobile charged groups) increased the swelling of films.

ASSOCIATED CONTENT

Supporting Information. Expanded description of ellipsometry technique and film characterization. Expanded discussion of polarisability of ions and additional data for crosslinking dependent film swelling. (PDF)

AUTHOR INFORMATION

Corresponding Author

*esth@kemi.dtu.dk

Department of Chemistry, Technical University of Denmark, 2800 Kgs. Lyngby, Denmark

Author Contributions

The manuscript was written through contributions of all authors. All authors have given approval to the final version of the manuscript.

Notes

The authors declear no conflicts of interests.

REFERENCES

(1)   Zhang, Z.; Chao, T.; Chen, S.; Jiang, S. Superlow Fouling Sulfobetaine and Carboxybetaine Polymers on Glass Slides. *Langmuir* **2006**, *22* (24), 10072–10077. https://doi.org/10.1021/la062175d.

(2)   Chang, Y.; Liao, S. C.; Higuchi, A.; Ruaan, R. C.; Chu, C. W.; Chen, W. Y. A Highly Stable Nonbiofouling Surface with Well-Packed Grafted Zwitterionic Polysulfobetaine for Plasma Protein Repulsion. *Langmuir* **2008**, *24* (10), 5453–5458. https://doi.org/10.1021/la800228c.

(3)   Zhang, Z.; Vaisocherová, H.; Cheng, G.; Yang, W.; Xue, H.; Jiang, S. Nonfouling Behavior of Polycarboxybetaine-Grafted Surfaces: Structural and Environmental Effects. *Biomacromolecules* **2008**, *9* (10), 2686–2692. https://doi.org/10.1021/bm800407r.

(4)   Kobayashi, M.; Terayama, Y.; Hosaka, N.; Kaido, M.; Suzuki, A.; Yamada, N.; Torikai, N.; Ishihara, K.; Takahara, A. Friction Behavior of High-Density Poly(2-Methacryloyloxyethyl Phosphorylcholine) Brush in Aqueous Media. *Soft Matter* **2007**, *3* (6), 740–746. https://doi.org/10.1039/b615780g.

(5)   Tadmor, R.; Janik, J.; Klein, J.; Fetters, L. J. Sliding Friction with Polymer Brushes. *Phys. Rev. Lett.* **2003**, *91* (11). https://doi.org/10.1103/PhysRevLett.91.115503.

(6)   Tairy, O.; Kampf, N.; Driver, M. J.; Armes, S. P.; Klein, J. Dense, Highly Hydrated Polymer Brushes via Modified Atom-Transfer-Radical-Polymerization: Structure, Surface Interactions, and Frictional Dissipation. *Macromolecules* **2015**, *48* (1), 140–151. https://doi.org/10.1021/ma5019439.

(7)   Wang, T.; Kou, R.; Liu, H.; Liu, L.; Zhang, G.; Liu, G. Anion Specificity of Polyzwitterionic Brushes with Different Carbon Spacer Lengths and Its Application for Controlling Protein Adsorption. *Langmuir* **2016**, *32* (11), 2698–2707. https://doi.org/10.1021/acs.langmuir.6b00293.

(8)   Wang, T.; Wang, X.; Long, Y.; Liu, G.; Zhang, G. Ion-Specific Conformational Behavior of Polyzwitterionic Brushes: Exploiting It for Protein Adsorption/Desorption Control.

Langmuir **2013**, *29* (22), 6588–6596. https://doi.org/10.1021/la401069y.

(9)   Cheng, N.; Brown, A. A.; Azzaroni, O.; Huck, W. T. S. Thickness-Dependent Properties of Polyzwitterionic Brushes. *Macromolecules* **2008**, *41* (17), 6317–6321. https://doi.org/10.1021/ma800625y.

(10)   Ehtiati, K.; Moghaddam, S. Z.; Klok, H.-A.; Daugaard, A. E.; Thormann, E. Specific Counterion Effects on the Swelling Behavior of Strong Polyelectrolyte Brushes. *Macromolecules* **2022**, *55*, 5130. https://doi.org/10.1021/acs.macromol.2c00411.

(11)   Wang, F.; Yang, J.; Zhao, J. Understanding Anti-Polyelectrolyte Behavior of a Well-Defined Polyzwitterion at the Single-Chain Level. *Polym. Int.* **2015**, *64* (8), 999–1005. https://doi.org/10.1002/pi.4907.

(12)   Mary, P.; Bendejacq, D. D.; Labeau, M. P.; Dupuis, P. Reconciling Low- and High-Salt Solution Behavior of Sulfobetaine Polyzwitterions. *J. Phys. Chem. B* **2007**, *111* (27), 7767–7777. https://doi.org/10.1021/jp071995b.

(13)   Huglin, M. B.; Radwan, M. A. Selective Adsorption of Potassium Thiocyanate to a Zwitterionic Polymethacrylate. *Macromolecules* **1992**, *25* (2), 999–1002. https://doi.org/10.1021/ma00028a077.

(14)   Higaki, Y.; Kobayashi, M.; Takahara, A. Hydration State Variation of Polyzwitterion Brushes through Interplay with Ions. *Langmuir* **2020**, *36* (31), 9015–9024. https://doi.org/10.1021/acs.langmuir.0c01672.

(15)   Berlinova, I. V.; Dimitrov, I. V.; Kalinova, R. G.; Vladimirov, N. G. Synthesis and Aqueous Solution Behaviour of Copolymers Containing Sulfobetaine Moieties in Side Chains. *Polymer (Guildf).* **2000**, *41* (3), 831–837. https://doi.org/10.1016/S0032-3861(99)00264-5.

(16)   Sakamaki, T.; Inutsuka, Y.; Igata, K.; Higaki, K.; Yamada, N. L.; Higaki, Y.; Takahara, A. Ion-Specific Hydration States of Zwitterionic Poly(Sulfobetaine Methacrylate) Brushes in Aqueous Solutions. *Langmuir* **2019**, *35* (5), 1583–1589. https://doi.org/10.1021/acs.langmuir.8b03104.

(17)   Delgado, J. D.; Schlenoff, J. B. Static and Dynamic Solution Behavior of a Polyzwitterion Using a Hofmeister Salt Series. *Macromolecules* **2017**, *50* (11), 4454–4464. https://doi.org/10.1021/acs.macromol.7b00525.

(18)   Yang, J.; Chen, H.; Xiao, S.; Shen, M.; Chen, F.; Fan, P.; Zhong, M.; Zheng, J. Salt-Responsive Zwitterionic Polymer Brushes with Tunable Friction and Antifouling Properties. **2015**. https://doi.org/10.1021/acs.langmuir.5b02119.

(19)   Zajforoushan Moghaddam, S.; Thormann, E. Hofmeister Effect of Salt Mixtures on Thermo-Responsive Poly(Propylene Oxide). *Phys. Chem. Chem. Phys.* **2015**, *17* (9), 6359–

6366. https://doi.org/10.1039/c4cp05677a.

(20)   Jungwirth, P.; Tobias, D. J. Molecular Structure of Salt Solutions: A New View of the Interface with Implications for Heterogeneous Atmospheric Chemistry. *J. Phys. Chem. B* **2001**, *105* (43), 10468–10472. https://doi.org/10.1021/JP012750G/ASSET/IMAGES/LARGE/JP012750GF00002.JPEG.

(21)   Jungwirth, P.; Tobias, D. J. Specific Ion Effects at the Air/Water Interface. *Chemical Reviews*. American Chemical Society April 2006, pp 1259–1281. https://doi.org/10.1021/cr0403741.

(22)   Yang, L.; Fan, Y.; Gao, Y. Q. Differences of Cations and Anions: Their Hydration, Surface Adsorption, and Impact on Water Dynamics. *J. Phys. Chem. B* **2011**, *115* (43), 12456–12465. https://doi.org/10.1021/jp207652h.

(23)   Morita, T.; Westh, P.; Nishikawa, K.; Koga, Y. How Much Weaker Are the Effects of Cations than Those of Anions? The Effects of K+ and Cs+ on the Molecular Organization of Liquid H2O. *J. Phys. Chem. B* **2014**, *118* (29), 8744–8749. https://doi.org/10.1021/jp504245c.

(24)   Pincus, P. Colloid Stabilization with Grafted Polyelectrolytes. *Macromolecules* **1991**, *24* (10), 2912–2919. https://doi.org/10.1021/ma00010a043.

(25)   Ehtiati, K.; Z. Moghaddam, S.; Daugaard, A. E.; Thormann, E. Crucial Nonelectrostatic Effects on Polyelectrolyte Brush Behavior. *Macromolecules* **2021**, *54* (7), 3388–3394. https://doi.org/10.1021/acs.macromol.0c02526.

(26)   de Gennes, P. G. Conformations of Polymers Attached to an Interface. *Macromolecules* **1980**, *13* (5), 1069–1075. https://doi.org/10.1021/ma60077a009.

(27)   Moh, L. C. H.; Losego, M. D.; Braun, P. V. Solvent Quality Effects on Scaling Behavior of Poly(Methyl Methacrylate) Brushes in the Moderate- and High-Density Regimes. *Langmuir* **2011**, *27* (7), 3698–3702. https://doi.org/10.1021/la2002139.

(28)   Zhulina, E. B.; Birshtein, T. M.; Borisov, O. V. Theory of Ionizable Polymer Brushes. *Macromolecules* **1995**, *28* (5), 1491–1499. https://doi.org/10.1021/ma00109a021.

(29)   Borisov, O. V; Zhulina, E. B.; Birshtein, T. M. Diagram of the States of a Grafted Polyelectrolyte Layer. *Macromolecules* **1994**, *27* (17), 4795–4803. https://doi.org/10.1021/ma00095a021.

(30)   Lyatskaya, Y. V.; Leermakers, F. A. M.; Fleer, G. J.; Zhulina, E. B.; Birshtein, T. M. Analytical Self-Consistent-Field Model of Weak Polyacid Brushes. *Macromolecules* **1995**, *28* (10), 3562–3569. https://doi.org/10.1021/ma00114a009.

(31) Ubbink, J.; Khokhlov, A. R. Poisson-Boltzmann Theory of the Charge-Induced Adsorption of Semi-Flexible Polyelectrolytes. *J. Chem. Phys.* **2004**, *120* (11), 5353–5365. https://doi.org/10.1063/1.1647048.

(32) Gauthier, M.; Carrozzella, T.; Penlidis, A. Sulfobetaine Zwitterionomers Based on N-Butyl Acrylate and 2-Ethoxyethyl Acrylate: Monomer Synthesis and Copolymerization Behavior. *J. Polym. Sci. Part A Polym. Chem.* **2002**, *40* (4), 511–523. https://doi.org/10.1002/pola.10138.

(33) Xu, X.; Billing, M.; Ruths, M.; Klok, H. A.; Yu, J. Structure and Functionality of Polyelectrolyte Brushes: A Surface Force Perspective. *Chemistry - An Asian Journal*. John Wiley and Sons Ltd November 16, 2018, pp 3411–3436. https://doi.org/10.1002/asia.201800920.

(34) Pincus, P. Colloid Stabilization with Grafted Polyelectrolytes. *Macromolecules* **1991**, *24* (10), 2912–2919. https://doi.org/10.1021/ma00010a043.

(35) Israëls, R.; Leermakers, F. A. M.; Fleer, G. J.; Zhulina, E. B. Charged Polymeric Brushes: Structure and Scaling Relations. *Macromolecules* **1994**, *27* (12), 3249–3261. https://doi.org/10.1021/ma00090a018.

(36) Dobrynin, A. V.; Rubinstein, M. Theory of Polyelectrolytes in Solutions and at Surfaces. *Progress in Polymer Science (Oxford)*. 2005, pp 1049–1118. https://doi.org/10.1016/j.progpolymsci.2005.07.006.

(37) Stuart, M. A. C.; Huck, W. T. S.; Genzer, J.; Müller, M.; Ober, C.; Stamm, M.; Sukhorukov, G. B.; Szleifer, I.; Tsukruk, V. V; Urban, M.; Winnik, F.; Zauscher, S.; Luzinov, I.; Minko, S. Emerging Applications of Stimuli-Responsive Polymer Materials. *Nature Materials*. 2010, pp 101–113. https://doi.org/10.1038/nmat2614.

(38) Willott, J. D.; Murdoch, T. J.; Webber, G. B.; Wanless, E. J. Physicochemical Behaviour of Cationic Polyelectrolyte Brushes. *Progress in Polymer Science*. Elsevier Ltd January 1, 2017, pp 52–75. https://doi.org/10.1016/j.progpolymsci.2016.09.010.

(39) Toomey, R.; Tirrell, M. Functional Polymer Brushes in Aqueous Media from Self-Assembled and Surface-Initiated Polymers. *Annual Review of Physical Chemistry*. Annu Rev Phys Chem 2008, pp 493–517. https://doi.org/10.1146/annurev.physchem.59.032607.093623.

(40) Kunz, W. Specific Ion Effects, Evidences. In *Encyclopedia of Applied Electrochemistry*; Springer, New York, NY, 2014; pp 2045–2050. https://doi.org/10.1007/978-1-4419-6996-5_26.

(41) Kunz, W. Specific Ion Effects in Colloidal and Biological Systems. *Current Opinion in*

Colloid and Interface Science. Elsevier April 1, 2010, pp 34–39. https://doi.org/10.1016/j.cocis.2009.11.008.

(42)   Moghaddam, S. Z.; Thormann, E. The Hofmeister Series: Specific Ion Effects in Aqueous Polymer Solutions. *Journal of Colloid and Interface Science*. Academic Press November 1, 2019, pp 615–635. https://doi.org/10.1016/j.jcis.2019.07.067.

(43)   Thormann, E. On Understanding of the Hofmeister Effect: How Addition of Salt Alters the Stability of Temperature Responsive Polymers in Aqueous Solutions. *RSC Adv.* **2012**, *2* (22), 8297–8305. https://doi.org/10.1039/c2ra20164j.

(44)   Cacace, M. G.; Landau, E. M.; Ramsden, J. J. The Hofmeister Series: Salt and Solvent Effects on Interfacial Phenomena. *Quarterly Reviews of Biophysics*. Cambridge University Press 1997, pp 241–277. https://doi.org/10.1017/S0033583597003363.

(45)   Zhang, Y.; Furyk, S.; Bergbreiter, D. E.; Cremer, P. S. Specific Ion Effects on the Water Solubility of Macromolecules: PNIPAM and the Hofmeister Series. *J. Am. Chem. Soc.* **2005**, *127* (41), 14505–14510. https://doi.org/10.1021/ja0546424.

(46)   Kunz, W.; Belloni, L.; Bernard, O.; Ninham, B. W. Osmotic Coefficients and Surface Tensions of Aqueous Electrolyte Solutions: Role of Dispersion Forces. *J. Phys. Chem. B* **2004**, *108* (7), 2398–2404. https://doi.org/10.1021/jp036113x.

(47)   Salis, A.; Ninham, B. W. Models and Mechanisms of Hofmeister Effects in Electrolyte Solutions, and Colloid and Protein Systems Revisited. *Chemical Society Reviews*. Royal Society of Chemistry October 6, 2014, pp 7358–7377. https://doi.org/10.1039/c4cs00144c.

(48)   Marcus, Y. Ion Properties, Marcus Dekker. *Inc, New York* **1997**, 1–33.

Supporting Information

Ion-specific antipolyelectrolyte effect on the swelling behavior of polyzwitterionic layers

Frederik Hegaard, Robert Biro, Koosha Ehtiati and Esben Thormann*

Department of Chemistry, Technical University of Denmark, 2800 Kgs. Lyngby, Denmark.

S1: Ellipsometry technique

To measure the thickness of the polymer films, a spectroscopic ellipsometer from J. A. Woollam (M-2000) was used. This instrument has a 5 ml liquid cell in which the solvent can be changed during measurements without changing the placement of the sample and the alignment of the light. The ability to change the solvent easily and the non-invasive nature of ellipsometry mean that this technique works well for repeated comparable measurements of the same film in different environments.

The refractive index of the solvent has to be known for each measuring point, as it is changing with the ionic strength and the type of ions. To find the refractive index of a specific solution, a wafer with a SiO_2 layer of known thickness is measured with the solution as the ambient medium. With a model of Si as the substrate, a 1 nm Si-SiO_2 transition layer, a SiO_2 layer, and ambient conditions described by a Cauchy model, the model is fitted to the data with the A and B values of the ambient solution as the only fitting parameters. The values found with this method are shown in Table S1. This method is found to give values of refractive index that fit well with known values found with different methods for determining refractive indices[1,2].

c [mM]	KCl A	KCl B [μm²]	KSCN A	KSCN B [μm²]	KBr A	KBr B [μm²]	CsCl A	CsCl B [μm²]	LiCl A	LiCl B [μm²]
0,01	1.320	0.00331	1.320	0.00331	1.320	0.00331	1.320	0.00331	1.320	0.00331
0.1	1.320	0.00333	1.320	0.00331	1.320	0.00333	1.320	0.00331	1.320	0.00331
1	1.320	0.00333	1.320	0.00331	1.320	0.00335	1.320	0.00331	1.320	0.00331
10	1.320	0.00333	1.320	0.00332	1.320	0.00337	1.320	0.00331	1.320	0.00331
30	1.320	0.00333	1.320	0.00333	1.320	0.00341	1.320	0.00332	1.320	0.00332
100	1.321	0.00335	1.321	0.00338	1.320	0.00353	1.321	0.00335	1.320	0.00338
200	1.322	0.00338	1.323	0.00345	1.320	0.00367	1.322	0.00337	1.321	0.00341
400	1.323	0.00343	1.326	0.00357	1.322	0.00376	1.324	0.00343	1.322	0.00345
800	1.327	0.00353	1.331	0.00379	1.327	0.00396	1.329	0.00354	1.325	0.00355
1200	1.330	0.00362	1.337	0.00400	1.331	0.00416	1.333	0.00365	1.328	0.00364
1600	1.333	0.00371	1.342	0.00420	1.335	0.00434	1.337	0.00376	1.331	0.00374
2200	1.337	0.00384	1.349	0.00449	1.340	0.00461	1.342	0.00391	1.335	0.00387
3000	1.342	0.00401	1.358	0.00478	1.348	0.00495	1.349	0.00409	1.340	0.00405

Table S1: Obtained A and B values of the Cauchy model for the refractive index of salt solution at varying concentrations for each of the five salts used.

The measurements were performed at 25 °C with a wavelength range from 250 nm to 1000 nm for all salts except for KSCN which is measured from 400 nm to 1000 nm because SCN⁻ is absorbing light at the lower wavelengths.

The ellipsometry measurement is done by hydrating the sample in a 0.01 mM salt solution inside the liquid cell for about 1 hour. Then exchange the liquid to a 3000 mM solution and back to 0.01 mM a couple of times to compress and re-swell the film to allow the polymers to reconfigure into a stable state. After this, the sample is kept at 0.01 mM until the drift in thickness is less than 0.5 nm in 2 minutes. Next, the salt concentration is increased by slowly flowing the next solution into the 5 ml liquid cell until a total of 30 ml liquid has been passed through the cell. The thickness is then usually stable within a couple of minutes and after the stabilization period, the thickness is determined as an average of 8 measurements over 2 minutes. This is repeated until the highest salt concentration is reached and the cell is then rinsed slowly with 1 L of ultra-pure water. To prepare the sample for measurements with a new salt, the sample is hydrated in a 100 mM solution of the new salt for 1 hour and then rinsed with a 0.01 mM solution of the new salt. This causes an exchange of the ions inside the polymer and the previous steps can then be repeated.

2

S2: Film characterizations

To ensure that the surface of the films was uniform in height, they were characterized by AFM. Figure S1 shows AFM images of the dry polycationic, polyanionic, and polyzwitterionic films (with 5 % crosslinker). From the R_q values, it is seen that the polyanionic film has a higher roughness than the polycationic film and that the polyzwitterionic film is very smooth, but all three film types are quite smooth and within what is judged reasonable flat for ellipsometry measurements.
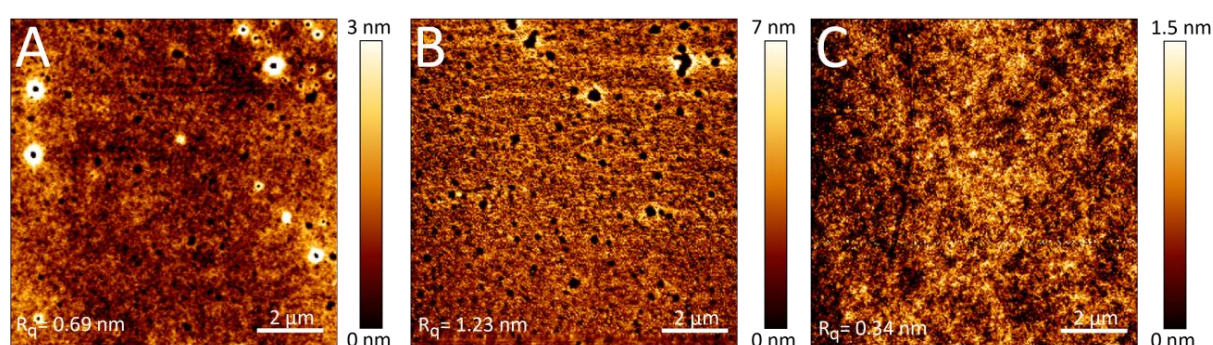
Figure S1: Representative AFM images of the dry films. A) Polycationic film, B) polyanionic film, and C) polyzwitterionic film all with 5 % of the crosslinking monomer. Roughness is calculated as the root mean square roughness (R_q).

To compare the swelling of the different films shown in this study, the thickness is converted to a swelling ratio which is defined by the thickness of the hydrated film divided by its dry thickness. The dry thicknesses obtained with ellipsometry are shown in Table S2.

Film Type	Cat - 5 %	Cat - 10 %	Cat - 15 %	An - 5 %	Zwitter - 5 %
Dry Thickness	96 nm	82 nm	98 nm	130 nm	80 nm

Table S2: Dry thickness of the polycationic films with varying degrees of crosslinked monomer, the polyanionic film, and the polyzwitterionic film measured with ellipsometry.

3

S3: Specific ion effects on polycationic films with 10 % and 15 % crosslinking monomer

Polycationic films with 10 % and 15 % crosslinking monomers swelling behavior in different salt concentrations with different ion types have also been measured. This is firstly relevant to include as a control to see whether or not the ion-specific effects observed are changing relative to each other when the crosslinking is changed. The assumption for understanding the film is that the effects of crosslinking and the specific ion effects are two competing effects that do not directly influence each other. Secondly, the effect of crosslinking is important to understand as we are considering the polyzwitterionic film's intrachain and interchain bonds as a crosslinking as well, although one that depends on salt concentration and ion types.
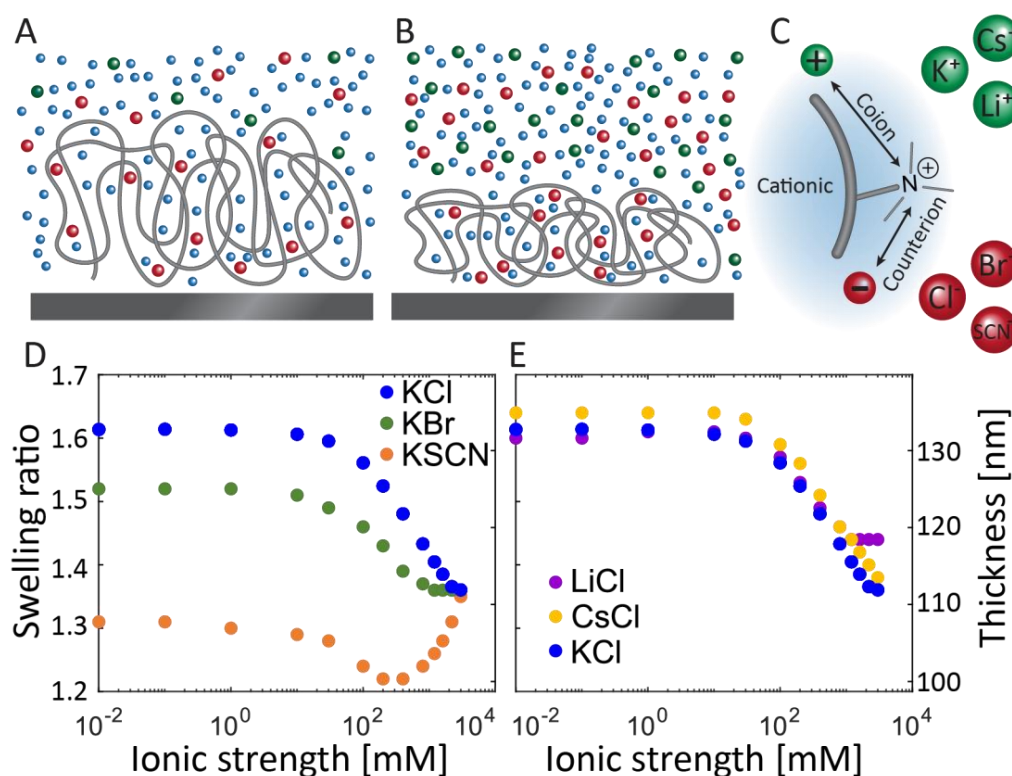
Figure S2: Illustration of a polycationic film with 10 mol % crosslinking monomer swelling when hydrated in low (A) and high (B) salt concentration and the ions' role when interacting with the polymers charged quaternary ammonium groups as either cationic coions or anionic counterions (C). Ellipsometry-based thickness of the polycationic film as a function of salt concentration in the presence of either potassium salts with various anionic counterions (D) or chloride salts with various cationic coions (E).

Figure S2D shows a polycation film with 10 mol % crosslinking monomer with a constant coion (K$^+$) and different counterions and Figure S2E shows the swelling of the same film with constant

counterion (Cl⁻) and different coions. Comparing these to the results from the polycationic film with 5 mol % crosslinker in Figure 3 the main difference is that the whole film is less swollen in the entire range. Variation of the salt used shows almost the same trends, except for a bit more separation between KCl and KSCN and what seems to be a small nonelectrostatic for LiCl.
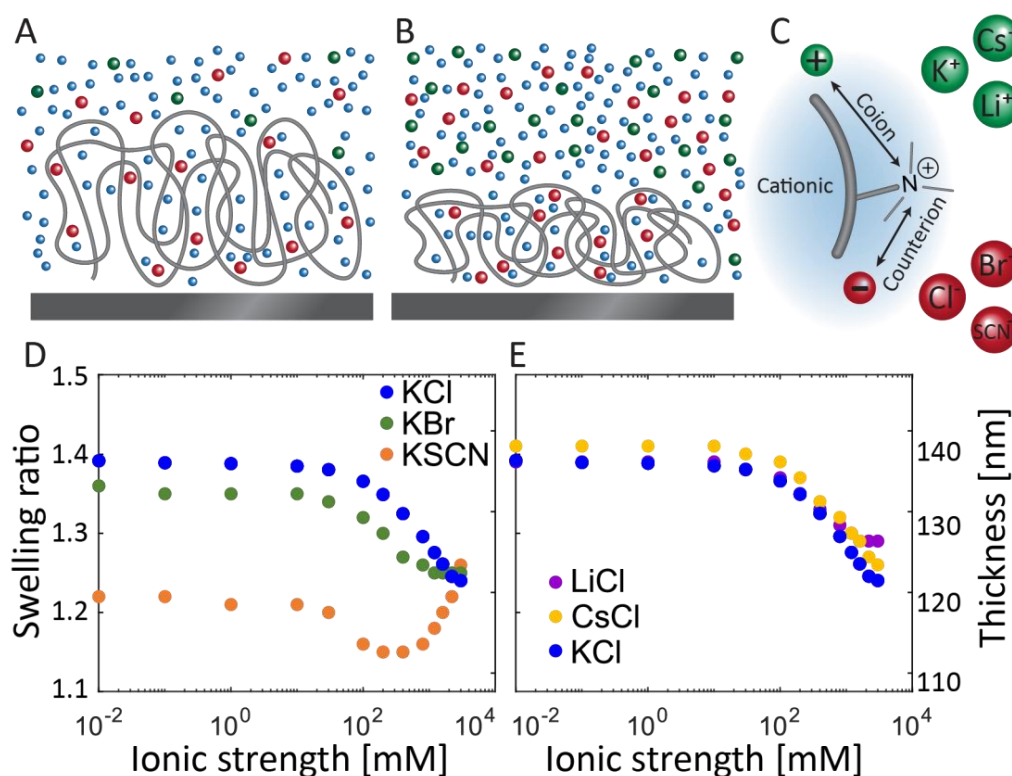
Figure S3: Illustration of a polycationic film with 15 mol % crosslinking monomer swelling when hydrated in low (A) and high (B) salt concentration and the ions' role when interacting with the polymers charged quaternary ammonium groups as either cationic coions or anionic counterions (C). Ellipsometry-based thickness of the polycationic film as a function of salt concentration in the presence of either potassium salts with various anionic counterions (D) or chloride salts with various cationic coions (E).

Similar Figure S3D shows a polycation film with 15 mol % crosslinking monomer with a constant coion (K⁺) and different counterions and Figure S3E shows the swelling of the same film with constant counterion (Cl⁻) and different coions. Again the largest effect of the increase in crosslinks is that the film is less swollen. The trends of the specific ion effects are still very similar to those seen in Figure 2 and for this film, the separation between KCl and KSCN and the non-electrostatic effect seen for LiCl is smaller than what was seen in Figure S2. This is taken as an indication that the small variations seen for the trends of the specific ions are not related to the increased crosslinking degree.

5

S4: Specific Ion Properties

We see that for the films in our study, the osmotic effects are dominating for most of the salt concentration range, and only at the highest salt concentrations, do the nonelectrostatic hydration effects start to play a role. Studies have found that a salt's ability to perform ion pairs with the film's charges is related to the ions' polarizability[2–4].
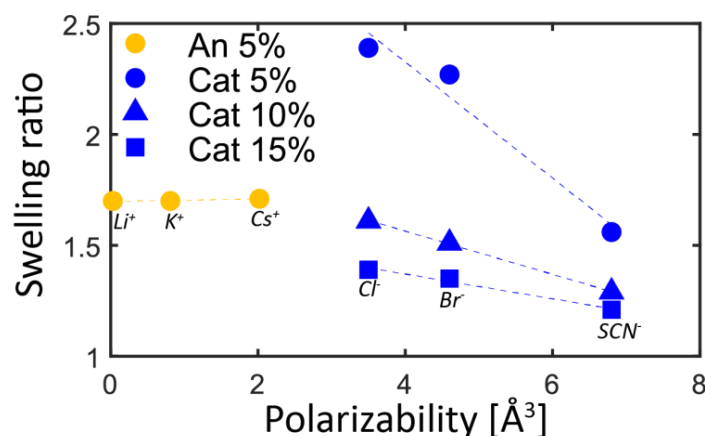
Figure S4: Swelling ratio at 10 mM salt concentration vs polarisability with either K+ or CL- as coion of polycationic/polyanionic films with either 5, 10, or 15 % crosslinker. Polarisability data from [5].

In Figure S4, the graph shows the swelling ratio at 10 mM, for the three polycationic films with different degrees of crosslinking and the polyanionic film, plotted against the polarisability of the counterions. The coions are either Cl- or K^+ for all the films. For the polycationic films, this shows that the change in swelling when the counterion is changed follows the polarisability of that ion, roughly linear. Since increased crosslinking restricts the film's ability to swell, the slope of the fit will be numerically lower for the more crosslinked film. From this, it seems that the polarisability of the ions can be used to predict the relative swelling in the osmotic regime. From the measurements performed on the polycationic films, it is found that the thickness of the film in the osmotic regime follows the same trend as the counterions polarizability, also at different degrees of crosslinking. For the polyanionic film, it was found that the swelling at low salt concentration was independent of the cationic counterions and in Figure S4 this independence is seen despite the ions' polarizability differing. Relative to the anions, the cations used as counterions for the polyanionic film have significantly lower polarizability. As this is linked to its ion paring ability, we suggest that this low polarizability results in so low ion pair formation

7

that it becomes negligibly small or that it doesn't happen at all. At higher salt concentrations the relative thicknesses across counterions cannot be explained solely from the polarizabilities. The competing effects become more complicated to describe, but they can possibly be partially captured by the partition coefficient for the polymer systems as shown in different studies[6,7].

Bibliography

(1)   Ehtiati, K.; Z. Moghaddam, S.; Daugaard, A. E.; Thormann, E. Crucial Nonelectrostatic Effects on Polyelectrolyte Brush Behavior. *Macromolecules* **2021**, *54* (7), 3388–3394. https://doi.org/10.1021/acs.macromol.0c02526.

(2)   Ehtiati, K.; Moghaddam, S. Z.; Klok, H.-A.; Daugaard, A. E.; Thormann, E. Specific Counterion Effects on the Swelling Behavior of Strong Polyelectrolyte Brushes. *Macromolecules* **2022**, *55*, 5130. https://doi.org/10.1021/acs.macromol.2c00411.

(3)   Kunz, W.; Belloni, L.; Bernard, O.; Ninham, B. W. Osmotic Coefficients and Surface Tensions of Aqueous Electrolyte Solutions: Role of Dispersion Forces. *J. Phys. Chem. B* **2004**, *108* (7), 2398–2404. https://doi.org/10.1021/jp036113x.

(4)   Salis, A.; Ninham, B. W. Models and Mechanisms of Hofmeister Effects in Electrolyte Solutions, and Colloid and Protein Systems Revisited. *Chemical Society Reviews*. Royal Society of Chemistry October 6, 2014, pp 7358–7377. https://doi.org/10.1039/c4cs00144c.

(5)   Marcus, Y. Ion Properties, Marcus Dekker. *Inc, New York* **1997**, 1–33.

(6)   Pegram, L. M.; Record, M. T. Hofmeister Salt Effects on Surface Tension Arise from Partitioning of Anions and Cations between Bulk Water and the Air-Water Interface. *J. Phys. Chem. B* **2007**, *111* (19), 5411–5417. https://doi.org/10.1021/jp070245z.

(7)   Moghaddam, S. Z.; Thormann, E. The Hofmeister Series: Specific Ion Effects in Aqueous Polymer Solutions. *Journal of Colloid and Interface Science*. Academic Press November 1, 2019, pp 615–635. https://doi.org/10.1016/j.jcis.2019.07.067.

9

Manuscript 2

Reducing ice adhesion to polyelectrolyte surfaces by counterion mediated nonfrozen hydration water

Robert A. Biro[§], Eric C. Tyrode[Γ], Esben Thormann[§*]

[§]Department of Chemistry, Technical University of Denmark, 2800 Kgs. Lyngby, Denmark
[Γ]Department of Chemistry, KTH Royal Institute of Technology, SE-10044 Stockholm, Sweden

*esth@kemi.dtu.dk

Abstract

Hydrophilic anti-icing coatings can be energy-effective passive solutions for combating ice accretion and reducing ice adhesion. However, their underlying mechanism of action remains inferential, and is not concretely defined from a molecular perspective. Here we systematically investigate the influence of the counterion identity on the shear ice adhesion strength on cationic polymer coatings having quaternary alkyl ammonium moieties as chargeable groups. Temperature-dependent molecular information of the hydrated polymer films is obtained using total internal reflection (TIR) Raman spectroscopy, complemented with differential scanning calorimetry (DSC) and ellipsometry. Ice adhesion measurements show a pronounced counterion-specific behaviour with a sharp increase in adhesion at temperatures that depend on the anion identity, following the order Cl^- < F^- < SCN^- < Br^- < I^-. Linked to the freezing of hydration water, the specific ordering results from differences in ion pairing and amount of water present within the polymer film. Moreover, similar effects can be promoted by varying the crosslinking density in the coating while keeping the anion identity fixed. These findings shed new light on low ice adhesion mechanisms and may inspire novel approaches for improved anti-icing coatings.

Introduction

Anti-icing coatings describe a category of surfaces designed to counter the critical issue of ice formation and ice adhesion that brings about significant economic, energy, and safety concerns in many facets of today's society. Passive anti-icing strategies rely on the intrinsic physical and chemical properties of the surface to prevent ice formation or facilitate its removal.[1,2] For instance, hydrophobic and superhydrophobic coatings can take advantage of the high contact angle of water

to delay the impending freezing of a water droplet. However, despite satisfactory initial anti-icing performance, these coatings are generally mechanically fragile and unreliable in the long term, as liquid, after a few freeze-thaw cycles, eventually accumulates in the micro/nanostructures, leading to a dramatic increase in ice adhesion.[3-5] Slippery liquid-infused porous surfaces (SLIPS) have also attracted attention, where significant reductions in ice adhesion strength have been achieved using typically a hydrophobic lubricating liquid that forms a near flawless and slippery layer between ice and the surface.[6] Nevertheless, SLIPS rely on a limited supply of infused liquid that needs to be replenished, making their remarked performance as an anti-icing coating unsustainable.[7-11] Another interesting approach consists in using hydrophilic polymer coatings, where hydration water supposedly lubricates the polymer-ice interface, resulting in lower ice adhesion.[12-14] Water molecules strongly interacting with polar or charged polymer moieties can remain liquid to temperatures significantly below the freezing point,[15-17] an effect that can, in principle, be further tuned by exchanging the counterion.[12] However, though concepts such as the aqueous lubricating layer[13,16,18], quasi-liquid layer[12,19], or liquid-like layer[20,21] have been put forward to explain the reduced ice adhesion strength, the detailed underlying mechanism has remained elusive, particularly from a molecular perspective. In this work, we systematically investigate the effect of the counterion identity on the shear ice adhesion strength on cationic polymer coatings having a controlled charge and crosslinking density and focus on the temperature-dependent properties of the hydration water in the polymer films.

Results and discussion

The starting point of the discussion is the temperature-dependent shear adhesion strengths of pure ice cylinders frozen on a cationic polymer coating with varying counterions (Figure 1a). Measurements were performed with a home-built ice adhesion apparatus (Figure 1b), and the polymer layers were chemically grafted on silica surfaces (Figure 1c). The charged group in the block copolymer consists of quaternary alkyl ammonium moieties in a 25% molar ratio, and the counterions considered are the halides anions and SCN⁻(see Material and Methods and SI, Section S1, for details of the polymer synthesis and counterion exchange). Figure 1a shows that the identity of the counterion has a marked effect not only on the recorded ice adhesion values but also on their temperature dependence. For instance, though the coatings containing F⁻ or Cl⁻ counterions exhibit very low ice adhesion strengths (<50kPa) down to -10 °C, they differ on their behaviour at lower temperatures. For the F⁻ case, the adhesion increases rapidly to ~170kPa at -15 °C and remains

almost constant down to -35 °C. The sudden increase is also observed for the Cl⁻ counterion, but at -20°C, while for lower temperatures, the adhesion plateaus at ~235kPa, a significantly higher value when compared to F⁻. Similar transitions between low and high ice adhesion are observed for the polymer coatings having Br⁻, I⁻, and SCN⁻ as counterions; yet they occur at higher temperatures and result in higher ice adhesion strengths after the transition.
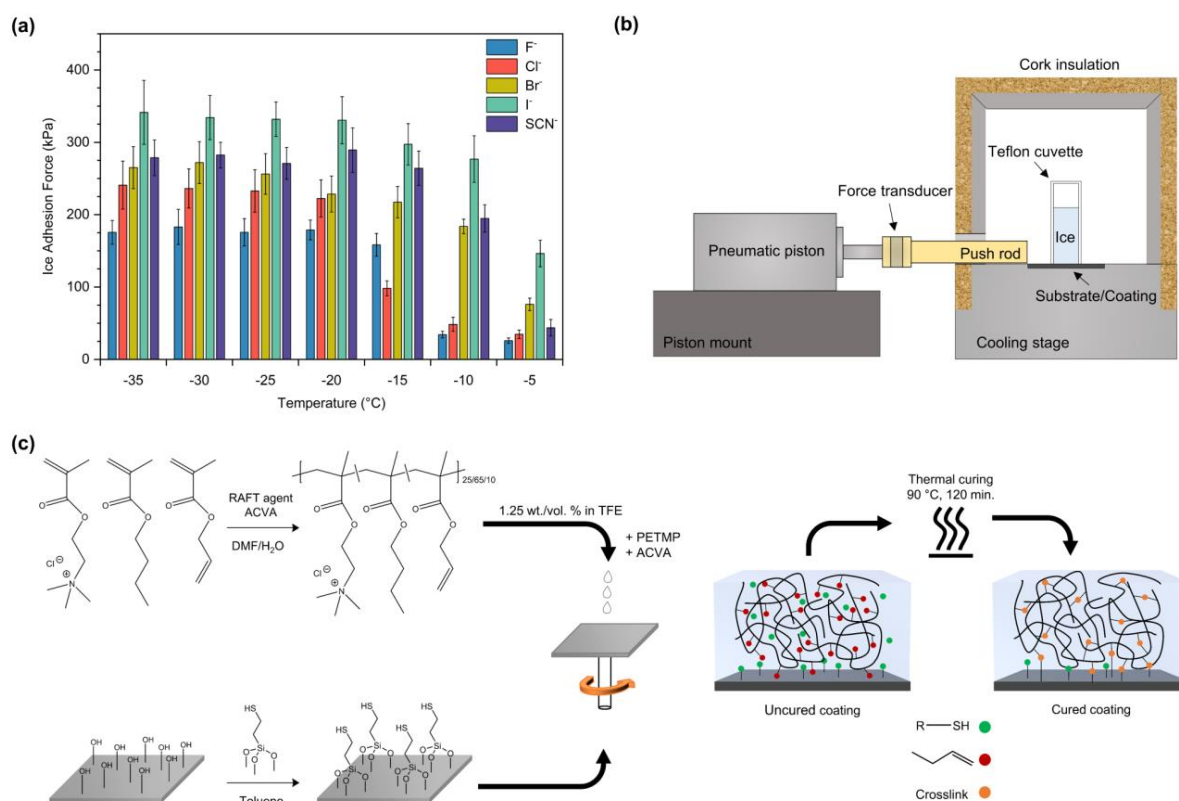
Figure 1: (a) Shear ice adhesion strength on cationic polymer coatings with varying counterions. Values displayed are an average of a minimum of three measurements, with corresponding standard deviation. (b) Schematic of home-built ice adhesion apparatus, in which water is frozen in a Teflon cylinder placed on a test substrate/coating. Ice is then exposed to an increasing shear force by a pneumatic piston applying a linearly increasing force to the ice (see Material and Methods and SI, Section S2, for further details). (c) Illustration describing the synthesis of cationic polymers, functionalization of the oxidized silicon substrate, spin coating of polymer films, and thermally initiated thiol-ene crosslinking (see Material and Methods and SI, Section S1, for further details).

These observations raise three central questions: (1) why does the sudden increase in ice adhesion strength occur at particular temperatures? (2) why does it vary with the type of counterions in the coating? And (3) what dictates the level of ice adhesion observed at the lowest temperatures? To

address these questions, we rely on molecular, morphological, and thermodynamic insights provided by TIR-Raman spectroscopy, ellipsometry and differential scanning calorimetry (DSC).

Freezing of hydration water

Water hydrating the polymer chains may not necessarily freeze at the same temperature as in the bulk.[22] Thus, knowing the physical state of the hydration water in the coating may be relevant for understanding the observed ice adhesion behaviour. To investigate the properties of water inside the polymer film we make use of TIR Raman spectroscopy (see SI, section S3). The method targets molecular vibrations and is sensitive to the hydrogen-bonding environment of water, which varies significantly between the liquid and solid forms.[23–25] Moreover, TIR Raman takes advantage of the properties of evanescent waves and allows selectively probing water molecules inside the polymer coating or further away in the bulk ice by changing the angle of incidence (AOI) of the exciting laser light (see Figure 2a).[26] This is illustrated in Figure 2c, where TIR Raman spectra of a polymer film at -10 $^{\circ}$C having Cl$^-$ as counterion is presented as a function of AOI. The spectral region shown corresponds to that of the CH (2800 -3050 cm^{-1}) and OH (3000-3650 cm^{-1}) stretching modes of the polymer and water (detailed assignments can be found in SI, section S4). At the lowest angles of incidence, the probing depth can be as long as a couple of micrometres, and the signal collected is dominated by the bulk ice phase with its characteristic sharp peak centred at ~3140 cm^{-1}. However, as the angle of incidence increases, the penetration depth of the exciting field decreases, and the TIR Raman response is progressively dominated by the polyelectrolyte layer. At an AOI of 77° the probing depth (~85 nm) is shorter than the thickness of the film (*vide infra*), and the spectral features observed are exclusively from the polymer layer and its hydration water, with essentially no contributions from bulk ice (Figure 2b). At this large AOI, the OH stretching bands not only decrease in intensity relative to those from the polymer (i.e., fewer H_2O molecules are probed) but, more interestingly, the spectral features change (broadening and shifting to higher wavenumbers) closely resembling the spectra of bulk liquid water. The direct implication is that water hydrating the polymer film is liquid at -10°C when having Cl$^-$ as counterion.
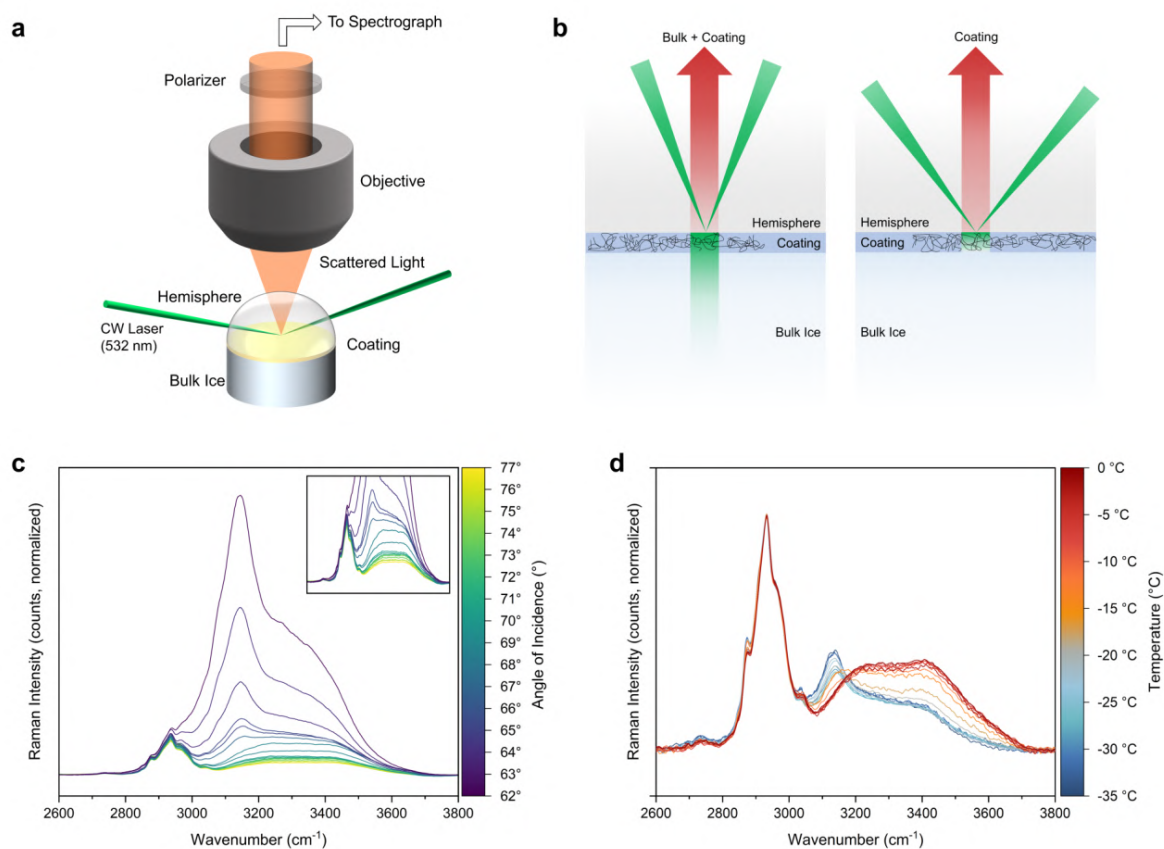
Figure 2: (a) Schematic illustration of the TIR Raman setup, adapted from[26], and (b) illustration of penetration depth dependence on angle of incidence (AOI). Higher AOI penetrate beyond the coating and into bulk ice, while lower AOI penetrate less, allowing for spectroscopy of the coating and its hydration water. (c) TIR Raman spectra at varying penetration depths of a cationic polyelectrolyte coating with Cl⁻ counterions at -10 °C. AOIs nearing 62° penetrate into the bulk ice, while AOIs approaching 77° near a steady penetration depth that observes only the coating and its hydration water (in liquid state at -10 °C). The spectra have been normalized to a corresponding polymer peak at ∼1450 cm⁻¹ to be independent of any contributions from bulk ice. (d) Temperature dependent TIR Raman spectra of the cationic polymer coating with Cl⁻ counterions are confirming a phase transition of the coating's hydration water from ice to liquid water at approximately -15 °C. The spectra have been normalized to the polymer peak at ∼2930 cm⁻¹, as there are no observed contributions from bulk ice beyond the coating. Spectra of coatings with all remaining counterions can be found in SI, Section S4.

In order to investigate the temperature dependence of the hydration water without contributions from bulk ice, all subsequent measurements were performed at a constant AOI of 77°. Figure 2d shows the corresponding TIR Raman spectra for the same coating with Cl⁻ counterions at temperatures ranging from -0.7 °C to -35 °C. The data provides clear evidence that the water in the

hydration layer remains liquids down to approximately -13 °C, and that it is mostly frozen at temperatures below -17°C, with a transition region found in between where features from the ice spectrum become gradually visible at the expense of those from the liquid phase. To quantify this transition, the spectra were accurately modelled as a linear combination of three reference spectra linked to the polymer, ice, and liquid water (see SI, Section S5 for details). The resulting ice fractions in the polymer film as a function of temperature are displayed in Figure 3, including those for all the other counterions, which were obtained following an identical procedure. Relevant to the discussion, the phase transition temperature, defined as the temperature corresponding to a 50% ice fraction, strongly depends on the identity of the counterion in the polymer film following the order $Cl^-< F^-<$ $SCN^-<Br^-< I^-$, with the extremes spanning from -15.8 °C to -3.2°C. As presented in Figure 3, the locations of the freezing transitions for the different counterions closely coincide with the observed rapid increase in ice adhesion strength. Consequently, the physical state of water hydrating the polymer film plays indeed a crucial role when sheering the adhered ice. When liquid, the greater molecular mobility and lack of mechanical interlocking between the coating and ice make it easier to detach. These advantages are lost at lower temperatures where the hydration water is frozen. After having established the importance of the physical state of the hydration water, we focus on understanding the observed counterion specificities.
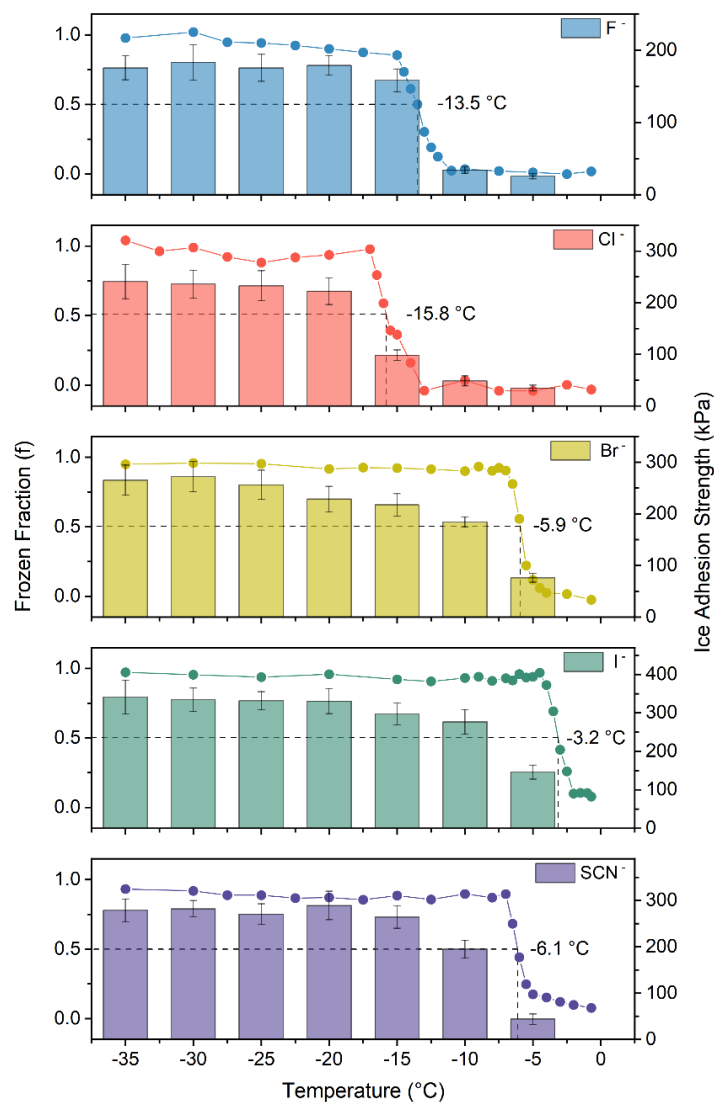
Figure 3: Phase transition of hydration water and corresponding shear ice adhesion strengths of cationic polymer coatings with varying counterions. Frozen fraction (f) was determined by analysis of TIR Raman data using a three-component linear combination model (detailed description in SI, Section S5). Phase transition temperatures are ascribed at f = 0.5, corresponding to mid-point in the transition from ice to liquid water.

Counterion dependent freezing of hydration water

The interaction affinities of the investigated counterions with the quaternary alkyl ammonium moieties in the polymer coating are known to depend on the anion's identity.[27,28] Within the Collin's concept of "water matching affinities",[29,30] the positively charged quaternary ammonium

functionality is considered a soft, polarisable entity[31,32] and thus expected to interact more strongly with the more polarisable anions, i.e., $SCN^- > I^- > Br^- > Cl^- > F^-$. Stronger interactions increase ion pairing and charge neutralization, with a concomitant decrease in the number of unbound counterions within the polymer film. However, a change in ion mobility will also directly affect the ion osmotic swelling of the polyelectrolyte coating and thus its total hydrated volume.[33] We argue that the concentration of these unbound anions is responsible for the observed counterion-dependent ice adhesion and hydration water freezing transitions. To corroborate this hypothesis, independent measurements of the coating swelling and the fraction of unbound counterions are required.

Figure 4a shows the thickness of the polymer coating and its swelling ratio (relative to the dry film) for the different anions as determined from ellipsometry measurements conducted at room temperature. Although relative to dry conditions, all polymer films expand in aqueous solution, they show a pronounced counterion dependence, with the swelling ratio being largest for F^- and smallest for SCN^- (1.92 compared to 1.36), following the order $F^- > Cl^- > Br^- > I^- > SCN^-$. These differences in swelling behaviour likely result from a combination of ion osmotic effects (different ion pairing ability) and other non-electrostatic abilities to drag different amounts of water into the coatings (e.g. different hydration strength of the counterions). However, based on these ellipsometry measurements alone, it is difficult to ascertain how much of the swelling is related to each effect.

In order to study the degree of counterion pairing independently from the coating swelling, DSC measurements on bulk mixtures of water with uncrosslinked polymers and the given counterions were performed. Figure 4b shows the DSC heating curves for the Cl^- case measured between -90 °C to 25 °C, where the water content in the mixture was precisely varied between 0.09 to 0.8. The DSC curves exhibit a single-phase transition (i.e., water melting) where the melting onset temperature shifts to lower values as the amount of water in the mixture is decreased. The T_m dependence as a function of polyelectrolyte concentration and type of counterions is summarized in Figure 4c for each counterion. The data illustrate how for a given water content, the onset melting temperature varies with the identity of the anion with $F^- \approx Cl^- < Br^- < SCN^- < I^-$.
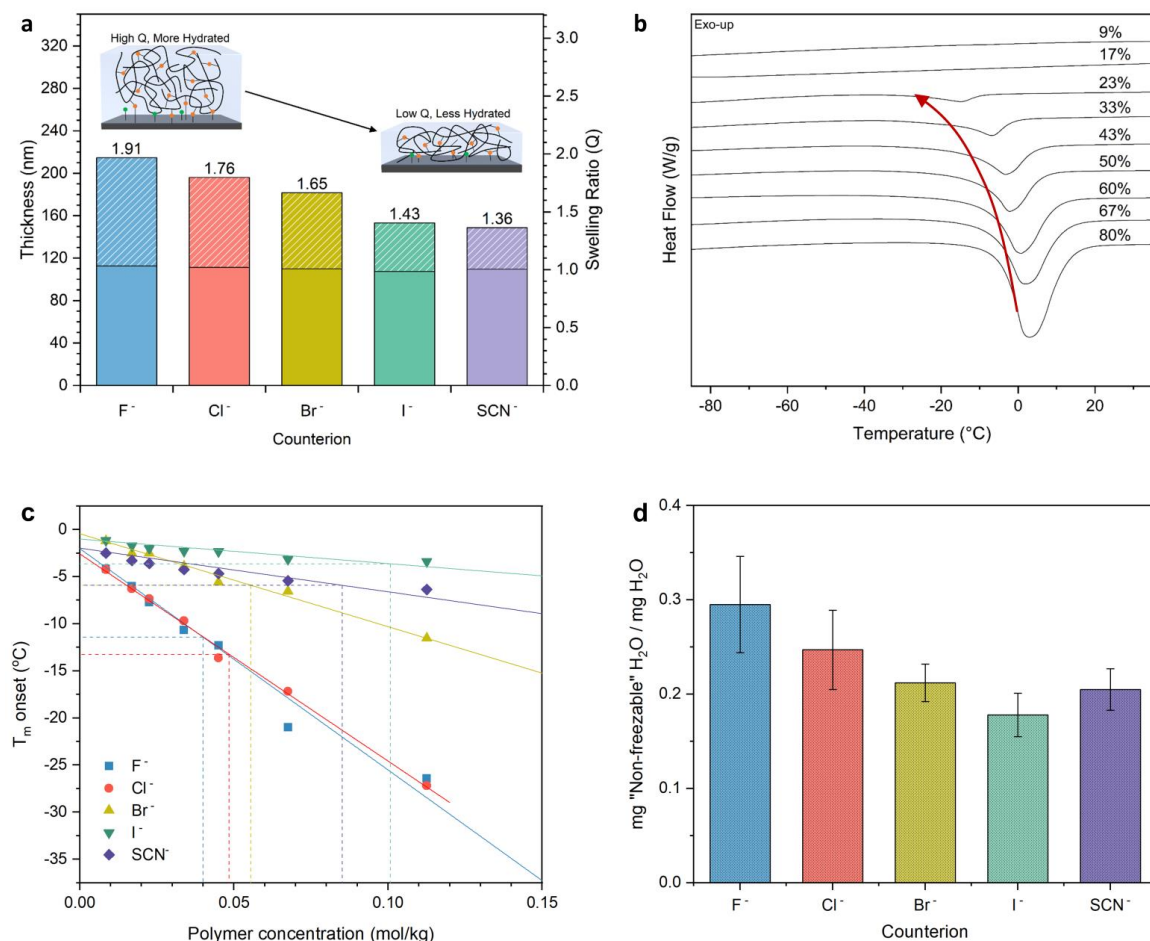
Figure 4: (a) Dry and hydrated thicknesses of cationic polymer coatings with varying counterions measured by ellipsometry (see Material and Method section and SI, Section S6, for details). The numbers refer to the swelling ratios of the coatings (b) DSC thermograms of bulk cationic polymer with Cl$^-$ counterions and water (exo-up). Labelled water fractions correspond to the weight fraction of water in the polyelectrolyte solutions. Onset melting temperatures (as indicated with the arrow) and integrations of the melting endotherm were used to quantify the freezing point depression and determine the amount of "non-freezable" water in the samples (see SI, Section S7 for further details). (c) DSC-based variation of onset melting temperature (°C) with the polyelectrolyte concentration (molality) for the five different investigated counterions. Linear fits are added for each data set, and corresponding drop lines are used to approximate the freezing point depression of hydration water found by combining DSC and ellipsometry data (see SI, Section S7 and S8 for more details). (d) The fractions of "non-freezable" water with respect to total hydration water in each polyelectrolyte coating with the five different investigated counterions (see SI, Section S7 for more details).

While it is well-known how the freezing point of an aqueous salt solution vary with ion concentration in the diluted regime it is less well described how the freezing point is affected in a concentrated polyelectrolyte solution. Early studies have demonstrated how the freezing point of solutions of uncharged polymers depends on the chain interaction (second virial coefficient) and the

142

excluded volumes.[22,34,35] For a specific polymer chemistry, this reduces to a dependence of polymer concentration and molecular weight. For a concentrated polyelectrolyte solution, as we have in the present case, the situation is further affected by the presence of unbound counterions, which like normal small solutes, such as free ions, will lower the freezing point through a colligative effect. At each given polyelectrolyte concentration shown in Figure 4c, the polymer chemistry, polymer concentration and polymer molecular weight is fixed and the differences in freezing points are thus ascribed to the different concentration of unbound counterions in each of the cases. Furthermore, for each type of counterions, we see a linear relationship between the freezing point and the polyelectrolyte concentration, which we interpret as a corresponding linear change in the concentration of unbound counterions. Thus, by first considering the case of having F^- and Cl^- as counterions, where the freezing point depression data are almost identical, we suggest that these systems have amounts of unbound counterions. Since F^- and Cl^- are the counterions, which are supposed to have the weakest ion pairing with the positively charged quaternary ammonium functionality, the obvious explanation for the almost identical counterion effects on the freezing point is that both these counterions are fully dissociated. Following that argument, we can then estimate the degrees of dissociation to be approximately 36% , 23%, and 12% for the cases of Br^-, SCN^- and I^- counterions, respectively (see SI, section S8 for more details).

The information about the different degrees of dissociation can next be used to discuss the ranking of freezing points of hydration water in the coatings with different counterions. The coating with F^- is slightly more hydrated than the coating with Cl^- counterions (Figure 4a). Thus, if both types of counterions are fully dissociated, the concentration of unbound counterions in the polymer coating will be moderately higher in the Cl^- case, and thus a larger freezing point depression will be expected. This prediction agrees with the location of the freezing transitions found by TIR-Raman spectroscopy and the corresponding location of the sudden increases in ice adhesion strength (Figure 3). Similarly, one can explain the relative locations of the freezing transitions for the other counterions. I^- is observed to give rise to the highest degree of counterion pairing (Figure 4c). However, the corresponding coating is marginally more hydrated than for SCN^-, which together explains why the freezing point depression is lowest for I^-. Comparing SCN^- and Br^- cases, the freezing transitions are located at very similar temperatures despite that Br^- is given rise to a lower degree of counterion pairing compared to SCN^-. However, in this case is the greater degree of dissociation is counteracted by a larger swelling, resulting in a similar overall concentration of unbound counterions.

"Non-freezable" water

After having explained the origin of the ion-specific sudden increase in shear ice adhesion, we focus on understanding the differences in ice adhesion forces recorded at the lowest temperatures. Besides providing evidence of a single-phase transition, the DSC measurements also reveal the presence of "non-freezable" water – which is a term used to describe the relative amount of missing enthalpic contribution to the melting transition of hydration water compared to the melting transition of an equal mass of bulk ice (see SI, section S7). [36–38]

First, we however note that our Raman data does not reveal a larger fraction of non-frozen water in the coatings at temperatures below the main freezing point of the hydration water. Therefore, we believe that the "non-freezable" water does not corresponds to bulk liquid water but rather is related to other properties that differentiates frozen hydration water from bulk ice. This could for example be the size of the crystalline domains and the interfacial environment of such domains. However, regardless of the molecular details, such differences are potentially important for ice adhesion since the properties of the frozen hydration water influences the mechanically properties of the coating. Specifically, we expect more "non-freezable" water (e.g. related to smaller frozen domains) to soften the coatings and reduce the ice adhesion strength. This expectation is correlated with the observed behaviour for all ions. For instance, the coating containing F^- as counterion, which had the largest proportion of "non-freezable" water, displayed the lowest ice adhesion strengths below the transition temperature (i.e., 29% and $\sim$ 175 kPa), while I^- was found at the opposite end (17% and $\sim$330 kPa).
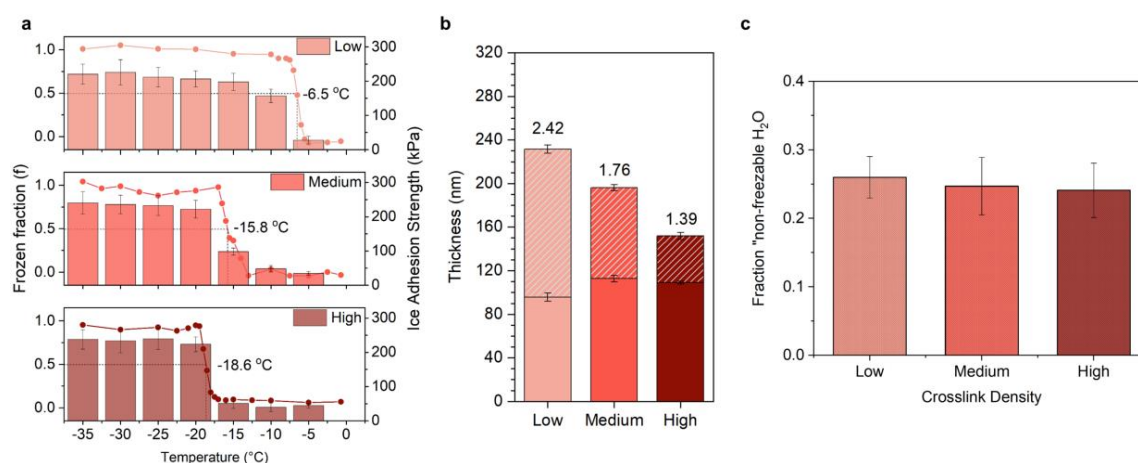
Figure 5: (a) Phase transition of hydration water and corresponding shear ice adhesion strength of cationic polymer coatings with Cl^- counterions and with varying crosslink densities. The frozen fractions of the hydration water are obtained from TIR Raman as described in relation to Figure 3 (see also SI, Section S9). Phase transition temperatures are ascribed at frozen fraction, f = 0.5,

corresponding to mid-point in the transition from ice to liquid water. (b) Dry and hydrated thicknesses of cationic polymer coatings with different crosslink densities, measured by ellipsometry. Swelling ratios are correspondingly labelled. (c) Mass fraction of "non-freezable" water with respect to total hydration water in the polymer coating, as discussed in relation to figure 4 (see also SI, Section S7 and Section S9).

Controlling ice adhesion with crosslinking density

We have so far demonstrated that the counterion identity in the coating can be used to tune the ice adhesion behaviour, primarily through changes in the unbound ion concentration within the polymer layer. However, varying the type of counterion is not the only possibility. An alternative approach is to control the absolute water content in the coating by changing the crosslink density. Polymer films having three different crosslinking densities denoted as "low", "medium", and "high", while containing identical proportions of the charged quaternary alkyl ammonium moieties, were prepared using Cl^- as counterion (the "medium" case corresponds to the same used in the previous sections). The samples were then investigated following a similar procedure to that presented above. The ice adhesion, TIR Raman, DSC, and ellipsometry results are summarized in Figure 5 (see SI, Section S9 for the complete data set). In connection with the ice adhesion behaviour, the freezing transition determined from TIR Raman inside the polymer film significantly varies with crosslinking density, starting at -6.5 °C for the "low" case, and shifting to -15.8 °C and -18.6 °C for "medium" and "high", respectively. Given that the number of unbound Cl^- counterions is the same for all coatings, the shift in phase transition temperature is a direct consequence of the hydration levels. The "high" crosslinked coating being more physically constrained, is less swollen (Figure 5b) and, thus, has a higher concentration of unbound Cl^- anions in the film that increases the magnitude of the freezing point depression. Interestingly, at the lowest temperatures, the magnitude of the ice adhesion strengths is similar for all three cases (Figure 5a), which correlates with the measured percentage of "non-freezable" water in the three polyelectrolyte coatings (Figure 5c).

Conclusion

The ice adhesion behaviour of cationic polyelectrolyte coatings has been rationalized and comprehensively explained using an experimental approach that probes both molecular and macroscopic measurable parameters. The temperature-dependent ice adhesion plots showed a sudden increase in the measured forces at temperatures that were strongly counterion specific. These observed transitions were proven by TIR Raman spectroscopy to be caused by the freezing of

the hydration water in the coating. Occurring at temperatures significantly below that of bulk ice, the transition temperatures are dependent on the identity of the counterion spanning more than 12°C with Cl⁻< F⁻< SCN⁻<Br⁻< I⁻. This peculiar ordering of the anions, which is inconsistent with the typical Hofmeister series arrangement, is explained by a combination of two competing but related effects that control the concentration of "free" or unbound ions present within the polymer coating: preferential counterion binding and total amount of water present within the coating. The former effect could be independently investigated by DSC measurements on bulk polymer solutions, showing a net preference for the more polarizable anions to bind to the quaternary alkyl ammonium moieties of the polyelectrolyte with I⁻> SCN⁻> Br⁻> Cl⁻ ≈ F. On the other hand, the amount of water within the film was estimated from the degree of swelling of the polymer films for the various counterions using ellipsometry and confirmed by TIR Raman at subzero temperatures, with F⁻ > Cl⁻> Br⁻> I⁻> SCN⁻. The coating having the largest concentration of "free" counterions displayed the largest freezing point depression. Interestingly, consistent with the above explanation, the counterion concentration in the coating could also be controlled by varying the crosslinking density rather than exchanging the counterion, with the transition temperature shifting to lower temperatures when increasing the number of crosslinks. Finally, even at the lowest temperatures, when the hydration water in the coating is mostly frozen, the ice adhesion strength was also counterion specific. This behaviour could be correlated with the presence of "non-freezable" water in the coating. The findings presented in this work provide novel mechanistic insights into reducing ice adhesion on polyelectrolyte surfaces, which can be used for designing passive anti-icing coatings with improved and tuneable properties.

Experimental

Reagents: 2-(methacryloyloxy)ethyl trimethylammonium chloride solution (METAC, 75 wt.% in H_2O, Sigma-Aldrich), *n*-butyl methacrylate (*n*-BMA, 99 %, Sigma-Aldrich), and allyl methacrylate (AMA, 98%, Sigma-Aldrich), were all passed through a column of basic activated aluminium oxide (Brockmann I, Sigma-Aldrich) before use. 4-cyano-4-[(dodecylsulfanylthiocarbonyl)sulfanyl] pentanoic acid (97%, Sigma-Aldrich), 4,4'-Azobis(4-cyanvaleric acid) (ACVA, ≥98 %, Sigma-Aldrich), 1,3,5-Trioxane (≥99 %, Sigma-Aldrich), 3-mercaptopropyl trimethoxysilane (3-MPTMS, 95%, Sigma-Aldrich), 1*H*,1*H,2H,2H*-perfluorooctyltriethoxysilane (98%, Sigma-Aldrich) pentaerythritol tetrakis (3-mercaptopropionate) (PETMP, ≥95 %, Sigma-Aldrich), toluene (≥99.8 %, VWR Chemicals BDH), dimethylformamide (≥99.9 %, VWR Chemicals BDH), diethyl ether (≥99.9%, VWR chemicals BDH) 2,2,2-trifluoroethanol (TFE, ≥99 %, Sigma-Aldrich), chromosulfuric acid (Merck), sodium fluoride

(≥99 %, Sigma-Aldrich), sodium fluoride (99.99%, Sigma-Aldrich), potassium chloride (99-100.5 %, Sigma-Aldrich), sodium chloride (99.999%, Sigma-Aldrich), sodium bromide (≥99 %, Sigma-Aldrich), sodium bromide (99.99%, Sigma-Aldrich), potassium iodide (≥99.5 %, Sigma-Aldrich), potassium iodide (≥99.99%, Sigma-Aldrich), sodium thiocyanate (≥98 %, Sigma-Aldrich), and sodium thiocyanate (≥99.99%, Sigma-Aldrich), were all used as received. All water used was passed through a Sartorius Arium Pro ultrapure water system or an equivalent Millipore Integral 15 filtration unit (resistivity of 18.2 MΩ cm).

Synthesis of polyelectrolytes: A 50mL, round-bottomed flask containing METAC (75 wt.% in H_2O, 1.996 mL, 1.654 g, 7.96 mmol), *n*-BMA (3.295 mL, 2.944 g, 20.7mmol), AMA (0.428 mL, 0.402 g, 3.18 mmol), 4-cyano-4-[(dodecylsulfanylthiocarbonyl)sulfanyl] pentanoic acid (63.5 mg, 0.157 mmol), ACVA (4.41 mg, 0.0157 mmol), DMF (10.84 mL), H_2O (0.81 mL), and 1,3,5-trioxane as internal standard (50 mg), was sparged with N_2 for approximately 30 min. The flask was kept under an inert nitrogen atmosphere and subsequently lowered into a pre-heated 70 °C oil bath and monitored via ^{1}H-NMR until completion (approximately 10 hours). The solution was removed from heat, exposed to atmosphere, and precipitated into a large excess of cold stirred diethyl ether, then collected and dried under vacuum at 30 °C overnight. The afforded polymer, poly(METAC-co-BMA-co-AMA)$_{25/65/10}$ was characterized by ^{1}H-NMR and stored at -18 °C. Analogous polymerizations were made containing 5 and 15 mole percent AMA, and 70 and 60 mole percent *n*-BMA respectively, to maintain the targeted 25 mole percent METAC functionality while increasing the functionality of AMA. Polymers made with 5, 10, or 15 mole percent AMA were labelled as "low", "medium" and "high" crosslinked, respectively. For data on characterization of the synthesised products, see SI, section S1.

Functionalisation of substrates: Thermally oxidized silicon wafers (19 mm x 19 mm) were rinsed with acetone, ethanol, and milli-Q water twice before treatment with H_2O plasma at 500 mTorr for 180 sec. Following this, the substrates were submerged in a lightly stirred solution of 3-MPTMS in toluene (25 mL, 5 vol. %) at room temperature for 3 h. The wafers were then dried under a stream of nitrogen and thermally cured at 130 °C for 2 h to induce condensation of the silane onto the substrate. A similar procedure was used for the silanization of silica hemispheres, whereby they were initially cleaned using chromosulfuric acid and washed thoroughly with Milli-Q water before plasma treatment.

Preparation of coatings: Previously synthesized polyelectrolyte ("low", "medium", "high") was dissolved in TFE (1.25 wt./vol. %) with equimolar amounts of ACVA and PETMP, with respect to the AMA content of the selected polyelectrolyte. The solution was stirred vigorously for 30 min and passed through a 0.22 μm filter. 225 μL of the prepared solution was spin-coated onto the

functionalized silicon wafers (2000 rpm for 40 sec), and the coatings placed in a 90 °C oven for 2 h to induce thermally initiated thiol-ene cure. The coatings were washed with excess water to remove any unattached material and dried under nitrogen before storage or use. For the silica hemispheres, an identical procedure with the exception that only 60 μL of solution was added for spin-coating, corresponding to the decrease in surface area.

<u>Counterion exchange:</u> In order to exchange the counterions of the coatings, the coatings were placed in a home-built sample holder and submerged in a stirred 100 mM solution of sodium or potassium salt accompanying the preferred counterion. The coatings were stirred for 30 min after which they were rinsed with excess water and dried under nitrogen. Solutions made of high-purity salts (≥99.99%) were used for counterion exchange in the TIR Raman spectroscopy setup.

<u>Ice Adhesion Measurements:</u> A home-built shear adhesion apparatus was used to measure the ice adhesion strength of the samples. A pneumatic piston (MQQTB16-50D, SMC Corp.) with a load cell (8413-5050, 50N, Blichfeld) attached to a plastic pushing rod, was used to push an ice-filled Teflon cuvette (pre-treated with 1*H*,1*H*,2*H*,2*H*-perfluorooctyltriethoxysilane). The pushing force was controlled using a pressure regulator (ARX20-F01, SMC Corp) set to 3.0 bar, with an adjustable flow restriction valve (AS1002F, SMC Corp.) set to 10mL min^{-1}. A cork-insulated stainless-steel chamber with square indents (20 mm x 20 mm x 0.5 mm) in which the coatings were placed and secured to the stage, was temperature controlled by a recirculating chiller (AD15R-30, 462-0230, VWR) flowing cooled fluid through a connected baseplate. Ice/coating samples were prepared by first placing the Teflon cuvettes into a home-built cuvette holder functioning as a weighted alignment piece, then inserting the holder into the pre-cooled chamber, and filling each cuvette with degassed pure water (0.7 mL). The samples were frozen at -20 °C for 1 h, before the measurement temperature was set and allowed to equilibrate for 1 h more. Further experimental details of ice adhesion measurements are given in SI, section S2.

<u>TIR Raman Spectroscopy:</u> A home-built spectrometer has been described in detail previously.[39] Briefly, a 532nm CW laser (20mW) was used as an excitation source. The beam was focused onto a coated silica hemisphere sample held in a custom sample holder (further details of setup can be found in SI, Section S3).[24] The Raman scattered light was collected using an ultra-long working distance objective (M-Plan Apo 50X, NA 0.55, Mititoyo, Japan) attached to modified microscope (Zeiss, Germany) and directed into a combined spectrometer and CCD camera (Shamrock 303i, Newton DU940N-BV, Andor, Ireland). The penetration depth of the evanescent wave into the sample was varied by changing the angle of incidence of the beam into the sample. Using polarisation optics (Thorlabs, USA) set in the beam path, spectra were collected using s-polarized incident light and y-

polarized scattered light, unless otherwise stated. The presented spectra have been smoothed using running average over five data points, baseline subtracted, and finally normalized to the highest intensity peak. An explanation of the analysis of the TIR Raman spectra and extraction of frozen phase fraction can be found in SI, Section S5.

Ellipsometry: A variable angle spectroscopic ellipsometer (M-2000, J.A. Woollam Co., USA) using CompleteEASE software (JA Woolam Co., USA) was employed to determine the thickness of the polyelectrolyte coatings. The presented data is a result of three identically prepared samples that were used for both dry and hydrated measurements in order to demonstrate the reproducibility of both sample preparation and the measurement technique. The dry measurements were conducted over a wavelength of 250 – 1000 nm at five angles of incidence (55°, 60°, 65°, 70°, and 75°), by placing the coating onto the sample stage at room temperature, where a steady stream of nitrogen was used to resolve any other ambient factors e.g., humidity. The Ψ and Δ data collected was modelled using a three-layer system composed of a silica substrate, a silicon dioxide layer, and a final empirical Cauchy model that is used to describe the polymer coating. The film was assumed to be homogenous and transparent, with no adsorption (k = 0), therefore the refractive index could be simply described by the following Cauchy equation:

$$n(\lambda) = A + B/\lambda^2$$

To determine the hydrated thickness of the coatings, a standard liquid cell (5mL Heat Liquid Cell) was set to 25 °C and used to collect the Ψ and Δ data at an angle of incidence of 75° over a wavelength of 250 – 1000nm. In this setup, water was flowed into the cell, and the samples left to equilibrate for at least 20 min before measurement. While the silica and silicon dioxide layers of the model used remained, the thickness of the hydrated polymer film was determined using a two-component layer consisting of the dry polymer (*A & B* given by dry measurements) and water. Furthermore, the volume fraction of water in the coating could be estimated according to the Bruggeman Effective Medium Approximation (BEMA). Further details of the fittings, refractive indexes, and optical constants are given in SI, Section S6.

Differential Scanning Calorimetry: To characterize the states of water in aqueous polymer systems, a TA Instruments Q200 DSC with RCS 90 (TA Instruments - Waters LLC, USA) was used. Given amounts of polymer, (e.g., medium crosslink density polymer with Cl- counterions) and water corresponding to a wide range of mass fractions of water (0.09 – 0.8) were hermetically sealed in aluminium pans (Tzero Pans and Tzero Hermetic Lids TA Instruments – Waters LLC, USA) and left to equilibrate over 48 h at room temperature. The sealed pans were weighed before and after DSC measurements to ensure no loss of mass through a possible puncture during the equilibration and measurement.

Samples were cooled from 25 °C to -90 °C, held for 10 min, and then heated to 40 °C at a rate of 5 °C min^{-1}.

References

1. Parent, O. & Ilinca, A. Anti-icing and de-icing techniques for wind turbines: Critical review. *Cold Reg. Sci. Technol.* **65**, 88–96 (2011).

2. Kenzhebayeva, A., Bakbolat, B., Sultanov, F., Daulbayev, C. & Mansurov, Z. A mini-review on recent developments in anti-icing methods. *Polymers (Basel).* **13**, (2021).

3. Kulinich, S. A., Farhadi, S., Nose, K. & Du, X. W. Superhydrophobic surfaces: Are they really ice-repellent? *Langmuir* **27**, 25–29 (2011).

4. Lazauskas, A. *et al.* Water droplet behavior on superhydrophobic SiO2 nanocomposite films during icing/deicing cycles. *Mater. Charact.* **82**, 9–16 (2013).

5. Farhadi, S., Farzaneh, M. & Kulinich, S. A. Anti-icing performance of superhydrophobic surfaces. *Appl. Surf. Sci.* **257**, 6264–6269 (2011).

6. Wong, T. S. *et al.* Bioinspired self-repairing slippery surfaces with pressure-stable omniphobicity. *Nature* **477**, 443–447 (2011).

7. Ozbay, S., Yuceel, C. & Erbil, H. Y. Improved Icephobic Properties on Surfaces with a Hydrophilic Lubricating Liquid. *ACS Appl. Mater. Interfaces* **7**, 22067–22077 (2015).

8. Niemelä-Anttonen, H. *et al.* Icephobicity of Slippery Liquid Infused Porous Surfaces under Multiple Freeze–Thaw and Ice Accretion–Detachment Cycles. *Adv. Mater. Interfaces* **5**, 1–8 (2018).

9. Liu, C. *et al.* Robust Slippery Liquid-Infused Porous Network Surfaces for Enhanced Anti-icing/Deicing Performance. *ACS Appl. Mater. Interfaces* **12**, 25471–25477 (2020).

10. Heydarian, S., Jafari, R. & Momen, G. Recent progress in the anti-icing performance of slippery liquid-infused surfaces. *Prog. Org. Coatings* **151**, 106096 (2021).

11. Boinovich, L. B., Emelyanenko, K. A. & Emelyanenko, A. M. Superhydrophobic versus SLIPS: Temperature dependence and the stability of ice adhesion strength. *J. Colloid Interface Sci.* **606**, 556–566 (2022).

12. Chernyy, S. *et al.* Superhydrophilic polyelectrolyte brush layers with imparted anti-icing properties: Effect of counter ions. *ACS Appl. Mater. Interfaces* **6**, 6487–6496 (2014).

13. Tao, C. *et al.* Formation of zwitterionic coatings with an aqueous lubricating layer for antifogging/anti-icing applications. *Prog. Org. Coatings* **115**, 56–64 (2018).

14. Liang, B., Zhang, G., Zhong, Z., Huang, Y. & Su, Z. Superhydrophilic Anti-Icing Coatings Based on Polyzwitterion Brushes. *Langmuir* **35**, 1294–1301 (2019).

15. Chen, J. *et al.* Robust prototypical anti-icing coatings with a self-lubricating liquid water layer between ice and substrate. *ACS Appl. Mater. Interfaces* **5**, 4026–4030 (2013).

16. Dou, R. *et al.* Anti-icing coating with an aqueous lubricating layer. *ACS Appl. Mater. Interfaces* **6**, 6998–7003 (2014).

17. Chen, J. *et al.* Durable Anti-Icing Coatings Based on Self-Sustainable Lubricating Layer. *ACS Omega* **2**, 2047–2054 (2017).

18. Chen, J., Luo, Z., Fan, Q., Lv, J. & Wang, J. Anti-Ice coating inspired by ice skating. *Small* **10**, 4693–4699 (2014).

19. Chen, D., Gelenter, M. D., Hong, M., Cohen, R. E. & McKinley, G. H. Icephobic surfaces induced by interfacial nonfrozen water. *ACS Appl. Mater. Interfaces* **9**, 4202–4214 (2017).

20. Huang, B. *et al.* Hydrogels as durable anti-icing coatings inhibit and delay ice nucleation. *Molecules* **25**, (2020).

21. Jellinek, H. H. G. Liquid-like (transition) layer on ice. *J. Colloid Interface Sci.* **25**, 192–205 (1967).

22. Wang, S. C., Wang, C. K., Chang, F. M. & Tsao, H. K. Second virial coefficients of poly(ethylene glycol) in aqueous solutions at freezing point. *Macromolecules* **35**, 9551–9555 (2002).

23. Duričković, I. *et al.* Water-ice phase transition probed by Raman spectroscopy. *J. Raman Spectrosc.* **42**, 1408–1412 (2011).

24. Liljeblad, J. F. D., Furó, I. & Tyrode, E. C. The premolten layer of ice next to a hydrophilic solid surface: correlating adhesion with molecular properties. *Phys. Chem. Chem. Phys.* **19**, 305–317 (2017).

25. Xue, X., He, Z. Z. & Liu, J. Detection of water-ice phase transition based on Raman spectrum. *J. Raman Spectrosc.* **44**, 1045–1048 (2013).

26. Tyrode, E., Rutland, M. W. & Bain, C. D. Adsorption of CTAB on hydrophilic silica studied by linear and nonlinear optical spectroscopy. *J. Am. Chem. Soc.* **130**, 17434–17445 (2008).

27. Ehtiati, K., Moghaddam, S. Z., Klok, H., Daugaard, A. E. & Thormann, E. Speci fi c Counterion E ff ects on the Swelling Behavior of Strong Polyelectrolyte Brushes. (2022) doi:10.1021/acs.macromol.2c00411.

28. He, Z. *et al.* Tuning ice nucleation with counterions on polyelectrolyte brush surfaces. *Sci.*

Adv. **2**, (2016).

29. Collins, K. D., Neilson, G. W. & Enderby, J. E. Ions in water: Characterizing the forces that control chemical processes and biological structure. *Biophys. Chem.* **128**, 95–104 (2007).

30. Collins, K. D. Ions from the Hofmeister series and osmolytes: Effects on proteins in solution and in the crystallization process. *Methods* **34**, 300–311 (2004).

31. Vlachy, N. *et al.* Hofmeister series and specific interactions of charged headgroups with aqueous ions. *Adv. Colloid Interface Sci.* **146**, 42–47 (2009).

32. Vlachy, N., Drechsler, M., Touraud, D. & Kunz, W. Anion specificity influencing morphology in catanionic surfactant mixtures with an excess of cationic surfactant. *Comptes Rendus Chim.* **12**, 30–37 (2009).

33. Rumyantsev, A. M., Pan, A., Ghosh Roy, S., De, P. & Kramarenko, E. Y. Polyelectrolyte Gel Swelling and Conductivity vs Counterion Type, Cross-Linking Density, and Solvent Polarity. *Macromolecules* **49**, 6630–6643 (2016).

34. Kawai, T. Freezing point depression of polymer solutions and gels. *J. Polym. Sci.* **32**, 425–444 (1958).

35. Solms, D. J. & Rijke, A. M. Anomalous freezing behavior of polymer gels and solutions. *J. Phys. Chem.* **75**, 2623–2631 (1971).

36. Fushimi, H., Ando, I. & Iijima, T. States of water in cationically charged poly(vinyl alcohol) membranes. *Polymer (Guildf).* **32**, 241–248 (1991).

37. Li, W., Xue, F. & Cheng, R. States of water in partially swollen poly(vinyl alcohol) hydrogels. *Polymer (Guildf).* **46**, 12026–12031 (2005).

38. Guan, L., Xu, H. & Huang, D. The investigation on states of water in different hydrophilic polymers by DSC and FTIR. *J. Polym. Res.* **18**, 681–689 (2011).

39. Tyrode, E. & Liljeblad, J. F. D. Water structure next to ordered and disordered hydrophobic silane monolayers: A vibrational sum frequency spectroscopy study. *J. Phys. Chem. C* **117**, 1780–1790 (2013).

Supplemental Information

Reducing ice adhesion by counterion specific interactions with polyelectrolyte surfaces

Robert A. Biro[§], Eric C. Tyrode[Γ], Esben Thormann[§*]

[§]Department of Chemistry, Technical University of Denmark, 2800 Kgs. Lyngby, Denmark
[Γ]Department of Chemistry, KTH Royal Institute of Technology, SE-10044 Stockholm, Sweden

*esth@kemi.dtu.dk

S1: Preparation and characterization of cationic polymers

The RAFT polymerization of METAC, *n*-BMA, and AMA was monitored by ^{1}H-NMR for the duration of the reaction, with aliquots taken approximately every hour. As shown by the time vs. conversion plot in Figure S1, the linear monomer conversion into polymer demonstrates the controlled nature of the reaction, which allowed us to accurately quench the reaction after 10 h and precipitate the polymer. In addition to the high degree of control and conversion, a lack of any significant compositional drift was found. Whereas the monomer conversion was measured by the signal from the two terminal alkene protons for each monomer compared to an internal standard, the final polymer composition was roughly determined by the ratio between characteristic protons that represent each monomer. Figures SFigure S2-Figure S4 exhibit the final ^{1}H-NMR spectra of each cationic polymer with approximately 5, 10, or 15 mole percent AMA labelled "low", "medium" and "high" respectively. Analysis of the precipitated and dried polyelectrolytes produced confirmed the proportions of METAC, *n*-BMA, and AMA in the polymers were accurate to the targeted proportions, as summarized in

In greater detail, the allyl methacrylate vinyl proton (**a,** -R-C*H*=CH₂) appears at ∼5.92 ppm, while terminal alkene protons (**b**, -R-CH-C*H₂*) display signals at ∼5.37 (*cis* to vinyl) and 5.27 ppm (*trans* to vinyl), respectively. A peak corresponding to two allylic hydrogens (**f**, -C*H₂*-CH=CH₂)at ∼4.44 ppm is overlapped by a peak likely corresponding to two characteristic protons of METAC (**c**,

-COO-CH_2-CH$_2$-[N(CH$_3$)$_3$]$^+$), while the peak at ~3.91 ppm is presumed to be a combination of two sets of protons: (**e**, -COO-CH$_2$-CH_2-[N(CH$_3$)$_3$]$^+$) and (**g**, -COO-CH_2-CH$_2$-CH$_2$-CH$_3$). A distinguishably large signal at ~3.37-3.32 ppm is assigned to the protons of primary carbons in the quaternary alkyl ammonium group of METAC. However, the integrated area of the signal is far greater than anticipated and is evidently caused by a large H$_2$O signal. Remaining methylene protons of *n*-BMA (-COO-CH$_2$-CH_2-CH_2-CH$_3$) and the polymer backbone are broadly observed from ~2.20 to ~1.17 ppm, while methyl protons of *n*-BMA (-COO-CH$_2$-CH$_2$-CH$_2$-CH_3) and the backbone of all methacrylate monomers are seen from ~1.15-0.55 ppm. The percentage of each monomer was determined using peaks **b**, **f+c**, **g+e**, where first the expected area of each peak was calculated relative to **a** = 1.00, compared with the integration of the peaks, and the approximate mole percentage of each monomer then calculated (Table S1).
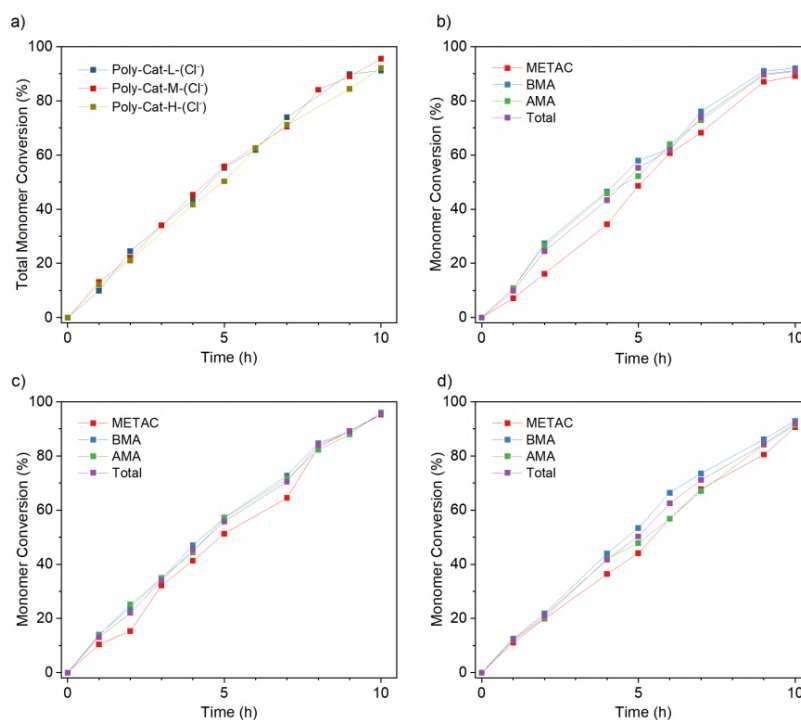
Figure S1: (a) Total monomer conversion of cationic polyelectrolytes with varying fractions of BMA and AMA. (b) Conversion of "low" (c) Conversion of "medium",(d) Conversion of "high"
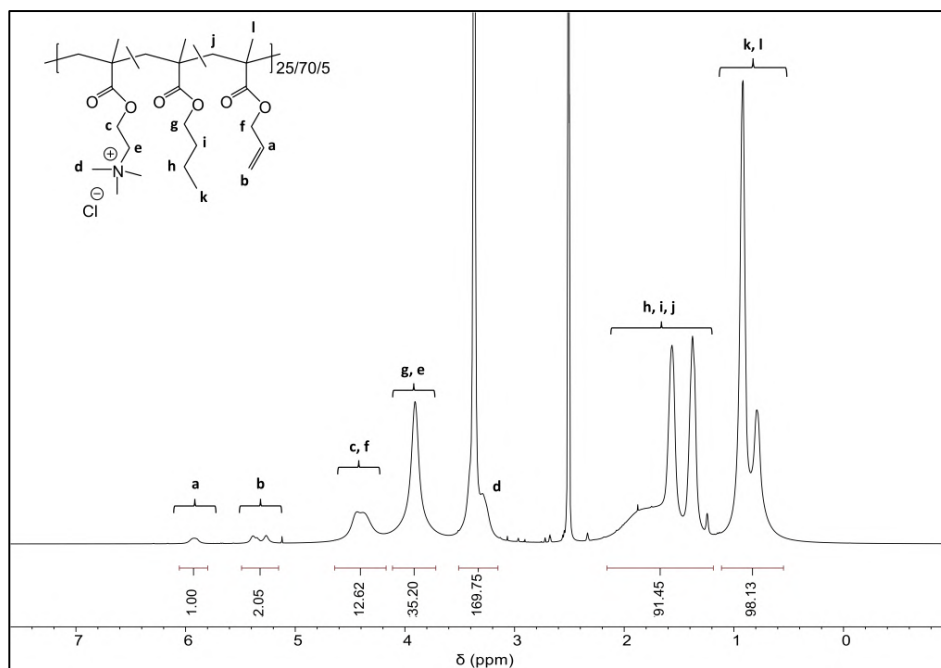
Figure S2: ^{1}H-NMR spectra (400 MHz, DMSO-d$_6$) of cationic polyelectrolyte with ~5 mol. %: δ 6.06-5.80 (b, 1.00H), 5.49-5.17 (b, 2.05H), 4.64-4.20 (b, 12.62H), 4.19-3.61 (b, 35.20H), 3.59-3.13 (b, 169.75H), 2.09-1.19 (b, 91.45H), 1.17-0.55 (b, 98.13H).
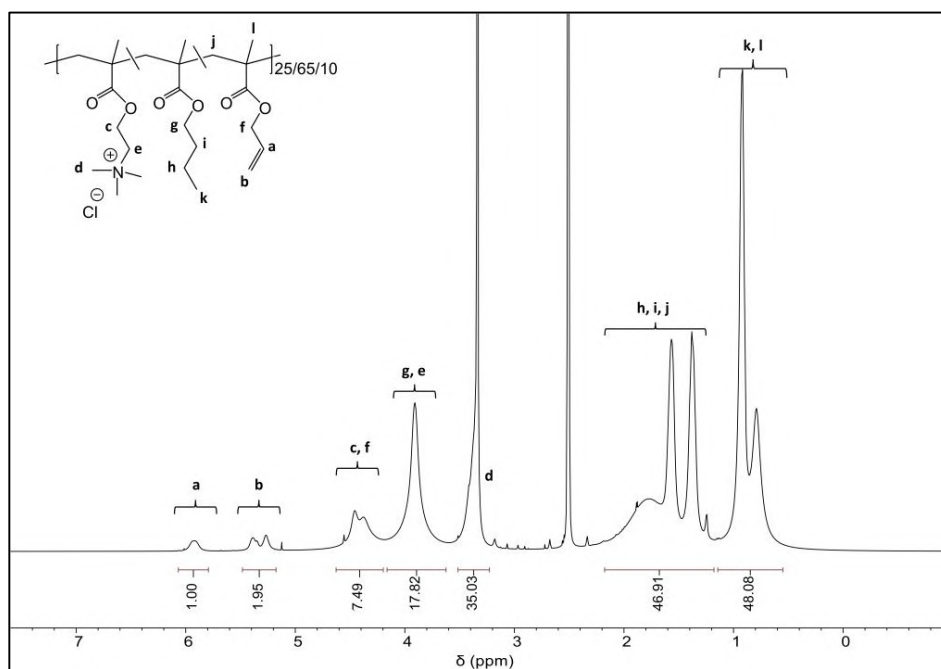
Figure S3: ^{1}H-NMR spectra (400 MHz, DMSO-d$_6$) of cationic polyelectrolyte with ~10 mol. % : δ 6.07-5.80 (b, 1.00H), 5.49-5.16 (b, 1.95H), 4.63-4.24 (b, 7.49H), 4.18-3.60 (b, 17.82H), 3.55-3.22 (b, 35.03H), 2.17-1.18 (b, 46.91H), 1.14-0.55 (b, 48.08H).
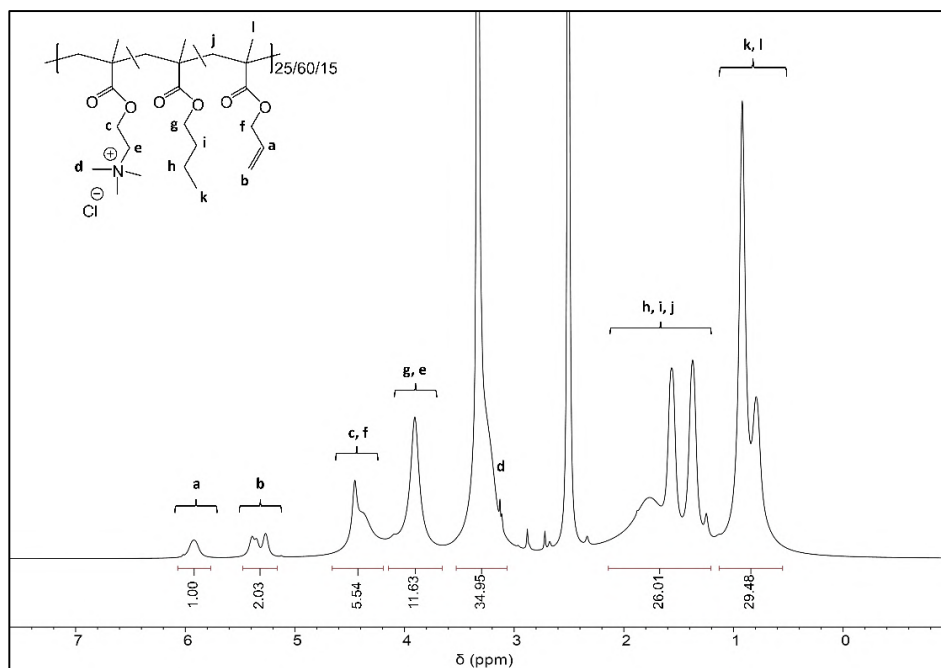
Figure S4: 1H-NMR spectra (400 MHz, DMSO-d$_6$) of cationic polyelectrolyte with ∼15 mol. % AMA :δ 6.07-5.77 (b, 1.00H), 5.53-5.16 (b, 2.03H), 4.66-4.19 (b, 5.54H), 4.15-3.66 (b, 11.63H), 3.63-2.98 (b, 34.95H), 2.18-1.20 (b, 26.01H), 1.13-0.55 (b, 29.48H).

Monomer/Polymer	"Low"	"Medium"	"High"
METAC	28.4	28.0	26.2
n-BMA	66.1	62.1	58.7
AMA	5.5	9.9	15.1

Table S1: Approximate monomer mole percentages in synthesized polymers calculated by 1H-NMR spectroscopy.

S2: Details on shear ice adhesion strength measurements

A home-built shear adhesion apparatus was designed and constructed to measure the shear adhesion of ice onto a surface. Figure S5 presents a detailed cutaway diagram of the apparatus, while Figure S6Figure S12 layout images taken of setup.

In an effort to provide greater details as to the design and experimental setup: the rod of the pneumatic piston (MQQTB16-50D, SMC Corp.) was connected to a custom insert that housed the load cell (8413-5050, 50N, Burster). Both the load cell and plastic pushing rod, snugly fit into the housing to prevent any movement that may interfere with the measurement, such as incorrect alignment of the pushing rod to the sample. Additionally, the end of the pushing rod was concave and neatly fit the custom Teflon cuvettes to prevent any localization of force. In order to prevent leaking of the cuvettes during loading, they were first rigorously washed with milli-Q water, ethanol, and acetone before a treatment with H_2O plasma at 500 mTorr for 180 sec. A 10 vol.% solution of 1*H*,1*H*,2*H*,2*H*-perfluorooctyltriethoxysilane in chloroform was made and placed into a desiccator containing the cleaned Teflon cuvettes, where they were treated by vacuum deposition overnight, before being heated in a 130 °C oven for at least 2 h.

The pushing force was controlled using a pressure regulator (ARX20-F01, SMC Corp) set to 3.0 bar, with an adjustable flow restriction valve (AS1002F, SMC Corp.) set to 10mL min^{-1}. This produced a linearly increasing force curve through ~1000 kPa, which sufficed for all ice adhesion measurements on coatings. However, validation on bare substrates (cleaned silicon wafers) required a greater pressure to produce a linearly increasing force curve through ~1300 kPa, and will discussed later. The stainless-steel chamber was insulated with at least 5 mm cork insulation on all sides and was temperature controlled by a recirculating chiller (AD15R-30, 462-0230, VWR) flowing cooled fluid through a connected stainless-steel base-plate. A weak flow of cool air was introduced in order to minimize any frost-build up in the chamber or on the samples. In order to not significantly affect the environment of the coating during measurements, a set of 8 holes (each corresponding to a particular surface) were bore into the chamber and plugged with a Teflon stopper when measurements were not ongoing.

The testing surfaces were placed in indents (20 x 20 x 0.5 mm) and clamped down in order to prevent surface movement from affecting adhesion strength. As the shear adhesion strength of ice has been found to be dependent on the distance from the shear plane that the probe applies a force, thus applying a torque, this distance was minimized to less than 1 mm.[1]

To prepare samples with adhered ice, the cuvettes were placed into a specially made brass cuvette holder, additionally serving two additional purposes as an alignment piece and a weight to

prevent any leakage during the freezing process. Once in place, and a stable temperature of -20 °C had been reached, 0.7 mL of degassed milli-Q water was carefully added into the cuvettes. The ice was allowed to freeze on the surfaces for 1 h, after which the brass cuvette holder was delicately removed; the desired testing temperature was set and allowed to equilibrate for 1 h before any measurements.

The shear adhesion force of all samples was recorded with DigiVision (Burster). Initial zero (or near-zero) values of ice adhesion strength correspond to situations where the pushing rod is not yet in contact with the Teflon-containing ice cylinder. For each coating, 3-5 surfaces were tested, and the average ice adhesion strength and standard deviation was reported.

Figure S13 displays representative pressure (force/area) vs. time profiles at all examined temperatures for the case of a medium crosslinked cationic coating with Cl⁻ as counterions. At higher temperatures, ice adhesion strengths were low, and either adhesive failure (a sudden decrease in adhesion strength after peak adhesion) or a slight sliding behaviour (a more gradual decrease in adhesion strength after peak adhesion) was observed. The latter behaviour has previously been reported in literature, however, on these surfaces it was not investigated further due to the inconsistent nature of its existence and appearance. Yet, at colder temperatures, greater ice adhesion strengths were observed alongside a steady adhesive failure mechanism.

To preliminarily ensure that the samples produced were robust, the ice adhesion of a single medium crosslink density coating with chloride counterions was repeatedly measured (20 measurements) at -20 °C. As exhibited in Figure S14, the ice adhesion strength does not vary or drift significantly over 20 icing/de-icing cycles and demonstrates that the coating design is sufficiently stable.

Although ice adhesion on surfaces has been covered in detail, reported values of ice adhesion strength of various surfaces can still vary significantly – mainly due to the differences between apparatuses.[2,3] Therefore, to bring better correspond, ice adhesion on cleaned silicon wafers was measured as function of temperature (Figure S15). Overall, the reported ice adhesion strengths on silicon by our home-built shear adhesion apparatus are similar to those produced by other groups [4,5]
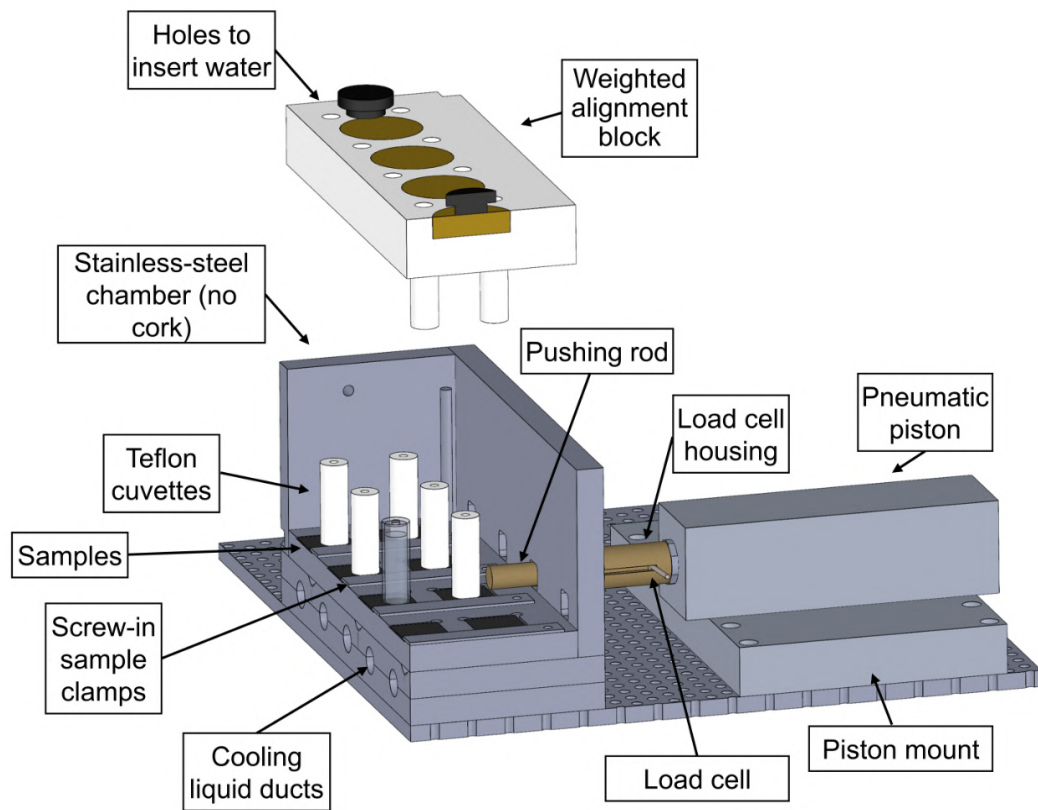
Figure S5: Cut-away diagram of shear ice adhesion apparatus. Cork insulation lining the stainless-steel chamber is not shown.
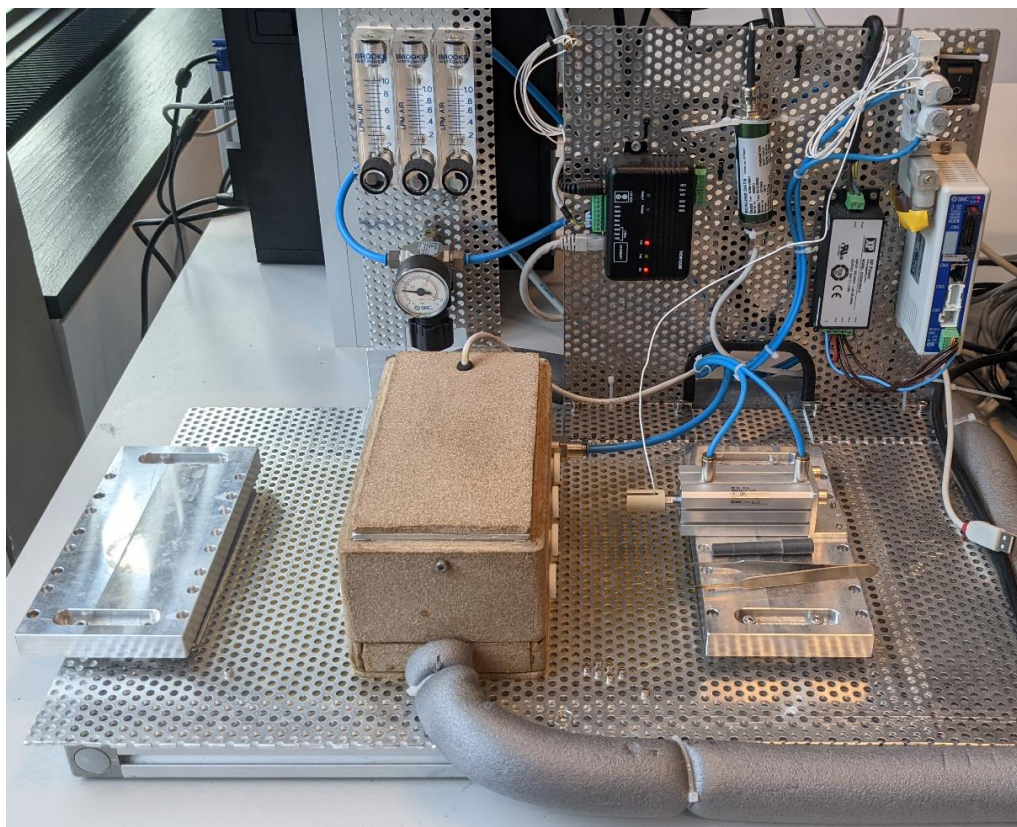
Figure S6: Home-built shear ice adhesion apparatus.
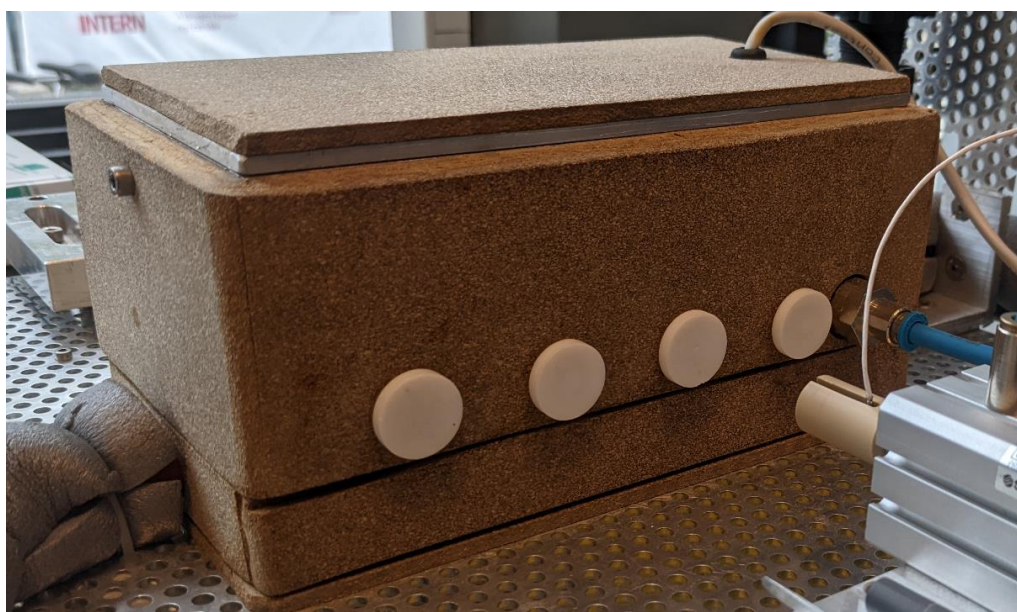
Figure S7: Exterior of cork-insulated stainless-steel chamber. White Teflon plugs seen are used to insulate the chamber when measurements are not currently underway.
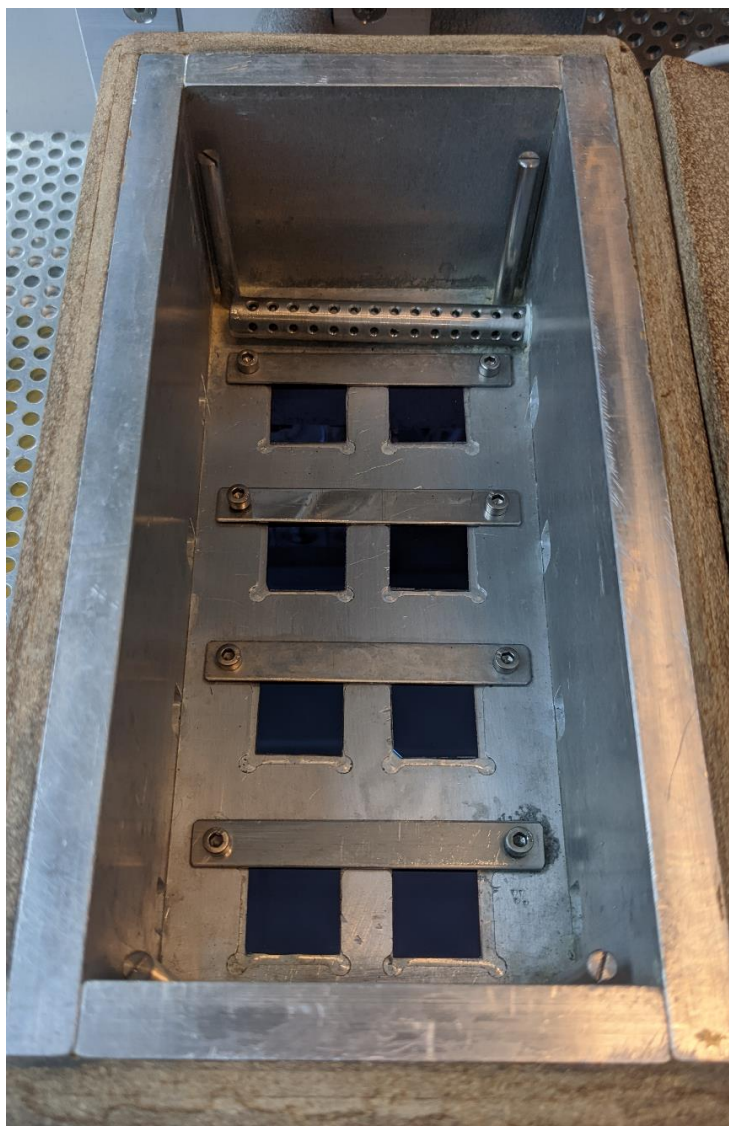
Figure S8: Coatings (on silicon wafers) placed in chamber. Insets are bore into the chamber (0.5 mm deep) and the coatings are placed in them and clamps are tightened to prevent the movement of the coatings.
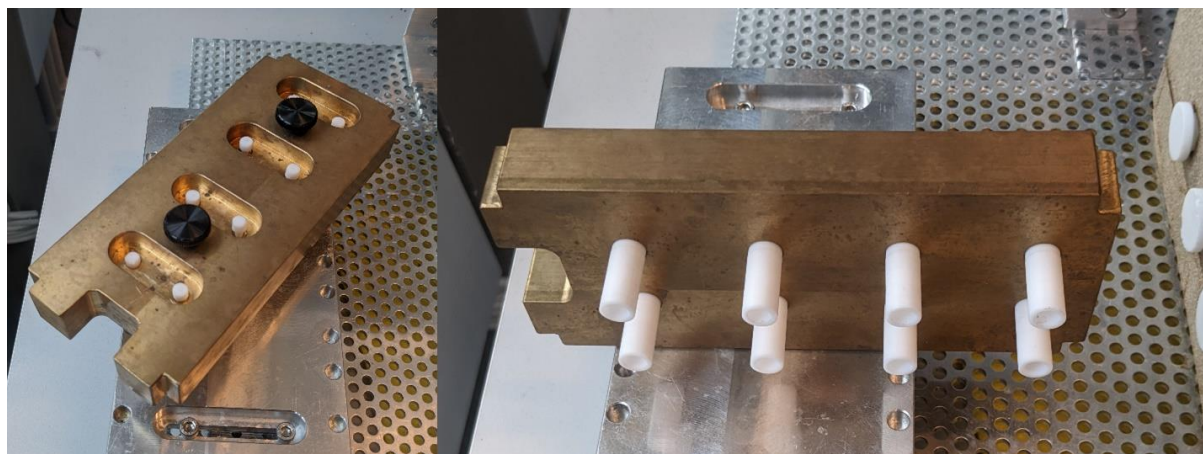
Figure S9: (left) Top view of weighted cuvette alignment-piece/holder. Teflon inserts are placed into the holes to secure the cuvettes during their alignment and placement onto the sample. (right) bottom/side view of alignment piece/holder.
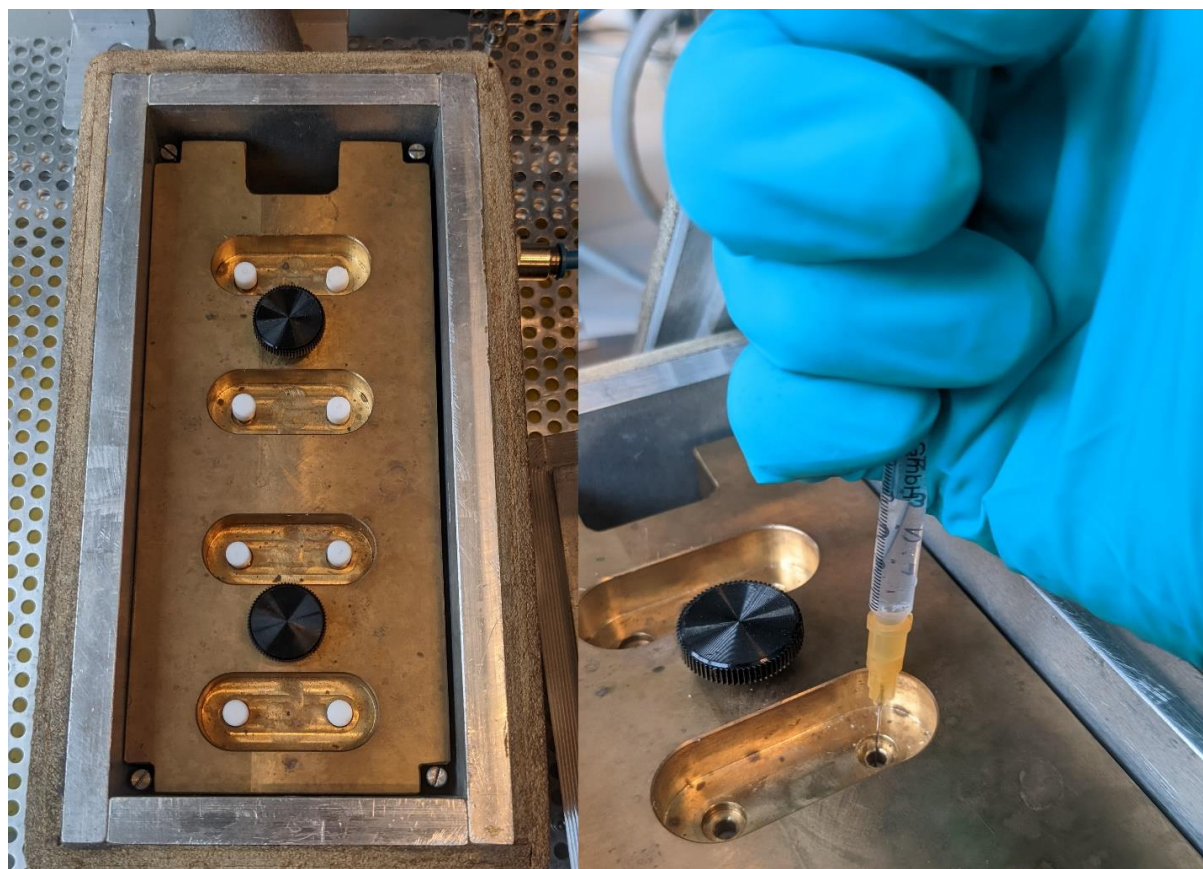
Figure S10: (left) Weighted cuvette alignment-piece/holder in chamber. (right) Loading of degassed ultrapure water into cuvettes.

Figure S11: Frozen ice cylinders (in cuvettes) on coatings.
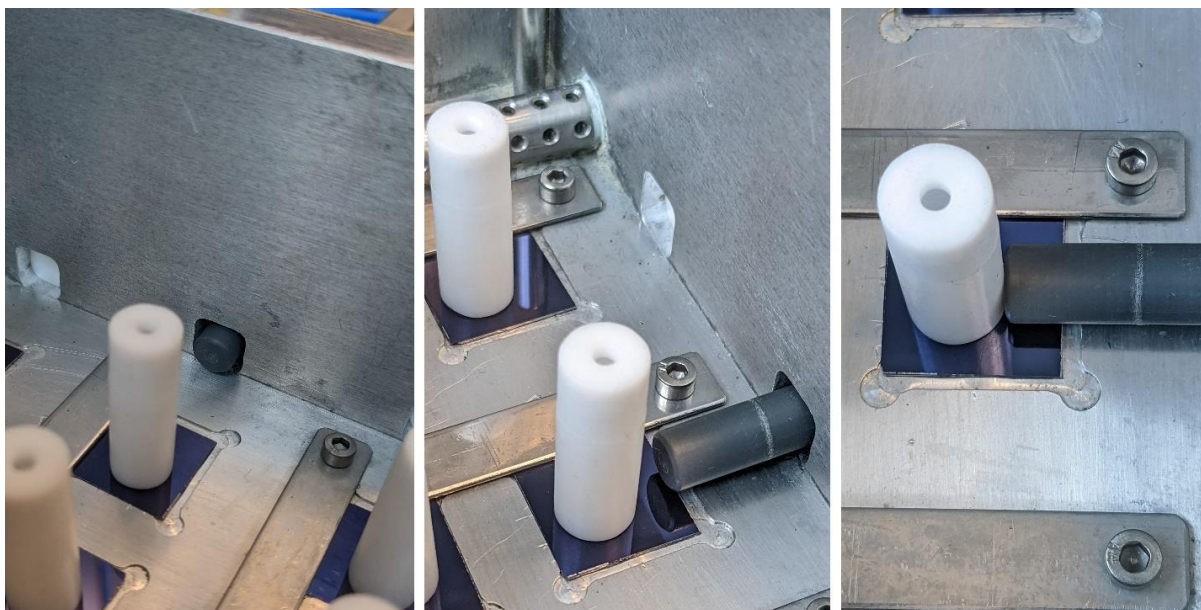
Figure S12: (left) Approach of pushing rod towards ice cylinder through a hole in the side of the chamber. Note that the adjacent hole is still plugged. (middle) Approach of pushing rod towards coating. Note the small gap between pushing rod and coating, set as such to minimize any torque. (right) Applying of force by the pushing rod onto the ice cylinder.
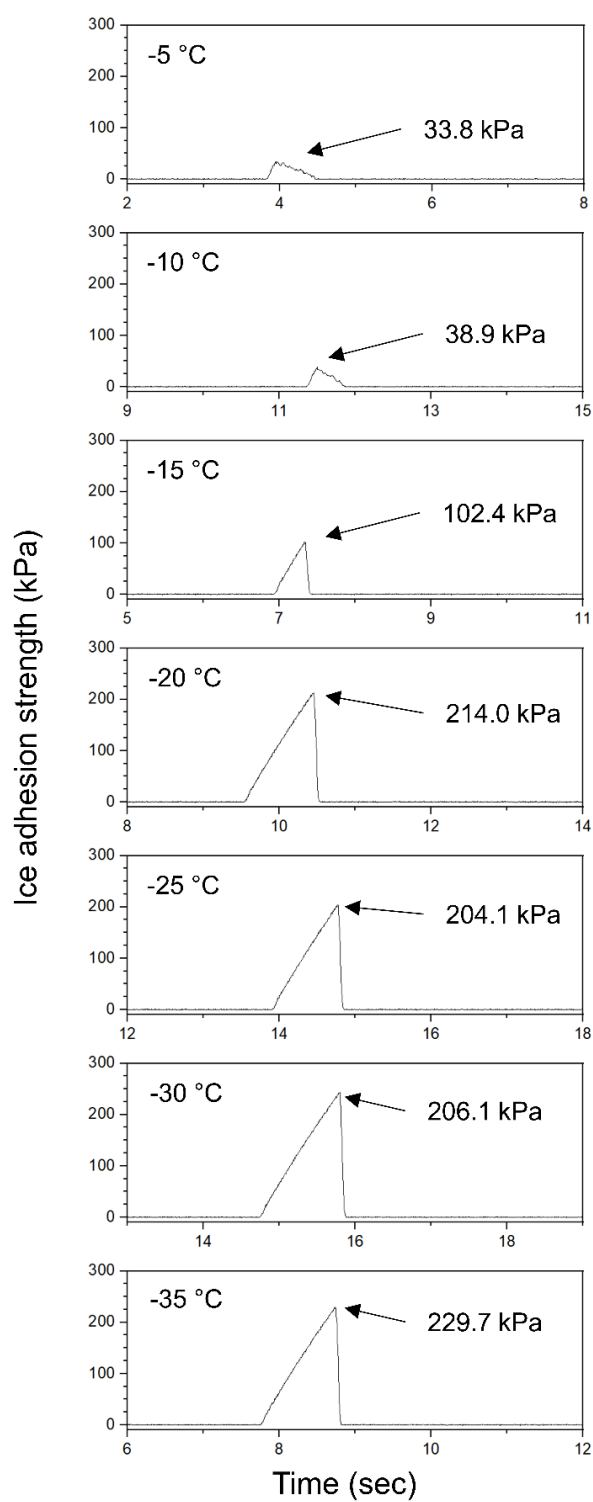
Figure S13: Representative profiles of ice adhesion strength vs. time on medium crosslink density cationic coatings with chloride counterions.
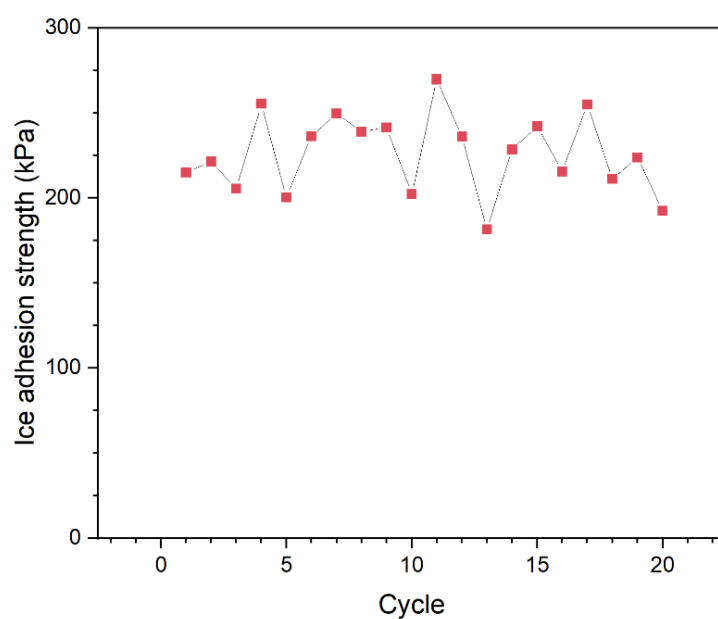
Figure S14: Ice adhesion strength on cationic coating (Cl⁻ counterion, medium crosslink density) over 20 cycles of icing/de-icing.
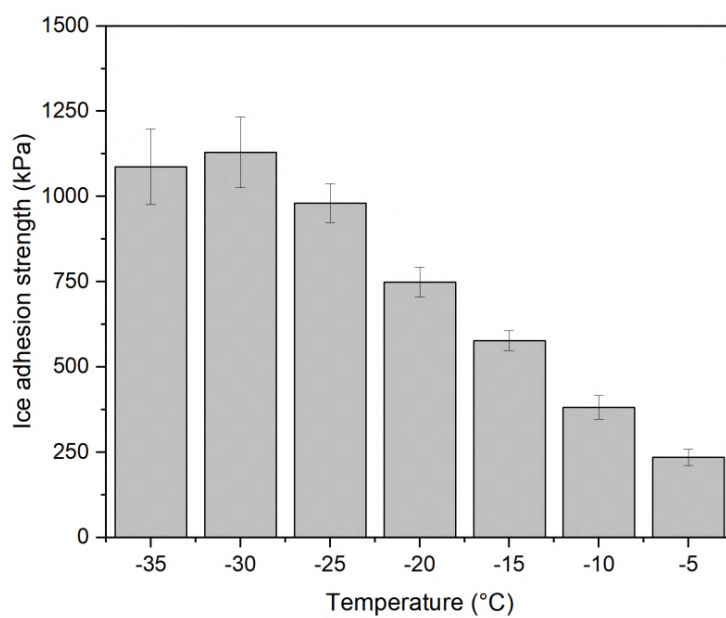
Figure S15: Temperature dependent ice adhesion strength on bare silicon surfaces.

S3: TIR Raman spectroscopy setup

The home-built sample holder was used for *in-situ* freezing experiments and is described as such here (Figure S16 and Figure S18). A stainless-steel body circulated cooling fluid at a desired temperature, set by Julabo FP50-ME and monitored by an embedded thermocouple placed in close proximity to silica-ice interface. The sample was fit by placing the coated silica hemisphere (radius = 5 mm) on top of a Viton O-ring and sealed using two homemade clamps made of high thermal conductivity polymer (CoolPoly-E5101, Cool Polymers/Celeanese, RI, USA) that were screwed into the stainless-steel cell body. A very weak laminar flow of dry cold air was established with two plastic tubes placed near the sample in order to purge any condensation on the hemisphere during freezing experiments that would impair the path of the excitation source or Raman scattered light. Degassed ultrapure water was carefully introduced into the sample fluid cell, filling the chamber in its entirety. Yet, as the expansion of ice would break the cell if in a completely, it was necessary to carefully introduce an air-bubble into the sample fluid chamber (Figure S17 depicts the aforementioned air bubble). In order to be analogous to the ice adhesion measurements and ensure that bulk ice is frozen onto the coating, the entire freezing process was conducted upside-down ensuring the air bubble would not be at the sample interface. Then, identically to ice adhesion measurements, the sample was frozen at -20 °C for a minimum of 1 h, before being orientated correctly and placed in the Raman spectroscopy setup. The temperature was subsequently lowered to -35 °C (temperature of the thermocouple at the silica-ice interface) and incrementally increased through to -0.7 °C. The sample was allowed to equilibrate for at least 15 min before spectra were collected at each temperature.

The design of the ice cell was such that counterion exchange could easily be accomplished without removing the hemisphere. Similar to the silicon-wafer based coatings, a 100 mM salt solution with the desired counterion was prepared after which the sample fluid chamber was filled with said solution and left undisturbed for 20 min. The solution was then drained, and more fresh salt solution was introduced and left to rest for another 20 min. After the second washing with the chosen salt solution, the chamber was drained and a minimum of 100 mL of degassed ultrapure water was used to wash the chamber of the cell before freezing measurements.
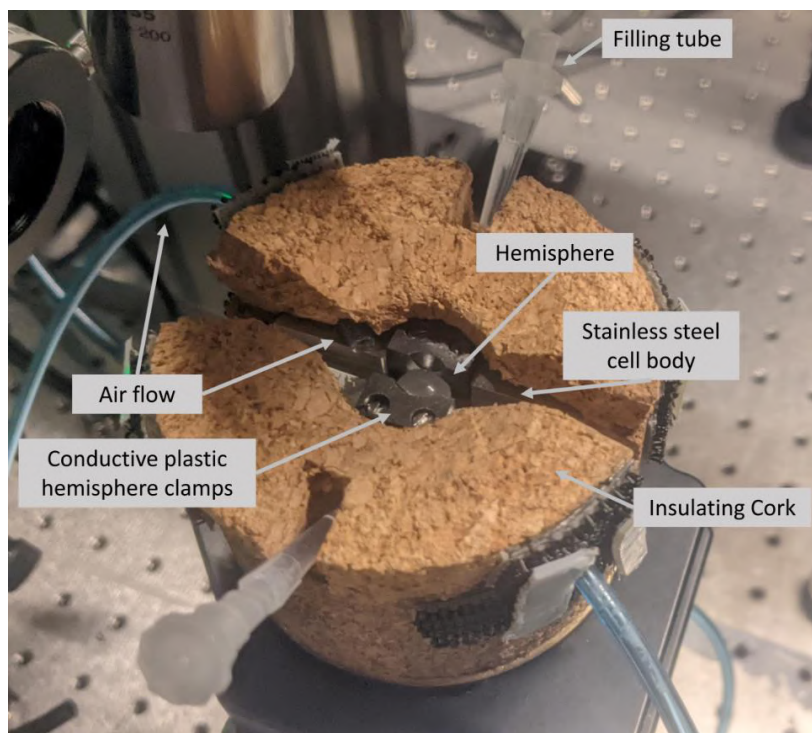
Figure S16: Picture of ice cell used for in-situ freezing experiments. Optics have been moved to provide a clearer image.

Figure S17: Picture of air-bubble introduced to sample fluid chamber before the freezing process.
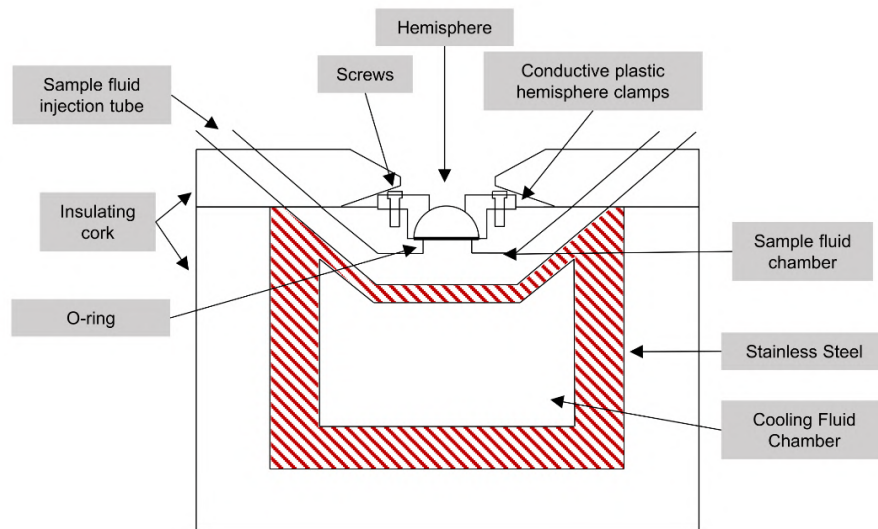
Figure S18: Schematic of the centerline of ice cell used in *in-situ* freezing experiments. Shaded areas represent the stainless-steel volume of the cell.

S4: Peak assignment of TIR Raman Spectra

Desired TIR Raman spectra were gathered using 24 sets of 5 sec. collection time spectra, giving a total collection time of 120 sec. Analysis of the sample spectra was completed by subtracting the background of the silica hemisphere (spectra taken beforehand), followed by a baseline subtraction of the remaining data, and normalization to a peak describing the C-H stretch of polymer coating at 2933 cm^{-1}. Normalization to the C-H deformation peak at 1450 cm^{-1} was done in only one instance where large contributions from bulk ice contributed to the 2933 cm^{-1} peak. Presented spectra were then smoothed over a running average of 5 data points.

To compare the spectra of coatings with different counterions, it was necessary to first gather spectra where the coatings and water would be in a similar environment, and then process all the spectra as ascribed above, resulting in Figure S19, a compilation of spectra with the different counterions taken at -20 °C at an AOI of 77°. Peak assignments corresponding the various stretches, deformations, rockings, or waggings are listed in Table S2, with many peaks corresponding to the polymer coating.
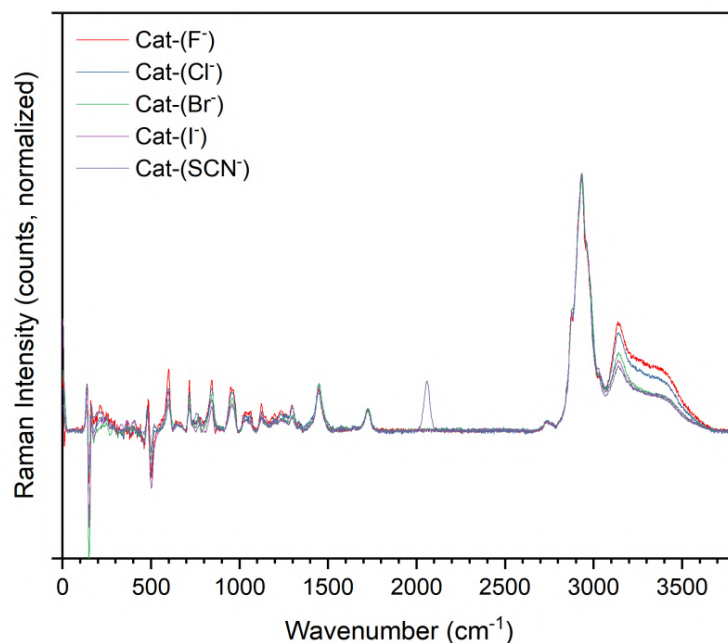
Figure S19: Sy polarized Raman spectra of Cat-(X-) with varying counterions. All spectra, taken at -20 °C at an AOI of 77°, are background and baseline subtracted.

Wavenumber (cm^{-1})	Peak Assignment
3250 – 3400	O – H asymmetric stretch of H_2O corresponding to water
3140 – 3150	O – H stretch corresponding of H_2O corresponding to ice
3030 – 3040	C – H asymmetric stretch of tetraalkylammonium salt
2955 – 2965	C – H asymmetric stretch of C-CH_3
2933	C – H asymmetric stretch of R – CH_2 – R
2870 – 2880	C – H symmetric stretch of C – CH_3
2058	C $\equiv$ N out-out-phase stretch of thiocyanate counterion
1725	C = O stretch of ester
1410 – 1490	C – H deformation of CH_2 and CH_3
1200 – 1300	C – S wag of crosslink node
1122	C – O asymmetric stretch of ester
955	C – H wag of *trans*-CH allyl protons
770	C – H rocking of CH_2
600	C = O wagging of ester

Table S2: Detailed peak assignments observed in Raman spectra.

S5: Detailed analysis of TIR Raman spectra
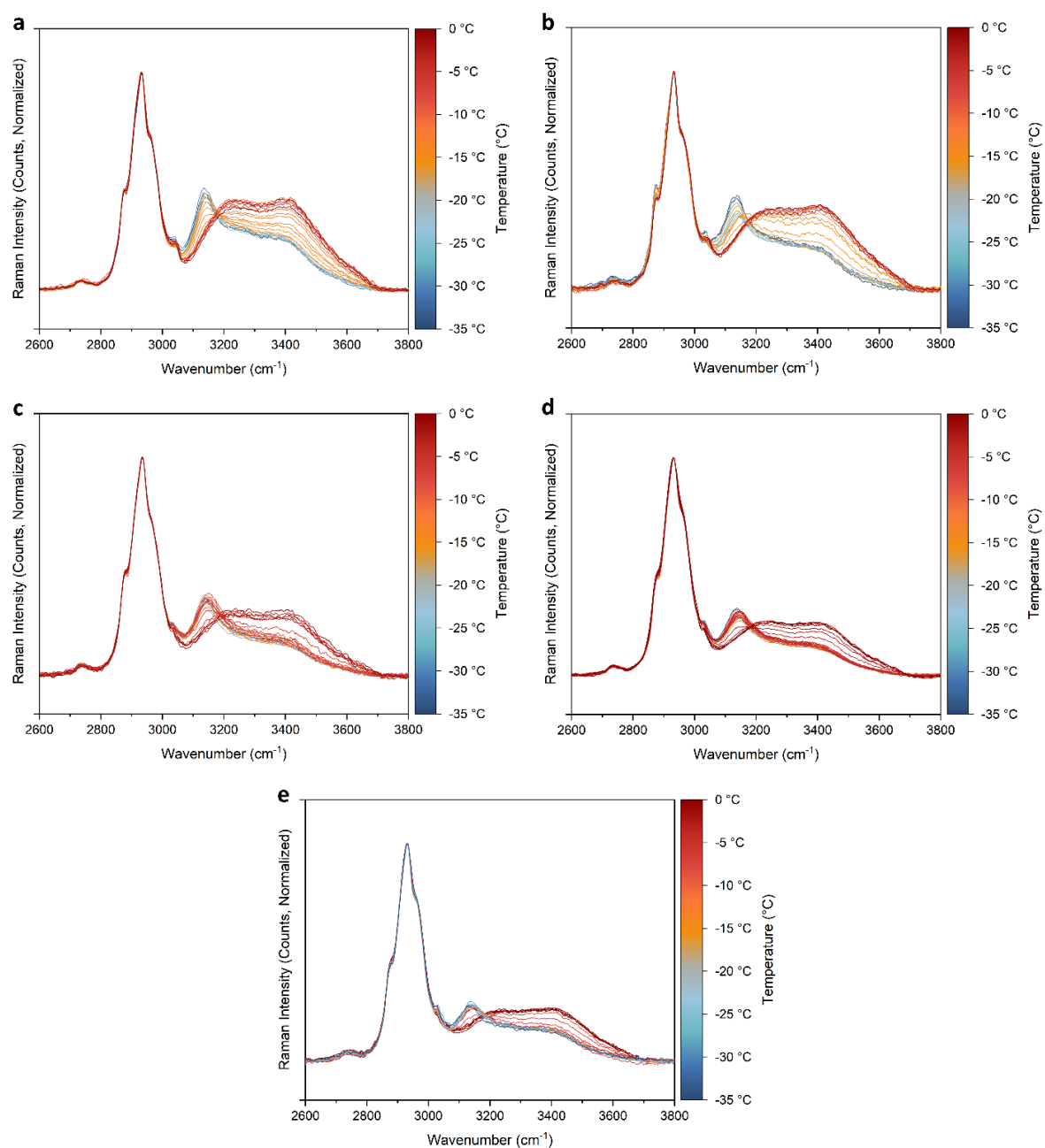
Figure S20: Temperature dependent Raman spectra of cationic polymer coatings with (a) F-, (b) Cl-, (c) Br-, (d) I-, (e) SCN-, counterions displaying the sub-zero phase transition of hydration water.

The observed phase transitions in Figure S20 were modelled by a three-component linear combination, seen in Eq. S1 below, consisting of a polymer component, a frozen-ice component, and a liquid-water component, where S, denotes the model spectrum, Ref_A, Ref_B, and Ref_C are given reference spectra, and X, Y, and Z are coefficients. The reference spectrum of the polymer component was produced by taking a spectrum of Cat-M-(Cl⁻) at 20 °C, and then creating a baseline over any remaining signal over 3080 cm⁻¹, that would pertain to signal from H_2O, resulting in Figure S21a. Suitable references of the frozen-ice and liquid-water components were produced using the spectra collected at -35 °C and -0.7 °C respectively. To produce a reference spectrum representing ice, the aforementioned polymer component, and its reference spectrum (Ref A) was scaled with regards to polymer peak height and subtracted from the spectrum collected at -35 °C, giving Figure S21b. A corresponding reference spectrum for liquid-water in the coating can be visualized in Figure S21c.

As evident by Figure S22, which displays the collected spectra of chloride containing polymer coating at various temperatures alongside the described model outlined by Eq. S1, the linear combination of these three reference spectra can undoubtedly be used to describe any of the spectra collected over a wide-range of temperatures. Therefore, by gathering coefficients relating to the scaling of the aforementioned reference spectra, one can determine the phase fraction of the water at a particular temperature. By employing Eqs. S2 and S3, it is possible to calculate the frozen and liquid phase fractions for a sample as a function of temperature, independent of polymer contributions. Values for X, Y, and Z, as well the corresponding frozen and liquid phase fraction are listed in Table S3-Table S7, and the frozen phase fraction (f) is plotted in Figure 3.

Eq. S1
$$S = (X \cdot Ref_A) + (Y \cdot Ref_B) + (Z \cdot Ref_C)$$

Eq. S2
$$Frozen\ phase\ fraction = \frac{\frac{Y}{X}}{\frac{Y}{X} + \frac{Z}{X}}$$

Eq. S3
$$Liquid\ phase\ fraction = \frac{\frac{Z}{X}}{\frac{Y}{X} + \frac{Z}{X}}$$
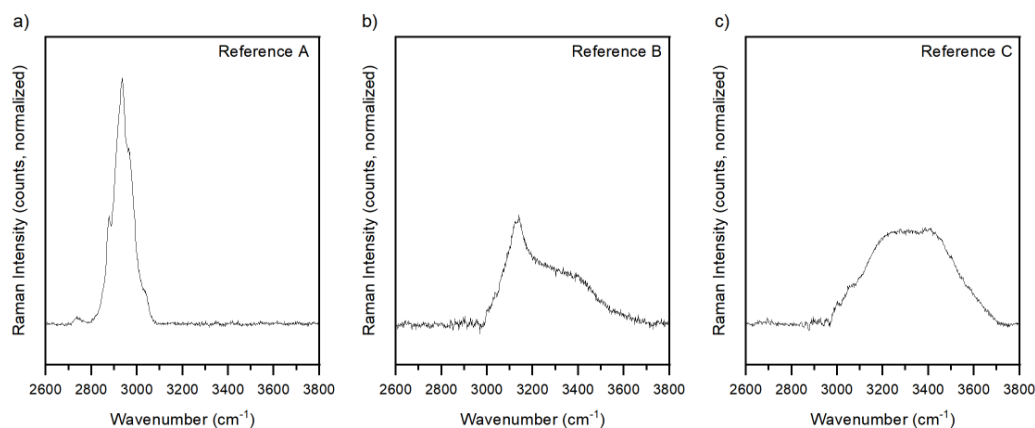
Figure S21:(a) Spectrum of reference A, representing the polymer coating, (b)spectrum of reference B, representing frozen-ice, and (c) spectrum of reference C, representing liquid-water.
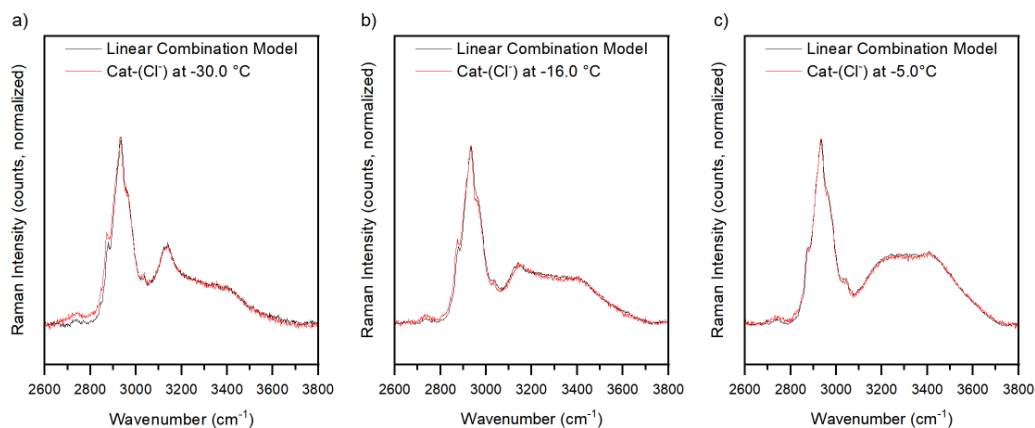
Figure S22: Comparison of linear combination model and collected spectra chloride containing coating at (a) -30.0 °C, (b) -16.0 °C, and (c) -5.0 °C.

Temperature (°C)	*X*	Y	Z	Frozen phase fraction (f)	Liquid phase fraction (l)
-35	1.01875	1.01465	0.02362	0.97725	0.02275
-30	1.0139	1.1078	-0.02166	1.01994	-0.01994
-27.5	1.0115	0.96434	0.05277	0.94812	0.05188
-25	1.01261	0.99397	0.06137	0.94185	0.05815
-22.5	1.0115	0.89784	0.07334	0.92448	0.07552
-20	1.02366	0.91454	0.10207	0.8996	0.1004
-17.5	1.01527	0.92426	0.13266	0.87448	0.12552
-15	1.01168	0.87794	0.14929	0.85467	0.14533
-14.5	1.03572	0.7493	0.27062	0.73466	0.26534
-14	1.03071	0.6117	0.38723	0.61236	0.38764
-13.5	1.03859	0.48632	0.48529	0.50053	0.49947
-13	1.02751	0.28555	0.65814	0.30259	0.69741
-12.5	1.03221	0.17736	0.75277	0.19068	0.80932
-12	1.02837	0.11871	0.83698	0.12421	0.87579
-11	1.03123	0.02404	1.00185	0.02344	0.97656
-10	1.02675	0.03381	0.96476	0.03386	0.96614
-7.5	1.03085	0.01959	0.93538	0.02051	0.97949
-5	1.00148	0.01005	0.95815	0.01039	0.98961
-2.5	1.03343	-0.00147	0.99408	-0.00149	1.00149
-0.7	1.01286	0.01619	0.90205	0.01763	0.98237

Table S3: Fitted coefficients representing contributions of polymer (X), ice (Y), and water (Z), used modelling the corresponding frozen and liquid phase fractions of the hydration water in coatings with F- counterions.

Temperature (°C)	X	Y	Z	Frozen phase fraction (f)	Liquid phase fraction (l)
-35	1.02767	1.08882	-0.04338	1.04149	-0.04149
-32.5	1.02343	0.99641	0.03856	0.96274	0.03726
-30	1.02929	1.01515	0.01121	0.98908	0.01092
-27.5	1.00883	0.79537	0.06661	0.92272	0.07728
-25	1.00278	0.9429	0.12667	0.88157	0.11843
-22.5	1.01341	0.983	0.08667	0.91897	0.08103
-20	1.03468	0.90665	0.06099	0.93697	0.06303
-17	1.01853	0.95498	0.02192	0.97756	0.02244
-16.5	1.01702	0.75817	0.19976	0.79147	0.20853
-16	1.00563	0.5521	0.38564	0.58876	0.41124
-15.5	1.00182	0.39108	0.60309	0.39337	0.60663
-15	1.00084	0.37543	0.65954	0.36274	0.63726
-14	1.00084	0.19688	1.0325	0.16015	0.83985
-13	1.00039	-0.03698	0.95864	-0.04012	1.04012
-10	0.9845	-0.03534	0.9994	-0.03666	1.03666
-7.5	0.98445	-0.03816	0.97506	-0.04073	1.04073
-5	0.98505	-0.04057	0.99983	-0.04229	1.04229
-2.5	0.98712	0.00128	0.91954	0.00139	0.99861
-0.7	0.99511	-0.03151	1.00343	-0.03242	1.03242

Table S4: Fitted coefficients representing contributions of polymer (X), ice (Y), and water (Z), used modelling the corresponding frozen and liquid phase fractions of the hydration water in coatings with Cl- counterions.

Temperature (°C)	X	Y	Z	Frozen phase fraction (f)	Liquid phase fraction (l)
-35	1.03747	1.01078	0.05412	0.94918	0.05082
-30	1.03217	1.0131	0.04396	0.95841	0.04159
-25	1.03361	0.97292	0.04761	0.95335	0.04665
-20	1.03994	0.86417	0.07961	0.91565	0.08435
-17.5	1.04364	1.04086	0.08355	0.92569	0.07431
-15	1.02608	0.92835	0.07812	0.92238	0.07762
-12.5	1.02611	0.88481	0.08345	0.91381	0.08619
-10	1.0255	0.97846	0.10776	0.90079	0.09921
-9	1.01626	0.99349	0.07194	0.93248	0.06752
-8	1.02635	0.9649	0.10392	0.90277	0.09723
-7.5	1.02747	0.96761	0.07978	0.92383	0.07617
-7	1.03025	0.97187	0.10345	0.9038	0.0962
-6.5	1.03115	0.87738	0.2086	0.80792	0.19208
-6	1.04087	0.57915	0.46085	0.55688	0.44313
-5.5	1.02728	0.21926	0.77448	0.22064	0.77936
-5	1.02811	0.11014	0.8286	0.11733	0.88267
-4.5	1.0248	0.05865	0.91911	0.05998	0.94002
-4	1.0322	0.02169	0.89213	0.02374	0.97626
-2.5	1.0345	0.01473	0.92086	0.01574	0.98426
-0.7	1.02256	-0.02505	0.9993	-0.02571	1.02571

Table S5: Fitted coefficients representing contributions of polymer (X), ice (Y), and water (Z), used modelling the corresponding frozen and liquid phase fractions of the hydration water in coatings with Br$^-$ counterions.

Temperature (°C)	X	Y	Z	Frozen phase fraction (f)	Liquid phase fraction (l)
-35	1.045	1.01203	0.02886	0.97227	0.02773
-30	1.05361	0.92446	0.0436	0.95496	0.04504
-25	1.04476	0.86884	0.05761	0.93782	0.06218
-20	1.03281	0.91412	0.03906	0.95902	0.04098
-15	1.03723	0.82002	0.07031	0.92103	0.07897
-12.5	1.04906	0.85981	0.08807	0.90709	0.09291
-10	1.0495	0.90736	0.06724	0.93101	0.06899
-9	1.05342	0.96104	0.06094	0.94037	0.05963
-8	1.05425	0.91841	0.09022	0.91055	0.08945
-7	1.04059	0.86224	0.06538	0.92952	0.07048
-6.5	1.03867	0.88094	0.08321	0.9137	0.0863
-6	1.05778	0.93677	0.0395	0.95954	0.04046
-5.5	1.06248	0.94072	0.06494	0.93543	0.06457
-5	1.06175	0.97796	0.06165	0.9407	0.0593
-4.5	1.05622	0.97084	0.03126	0.96881	0.03119
-4	1.05669	0.90538	0.12229	0.881	0.119
-3.5	1.04898	0.71347	0.31842	0.69142	0.30858
-3	1.03629	0.4174	0.5872	0.41549	0.58451
-2.5	1.06201	0.26128	0.74795	0.25889	0.74111
-2	1.04056	0.10108	0.91612	0.09937	0.90063
-1.5	1.05644	0.10891	0.9311	0.10472	0.89528
-1	1.04893	0.10513	0.90362	0.10422	0.89578
-0.7	1.05659	0.08133	0.96292	0.07788	0.92212

Table S6: Fitted coefficients representing contributions of polymer (X), ice (Y), and water (Z), used modelling the corresponding frozen and liquid phase fractions of the hydration water in coatings with I⁻ counterions.

Temperature (°C)	X	Y	Z	Frozen phase fraction (f)	Liquid phase fraction (l)
-35	1.03266	0.94604	0.06858	0.93241	0.06759
-30	1.04405	0.96324	0.08482	0.91907	0.08093
-27.5	1.04436	0.94254	0.1195	0.88748	0.11252
-25	1.03241	0.91687	0.11582	0.88785	0.11215
-22.5	1.03494	0.90315	0.13885	0.86674	0.13326
-20	1.02787	0.8732	0.12864	0.8716	0.1284
-17.5	1.03537	0.87804	0.14846	0.85537	0.14463
-15	1.03873	0.84681	0.17673	0.82733	0.17267
-12.5	1.04446	0.87866	0.16462	0.84221	0.15779
-10	1.04692	0.80884	0.23142	0.77754	0.22246
-8	1.05731	0.83988	0.21249	0.79808	0.20192
-7	1.04633	0.91242	0.10608	0.89585	0.10415
-6.5	1.04223	0.72234	0.3358	0.68265	0.31735
-6	1.03835	0.45937	0.58107	0.44152	0.55848
-5.5	1.04026	0.25884	0.78731	0.24742	0.75258
-5	1.04873	0.18982	0.89697	0.17466	0.82534
-4	1.04774	0.19202	0.89173	0.17718	0.82282
-3	1.05039	0.1306	0.95255	0.12057	0.87943
-2	1.05236	0.10562	0.96979	0.09821	0.90179
-0.7	1.04073	0.07875	0.95185	0.07641	0.92359

Table S7: Fitted coefficients representing contributions of polymer (X), ice (Y), and water (Z), used modelling the corresponding frozen and liquid phase fractions of the hydration water in coatings with SCN⁻ counterions.

S6: Ellipsometry data, modelling, and results

Coating thickness in both dry and hydrated states was determined using a spectroscopic ellipsometer (M-2000, J.A. Woollam Co., USA). The instrument has a cell to measure the thickness of polymer films under dry/ambient conditions. A dry-stream of nitrogen was flowed over the samples in order to minimize any effects of ambient humidity hydrating the polymer film. A 5 mL liquid cell was used to measure the thickness of the coating under hydrated conditions at 25 °C. In each case, three coatings were measured under both dry and hydrated conditions. The plotted values in the article represent the average of those measurements, and error bars the standard deviation.

Measurements of dry polymer coatings were analyzed using the instrument's software, CompleteEase. A slab model was used to describe the sample, where Si is the substrate, a 1 nm intermediate Si-SiO$_2$ layer, a 100 nm SiO$_2$ layer, and a uniform polymer film without light absorption (k = 0). The polymer film was described with a Cauchy model with the form $n(\lambda) = A + B/\lambda^2$, in which A and B are fitting parameters for the film thickness. Similarly, hydrated measurements were analyzed with slab model consisting of an identical Si substrate, a 1 nm intermediate Si-SiO$_2$ layer, a 100 nm SiO$_2$ layer, and two-component layer consisting of the dry polymer consisting of the dry polymer (A and B parameters given by dry measurements) and water. Fitting according to the Bruggeman Effective Medium Approximation (BEMA) model provided the hydrated film thicknesses, and the volume fractions of water in the coatings.

Thickness, mean square error, and optical constants of the dry films are listed below in Table S8, along with fittings of the model, and variable angle Ψ and $\boldsymbol{\Delta}$ data. Analogously, Table S9 lists the hydrated film thickness, mean square error, and volume % of H$_2$O in the film, as well as fittings of the optical model described, and Ψ and $\boldsymbol{\Delta}$ data taken at an angle of incidence (AOI) of 75°.

Coating	Fit Results	Optical Model	Ψ (Psi) Data & Model	Δ (Delta) Data & Model
F⁻	MSE = 17.954 Thickness # 3 = 112.46 ± 0.067 nm A = 1.486 ± 0.00031494 B = 0.00575 ± 4.9702E-05	- Layer # 3 = Cauchy Thickness # 3 = 112.46 nm (fit) A = 1.486 (fit) B = 0.00575 (fit) C = 0.0000 + Urbach Absorption Parameters Layer # 2 = SIO2_JAW Thickness # 2 = 100.00 nm Layer # 1 = INTR_JAW Thickness # 1 = 1.00 nm Substrate = SI_JAW		
Cl⁻	MSE = 17.978 Thickness # 3 = 111.33 ± 0.067 nm A = 1.491 ± 0.00031815 B = 0.00583 ± 5.0306E-05	- Layer # 3 = Cauchy Thickness # 3 = 111.33 nm (fit) A = 1.491 (fit) B = 0.00583 (fit) C = 0.0000 - Urbach Absorption Parameters k Amplitude = 0.0000 Exponent = 1.500 Band Edge = 400.0 nm Layer # 2 = SIO2_JAW Thickness # 2 = 100.00 nm Layer # 1 = INTR_JAW Thickness # 1 = 1.00 nm Substrate = SI_JAW		
Br⁻	MSE = 21.493 Thickness # 3 = 109.87 ± 0.080 nm A = 1.498 ± 0.00038455 B = 0.00592 ± 6.0953E-05	- Layer # 3 = Cauchy Thickness # 3 = 109.87 nm (fit) A = 1.498 (fit) B = 0.00592 (fit) C = 0.0000 + Urbach Absorption Parameters Layer # 2 = SIO2_JAW Thickness # 2 = 100.00 nm Layer # 1 = INTR_JAW Thickness # 1 = 1.00 nm Substrate = SI_JAW		
I⁻	MSE = 16.975 Thickness # 3 = 107.37 ± 0.062 nm A = 1.508 ± 0.00031006 B = 0.00743 ± 5.1125E-05	- Layer # 3 = Cauchy Thickness # 3 = 107.37 nm (fit) A = 1.508 (fit) B = 0.00743 (fit) C = 0.0000 + Urbach Absorption Parameters Layer # 2 = SIO2_JAW Thickness # 2 = 100.00 nm Layer # 1 = INTR_JAW Thickness # 1 = 1.00 nm Substrate = SI_JAW		
SCN⁻	MSE = 31.418 Thickness # 3 = 109.46 ± 0.173 nm A = 1.521 ± 0.001056 B = 0.00376 ± 0.00016795	- Layer # 3 = Cauchy Thickness # 3 = 109.46 nm (fit) A = 1.521 (fit) B = 0.00376 (fit) C = 0.0000 - Urbach Absorption Parameters k Amplitude = 0.0000 Exponent = 1.500 Band Edge = 400.0 nm Layer # 2 = SIO2_JAW Thickness # 2 = 100.00 nm Layer # 1 = INTR_JAW Thickness # 1 = 1.00 nm Substrate = SI_JAW		

Table S8: Dry ellipsometry results, fittings, and measurements of medium crosslink density cationic polymer coatings with varying counterions.

Coating	Fit Results	Optical Model	Ψ (Psi) and Δ (Delta) Data & Model
F⁻	MSE = 40.079 Thickness # 3 = 214.56 ± 0.518 nm EMA % (Mat 2) = 47.6 ± 0.21	- Layer # 3 = EMA Thickness # 3 = **214.56 nm** (fit) # of Constituents = 2 - Material 1 = Cauchy A = 1.488 B = 0.00575 C = 0.0000 - Urbach Absorption Parameters k Amplitude = 0.0000 Exponent = 1.500 Band Edge = 400.0 nm Material 2 = H2O EMA % (Mat 2) = **47.6** (fit) Depolarization = 0.333 Analysis Mode = Bruggeman Layer # 2 = SiO2_JAW Thickness # 2 = 100.00 nm Layer # 1 = INTR_JAW Thickness # 1 = 1.00 nm Substrate = SI_JAW	
Cl⁻	MSE = 35.143 Thickness # 3 = 196.05 ± 0.431 nm EMA % (Mat 2) = 43.2 ± 0.18	- Layer # 3 = EMA Thickness # 3 = **196.05 nm** (fit) # of Constituents = 2 - Material 1 = Cauchy A = 1.491 B = 0.00583 C = 0.0000 - Urbach Absorption Parameters k Amplitude = 0.0000 Exponent = 1.500 Band Edge = 400.0 nm Material 2 = H2O EMA % (Mat 2) = **43.2** (fit) Depolarization = 0.333 Analysis Mode = Bruggeman Layer # 2 = SiO2_JAW Thickness # 2 = 100.00 nm Layer # 1 = INTR_JAW Thickness # 1 = 1.00 nm Substrate = SI_JAW	
Br⁻	MSE = 31.837 Thickness # 3 = 181.61 ± 0.381 nm EMA % (Mat 2) = 39.5 ± 0.18	- Layer # 3 = EMA Thickness # 3 = **181.61 nm** (fit) # of Constituents = 2 - Material 1 = Cauchy A = 1.498 B = 0.00592 C = 0.0000 - Urbach Absorption Parameters k Amplitude = 0.0000 Exponent = 1.500 Band Edge = 400.0 nm Material 2 = H2O EMA % (Mat 2) = **39.5** (fit) Depolarization = 0.333 Analysis Mode = Bruggeman Layer # 2 = SiO2_JAW Thickness # 2 = 100.00 nm Layer # 1 = INTR_JAW Thickness # 1 = 1.00 nm Substrate = SI_JAW	
I⁻	MSE = 23.174 Thickness # 3 = 153.17 ± 0.267 nm EMA % (Mat 2) = 29.9 ± 0.15	- Layer # 3 = EMA Thickness # 3 = **153.17 nm** (fit) # of Constituents = 2 - Material 1 = Cauchy A = 1.508 B = 0.00743 C = 0.0000 - Urbach Absorption Parameters k Amplitude = 0.0000 Exponent = 1.500 Band Edge = 400.0 nm Material 2 = H2O EMA % (Mat 2) = **29.9** (fit) Depolarization = 0.333 Analysis Mode = Bruggeman Layer # 2 = SiO2_JAW Thickness # 2 = 100.00 nm Layer # 1 = INTR_JAW Thickness # 1 = 1.00 nm Substrate = SI_JAW	
SCN⁻	MSE = 34.828 Thickness # 3 = 148.17 ± 0.399 nm EMA % (Mat 2) = 26.4 ± 0.21	- Layer # 3 = EMA Thickness # 3 = **148.17 nm** (fit) # of Constituents = 2 - Material 1 = Cauchy A = 1.521 B = 0.00376 C = 0.0000 - Urbach Absorption Parameters k Amplitude = 0.0000 Exponent = 1.500 Band Edge = 400.0 nm Material 2 = H2O EMA % (Mat 2) = **26.4** (fit) Depolarization = 0.333 Analysis Mode = Bruggeman Layer # 2 = SiO2_JAW Thickness # 2 = 100.00 nm Layer # 1 = INTR_JAW Thickness # 1 = 1.00 nm Substrate = SI_JAW	

Table S9: Hydrated ellipsometry results, fittings, and measurements of medium crosslink density cationic polymer coatings with varying counterions.

S7: DSC data and analysis of polymer and water mixtures

In addition, the melting onset temperature, T_m was measured instead of the melting peak temperature, which is far more dependent on heating rate and sample mass. Onset temperature is defined here as the intersection point between a linearly extrapolated baseline, and a tangent line that intersects the melting peak at its steepest point.[6]

Mixtures of various amounts of bulk uncrosslinked polymer and water and the resulting melting endotherms observed by DSC (Figure S23) were analyzed to determine the amounts and fractions of freezable water and "non-freezable" water in the samples, shown in Table S11Table S15. The masses of freezable and "non-freezable" water from were determined using Equations S4 and S5 respectively. Corresponding mass fractions of "non-freezable" water were calculated with respect to either the total water in the sample or the mass dried polymer, by Equations S6 and S7. $m_{H_2O\,non-freezable}$ is believed to be constant value for a specific polymer, representing the "non-freezable" water fraction with respect to the mass of polymer, and thus was averaged for each system.

Eq. S4
$$m_{H_2O\,freezable} = \Delta H_f \Big/ 334\,mJ/mg$$

Eq. S5
$$m_{H_2O\,"non-freezable"} = m_{H_2O\,total} - m_{H_2O\,freezable}$$

Eq. S6
$$\frac{m_{H_2O\,"non\text{-}freezable"}}{mg\,H_2O} = \frac{m_{H_2O\,"non\text{-}freezable"}}{m_{H_2O}\,total}$$

Eq. S7
$$\frac{m_{H_2O\,"non\text{-}freezable"}}{mg\,polymer} = \frac{m_{H_2O\,"non-freezable"}}{m_{polymer}}$$

Table S16 describes the water in each polymer coating. Converting from w_{H_2O} using Eq. S8, the mass of water per mg polymer coating could be determined. A further breakdown of the mass of water in each polymer coating into "non-freezable" and freezable, was also possible using Eq. S9 and S10, respectively. Finally, Eq. S11is used to solve for the mass fraction of "non-freezable" water in the total hydration water, simplifying into Eq. S7. The calculated values are used in Figures 4d and 5c to quantify the counterion specific or crosslink density dependent fraction of "non-freezable" water in the hydrating the film.

Eq. S8
$$\frac{m_{H_2O}}{mg\ polymer\ coating} = \frac{w_{H_2O}}{1 - w_{H_2O}}$$

Eq. S9
$$\frac{m_{H_2O\ "non-freezable"}}{mg\ polymer\ coating} = \frac{m_{H_2O\ "non-freezable"}}{mg\ polymer} \cdot \frac{m_{H_2O}}{mg\ polymer\ coating}$$

Eq. S10
$$\frac{m_{H_2O\ freezable}}{mg\ polymer\ coating} = \frac{m_{H_2O}}{mg\ polymer\ coating} - \frac{m_{H_2O\ "non-freezable"}}{mg\ polymer\ coating}$$

Eq. S11
$$\left(\frac{m_{H_2O\ non-freezable}}{m_{H_2O\ in\ coating}}\right) = \frac{\left(\frac{m_{H_2O\ "non-freezable"}}{mg\ coating}\right)}{\left[\left(\frac{m_{H_2O\ "non-freezable"}}{mg\ coating}\right) + \left(\frac{m_{H_2O\ freezable}}{mg\ coating}\right)\right]} = \frac{m_{H_2O\ "non-freezable"}}{m_{H_2O\ total}}$$

The estimation of phase transition temperature was also accomplished using a combination of DSC and ellipsometry. Here, DSC measurements of each sample's onset melting temperature were plotted against the respective mass fraction of water. In order to ascertain the mass fraction of water in the polymer coating, ellipsometry measurements and polymer density information was necessary. Ellipsometry derived volume fractions of water in each coating, were transformed to a mass fraction, necessitating the density of the dry polymer. The approximate density of the dry polymer was measured roughly to be 1.071 g/mL using the method described hereafter. 1.927 g of dry polymer was added to 25 mL of hexanes sealed and left to equilibrate. After 1 week, the volume and mass were recorded to be 26.8 mL and 18.21 g, respectively. The volume of the polymer (~1.8 mL) was found by subtracting volume of hexanes from the total polymer. Dividing the dry polymer mass over the volume of the polymer gives the density of the polymer. The density of the polymer was assumed to be nearly constant regardless of nature of the counterion or crosslink density.

The mass fraction of water in the coating was determine and could be the converted to molality using Eq. S13 and S14. The melting phase transition temperatures of samples were then plotted against the polymer concentration (in terms of molality), resulting in Figure 4c. Linear trend-lines were fitted to this data, from which approximate the phase transition temperature of the hydration water in a polymer coating. To this end, the polymer molality in a hydrated coating was determined using Eq. S15, and the resulting estimates are listed in Table S10. The phase transition of water in the coatings can be accurately estimated for all samples and aligns to ±1.5 °C

of the TIR Raman measurements. This coordination between the transition obtained by the combination of DSC and ellipsometry measurements and by TIR Raman, respectively, with the ice adhesion behaviour is rather remarkable (Figure 3).

Counterion	Polymer concentration in coating (molality)	Estimate of phase transition temperature of coating hydration water (°C)
F⁻	0.0421	-11.9
Cl⁻	0.0519	-14
Br⁻	0.0577	-6.1
I⁻	0.1029	-3.7
SCN⁻	0.0872	-6.0

Table S10: Estimations of phase transition temperature in hydration water of coatings with different counterions

Eq. S12
$$w_{H_2O} = \frac{\left(\varphi_{H_2O} \cdot \rho_{H_2O}\right)}{\left(\left(\varphi_{H_2O} \cdot \rho_{H_2O}\right) + \left(1 - \varphi_{H_2O}\right) \cdot \rho_{polymer}\right)}$$

ρ_{H_2O} is 0.997 g/mL, and $\rho_{polymer}$ is 1.071 g/mL

$$Molar\ mass\ Polymer\ (M_{polymer}) = \sum_{i=1}^{N} M_i \cdot D_p \cdot x_i$$

Eq. S13
Here, M_i for each monomer is 172.25 g/mol (METAC), 142.20 g/mol (*n*-BMA), and 126.15 g/mol (AMA). D_p , the degree of polymerization, is 200, the targeted value. For "medium" crosslink density polymer, the targeted mole fractions are: x_{METAC} = 0.25, x_{BMA}= 0.65, x_{AMA} = 0.10. Polymer molecular weight was calculated as ~29.6 kg/mol.

Eq. S14
$$Polymer\ molality = \frac{m_{polymer}}{M_{polymer}} \Big/ m_{H_2O\ total}$$

$m_{polymer}$ is in units of grams, $M_{polymer}$ is in g/mol, and $m_{H_2O\ total}$ is in kg/mol.

Eq. S15
$$Polymer\ molality_{coating} = \frac{\left(\frac{\left(1 - w_{H_2O}\right)}{1000}\right) \Big/ M_{polymer}}{\left(\frac{w_{H_2O}}{1 \cdot 10^6}\right)}$$
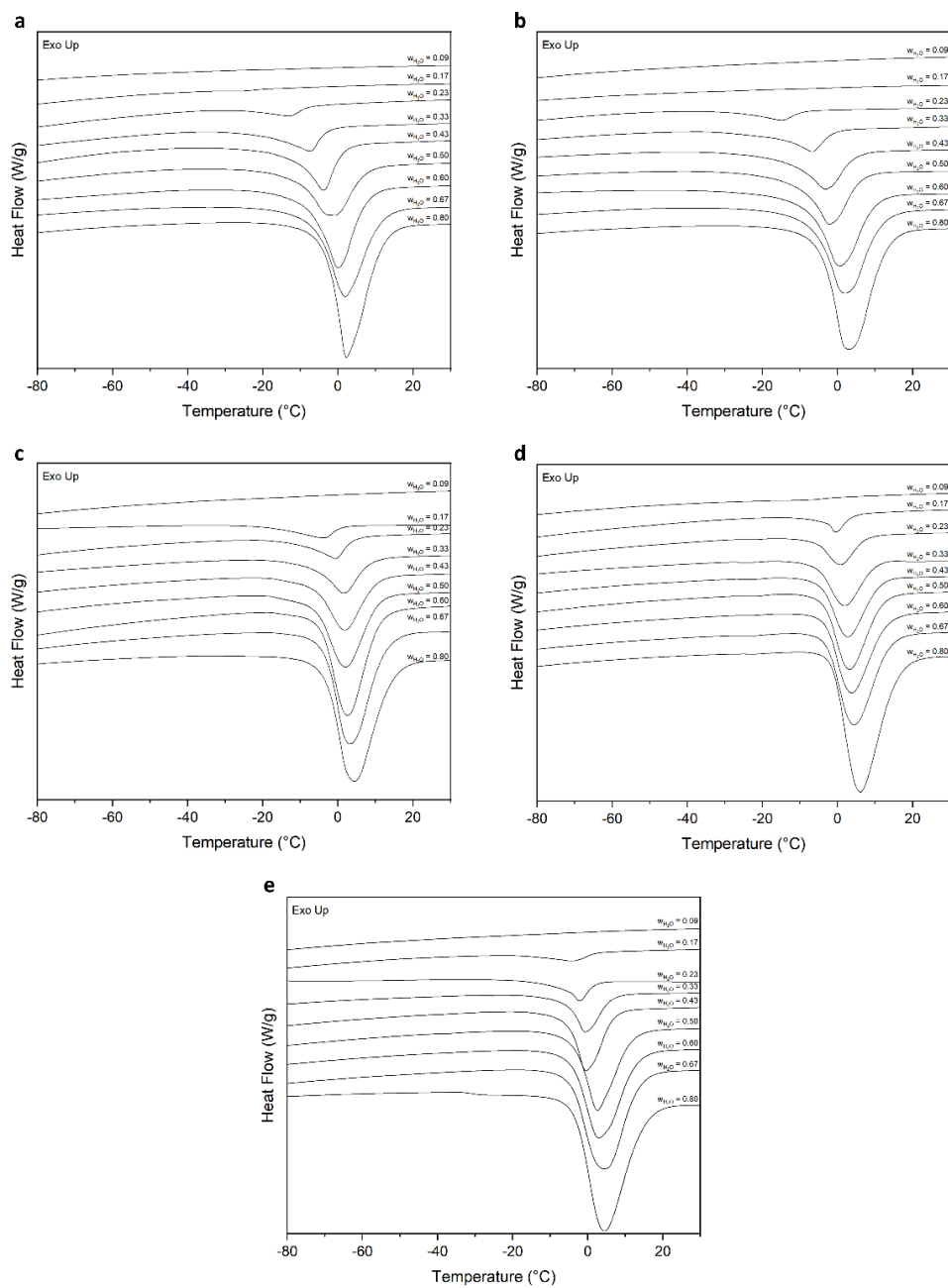
Figure S23: Raw DSC heating curves of binary water and cationic polymer with (a) F-, (b) Cl-, (c) Br-, (d) I-, or (e) SCN- counterions, at varying mass fractions of water, $w_{H_2O} = 0.09 – 0.80$.

w_{H_2O}	Mass Polymer Cat-(F^-) (mg)	Mass H$_2$O (mg)	ΔH_f (mJ)	$m_{H_2O\,freezable}$ (mg)	$m_{H_2O\,nonfreezable}$ (mg)	$\dfrac{m_{H_2O\,"non\text{-}freezable"}}{mg\ H_2O}$	$\dfrac{m_{H_2O\,nonfreezable}}{m\ polymer}$
0.09	15.6	1.56	-	-	-	-	-
0.17	15.4	3.08	1.692	0.005	3.075	0.911	0.200
0.23	11.7	3.51	211.1	0.632	2.878	0.820	0.246
0.33	11.8	5.90	845.2	2.530	3.370	0.571	0.286
0.43	9.5	7.13	1386	4.150	2.975	0.418	0.313
0.5	10.2	10.20	2350	7.036	3.164	0.310	0.310
0.6	8.5	12.75	3341	10.00	2.749	0.216	0.323
0.67	8.2	16.40	4529	13.56	2.841	0.173	0.346
0.8	4.0	16.00	4878	14.60	1.395	0.087	0.349
Averages							0.295 ± 0.051

Table S11: Assessment of water states by DSC in samples of F$^-$ "medium" polymer and water.

w_{H_2O}	Mass Polymer Cat-(Cl^-) (mg)	Mass H$_2$O (mg)	ΔH_f (mJ)	$m_{H_2O\,freezable}$ (mg)	$m_{H_2O\,nonfreezable}$ (mg)	$\dfrac{m_{H_2O\,"non\text{-}freezable"}}{mg\ H_2O}$	$\dfrac{m_{H_2O\,nonfreezable}}{mg\ polymer}$
0.09	18.54	1.85	-	-	-	-	-
0.17	16.04	3.21	-	-	-	-	-
0.23	15.63	4.69	385.5	1.154	3.535	0.754	0.226
0.33	12.60	6.30	1188	3.557	2.743	0.435	0.218
0.43	13.43	10.07	2315	6.932	3.141	0.312	0.234
0.5	11.25	11.25	2864	8.576	2.674	0.238	0.238
0.6	9.46	14.19	4032	12.07	2.117	0.149	0.224
0.67	8.38	16.76	4860	14.55	2.210	0.132	0.264
0.8	4.24	16.96	5200	15.57	1.390	0.082	0.328
Averages							0.247 ± 0.042

Table S12:Assessment of water states by DSC in samples of Cl$^-$ "medium" polymer and water.

w_{H_2O}	Mass Polymer Cat-(Br^-) (mg)	Mass H$_2$O (mg)	ΔH_f (mJ)	$m_{H_2O\,freezable}$ (mg)	$m_{H_2O\,nonfreezable}$ (mg)	$\dfrac{m_{H_2O\,"non\text{-}freezable"}}{mg\ H_2O}$	$\dfrac{m_{H_2O\,nonfreezable}}{mg\ polymer}$
0.09	19.65	1.97	-	-	-	-	-
0.17	12.12	2.42	0.880	0.026	2.398	0.925	0.198
0.23	13.91	4.17	485.3	1.453	2.720	0.652	0.196
0.33	15.52	7.76	1529	4.577	3.183	0.410	0.205
0.43	6.30	4.73	1155	3.459	1.266	0.268	0.201
0.5	8.33	8.33	2097	6.280	2.050	0.246	0.246
0.6	5.55	8.33	2420	7.245	1.080	0.130	0.195
0.67	4.74	9.48	2823	8.451	1.029	0.109	0.217
0.8	3.58	14.32	4498	13.47	0.852	0.060	0.238
Averages							0.212 ± 0.020

Table S13: Assessment of water states by DSC in samples of Br$^-$ "medium" polymer and water.

w_{H_2O}	Mass Polymer Cat-(I$^-$) (mg)	Mass H$_2$O (mg)	ΔH_f (mJ)	$m_{H_2O\,freezable}$ (mg)	$m_{H_2O\,nonfreezable}$ (mg)	$\dfrac{m_{H_2O\,\text{"non-freezable"}}}{mg\,H_2O}$	$\dfrac{m_{H_2O\,nonfreezable}}{mg\,polymer}$
0.09	19.90	1.99	-	-	-	-	-
0.17	13.85	2.77	3.390	0.010	2.760	0.780	0.199
0.23	14.15	4.25	614.2	1.839	2.406	0.567	0.170
0.33	15.84	7.92	1638	4.904	3.016	0.381	0.190
0.43	10.49	7.87	2129	6.376	1.492	0.190	0.142
0.5	9.43	9.43	2661	7.968	1.462	0.155	0.155
0.6	3.38	5.07	1507	4.511	0.559	0.110	0.165
0.67	6.88	13.76	4122	12.34	1.419	0.103	0.206
0.8	3.68	14.72	4675	14.00	0.722	0.049	0.196
Averages							0.178 ± 0.023

Table S14:Assessment of water states by DSC in samples of I- "medium" polymer and water.

w_{H_2O}	Mass Polymer Cat-(SCN$^-$) (mg)	Mass H$_2$O (mg)	ΔH_f (mJ)	$m_{H_2O\,freezable}$ (mg)	$m_{H_2O\,nonfreezable}$ (mg)	$\dfrac{m_{H_2O\,\text{"non-freezable"}}}{mg\,H_2O}$	$\dfrac{m_{H_2O\,nonfreezable}}{mg\,polymer}$
0.09	18.85	1.89	-	-	-	-	-
0.17	16.34	3.27	8.141	0.024	3.244	0.620	0.199
0.23	13.79	4.14	503.2	1.507	2.630	0.636	0.191
0.33	12.95	6.48	1152	3.449	3.026	0.467	0.234
0.43	11.73	8.80	2003	5.998	2.800	0.318	0.239
0.5	8.48	8.48	2254	6.748	1.732	0.204	0.204
0.6	6.73	10.10	2896	8.669	1.426	0.141	0.212
0.67	4.31	8.62	2609	7.812	0.808	0.094	0.187
0.8	4.74	18.96	6055	18.13	0.830	0.044	0.175
Averages							0.205 ± 0.022

Table S15: Assessment of water states by DSC in samples of SCN- "medium" polymer and water.

Polymer Counterion	Volume Fraction H$_2$O $(\varphi_{H_2O})^a$	Mass Fraction H$_2$O $(w_{H_2O})^b$	$\left(\dfrac{m_{H_2O}}{mg\,coating}\right)^c$	$\left(\dfrac{m_{H_2O\,non-freezable}}{m_{polymer}}\right)^d$	$\left(\dfrac{m_{H_2O\,non-freezable}}{mg\,coating}\right)^e$	$\left(\dfrac{m_{H_2O\,freezable}}{mg\,coating}\right)^f$	$\left(\dfrac{m_{H_2O\,non-freezable}}{m_{H_2O\,in\,coating}}\right)^g$
F$^-$	0.476	0.458	0.845	0.295 ± 0.051	0.249 ± 0.043	0.596 ± 0.043	0.295 ± 0.051
Cl$^-$	0.432	0.414	0.707	0.247 ± 0.042	0.175 ± 0.030	0.532 ± 0.030	0.247 ± 0.042
Br$^-$	0.395	0.378	0.608	0.212 ± 0.020	0.129 ± 0.012	0.479 ± 0.012	0.212 ± 0.020
I$^-$	0.299	0.284	0.397	0.178 ± 0.023	0.071 ± 0.009	0.326 ± 0.009	0.178 ± 0.023
SCN$^-$	0.264	0.250	0.335	0.205 ± 0.022	0.068 ±0.007	0.265 ± 0.017s	0.205 ± 0.022

Table S16: Combination of DSC and ellipsometry measurements in order to describe the amounts of various states of water in the coatings. [a]Determined by ellipsometry measurements SI Section S6. [b]Conversion of volume fraction to mass fraction with each component's density [c]Calculated by Eq. S8 [d]Averaged "non-freezable" water capacities for each polymer. [e]Product of "non-freezable" water capacity and mass of water in the polymer coating (Eq. S9). [f]Remaining water in polymer coating is assumed to be freezable (Eq. S10). [g] Fraction of "non-freezable" hydration water (Eq. S11).

S8: Freezing point depression of concentrated polyelectrolyte solutions

Additionally, the activity of the counterions can be qualitatively discerned this way, and a more quantitative analysis is possible when plotting the observed onset melting temperatures, T_m (° C), against the concentration of polymer chains (molality). From here, estimates of the freezing phase transition of hydration water is possible, as in SI Section S7 in Table S10. Inputting these values into the ideal freezing point depression equation, we can calculate respective Van't hoff factors (Eq. S16). Here, we assume that the strongly hydrating counterion F⁻ is completely dissociated. Therefore, to estimate the relative degrees of dissociation in the remaining counterions, we divide by this value, arriving at the Table S17.

$$\Delta T = i\, K_f\, m$$

Eq. S16   Where 'i' is the van't hoff factor, K_f is the freezing point constant (1.86 kg/mol) in water, and m is the polymer concentration.

Counterion	Polymer concentration in coating (molality)	Estimate of phase transition temperature of coating hydration water (°C)	Calculated Van't Hoff Factor	Relative Counterion dissociation (%)
F⁻	0.0421	-11.9	3.04	100
Cl⁻	0.0519	-14	2.90	95
Br⁻	0.0577	-6.1	1.14	36
I⁻	0.1029	-3.7	0.39	12
SCN⁻	0.0872	-6.0	0.74	23

Table S17: Estimations of van't hoff factor and relative counterion dissociation.

S9: Collected TIR Raman, DSC, and ellipsometry data for cationic polymer films with different crosslink densities.

Here, we present the analogous data presented in the sections above, in order to explain the temperature dependent ice adhesion strength on cationic polymer films with varying crosslink densities. The observed behavior pointed towards the again pointed towards the phase transition of hydration water in the coating, however rather than being a function of counterion-identity, a crosslink dependent relationship was observed. TIR Raman spectroscopy was again employed to inspect the physical state of the hydration water in a swollen coating with adhered ice. The collected spectra are presented in Figure S24, and is analyzed according to the process described in SI Section S4, resulting in Table S18 -Table S20. Values of frozen phase fraction are then used in Figure 5a, an overlayed plot comparing the temperature dependent ice adhesion strength on variably crosslinked cationic polymer coatings. Hydrated and dry ellipsometry measurements in Table S21- Table S22 present sample measurements, collectively displayed in Figure 5b. Finally, in an identical manner to SI Section S7, the masses and fractions of "non-freezable" and freezable water are calculated and collected in Table S23- Table S26, allowing for both the independent estimation of the phase transition temperature in variably crosslinked hydrated coatings (Table S27). Significantly, the estimated phase transition temperatures align and agree with values of an experimentally proven phase transition of hydration water in the coating afforded by TIR Raman spectroscopy. In an identical manner to the counterion-specific study, the combination of ellipsometry and DSC were used to correlate the independent nature of low temperature ice adhesion strength on variably crosslinked coatings, with the fraction of "non-freezable" water in the coatings (Figure 5c).
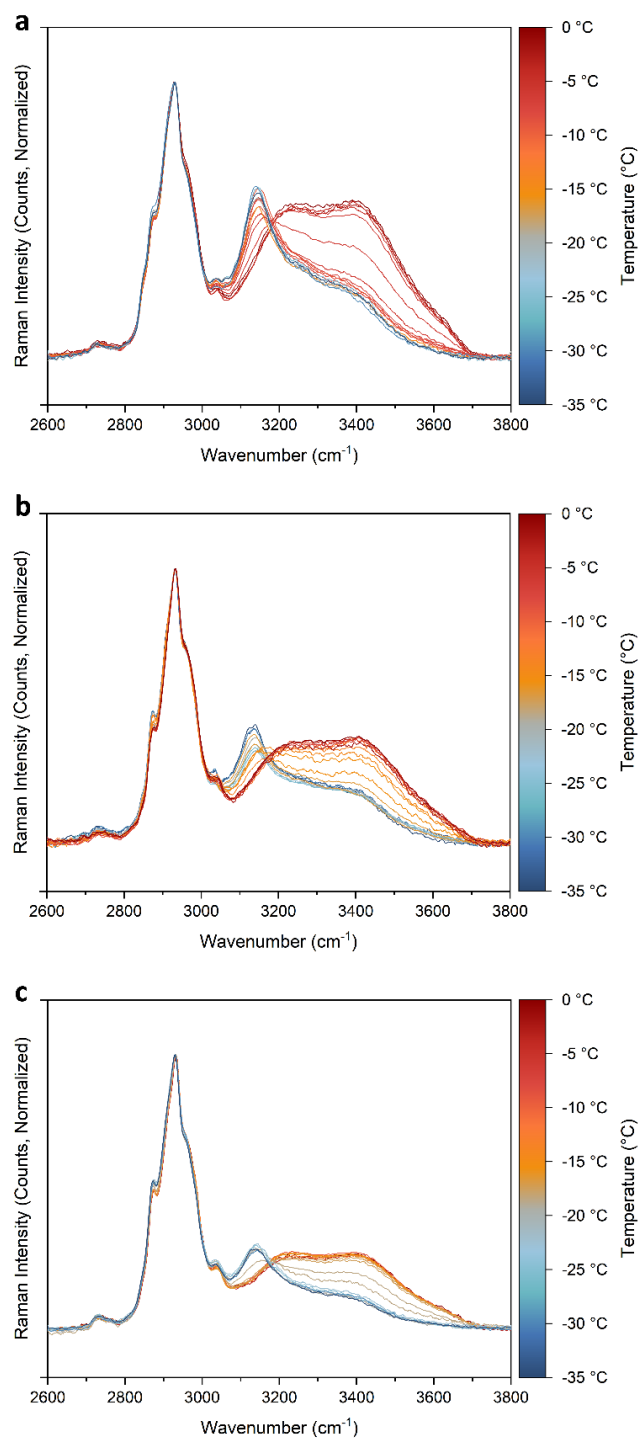
Figure S24: Temperature dependent Raman spectroscopy of cationic chloride polymer with (a) low (b) medium or (c) high, crosslink density, displaying the sub-zero phase transition of hydration water.

Temperature (°C)	X	Y	Z	Frozen phase fraction (f)	Liquid phase fraction (l)
-35	1.03954	1.00489	-0.0079	1.00792	-0.00792
-30	1.05088	1.04797	-0.05119	1.05136	-0.05136
-25	1.0311	1.02649	-0.00944	1.00928	-0.00928
-20	1.04813	0.98008	-0.00407	1.00417	-0.00417
-15	1.03622	0.87413	0.04449	0.95157	0.04843
-10	1.04727	0.98123	0.05628	0.94576	0.05424
-9	1.03333	0.88226	0.09728	0.90069	0.09931
-8	1.02843	0.8444	0.0945	0.89935	0.10065
-7.5	1.02694	0.87699	0.11722	0.8821	0.1179
-7	1.03071	0.71611	0.22268	0.7628	0.2372
-6.5	1.03306	0.46448	0.50844	0.47741	0.52259
-6	1.02698	0.13004	0.83282	0.13506	0.86494
-5.5	1.03597	-0.02825	0.93215	-0.03126	1.03126
-5	1.03588	-0.0656	0.97634	-0.07203	1.07203
-2.5	1.04059	-0.06	0.9626	-0.06647	1.06647
-0.7	1.04873	-0.05139	0.99335	-0.05456	1.05456

Table S18: Fitted coefficients representing contributions of polymer (X), ice (Y), and water (Z), used modelling the corresponding frozen and liquid phase fractions of the hydration water in low crosslink density coatings with Cl- counterions.

Temperature (°C)	X	Y	Z	Frozen phase fraction (f)	Liquid phase fraction (l)
-35	1.02767	1.08882	-0.04338	1.04149	-0.04149
-32.5	1.02343	0.99641	0.03856	0.96274	0.03726
-30	1.02929	1.01515	0.01121	0.98908	0.01092
-27.5	1.00883	0.79537	0.06661	0.92272	0.07728
-25	1.00278	0.9429	0.12667	0.88157	0.11843
-22.5	1.01341	0.983	0.08667	0.91897	0.08103
-20	1.03468	0.90665	0.06099	0.93697	0.06303
-17	1.01853	0.95498	0.02192	0.97756	0.02244
-16.5	1.01702	0.75817	0.19976	0.79147	0.20853
-16	1.00563	0.5521	0.38564	0.58876	0.41124
-15.5	1.00182	0.39108	0.60309	0.39337	0.60663
-15	1.00084	0.37543	0.65954	0.36274	0.63726
-14	1.00084	0.19688	1.0325	0.16015	0.83985
-13	1.00039	-0.03698	0.95864	-0.04012	1.04012
-10	0.9845	-0.03534	0.9994	-0.03666	1.03666
-7.5	0.98445	-0.03816	0.97506	-0.04073	1.04073
-5	0.98505	-0.04057	0.99983	-0.04229	1.04229
-2.5	0.98712	0.00128	0.91954	0.00139	0.99861
-0.7	0.99511	-0.03151	1.00343	-0.03242	1.03242

Table S19: A copy of Table S4, fitted coefficients representing contributions of polymer (X), ice (Y), and water (Z), used modelling the corresponding frozen and liquid phase fractions of the hydration water in medium crosslink density coatings with Cl^- counterions.

Temperature (°C)	X	Y	Z	Frozen phase fraction (f)	Liquid phase fraction (l)
-35	1.03435	0.9528	0.04541	0.95451	0.04549
-30	1.03446	0.89864	0.10003	0.89984	0.10016
-25	1.03655	0.97228	0.07829	0.92548	0.07452
-22.5	1.04849	0.96724	0.12502	0.88554	0.11446
-21	1.02604	0.91811	0.08385	0.91631	0.08369
-20	1.03364	0.94594	0.05227	0.94764	0.05236
-19.5	1.02876	0.93656	0.0606	0.93922	0.06078
-19	1.03492	0.77842	0.3703	0.67764	0.32236
-18.5	1.01554	0.48905	0.64939	0.42958	0.57042
-18	1.01438	0.21143	0.97629	0.17802	0.82198
-17.5	1.01231	0.14983	1.044	0.1255	0.8745
-17	1.01004	0.11783	1.09538	0.09712	0.90288
-16	1.01232	0.10719	1.12502	0.08699	0.91301
-15	1.01396	0.11707	1.11191	0.09526	0.90474
-12.5	1.02141	0.10584	1.1011	0.0877	0.9123
-10	1.01238	0.10395	1.15108	0.08283	0.91717
-5	1.00705	0.07157	1.10656	0.06075	0.93925
-0.7	1.01658	0.08311	1.13355	0.06831	0.93169

Table S20: Fitted coefficients representing contributions of polymer (X), ice (Y), and water (Z), used modelling the corresponding frozen and liquid phase fractions of the hydration water in high crosslink density coatings with Cl- counterions.

Coating	Fit Results	Optical Model	Ψ (Psi) Data & Model	Δ (Delta) Data & Model
Low	MSE = 12.744 Thickness # 3 = 95.76 ± 0.042 nm A = 1.482 ± 0.00021178 B = 0.00598 ± 3.6425E-05	- Layer # 3 = Cauchy Thickness # 3 = **95.76 nm** (fit) A = **1.482** (fit) B = **0.00598** (fit) C = 0.0000 - **Urbach Absorption Parameters** k Amplitude = 0.0000 Exponent = 1.500 Band Edge = 400.0 nm Layer # 2 = SIO2_JAW Thickness # 2 = 100.00 nm Layer # 1 = INTR_JAW Thickness # 1 = 1.00 nm Substrate = SI_JAW		
Medium	MSE = 15.634 Thickness # 3 = 112.61 ± 0.058 nm A = 1.487 ± 0.00027390 B = 0.00523 ± 4.2202E-05	- Layer # 3 = Cauchy Thickness # 3 = **112.61 nm** (fit) A = **1.487** (fit) B = **0.00523** (fit) C = 0.0000 - **Urbach Absorption Parameters** k Amplitude = 0.0000 Exponent = 1.500 Band Edge = 400.0 nm Layer # 2 = SIO2_JAW Thickness # 2 = 100.00 nm Layer # 1 = INTR_JAW Thickness # 1 = 1.00 nm Substrate = SI_JAW		
High	MSE = 11.387 Thickness # 3 = 109.14 ± 0.042 nm A = 1.494 ± 0.00020060 B = 0.00605 ± 3.2146E-05	- Layer # 3 = Cauchy Thickness # 3 = **109.14 nm** (fit) A = **1.494** (fit) B = **0.00605** (fit) C = 0.0000 - **Urbach Absorption Parameters** k Amplitude = 0.0000 Exponent = 1.500 Band Edge = 400.0 nm Layer # 2 = SIO2_JAW Thickness # 2 = 100.00 nm Layer # 1 = INTR_JAW Thickness # 1 = 1.00 nm Substrate = SI_JAW		

Table S21: Dry ellipsometry results, fittings, and measurements of medium crosslink density cationic polymer coatings with varying crosslink density.

Coating	Fit Results	Optical Model	Ψ (Psi) and Δ (Delta) Data & Model
Low	MSE = 41.360 Thickness # 3 = 231.60 ± 0.556 nm EMA % (Mat 2) = 58.6 ± 0.18	- Layer # 3 = EMA Thickness # 3 = **231.60 nm** (fit) # of Constituents = **2** - Material 1 = Cauchy A = 1.482 B = 0.00598 C = 0.0000 - Urbach Absorption Parameters k Amplitude = 0.0000 Exponent = 1.500 Band Edge = 400.0 nm Material 2 = H2O EMA % (Mat 2) = **58.6** (fit) Depolarization = 0.333 Analysis Mode = Bruggeman Layer # 2 = SIO2_JAW Thickness # 2 = 100.00 nm Layer # 1 = INTR_JAW Thickness # 1 = 1.00 nm Substrate = SI_JAW	
Medium	MSE = 35.143 Thickness # 3 = 196.05 ± 0.431 nm EMA % (Mat 2) = 43.2 ± 0.18	- Layer # 3 = EMA Thickness # 3 = **196.05 nm** (fit) # of Constituents = **2** - Material 1 = Cauchy A = 1.491 B = 0.00583 C = 0.0000 - Urbach Absorption Parameters k Amplitude = 0.0000 Exponent = 1.500 Band Edge = 400.0 nm Material 2 = H2O EMA % (Mat 2) = **43.2** (fit) Depolarization = 0.333 Analysis Mode = Bruggeman Layer # 2 = SIO2_JAW Thickness # 2 = 100.00 nm Layer # 1 = INTR_JAW Thickness # 1 = 1.00 nm Substrate = SI_JAW	
High	MSE = 34.379 Thickness # 3 = 151.90 ± 0.409 nm EMA % (Mat 2) = 28.2 ± 0.23	- Layer # 3 = EMA Thickness # 3 = **151.90 nm** (fit) # of Constituents = **2** - Material 1 = Cauchy A = 1.494 B = 0.00605 C = 0.0000 + Urbach Absorption Parameters Material 2 = H2O EMA % (Mat 2) = **28.2** (fit) Depolarization = 0.333 Analysis Mode = Bruggeman Layer # 2 = SIO2_JAW Thickness # 2 = 100.00 nm Layer # 1 = INTR_JAW Thickness # 1 = 1.00 nm Substrate = SI_JAW	

Table S22: Ellipsometry results, fittings, and measurements of hydrated cationic polymer coatings with varying crosslink density
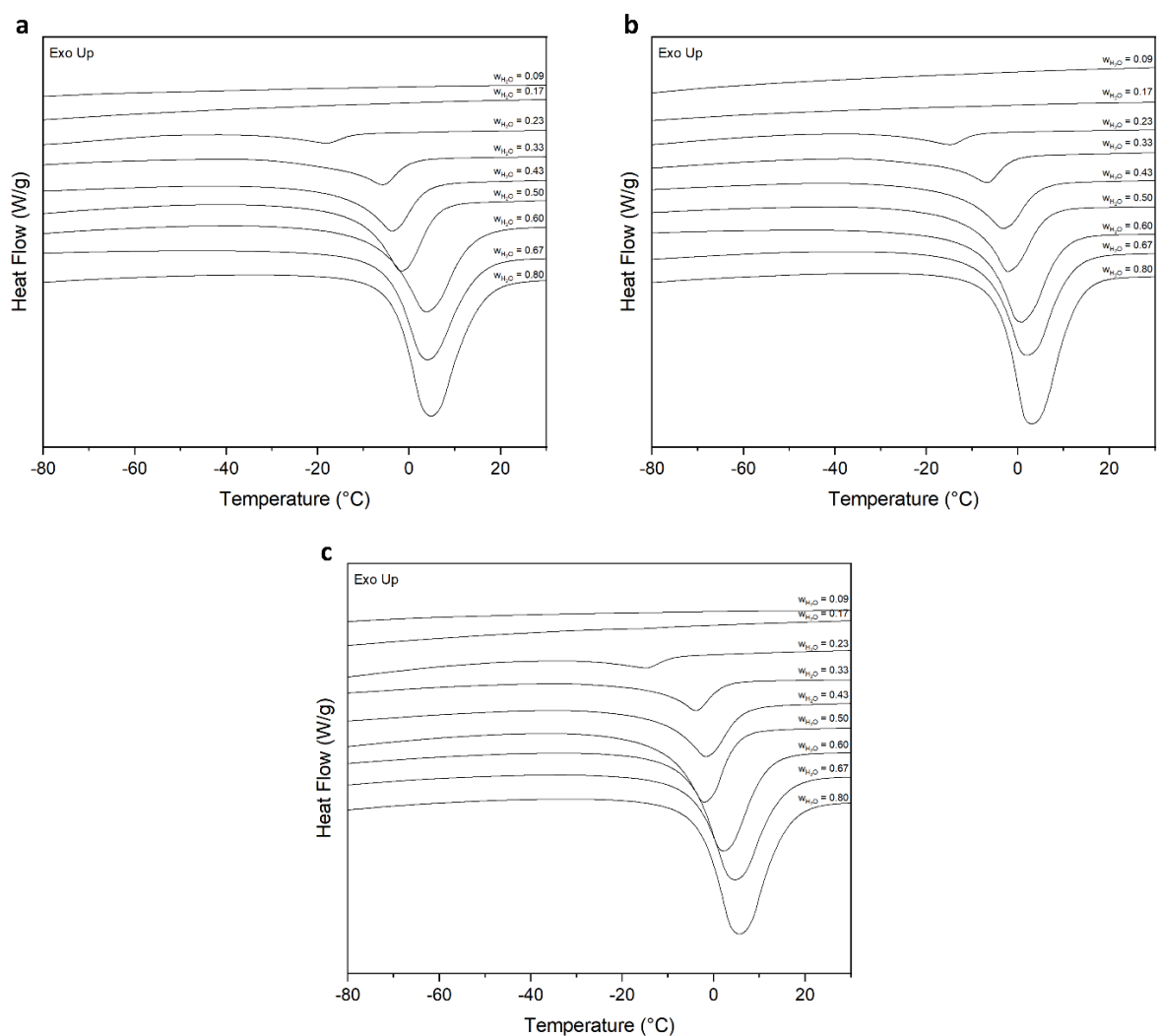
Figure S25: Raw DSC heating curves of binary water and (a) low (b) medium and (c) high crosslink density cationic polymer mixtures, at varying mass fractions of water, w_{H2O} = 0.09 – 0.80.

w_{H_2O}	Mass Polymer "low" (mg)	Mass H$_2$O (mg)	ΔH_f (mJ)	$m_{H_2O\,freezable}$ (mg)	$m_{H_2O\,nonfreezable}$ (mg)	$\dfrac{m_{H_2O\text{ "non-freezable"}}}{mg\ H_2O}$	$\dfrac{m_{H_2O\,nonfreezable}}{mg\ polymer}$
0.09	21.71	2.17	-	-	-	-	-
0.17	15.44	3.09	-	-	-	-	-
0.23	16.23	4.87	499.84	1.497	3.372	0.693	0.208
0.33	14.00	7.00	1207.08	3.614	3.386	0.484	0.242
0.43	13.95	10.46	2119.74	6.347	4.116	0.393	0.295
0.5	8.80	8.80	2212.32	6.624	2.176	0.247	0.247
0.6	8.31	12.47	3429.95	10.27	2.196	0.176	0.264
0.67	7.23	14.46	4151.47	12.43	2.030	0.140	0.281
0.8	5.99	23.96	7433.59	22.26	1.704	0.071	0.284
Averages							0.260 ± 0.030

Table S23: Assessment of water states by DSC in samples of low crosslink density polymer and water.

w_{H_2O}	Mass Polymer "medium" (mg)	Mass H$_2$O (mg)	ΔH_f (mJ)	$m_{H_2O\,freezable}$ (mg)	$m_{H_2O\,nonfreezable}$ (mg)	$\dfrac{m_{H_2O\text{ "non-freezable"}}}{mg\ H_2O}$	$\dfrac{m_{H_2O\,nonfreezable}}{mg\ polymer}$
0.09	18.54	1.85	-	-	-	-	-
0.17	16.04	3.21	-	-	-	-	-
0.23	15.63	4.69	385.5	1.154	3.535	0.7539	0.226
0.33	12.60	6.30	1188	3.557	2.743	0.4354	0.218
0.43	13.43	10.07	2315	6.932	3.141	0.3118	0.234
0.5	11.25	11.25	2864	8.576	2.674	0.2377	0.238
0.6	9.46	14.19	4032	12.07	2.117	0.1492	0.224
0.67	8.38	16.76	4860	14.55	2.210	0.1319	0.264
0.8	4.24	16.96	5200	15.57	1.390	0.0820	0.328
Averages							0.247 ± 0.042

Table S24: Assessment of water states by DSC in samples of low crosslink density polymer and water.

w_{H_2O}	Mass Polymer "high" (mg)	Mass H$_2$O (mg)	ΔH_f (mJ)	$m_{H_2O\,freezable}$ (mg)	$m_{H_2O\,nonfreezable}$ (mg)	$\dfrac{m_{H_2O\,freezable}}{mg\ polymer}$	$\dfrac{m_{H_2O\,nonfreezable}}{mg\ polymer}$
0.09	18.54	1.85	-	-	-	-	-
0.17	16.04	3.21	-	-	-	-	-
0.23	15.63	4.69	530.37	1.588	2.417	0.6035	0.181
0.33	12.60	6.30	1261.13	3.776	3.249	0.4625	0.231
0.43	13.43	10.07	2004.81	6.002	2.833	0.3206	0.240
0.5	11.25	11.25	2734.76	8.188	3.122	0.2760	0.276
0.6	9.46	14.19	4059.90	12.16	1.885	0.1342	0.201
0.67	8.38	16.76	5328.40	15.95	2.587	0.1395	0.279
0.8	4.24	16.96	8722.35	26.11	1.965	0.0700	0.280
Averages							0.241 ± 0.040

Table S25: Assessment of water states by DSC in samples of low crosslink density polymer and water.

Crosslink Density	Volume Fraction H_2O $(\varphi_{H_2O})^a$	Mass Fraction H_2O $(w_{H_2O})^b$	$\left(\dfrac{m_{H_2O}}{mg\ coating}\right)^c$	$\left(\dfrac{m_{H_2O\ non-freezable}}{m_{polymer}}\right)^d$	$\left(\dfrac{m_{H_2O\ non-freezable}}{mg\ coating}\right)^e$	$\left(\dfrac{m_{H_2O\ freezable}}{mg\ coating}\right)^f$	$\left(\dfrac{m_{H_2O\ non-freezable}}{m_{H_2O\ in\ coating}}\right)^g$
F⁻	0.586	0.569	1.321	0.260 ± 0.030	0.343 ± 0.040	0.978 ± 0.040	0.260 ± 0.030
Cl⁻	0.432	0.414	0.707	0.247 ± 0.042	0.175 ± 0.030	0.532 ± 0.030	0.247 ± 0.042
Br⁻	0.282	0.267	0.365	0.241 ± 0.040	0.088 ± 0.015	0.277 ± 0.015	0.241 ± 0.040

Table S26: Combination of DSC and ellipsometry measurements in order to describe the amounts of various states of water in the coatings. [a]Determined by ellipsometry measurements SI Section S6. [b]Conversion of volume fraction to mass fraction with each component's density [c]Calculated by Eq. S8 [d]Averaged "non-freezable" water capacities for each polymer. [e]Product of "non-freezable" water capacity and mass of water in the polymer coating (Eq. S9). [f]Remaining water in polymer coating is assumed to be freezable (Eq. S10). [g] Fraction of "non-freezable" hydration water (Eq. S11).
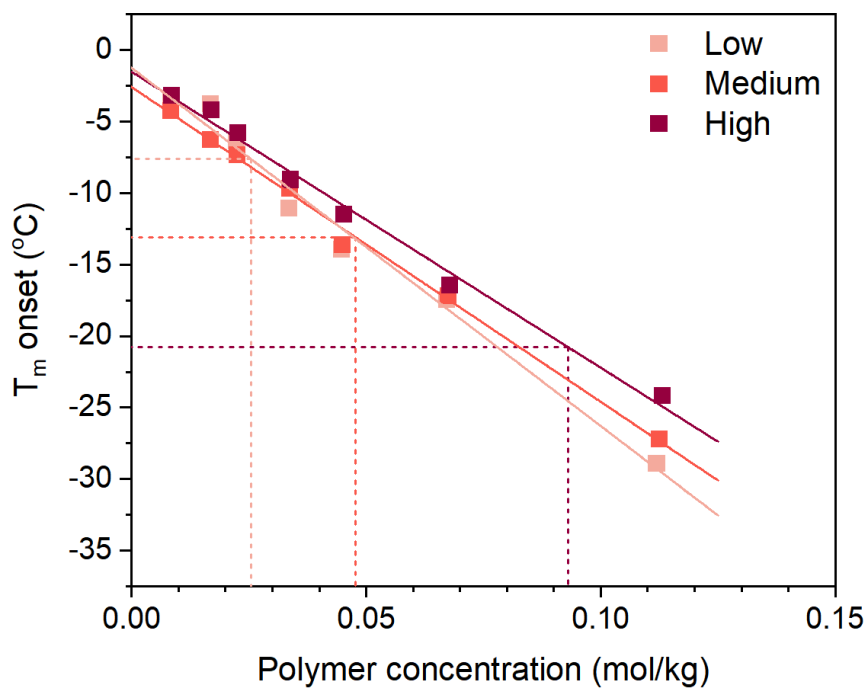
Figure S26: $T_{m\ onset}$ of binary water/polymer mixtures of cationic-chloride (Cat-(Cl-)) polymers at different crosslink densities. Drop-lines to x-axis are signifying the fraction of water in the system, as derived from ellipsometry.

Crosslink density	Polymer concentration in coating (molality)	Estimate of phase transition temperature of coating hydration water (°C)
Low	0.0254	-7.6
Medium	0.0485	-13.3
High	0.0930	-20.8

Table S27: Estimations of phase transition temperature in hydration water of coatings with varying crosslink density.

References:

(1)   Wang, C.; Zhang, W.; Siva, A.; Tiea, D.; Wynne, K. J. Laboratory Test for Ice Adhesion Strength Using Commercial Instrumentation. *Langmuir* **2014**, *30* (2), 540–547. https://doi.org/10.1021/la4044254.

(2)   Rønneberg, S.; Zhuo, Y.; Laforte, C.; He, J.; Zhang, Z. Interlaboratory Study of Ice Adhesion Using Different Techniques. *Coatings* **2019**, *9* (10), 1–12. https://doi.org/10.3390/coatings9100678.

(3)   Bleszynski, M.; Clark, E. Current Ice Adhesion Testing Methods and the Need for a Standard: A Concise Review. *Standards* **2021**, *1* (2), 117–133. https://doi.org/10.3390/standards1020011.

(4)   Liljeblad, J. F. D.; Furó, I.; Tyrode, E. C. The Premolten Layer of Ice next to a Hydrophilic Solid Surface: Correlating Adhesion with Molecular Properties. *Phys. Chem. Chem. Phys.* **2017**, *19* (1), 305–317. https://doi.org/10.1039/c6cp05303c.

(5)   Chen, D.; Gelenter, M. D.; Hong, M.; Cohen, R. E.; McKinley, G. H. Icephobic Surfaces Induced by Interfacial Nonfrozen Water. *ACS Appl. Mater. Interfaces* **2017**, *9* (4), 4202–4214. https://doi.org/10.1021/acsami.6b13773.

(6)   Araújo, A. A. S.; Bezerra, M. D. S.; Storpirtis, S.; Matos, J. D. R. Determination of the Melting Temperature, Heat of Fusion, and Purity Analysis of Different Samples of Zidovudine (AZT) Using DSC. *Brazilian J. Pharm. Sci.* **2010**, *46* (1), 37–43. https://doi.org/10.1590/S1984-82502010000100005.

Manuscript 3

Ice adhesion to cationic, anionic, zwitterionic, and non-ionic polymer surfaces: on the understanding of the role of hydration water

Robert A. Biro[§], Esben Thormann[§*]

§Department of Chemistry, Technical University of Denmark, 2800 Kgs. Lyngby, Denmark

*esth@kemi.dtu.dk

Abstract

Charged polymer coatings have shown promising potential as passive anti-icing coatings due to reduced ice adhesion strength. Yet, a comprehensive understanding as to the effects of polymer charge and coating crosslink density on the adhesion strength of ice to charged polymer surfaces remains absent. To bridge this gap, we have developed a tailorable coating structure to give thiol-ene curable coatings with cationic, anionic, zwitterionic, and non-ionic functionalities, with additional tunability in the crosslink density. Shear ice adhesion on charged polymer coatings exhibited a mechanism based on the physical state of hydration water, showing dependence on both the nature of the charge and coating crosslink density. In order affirm a phase transition, spectroscopic ellipsometry and differential scanning calorimetry was used first to investigate the swelling and polymer-induced freezing point depressions as a function of both polymer charge and crosslink density. Later partnering these measurements, we were able to estimate of the phase transition temperature of coating hydration water, which strongly correlated to the observed jumps in ice adhesion. Additionally, low temperature ice adhesion strength was also correlated to fractions of "non-freezable" water, in the polymer coating, dependent solely on the nature of the charges present in the coating. These insights on the effects of charge and coating structure on ice adhesion strength, reveal new relationships that could be beneficial in the development of passive charged anti-icing surfaces.

1. Introduction

The formation and build-up of ice on surfaces can lead to significant operation difficulties and safety concerns for aircraft, power and telecommunications networks, wind turbines, heat exchangers, and so forth.[1–4] As an example, icing of the aerofoil structures of airplane wings and wind turbine blades changes their shape, roughness, and perhaps most critically, their weight, leading to a critical decline in performance that eventually may halt any operations.[5–8] It that event, it is common practice to spray an ethylene or propylene glycol de-icing solution onto the surface, melting ice by depressing its freezing point significantly.[9,10] Active ice-removal

methods such as this are often economically and environmentally costly, energy-intensive, and sometimes even laborious tasks, therefore it is only rational to investigate the feasibility of passive anti-icing systems.[2,11–14]

To this end, efforts have seen the development of passive anti-icing surfaces, to delay or supress icing, or to lower the adhesion strength of ice significantly based solely on the characteristics of the surface.[2,11–15] Hydrophobic coatings naturally repel water and have the ability to shed super-cooled water droplets before they freeze. Yet, despite this potential, the greater surface texture of these materials often gives way to stronger ice adhesion, due to the increased surface area and mechanical interlocking between ice and the substrate.[16–18] Furthermore, the successive icing/de-icing tests have shown the deteriorating anti-icing capabilities of hydrophobic coatings due increasing surface texture. In contrast, slippery liquid-infused porous surfaces (SLIPS) seemingly erase any surface significant surface texture by employing a defect-free smooth liquid surface to both repel water droplets and dramatically reduce the adhesion strength of strength.[19–21] Numerous investigations into SLIPS as anti-icing surfaces, have outlined the importance of infusing a liquid that preferentially wets the surface over water/ice and that remains liquid at sub-zero temperatures, thus lubricating and wetting the interface and weakening any interactions between water/ice and the surface.[22] One shortcoming of infusing with hydrophilic liquids is their eventual dilution and consumption, gradually deteriorating the ice repellent properties over of SLIPS.[23,24] Although longer longevity was achieved using more hydrophobic liquids that are not be so easily wicked by water, these surfaces still necessitated the replenishment of the infused liquid to re-establish favourable anti-icing properties.[25,26]

Alternatively, rather than using an expendable finite amount of liquid to infuse a surface, hydrophilic polymer coatings can employ water which can be naturally replenished from ambient conditions to impart comparably beneficial anti-icing properties. The past decade of research has focused on promoting a self-sustainable aqueous lubricating layer at the interface, primarily drawing inspiration from ice-skating, as early studies have accomplished.[27–30] Yet, the importance of hydration water and its associations with the hydrophilic polymer coating cannot be understated, as these have been shown to be significant enough to depress the freezing point of water such that the hydration water remains liquid at sub-zero temperatures, and thereby reducing the adhesion strength of ice to the coating.[31–33] Furthermore, it is well known that sufficiently strong coordination between water and hydrophilic or charged moieties can cause a fraction of the hydration water molecules to remain "non-freezable", also leading to lower ice adhesion.[34,35] Charged polymers, i.e., polyelectrolytes and zwitterionic polymers, have therefore become main focus as potential anti-icing coatings, due to their innate ability to associate, coordinate, and supress the freezing of hydration water.[36,37]

In our previous work, we have brought new insight to low ice adhesion mechanisms of cationic polyelectrolytes, showing counterion specific behaviour that is linked the physical state of hydration water.[38] Building off this, variations in polymer charge and coating structure are too expected to have a similar effect on the swelling and freezing point depression of hydration water in the coating, as well as the fraction of "non-freezable" water. Therefore, in an aim to shed light on the role of these factors towards to ice adhesion, we have systematically produced cationic, anionic, zwitterionic, and non-ionic coatings, each with three distinct

crosslink densities. Resulting measures of ice adhesion pointed towards a phase transition in the coating's hydration water, presenting both a charge and crosslink dependent relationship. These observations were then affirmed by partnering ellipsometry and differential scanning calorimetry to accurately estimate of the phase transition temperature of the hydration water in the coatings. Moreover, the fraction of "non-freezable" water and its value towards low ice adhesion is resolved, and altogether presents promising potential for charged polymers as anti-icing coatings.

2. Experimental Section

Reagents: 2-(methacryloyloxy)ethyl trimethylammonium solution (METAC, 75wt.% in H2O, Sigma-Aldrich), *n*-butyl methacrylate (*n*-BMA, 99%, Sigma-Aldrich), allyl methacrylate (AMA, 98%, Sigma-Aldrich), and 2-dimethylamino methacrylate (DMAEMA, 98%, Sigma-Aldrich) were all passed through a column of basic activate aluminium oxide (Brockmann I, Sigma-Aldrich) before use. 3-sulfopropyl methacrylate potassium salt (SPMA-K, 98%, Sigma-Aldrich), 1,4-butane sultone (≥99%, Sigma-Aldrich), 4-cyano-4-[(dodecylsulfanylthiocarbonyl)sulfanyl]pentanoic acid (97%, Sigma-Aldrich), 4,4-azobis(4-cyanvaleric acid) (ACVA, ≥98%, Sigma-Aldrich), 1,3,5-Trioxane (≥99%, Sigma-Aldrich), 3-mercaptopropyl trimethoxysilane (3-MPTMS, 95%, Sigma-Aldrich), 1H,1H,2H,2H- perfluorooctyltriethoxysilane (98% , Sigma-Aldrich), pentaerythritol tetrakis (3-mercaptopropionate) (PETMP, ≥95%, Sigma-Aldrich), toluene (≥99.8%, VWR Chemicals BDH), acetonitrile (≥99.9%, VWR Chemicals BDH), isopropyl alcohol (IPA, ≥99.8%, VWR Chemicals BDH), dimethylformamide (DMF, ≥99.9%, VWR Chemicals BDH), diethyl ether (≥99.9%, VWR chemicals BDH) 2,2,2-trifluoroethanol (TFE, ≥99%, Sigma-Aldrich) were all used as received.

Synthesis of cationic polyelectrolytes: METAC (75 wt.% in H_2O, 1.986 mL, 1.654 g), *n*-BMA (3.295 mL, 2.944 g, 20.7 mmol), AMA (0.428 mL, 0.402 g, 3.186 mmol),), 4-cyano-4-[(dodecylsulfanylthiocarbonyl)sulfanyl] pentanoic acid (63.5 mg, 0.157 mmol), ACVA (4.41 mg, 0.0157 mmol), DMF (10.84 mL), H_2O (0.81 mL), and 1,3,5-trioxane as internal standard (~50 mg), was combined in a round bottom flask and sparged with N_2 for approximately 30 min before being lowered into a pre-heated 70 °C oil bath. The polymerization was monitored by ^{1}H-NMR, until completion, after which it was precipitated into a large excess of diethyl ether, before being collected and dried under vacuum overnight. The afforded polymer targets a composition of 10 mole percent AMA, and is labelled at Cat-M with 65 mole percent *n*-BMA. Polymerizations with 5 and 15 mole percent AMA and 70 and 60 mole percent *n*-BMA, were labelled as Cat-L, and Cat-H.

Synthesis of anionic polyelectrolytes: SPMA-K (1.886g, 7.502 mmol) *n*-BMA (3.103 mL, 2.774 g, 19.5 mmol), AMA (0.404 mL, 0.379 g, 3.000 mmol),), 4-cyano-4-[(dodecylsulfanylthiocarbonyl)sulfanyl] pentanoic acid (59.84 mg, 0.148 mmol), ACVA (4.15 mg, 0.0148 mmol), DMF (8.11 mL), H_2O (2.69 mL), and 1,3,5-trioxane as internal standard (~50 mg), was added to round bottom flask. The solution was stirred and sparged with N_2 for approximately 30 minutes, before the flask was placed into a pre-heated 70 °C oil bath and monitored by ^{1}H-NMR until completion. The product was then precipitated into a large excess of cold isopropanol, collected by vacuum filtration, redissolved in a minimal amount of DMF/H_2O, and precipitated into diethyl ether. The

afforded polymer was again collected, and dried overnight under vacuum, and is denoted as An-M, corresponding to its targeted 10 mole percent AMA composition. Analogous polymerization targeting 5 and 15 mole percent AMA, and 70 and 60 mole percent n-BMA, were labelled as An-L and An-H, respectively.

Synthesis of zwitterionic polymers: 3-(N-2-methacryloyloxyethyl-N-N-dimethyl) ammonatobutanesulfone (MABS) zwitterionic monomer was prepared beforehand accordingly.[39] A round bottom flask containing zwitterionomer MABS (2.056 g, 7.007 mmol), n-BMA (2.900 mL, 2.591 g, 18.22 mmol), AMA (0.377 mL, 0.354 g, 2.803 mmol),), 4-cyano-4-[(dodecylsulfanylthiocarbonyl)sulfanyl] pentanoic acid (55.94 mg, 0.139 mmol), ACVA (3.88 mg, 0.0139 mmol), TFE (10.09 mL) and 1,3,5-trioxane as internal standard (~50 mg) was sparged with N_2 while stirring for approximately 30 min, after which it was placed into a 70 °C oil bath and monitored by ^{1}H-NMR. Once near completion, the solution was precipitated into a large excess of cold stirred diethyl ether, collected by vacuum filtration, and dissolved once more in a minimal amount of TFE, before reprecipitating once more into diethyl ether. The product was collected and dried overnight in under vacuum, and given the label Zwitt-M, as it targets 10 mole percent AMA. Similar polymerizations targeting 5 and 15 mole percent AMA, and 70 and 60 mole percent n-BMA, were conducted, resulting in Zwitt-L and Zwitt-H, respectively.

Synthesis of non-ionic polymer: n-BMA (1.012 mL, 0.910 g, 6.401 mmol), AMA (0.096 mL, 0.0900 g, 0.711 mmol), 4-cyano-4-[(dodecylsulfanylthiocarbonyl)sulfanyl] pentanoic acid (14.15 mg, 35.1 µmol), ACVA (0.98 mg, 3.51 µmmol), DMF (2.56 mL) and 1,3,5-trioxane as internal standard (~10 mg) was added to a round bottom flask before being sparged with N_2 while stirring for approximately 30 min. The flask was then placed into a 70 °C oil bath and ran until completion, before being precipitated directly into a large excess of cold methanol, before being collected by vacuum filtration, and dried overnight under vacuum. The resulting polymer had a targeted AMA composition of 10 mole percent, and is therefore correspondingly labelled as Non-M.

Functionalization of substrates: Thermally oxidized silicon wafers were cut into 19 mm x 19 mm squares and rinsed thoroughly with acetone, ethanol, and milli-Q water twice, before a treatment with H_2O plasma at 500 mTorr for 180 sec. The plasma-cleaned substrates were then immersed into a 5 vol.% 3-MPTMS solution in toluene, for 3 h, after which they were lightly rinsed with toluene, dried under a stream of nitrogen, and thermally cured at 130 °C for 2 h, inducing the condensation of the silane onto the silicon substrate.

Preparation of coatings: Charged polymers were dissolved in TFE, and non-ionic polymer in DMF, 1.25 wt./vol.%. with an equimolar amount of PETMP and ACVA with respect to the AMA content of the polymer. The solution was then mixed vigorously for at least 30 minutes and allowed to settle before passing through a 0.22 µm filter. ~225 µL of solution was then spin-coated onto the 3-MPTMS functionalized substrates (2000 rpm for 40 sec.). To cure the polymer chains to one another and to the substrate, a thermally-initiated thiol-ene cure was conducted by placing the spin-coated samples in a 90 °C oven for 2 h. Resulting coatings were washed with excess water to remove any unattached material and dried under a nitrogen stream before us.

Ice adhesion measurements: A home-built ice adhesion test apparatus was used to all measurements and is previously described elsewhere.[38] Briefly, a pneumatic piston (MQQTB16-50D, SMC Corp.) was used to push

an ice-filled Teflon cylinder adhered to a sample. The pushing force was controlled by a regulator (ARX0-F01, SMC Corp) and adjustable restrictive flow valve (AS1002, SMC Corp), set to give a linearly increasing and reproducible force, that is measured by a miniature load cell (8413-5050, 50N, Blichfeld) connected to the pushing rod of the pneumatic piston. Temperature control of the samples was achieved using a recirculating chiller (AD15R-30, 462-0230VWR), flowing a cooled fluid of aqueous ethylene glycol (~65 vol.% ethylene glycol) through the stainless-steel baseplate of the chamber, above which samples were placed into square indents and secured in place by fastening clamps onto one edge. The adhesion of ice to the coatings was accomplished using a custom-built weighted alignment piece in which the Teflon cuvettes were inserted, secured, and placed into the chamber on sample surfaces. Chilled degasses milli-Q water was then added to the cuvettes (~0.7 mL) when the temperature of the surface was -20 °C, and left to freeze for at 1 hour, before the weighted alignment piece was removed, and measurement temperature set. After equilibrating for at least another hour, measurements of ice adhesion strength on surfaces were then run.

Ellipsometry: The thickness of dry and hydrated polymer coatings was measured using a spectroscopic ellisometer (M-2000, J.A. Woollam Co., USA). Dry measurements were variable angle (55°, 60°, 65°, 70 °, and 75°) and conducted over a wavelength of 250 nm to 1000 nm, at room temperature, with an accompanying light flow of dry nitrogen used to remove any significant humidity effects from the film. Analysis of the coatings was completed using CompleteEase software, and fitting a proposed slab model consisting of a Si substate, a 1nm Si-SiO_2 intermediate layer, a 100 nm thick SiO_2 layer, and a final Cauchy layer. Meanwhile hydrated measurements were conducted using a liquid cell with a fixed angle of incidence (75°) over a identical wavelength range. Samples were flooded with water and allowed to equilibrate for 20 min before measurement. Modelling here was similar slab model but with a final two-component Bruggeman Effective Medium Approximation model, consisting of water and a Cauchy model with parameters derived from the measured dry surfaces (See SI Section S2 for more detailed information).

Differential scanning calorimetry (DSC): A TA Instruments Q200 with RCS 90 was used to measure the onset melting temperature and fractional states of water (freezable and "non-freezable" water) in aqueous polymer systems. Here, specific amounts of polymer and water (corresponding to w_{H2O} = 0.09 – 0.8) were loaded into hermetically sealed aluminum pans (Tzero Pans and Tzero hermetic lids, TA Instruments- Waters LLC). The sample were left to equilibrate for at least 48 h at room temperature before they were cooled to -90 °C, held 10 minutes, and heated at a rate of 5 °C min^{-1} to 40 °C. Data was analysed using Universal Analysis software, and is covered in greater detail in SI sections S4 and S6.

3. Results and Discussion

3.1. Preparation of anti-icing coatings

In order to investigate the effects of variable charge and crosslink density on the resulting coating's ice repellency, the design of an easily tailorable polymer is paramount. To this end, reversible addition fragmentation chain-transfer (RAFT) polymerization was used to synthesize all polymers due to its versatility and ability to maintain a constant charged monomer composition while still providing the desired tunability of crosslink density and hydrophobic character through AMA and n-BMA respectively. The crosslink density of the coatings was controlled through the incorporation of AMA in the polymer, the targeted x_{AMA} = 0.05, 0.1, or 0.15, corresponding to coatings with low (L), medium (M), or high (H) crosslink densities. A high mole fraction of n-BMA was added in each system ($x_{n\text{-}BMA}$ = 0.6-0.7) in order to give favourable solubility in organic solvents, simultaneously resulting in a lower mole fraction of charged monomer (x_{charge} = 0.25). METAC, SPMAK, and MABS were used as monomers to produce cationic, anionic, and zwitterionic polymers, while non-ionic polymers consisted of solely AMA and n-BMA. Despite the high disparity in terms of charge character and hydrophobicity, the polymerization of all monomers was straightforward and accurate to the targeted fraction of each component (see SI, section S1). The synthesized polymers were spin-coated with an equimolar amount of tetrafunctional thiol and thermal radical initiator onto thiol-functionalized silicon substrates, followed by a thermally initiated thiol-ene cure to produce surface-attached polymer hydrogels with both variable polymer charge character, and crosslink density, as depicted in Figure 1.
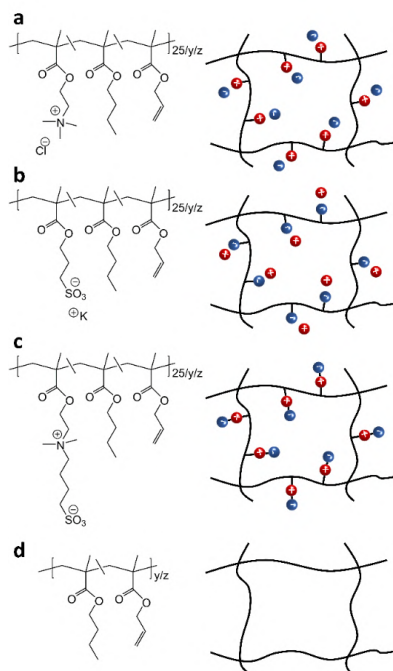

Figure 1: Chemical structures of synthesized polymer and representative polymer-bound charge character of (a) cationic, (b) anionic, (c) zwitterionic, and (d) non-ionic coatings.

3.2. Ice adhesion on charged polymer coatings

It has been found that charged surfaces can lead to substantial reductions in ice adhesion strength when compared to bare surfaces or hydrophobic films.[35,37,38,40] Following this thinking, we examine the ice adhesion strength of our coatings with distinct polymer charge identities, aiming to draw inferences from their temperature-dependent behaviour in order to better understand the mechanism of their anti-icing properties. This was accomplished using a home-built shear apparatus at seven temperatures, ranging from -5 °C and -35 °C, where the average strength of ice adhesion was defined as the maximum shear force divided the ice-surface interfacial area. A comparison of the temperature-dependent ice adhesion strength on coatings with various charged functionalities is presented in Figure 2. As a standard, the strength of ice adhesion to a non-hydrated hydrophobic coating (Non-M), was measured and seen to linearly increase from -5 C to approximately -20 °C, followed by a near constant value at lower temperatures due to cohesive failure at the coating-ice interface, evident by traces of ice left on the surface. In contrast, ice adhesion to charged polymer coatings, inherently hydrated due to their hydrophilic nature, displayed a wholly different performance. First, it should be noted that adhesive failure was observed between the ice cylinder and all charged polymer coatings at low temperatures. Next, polyelectrolyte coatings Cat-M and An-M exhibited very low ice adhesion strength through -10 °C (<60 kPa), followed by a distinct jump at -15 °C, below which the adhesion strength was seemingly constant (~240 kPa). In stride, zwitterionic polymer coating Zwitt-M, exhibited remarkably similar behaviour from -5 °C through -15 °C, with a single increase in ice adhesion strength occurring at approximately -17.5 °C, after which a steady yet markedly lower adhesion strength (~150 kPa) was reached.

In order to gleam information as to mechanism of the temperature dependence of the ice adhesion, we here compare the various temperature-dependent ice adhesion behavior observed between the coating. Tellingly, ice adhesion to Non-M resembled the adhesion of ice to bare substrates or smooth hydrophobic coatings.[31,41,42] However, the behaviour of charged polymer coatings was indicative of a phase transition in the coating's hydration water.[38] When the physical state of the hydration water is liquid, the adhesion of ice onto the coating is intrinsically low, as ice adhesion on liquid-like surfaces benefits greatly from increased molecular mobility.[38,41,43–45] Yet, once the hydration water is frozen, the ice adhesion strength increases as a result of greater mechanical interlocking between ice and the substrate. The intersection of these two states is a proven phase transition of the coating's hydration water, resulting in a characteristic jump in ice adhesion strength.[27,32] However, the proposed phase transition of hydration water in the charged polymer coatings does not explain the disparity between the values of ice adhesion strength at low temperatures, and will be examined later.
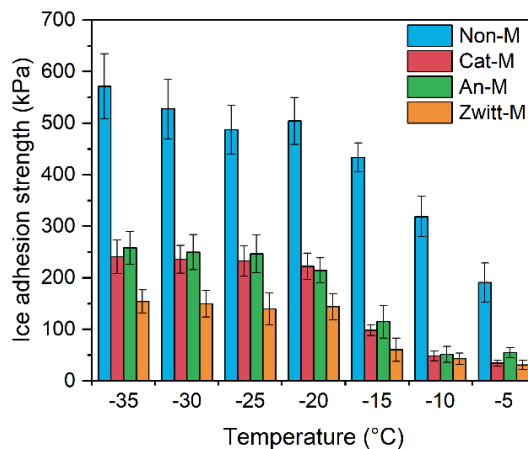
Figure 2: Temperature dependent shear ice adhesion strength on non-ionic and charged polymer coatings. Values displayed are an average of a minimum of 3 measurements, with corresponding standard deviation.
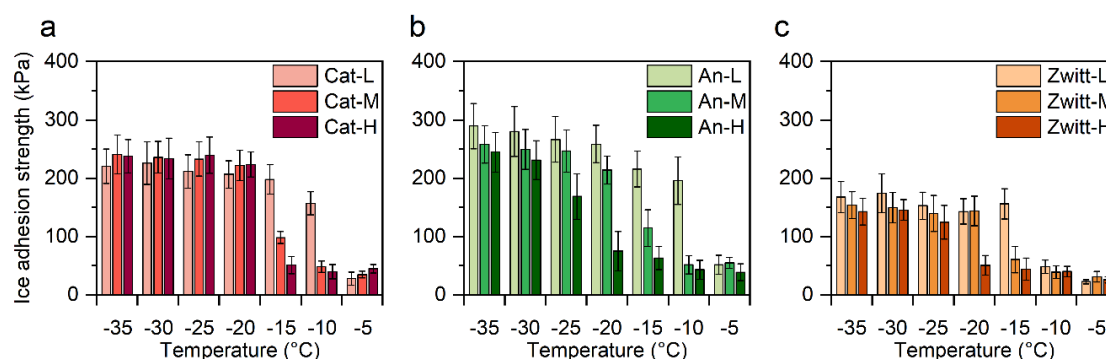
Figure 3: Temperature dependent shear adhesion strength of ice on (a) cationic, (b) anionic, and (c) zwitterionic polymer coating with varying crosslink density.

Tuning of the crosslink density of polymer coatings has also been reported to affect the anti-icing properties of hydrophilic films.[29,32,38] Therefore, we have also investigated the temperature-dependent ice adhesion strength on charged polymer coating with variable crosslink density, compiled in Figure 3. Expectedly, the relatively small changes in monomer composition did not point to a different mechanism at play, rather, changes in crosslink density exemplified the broad temperature range over which a proposed phase transition can affect the ice adhesion strength. Whereas the temperature of the observed jump in ice adhesion strength (defined in greater details in SI Section 5) of Cat-M, An-M, and Zwitt-M are more-or-less aligned, the jumps in ice adhesion strength between crosslink densities of a single polymer charge functionality occur over a far wider range, where consistently, more tightly crosslinked coatings seemingly delay this jump to lower temperatures. As an example, the estimated observed jump in ice adhesion strength occurs at

approximately -12.5 °C for Zwitt-L, -17.5 °C for Zwitt-M, and -22.5 °C for Zwitt-H. Therefore, it is expected that the proposed phase transition of a coating's hydration water must be a function of both the polymer charge and the crosslink density of the coating.

3.3. Phase transition in coating hydration water

In order to confirm that the sudden increases in ice adhesion strength are indeed the result of a phase transition in the water hydrating the coatings in all the cases, we employ a previously developed method of combining ellipsometry and differential scanning calorimetry (DSC) as a way to estimate the phase transition temperature of the hydration water in the coatings.[38] Independently, ellipsometry measures can provide valuable information regarding the amount of hydration water in the polymer coating. Separately, DSC experiments can offer insight into the polymer-induced freezing point depression and its dependence on polymer charge and composition. Combining these data not only allows for the phase transition temperature of hydration water in a particular coating to be estimated, but a more in-depth discussion into the roles of both polymer charge and coating crosslink density on hydration water.
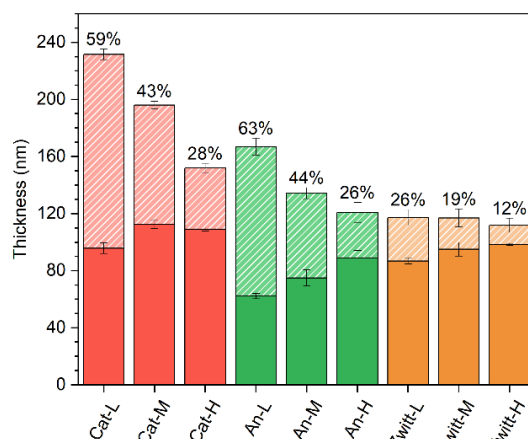
Figure 4: Dry (solid bars) and hydrated (striped bars) thicknesses of cationic (red), anionic (green), and zwitterionic (orange) polymer coatings with varying crosslink density, derived from ellipsometry. Additional labels report the volume fraction of water in each polymer coating, φ_{H_2O}.

3.3.1 Swelling of charged polymer films

Naturally, hydrophilic polymer coatings will hydrate when in contact with liquid water, causing them to swell, and is primarily dependent on the charge identity and crosslink density that promote and restrict swelling respectively. First, we present the ellipsometry-derived dry and hydrated thicknesses of each polymer coating (Figure 4), where it is clear that cationic and anionic polyelectrolyte coatings swell similarly, while zwitterionic coatings evidently do not swell to the same extent. Bringing attention to the medium crosslink density coatings, Cat-M and An-M were found to have 43 vol. % and 44 vol.% water respectively, whereas Zwitt-

M exhibited an equilibrium water content of only 19 vol.%. This behaviour can be rationalized as cationic and anionic polyelectrolyte coatings inherently have a concentration of mobile counterions defining an ion osmotic pressure difference between the coating and surrounding environment, that primarily drives hydration water into the coating.[46] Yet, the covalently bound nature of both charges in zwitterionic polymers does give rise to any counterion induced osmotic pressure, and instead hydration is dependent on various non-electrostatic effects to pull water into the coating, restricting their swelling immensely.[47] Expectedly, crosslink density also plays a crucial role in controlling the hydration of the films, such that coatings with lower crosslink density bring about more hydration water than their higher crosslinked counterparts. As demonstrated here, both the nature of the polymer-charge and crosslink density affect the amount of hydration water in the coating. Therefore, it is only logical that different amounts of water in the coating may lead to correspondingly different phase transition temperatures.

3.3.2. Polymer-induced freezing point depression

Next, we seek to describe the effect of both polymer charge and crosslink density on the freezing point depression of aqueous polymer solutions. DSC was employed to measure the melting onset temperature ($T_{m\ onset}$) of a single-phase transition corresponding to the melting of water, in samples with varying amounts of polymer and water. In order to discern any effects of polymer charge or crosslink density, melting onset temperatures were plotted in terms of polymer concentration (mol/kg), as explained in SI, section S4. The resulting Figure 5 invariably displays a linearly increasing freezing point depression corresponding to greater polymer concentration. Yet it is clearly seen that the slopes of the trend lines can vary, as seen in a comparison between Zwitt-M and polyelectrolytes Cat-M and An-M. Therefore, we interpret the linear relationship to be a function of polymer chemistry and the concentration of mobile counterions. Here, however, the effect of changes polymer chemistry, through compositional changes in polymer charge or AMA content, is noticeably weak, as the bulk of the polymers being compared are predominantly identical. Therefore, the freezing point depression can be simply described as an effect of a mostly fixed polymer chemistry, and the observed variations caused by the contribution of mobile counterions to the system.

Cationic and anionic polyelectrolytes display equal magnitudes of freezing point depression with regards to polymer concentration (Figure 5a). Based on our previous work, it was offered that the cationic and anionic polyelectrolyte layers with chloride counterions are systems in which the counterions are fully dissociated.[38,47] In contrast, the distinctly weaker freezing point depression exhibited in zwitterionic polymers was rationalized through a lack of any contribution of mobile counterions to the system, whereby only the chemistry of the polymer depresses the freezing point of water. Therefore, the presence of the counterions here plays a dramatic role in enhancing the freezing point depression of water.
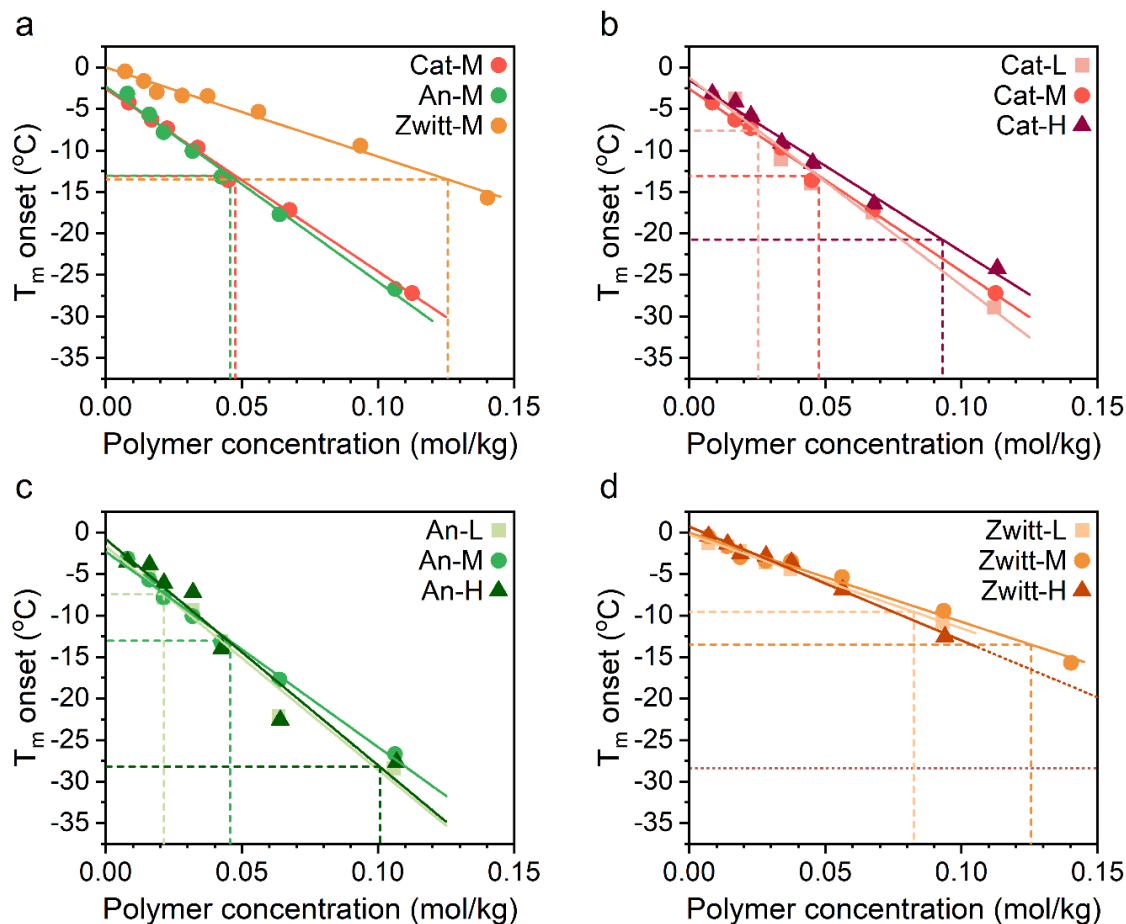
Figure 5: DSC-based variation in onset melting temperature versus the molality of polymer for (a) charged polymers at medium crosslink density and (b) cationic (c) anionic (d) zwitterionic coatings with varying crosslink density. Linear fits are added to each data set, and corresponding drop lines are used to approximate the phase transition temperature of hydration water in the coating.

3.3.3 Phase transition temperature of hydration water

However, despite the superior freezing point depression of water by polyelectrolytes, it remains to be seen how the amount of water in each sample effects the phase transitions. Dashed drop-lines, corresponding to the calculated concentration of polymer in the coating (see SI, section S4 for details), derived from the collected ellipsometry data, were applied to the linear fit of freezing point depression. Correlating the polymer concentration to the $T_{m\ onset}$, we here estimate the freezing point depression of water in the polymer coating, and therefore the phase transition temperature at which the hydration water freezes.

As seen in Figure 5a, freezing phase transitions were estimated at -13.1 °C for Cat-M, -13.0 °C for An-M, and -13.5 °C for Zwitt-M, coinciding despite differences in swelling and freezing point depression. The greater hydration observed in polyelectrolyte coatings in turn results in a more a more diluted polymer coating,

where the polymer concentration (given in terms of molality) is calculated to be m = 0.046 and 0.048 for Cat-M and An-M respectively. However, the more collapsed state of hydrated zwitterionic polymer coatings has the reverse effect, such that m = 0.0126, giving a remarkably similar estimate of freezing point depression for the hydration water in the coating. A broader range of estimated phase transition temperatures was noticed comparing identically charged polymer samples with different crosslink densities. Focusing on zwitterionic polymer coatings, the hydration water in Zwitt-L is estimated to freeze at -9.5 °C, while the hydration water in the more concentrated system of Zwitt-H is predicted to approximately -28.3 °C. Here, the nearly identical freezing point depression observed by the polymers (Figure 5d), exemplifies the role of the amount of hydration water, such that more tightly crosslinked coatings correlate to lower estimates in the phase transition temperature.

Altogether, by balancing the polymer-induced freezing point depressions with the characteristic swelling behaviour of the coatings, we have resolved the differences between estimates of phase transition temperature of a coating's hydration water. Yet, perhaps most significantly, is the apparent strong correlation between estimation of the phase transition temperature and the temperature of the observed jump in ice adhesion strength, plotted in Figure 6 (see SI, section S5 for further details).
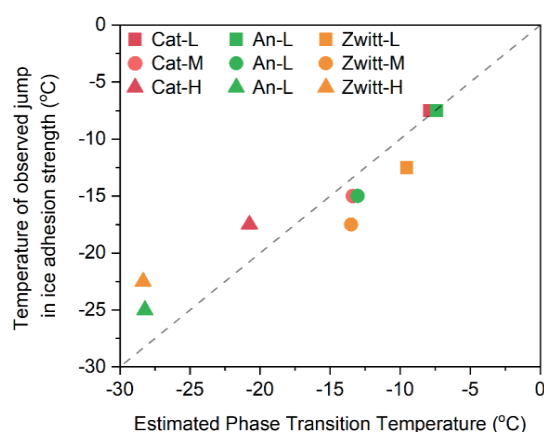
Figure 6: Correlation between observed phase transition temperature (from ice adhesion strength measurements) and estimated phase transition temperatures (calculated by a combination of ellipsometry and DSC). The dashed diagonal line acts as a guide to the eye, where the observed and estimated phase transition temperatures are equivalent.

3.4. Effect of "non-freezable" water on ice adhesion strength

While the sudden increase in ice adhesion strength on charged polymer coatings can be rationalized by the freezing transition of the hydration water in the coating, the low temperature ice adhesion strength cannot, and though requires a different explanation. As previously stated, ice adhesion strengths evidently plateau when the hydration water of the coating is frozen, yielding strengths of 228 ± 18 kPa, 250 ± 24 kPa, and 149 ± 13 kPa for cationic, anionic, and zwitterionic coatings respectively. Furthermore, the crosslink density

of the coatings does not significantly affect these values, exemplifying that this observation is solely depending on the nature of the polymer-bound charge. Previous investigations have demonstrated that greater nonfrozen water content eases the adhesion of ice on charged polymer films, and following in suit, we propose that greater fractions of "non-freezable" water will lessen the adhesion strength of ice to a coating in which the hydration water is already frozen.[34,35] The DSC measurements also unveiling the existence of "non-freezable" water, defined here as the difference between the expected value of the enthalpic melting transition, assuming all water was frozen, and the measured magnitude of the phase transition (see SI section S6). Figure 7a plots the mass fraction of "non-freezable" hydration water with respect to the total amount of hydration water, noting that the amount of crosslinkable groups in the polymers does not appear to have any effect. More significantly, it is clear that the fraction of "non-freezable" water is dependent solely on the identity of the charge bound to the polymer, ranking as anionic $\approx$ cationic < zwitterionic.
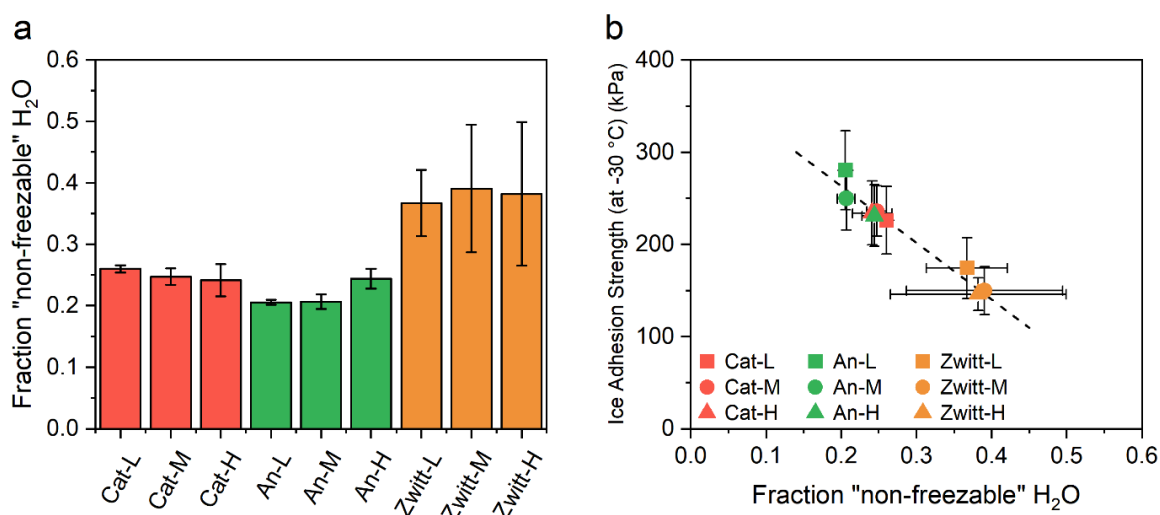
Figure 7: (a) mass fraction of "non-freezable" water in terms of total hydration water. (b) Ice adhesion strength at -30 °C versus the fraction of "non-freezable" hydration water in the polymer coatings.

Polyelectrolytes are known to disrupt the hydrogen bonding environment of water through electrostatic strong polar interactions and structure water according to the characteristics of their charged moieties.[36,48] Meanwhile, zwitterionic polymers naturally have both cationic and anionic charged moieties, forming a strong dipole that when in conjunction with the inherent electrostatic effects, have a stronger interaction with the surrounding water.[49-51] Evidently, this takes shape in the form of greater fractions of "non-freezable" hydration water and is critical for the anti-fouling applications in which zwitterionic polymers are typically employed.[48] To visualize the anti-icing capabilities of charged polymer coatings with respect to their fraction of "non-freezable" hydration water, we present Figure 7b. Here, a correlation can be observed, such that greater fractions of "non-freezable" water will lead to lower ice adhesion strength, validating our previous supposition.

4. Conclusion

In this work, we have designed and synthesized a usable framework for charged anti-icing coatings where the nature of the charge and crosslink density can be systematically and independently controlled. Temperature-dependent ice adhesion measurements, in particular, sudden increases in observed ice adhesion strength, suggested a mechanism on which the adhesion strength of ice is reliant on the physical state of water hydrating the polymer coating. Using a combination of ellipsometry and DSC to estimate the phase transition temperature of a coating's hydration water, a strong correlation was found, demonstrating both the efficacy of the method, and affirming the presence of a phase transition. This explanation satisfied not only the comparison between cationic, anionic, and zwitterionic polymer coatings, but also the differentiation between charged coatings with varying crosslink. In short, charged polymer coatings with high activities and a tightly bound network structure will suppress the freezing of hydration water significantly, resulting in the weak adhesion of ice to lower temperatures. Additionally, at sufficiently low temperatures where the majority of hydration water is frozen, the resulting ice adhesion strength was found to be specific to the nature of the polymer-bound charge and independent of crosslink density. Based on insights into the presence of "non-freezable" water afforded by DSC measurements, we have correlated lower ice adhesion behaviour to a greater fraction of "non-freezable" hydration water that remains nonfrozen, providing molecular mobility and a reduction in interlocking between ice and the surface. Altogether, these findings lay the groundwork onto which charged polymer coatings as anti-icing surfaces can be investigated and enhanced, building on both the suppression of a freezing phase transition and the promotion of high fractions of "non-freezable" water, in the coating's hydration water .

References

(1)   Farzaneh, M. *Atmospheric Icing of Power*; 2008; Vol. 84.

(2)   Parent, O.; Ilinca, A. Anti-Icing and de-Icing Techniques for Wind Turbines: Critical Review. *Cold Reg. Sci. Technol.* **2011**, *65* (1), 88–96. https://doi.org/10.1016/j.coldregions.2010.01.005.

(3)   Yao, X.; Song, Y.; Jiang, L. Applications of Bio-Inspired Special Wettable Surfaces. *Adv. Mater.* **2011**, *23* (6), 719–734. https://doi.org/10.1002/adma.201002689.

(4)   Ryerson, C. C. Ice Protection of Offshore Platforms. *Cold Reg. Sci. Technol.* **2011**, *65* (1), 97–110. https://doi.org/10.1016/j.coldregions.2010.02.006.

(5)   Gao, L.; Hu, H. Wind Turbine Icing Characteristics and Icing-Induced Power Losses to Utility-Scale Wind Turbines. *Proc. Natl. Acad. Sci. U. S. A.* **2021**, *118* (42), 4–6. https://doi.org/10.1073/pnas.2111461118.

(6)   Wu, Z.; Wang, Q. Effect of and Protection from Ice Accretion on Aircraft. In *Ice Adhesion: Mechanism, Measurement and Mitigation*; 2020; pp 567–606. https://doi.org/10.1002/9781119640523.ch19.

(7)   Liu, Y.; Hu, H. Experimental Investigations on Bio-Inspired Icephobic Coatings for Aircraft Inflight Icing Mitigation. In *Ice Adhesion: Mechanism, Measurement and Mitigation*; 2020; pp 547–575. https://doi.org/10.1002/9781119640523.ch18.

(8)   Dalili, N.; Edrisy, A.; Carriveau, R. A Review of Surface Engineering Issues Critical to Wind Turbine Performance. *Renew. Sustain. Energy Rev.* **2009**, *13* (2), 428–438. https://doi.org/10.1016/j.rser.2007.11.009.

(9)   Libisch, B.; French, H. K.; Hartnik, T.; Anton, A.; Biró, B. Laboratory-Scale Evaluation of a Combined Soil Amendment for the Enhanced Biodegradation of Propylene Glycol-Based Aircraft de-Icing Fluids. *Environ. Technol.* **2012**, *33* (6), 717–724. https://doi.org/10.1080/09593330.2011.592222.

(10)   Ma, H.; Ma, H.; Yu, H.; Da, B.; Gong, W.; Zhang, N. The Physical Properties of Organic Aircraft Deicers under Low Temperature. *Cold Reg. Sci. Technol.* **2022**, *196* (April 2021). https://doi.org/10.1016/j.coldregions.2021.103471.

(11)   Zhuo, Y.; Xiao, S.; Amirfazli, A.; He, J.; Zhang, Z. Polysiloxane as Icephobic Materials – The Past, Present and the Future. *Chem. Eng. J.* **2021**, *405* (September 2020), 127088. https://doi.org/10.1016/j.cej.2020.127088.

(12)   Wang, T.; Zheng, Y.; Raji, A. R. O.; Li, Y.; Sikkema, W. K. A.; Tour, J. M. Passive Anti-Icing and Active Deicing Films. *ACS Appl. Mater. Interfaces* **2016**, *8* (22), 14169–14173. https://doi.org/10.1021/acsami.6b03060.

(13)   He, Z.; Zhuo, Y.; Zhang, Z.; He, J. Design of Icephobic Surfaces by Lowering Ice Adhesion Strength: A Mini Review. *Coatings* **2021**, *11* (11), 1–26. https://doi.org/10.3390/coatings11111343.

(14)   Kenzhebayeva, A.; Bakbolat, B.; Sultanov, F.; Daulbayev, C.; Mansurov, Z. A Mini-Review on Recent Developments in Anti-Icing Methods. *Polymers (Basel).* **2021**, *13* (23). https://doi.org/10.3390/polym13234149.

(15)   Golovin, K.; Kobaku, S. P. R.; Lee, D. H.; DiLoreto, E. T.; Mabry, J. M.; Tuteja, A. Designing Durable Icephobic Surfaces. *Sci. Adv.* **2016**, *2* (3). https://doi.org/10.1126/sciadv.1501496.

(16)   Zou, M.; Beckford, S.; Wei, R.; Ellis, C.; Hatton, G.; Miller, M. A. Effects of Surface Roughness and Energy on Ice Adhesion Strength. *Appl. Surf. Sci.* **2011**, *257* (8), 3786–3792. https://doi.org/10.1016/j.apsusc.2010.11.149.

(17)   Chen, J.; Liu, J.; He, M.; Li, K.; Cui, D.; Zhang, Q.; Zeng, X.; Zhang, Y.; Wang, J.; Song, Y. Superhydrophobic Surfaces Cannot Reduce Ice Adhesion. *Appl. Phys. Lett.* **2012**, *101* (11), 95–98. https://doi.org/10.1063/1.4752436.

(18)   Jung, S.; Dorrestijn, M.; Raps, D.; Das, A.; Megaridis, C. M.; Poulikakos, D. Are Superhydrophobic Surfaces Best for Icephobicity? *Langmuir* **2011**, *27* (6), 3059–3066. https://doi.org/10.1021/la104762g.

(19)   Liu, C.; Li, Y.; Lu, C.; Liu, Y.; Feng, S.; Liu, Y. Robust Slippery Liquid-Infused Porous Network Surfaces for Enhanced Anti-Icing/Deicing Performance. *ACS Appl. Mater. Interfaces* **2020**, *12* (22), 25471–25477. https://doi.org/10.1021/acsami.0c05954.

(20)   Boinovich, L. B.; Emelyanenko, K. A.; Emelyanenko, A. M. Superhydrophobic versus SLIPS: Temperature Dependence and the Stability of Ice Adhesion Strength. *J. Colloid Interface Sci.* **2022**, *606*, 556–566. https://doi.org/10.1016/j.jcis.2021.08.030.

(21)   Wong, T. S.; Kang, S. H.; Tang, S. K. Y.; Smythe, E. J.; Hatton, B. D.; Grinthal, A.; Aizenberg, J. Bioinspired Self-Repairing Slippery Surfaces with Pressure-Stable Omniphobicity. *Nature* **2011**, *477* (7365), 443–447. https://doi.org/10.1038/nature10447.

(22)   Stone, H. A. Ice-Phobic Surfaces That Are Wet. *ACS Nano* **2012**, *6* (8), 6536–6540. https://doi.org/10.1021/nn303372q.

(23)   Li, T.; Ibáñez-Ibáñez, P. F.; Håkonsen, V.; Wu, J.; Xu, K.; Zhuo, Y.; Luo, S.; He, J.; Zhang, Z. Self-Deicing Electrolyte Hydrogel Surfaces with Pa-Level Ice Adhesion and Durable Antifreezing/Antifrost Performance. *ACS Appl. Mater. Interfaces* **2020**, *12* (31), 35572–35578. https://doi.org/10.1021/acsami.0c06912.

(24)   Ozbay, S.; Yuceel, C.; Erbil, H. Y. Improved Icephobic Properties on Surfaces with a Hydrophilic Lubricating Liquid. *ACS Appl. Mater. Interfaces* **2015**, *7* (39), 22067–22077. https://doi.org/10.1021/acsami.5b07265.

(25)   Yuan, Y.; Xiang, H.; Liu, G.; Wang, L.; Liu, H.; Liao, R. Self-Repairing Performance of Slippery Liquid Infused Porous Surfaces for Durable Anti-Icing. *Adv. Mater. Interfaces* **2022**, *9* (10), 1–10. https://doi.org/10.1002/admi.202101968.

(26)   Niemelä-Anttonen, H.; Koivuluoto, H.; Tuominen, M.; Teisala, H.; Juuti, P.; Haapanen, J.; Harra, J.; Stenroos, C.; Lahti, J.; Kuusipalo, J.; Mäkelä, J. M.; Vuoristo, P. Icephobicity of Slippery Liquid Infused Porous Surfaces under Multiple Freeze–Thaw and Ice Accretion–Detachment Cycles. *Adv. Mater. Interfaces* **2018**, *5* (20), 1–8. https://doi.org/10.1002/admi.201800828.

(27)   Chen, J.; Dou, R.; Cui, D.; Zhang, Q.; Zhang, Y.; Xu, F.; Zhou, X.; Wang, J.; Song, Y.; Jiang, L. Robust Prototypical Anti-Icing Coatings with a Self-Lubricating Liquid Water Layer between Ice and Substrate. *ACS Appl. Mater. Interfaces* **2013**, *5* (10), 4026–4030. https://doi.org/10.1021/am401004t.

(28)   Dou, R.; Chen, J.; Zhang, Y.; Wang, X.; Cui, D.; Song, Y.; Jiang, L.; Wang, J. Anti-Icing Coating with an Aqueous Lubricating Layer. *ACS Appl. Mater. Interfaces* **2014**, *6* (10), 6998–7003. https://doi.org/10.1021/am501252u.

(29)   Chen, J.; Luo, Z.; Fan, Q.; Lv, J.; Wang, J. Anti-Ice Coating Inspired by Ice Skating. *Small* **2014**, *10* (22), 4693–4699. https://doi.org/10.1002/smll.201401557.

(30)   He, Z.; Zhuo, Y.; Wang, F.; He, J.; Zhang, Z. Design and Preparation of Icephobic PDMS-Based Coatings by Introducing an Aqueous Lubricating Layer and Macro-Crack Initiators at the Ice-Substrate Interface. *Prog. Org. Coatings* **2020**, *147* (April), 105737. https://doi.org/10.1016/j.porgcoat.2020.105737.

(31)   Chen, D.; Gelenter, M. D.; Hong, M.; Cohen, R. E.; McKinley, G. H. Icephobic Surfaces Induced by Interfacial Nonfrozen Water. *ACS Appl. Mater. Interfaces* **2017**, *9* (4), 4202–4214. https://doi.org/10.1021/acsami.6b13773.

(32)   Chen, J.; Li, K.; Wu, S.; Liu, J.; Liu, K.; Fan, Q. Durable Anti-Icing Coatings Based on Self-Sustainable Lubricating Layer. *ACS Omega* **2017**, *2* (5), 2047–2054. https://doi.org/10.1021/acsomega.7b00359.

(33)   Huang, B.; Jiang, S.; Diao, Y.; Liu, X.; Liu, W.; Chen, J.; Yang, H. Hydrogels as Durable Anti-Icing Coatings Inhibit and Delay Ice Nucleation. *Molecules* **2020**, *25* (15). https://doi.org/10.3390/molecules25153378.

(34)   Tao, C.; Bai, S.; Li, X.; Li, C.; Ren, L.; Zhao, Y.; Yuan, X. Formation of Zwitterionic Coatings with an Aqueous Lubricating Layer for Antifogging/Anti-Icing Applications. *Prog. Org. Coatings* **2018**, *115* (November 2017), 56–64. https://doi.org/10.1016/j.porgcoat.2017.11.002.

(35)   Liang, B.; Zhang, G.; Zhong, Z.; Huang, Y.; Su, Z. Superhydrophilic Anti-Icing Coatings Based on Polyzwitterion Brushes. *Langmuir* **2019**, *35* (5), 1294–1301. https://doi.org/10.1021/acs.langmuir.8b01009.

(36)   Bai, S.; Li, X.; Zhang, R.; Li, C.; Zhu, K.; Sun, P.; Zhao, Y.; Ren, L.; Yuan, X. Enhancing Antifogging/Frost-Resisting Performances of Amphiphilic Coatings via Cationic, Zwitterionic or Anionic Polyelectrolytes. *Chem. Eng. J.* **2019**, *357* (July 2018), 667–677. https://doi.org/10.1016/j.cej.2018.09.177.

(37)   He, Z.; Wu, C.; Hua, M.; Wu, S.; Wu, D.; Zhu, X.; Wang, J.; He, X. Bioinspired Multifunctional Anti-Icing Hydrogel. *Matter* **2020**, *2* (3), 723–734. https://doi.org/10.1016/j.matt.2019.12.017.

(38)   Biro, R. A.; Tyrode, E. C.; Thormann, E. Reducing Ice Adhesion to Polyelectrolyte Surfaces by Counterion Mediated Nonfrozen Hydration Water. *Prep.* **2022**.

(39)   Gauthier, M.; Carrozzella, T.; Penlidis, A. Sulfobetaine Zwitterionomers Based on N-Butyl Acrylate and 2-Ethoxyethyl Acrylate: Monomer Synthesis and Copolymerization Behavior. *J. Polym. Sci. Part A Polym. Chem.* **2002**, *40* (4), 511–523. https://doi.org/10.1002/pola.10138.

(40)   Chernyy, S.; Järn, M.; Shimizu, K.; Swerin, A.; Pedersen, S. U.; Daasbjerg, K.; Makkonen, L.; Claesson, P.; Iruthayaraj, J. Superhydrophilic Polyelectrolyte Brush Layers with Imparted Anti-Icing Properties: Effect of Counter Ions. *ACS Appl. Mater. Interfaces* **2014**, *6* (9), 6487–6496. https://doi.org/10.1021/am500046d.

(41)   Liljeblad, J. F. D.; Furó, I.; Tyrode, E. C. The Premolten Layer of Ice next to a Hydrophilic Solid Surface: Correlating Adhesion with Molecular Properties. *Phys. Chem. Chem. Phys.* **2017**, *19* (1), 305–317. https://doi.org/10.1039/c6cp05303c.

(42)   Meuler, A. J.; Smith, J. D.; Varanasi, K. K.; Mabry, J. M.; McKinley, G. H.; Cohen, R. E. Relationships between Water Wettability and Ice Adhesion. *ACS Appl. Mater. Interfaces* **2010**, *2* (11), 3100–3110. https://doi.org/10.1021/am1006035.

(43)   Jian, Y.; Handschuh-Wang, S.; Zhang, J.; Lu, W.; Zhou, X.; Chen, T. Biomimetic Anti-Freezing Polymeric Hydrogels: Keeping Soft-Wet Materials Active in Cold Environments. *Mater. Horizons* **2021**, *8* (2), 351–369. https://doi.org/10.1039/d0mh01029d.

(44)   Makkonen, L. Surface Melting of Ice. *J. Phys. Chem. B* **1997**, *101* (32), 6196–6200. https://doi.org/10.1021/jp963248c.

(45)   Jellinek, H. H. G. Liquid-like (Transition) Layer on Ice. *J. Colloid Interface Sci.* **1967**, *25* (2), 192–205. https://doi.org/10.1016/0021-9797(67)90022-7.

(46)   Ehtiati, K.; Moghaddam, S. Z.; Klok, H.; Daugaard, A. E.; Thormann, E. Speci Fi c Counterion E Ff Ects on the Swelling Behavior of Strong Polyelectrolyte Brushes. **2022**. https://doi.org/10.1021/acs.macromol.2c00411.

(47)   Hegaard, F.; Biro, R. A.; Ehtiati, K.; Thormann, E. Understanding the Ion-Specific Antipolyelectrolyte Effect on Swelling Behaviour of Polyzwitterionic Layers. *Prep.*

(48)   Kardela, J. H.; Millichamp, I. S.; Ferguson, J.; Parry, A. L.; Reynolds, K. J.; Aldred, N.; Clare, A. S. Nonfreezable Water and Polymer Swelling Control the Marine Antifouling Performance of Polymers with Limited Hydrophilic Content. *ACS Appl. Mater. Interfaces* **2019**, *11* (33), 29477–29489. https://doi.org/10.1021/acsami.9b05893.

(49)   Bredas, J. L.; Chance, R. R.; Silbey, R. Head-Head Interactions in Zwitterionic Associating Polymers. *Macromolecules* **1988**, *21* (6), 1633–1639. https://doi.org/10.1021/ma00184a019.

(50)   Georgiev, G. S.; Kamenska, E. B.; Vassileva, E. D.; Kamenova, I. P.; Georgieva, V. T.; Iliev, S. B.; Ivanov, I. A. Self-Assembly, Antipolyelectrolyte Effect, Nonbiofouling Properties of Polyzwitterions.

Biomacromolecules **2006**, *7* (4), 1329–1334. https://doi.org/10.1021/bm050938q.

(51)   Erfani, A.; Seaberg, J.; Aichele, C. P.; Ramsey, J. D. Interactions between Biomolecules and Zwitterionic
        Moieties: A Review. *Biomacromolecules* **2020**, *21* (7), 2557–2573.
        https://doi.org/10.1021/acs.biomac.0c00497.

Supplemental Information

Ice adhesion to cationic, anionic, zwitterionic ,and non-ionic polymer surfaces: on the understanding of the role of hydration water

Robert A. Biro[§], Esben Thormann[§*]

[§]Department of Chemistry, Technical University of Denmark, 2800 Kgs. Lyngby, Denmark

*esth@kemi.dtu.dk

S1: Characterization of cationic, anionic, and zwitterionic polymers

RAFT was used for the successful synthesis of all polymers used in this study. Conversion was monitored by ^{1}H-NMR as the products were precipitated at near full conversion in order to for the polymer composition to be accurate to the targeted composition in each polymerization. Final ^{1}H-NMR spectra of the cationic polyelectrolytes with a target AMA mole fraction of 0.05, 0.1, and 0.15, corresponding to the eventual coating crosslink density "low" (L), "medium" (M), and "high" (H), respectively, and have been reported in our previous study are replicated here in Figures S1-S3.[1] Corresponding spectra of anionic polyelectrolytes in Figures S4-S6 and zwitterionic polymers in Figures S7-S9 are also provided. These characterizations allow us to quantify the composition of the polymers and compare them with their respective targets and is summarized in Table S1.

Polymer	Targeted Compositiion (mole percent)			Calculated Composition (mole percent)		
	Charge Monomer	n-BMA	AMA	Charged Monomer	n-BMA	AMA
Cat-L	25	70	5	28.4	66.1	5.5
Cat-M	25	65	10	28.0	62.1	9.9
Cat-H	25	60	15	26.2	58.7	15.1
An-L	25	70	5	24.9	69.8	5.3
An-M	25	65	10	25.0	64.8	10.2
An-H	25	60	15	24.9	59.7	15.5
Zwitt-L	25	70	5	23.9	71.4	4.7
Zwitt-M	25	65	10	24.3	67.2	8.5
Zwitt-H	25	60	15	23.9	61.8	14.3

Table 1: Targeted and calculated monomer compositions in the polymer. Remaining polymer composition is n-BMA.
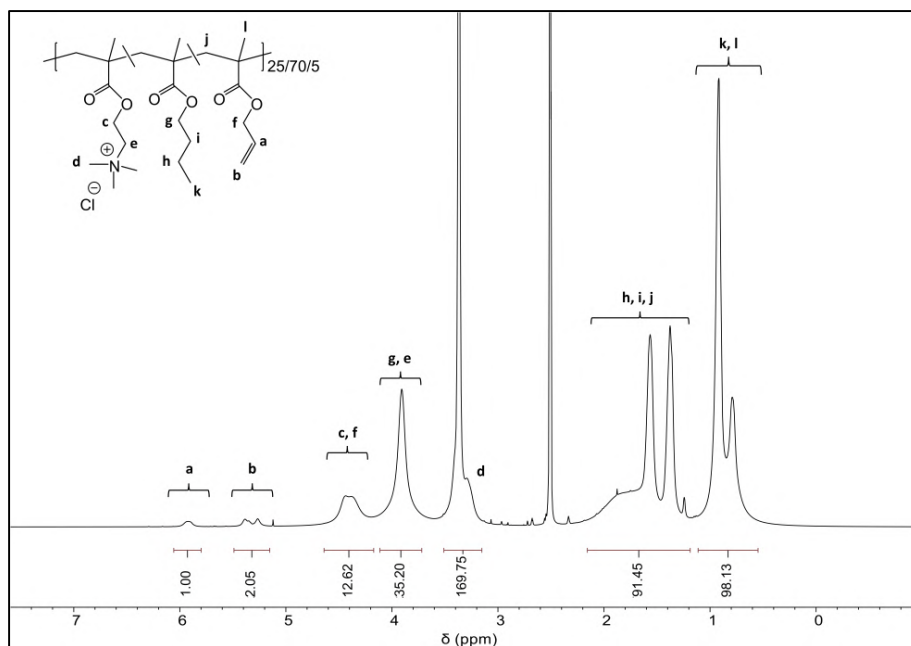
Figure S1: 1H-NMR spectra (400 MHz, DMSO-d$_6$) of cationic polyelectrolyte with ∼5 mol. %: δ 6.06-5.80 (b, 1.00H), 5.49-5.17 (b, 2.05H), 4.64-4.20 (b, 12.62H), 4.19-3.61 (b, 35.20H), 3.59-3.13 (b, 169.75 H), 2.09-1.19 (b, 91.45H), 1.17-0.55 (b, 98.13H).
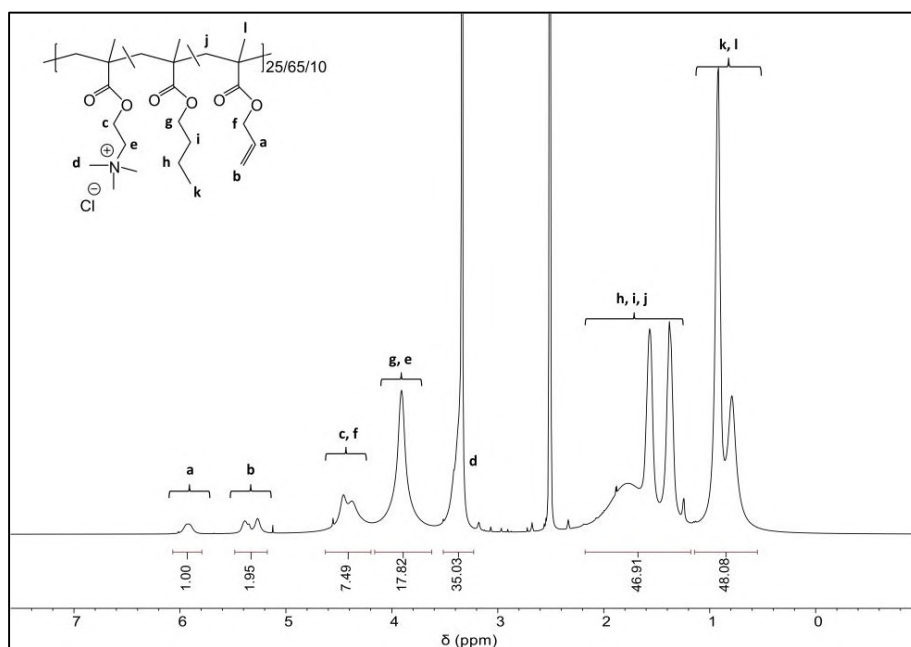
Figure S2 : 1H-NMR spectra (400 MHz, DMSO-d$_6$) of cationic polyelectrolyte with ∼10 mol. % : δ 6.07-5.80 (b, 1.00H), 5.49-5.16 (b, 1.95H), 4.63-4.24 (b, 7.49H), 4.18-3.60 (b, 17.82H), 3.55-3.22 (b, 35.03 H), 2.17-1.18 (b, 46.91H), 1.14-0.55 (b, 48.08H).
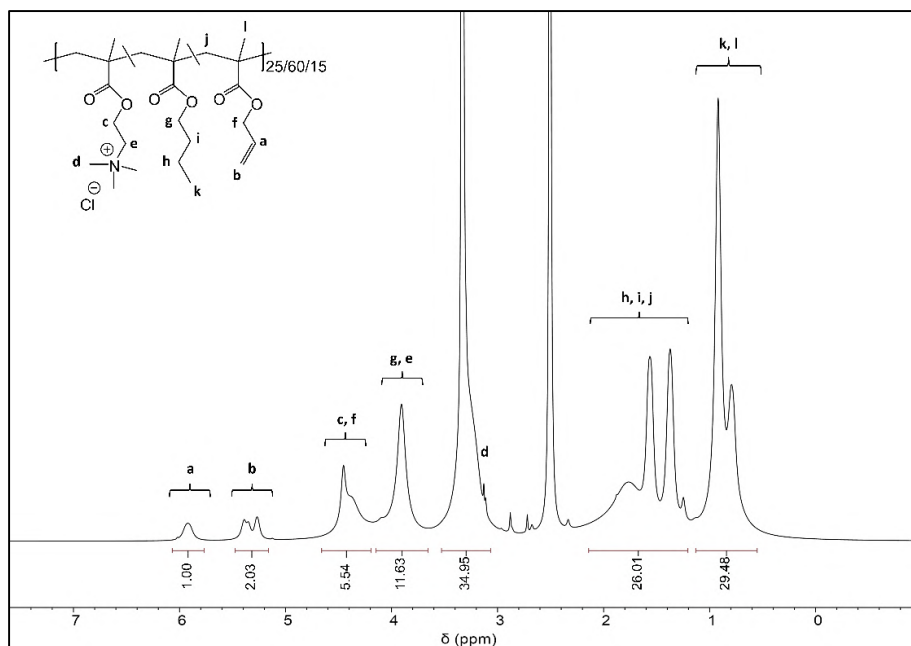
Figure S3: ^{1}H-NMR spectra (400 MHz, DMSO-d$_6$) of cationic polyelectrolyte with ~15 mol. % AMA: δ 6.07-5.77 (b, 1.00H), 5.53-5.16 (b, 2.03H), 4.66-4.19 (b, 5.54H), 4.15-3.66 (b, 11.63H), 3.63-2.98 (b, 34.95H), 2.18-1.20 (b, 26.01H), 1.13-0.55 (b, 29.48H).
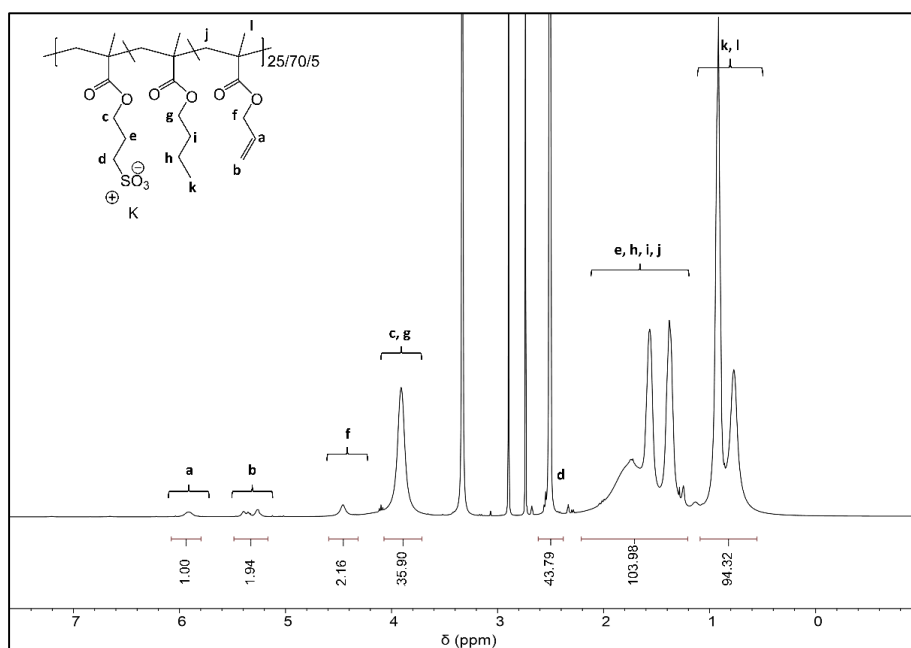
Figure S4: ^{1}H-NMR spectra (400 MHz, DMSO-d$_6$) of anionic polyelectrolyte with ~5 mol. % AMA. δ 6.06-5.80 (b, 1.00H), 5.47-5.19 (b, 1.94H), 4.59-4.32 (b, 2.16H), 4.09-3.72 (b, 35.90H), 2.63-2.40 (b, 43.79H), 2.21-1.22 (b,103.98H), 1.06 – 0.55 (b, 90.32H).
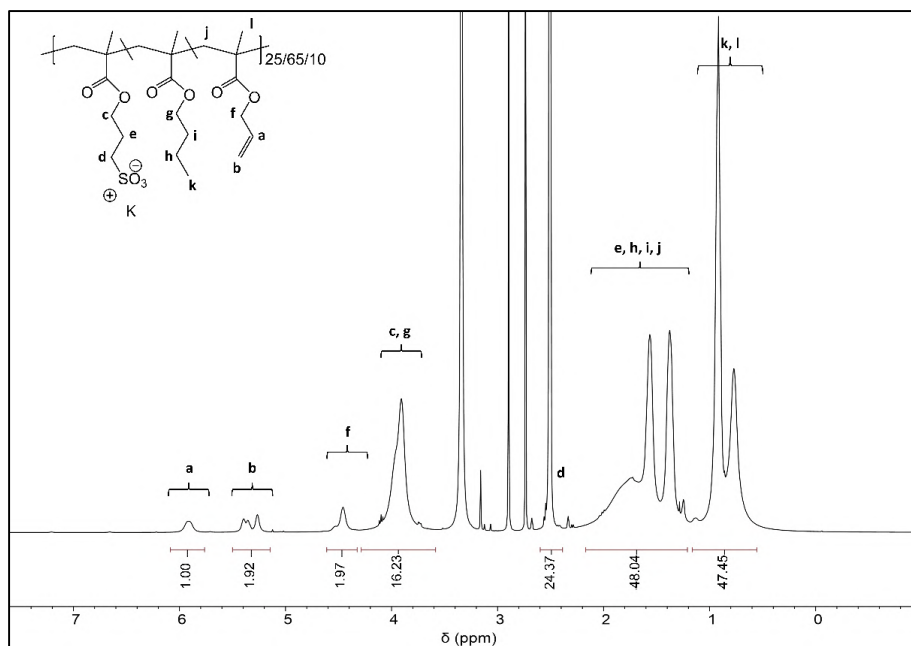
Figure S5: ¹H-NMR spectra (400 MHz, DMSO-d$_6$) of anionic polyelectrolyte with ∼10 mol. % AMA. δ 6.08-5.77 (b, 1.00H), 5.49-5.15 (b, 1.92H), 4.60-4.33 (b, 1.97H), 4.28-3.58 (b, 16.23H), 2.60-2.39 (b, 24.37H), 2.17-1.21 (b,48.04H), 1.17 – 0.54 (b, 47.45H).
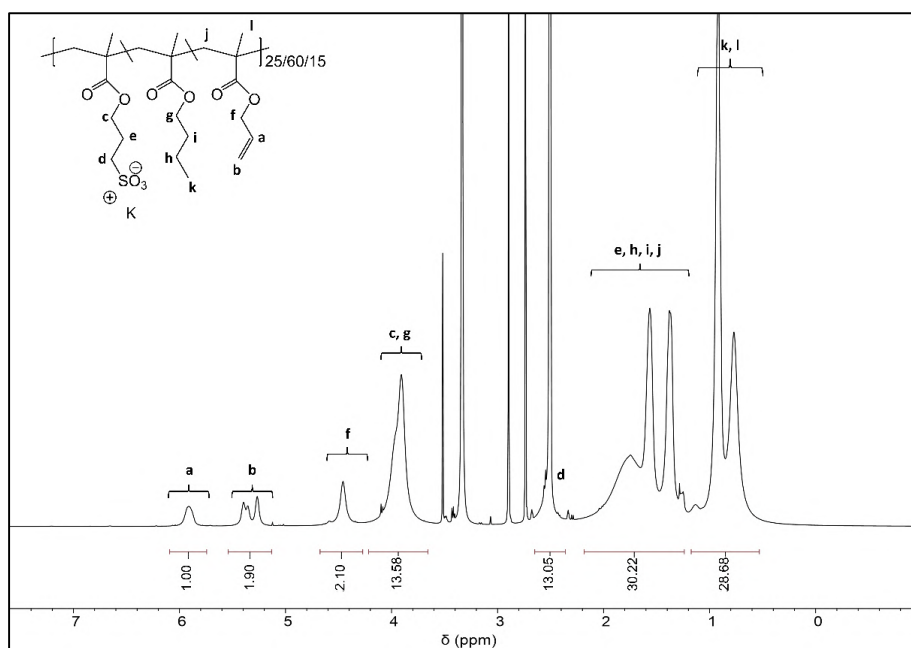
Figure S6: ¹H-NMR spectra (400 MHz, DMSO-d$_6$) of anionic polyelectrolyte with ∼15 mol. % AMA. δ 6.08-5.75 (b, 1.00H), 5.55-5.14 (b, 1.90H), 4.68-4.29 (b, 2.10H), 4.22-3.66 (b, 13.58H), 2.68-2.37 (b, 13.05H), 2.19-1.24 (b, 30.22H), 1.17 – 0.54 (b, 28.68H).
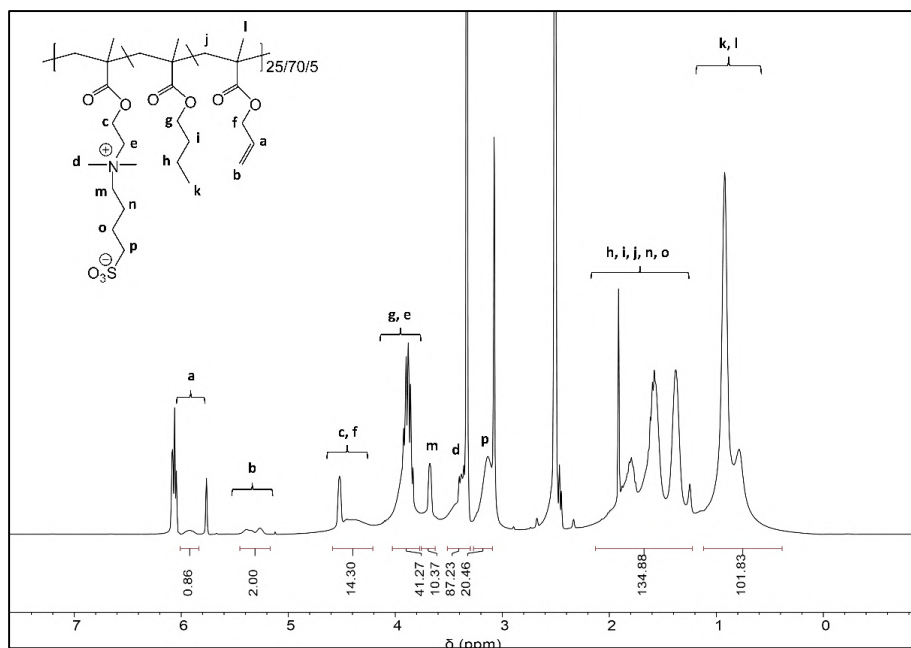
Figure S7: ^{1}H-NMR spectra (400 MHz, DMSO-d$_6$) zwitterionic polymer with ~5 mol. % AMA. δ 6.04-5.82 (b, 0.86H), 5.45-5.17 (b, 2.00H), 4.59-4.22 (b, 14.30H), 4.04-3.77 (b, 41.27H), 3.76-3.63 (b, 10.37H), 3.52-3.30 (b, 87.23H), 3.27-3.09 (b, 20.46H), 2.14-1.22 (b, 134.88H), 1.12- 0.41 (b, 101.83H).
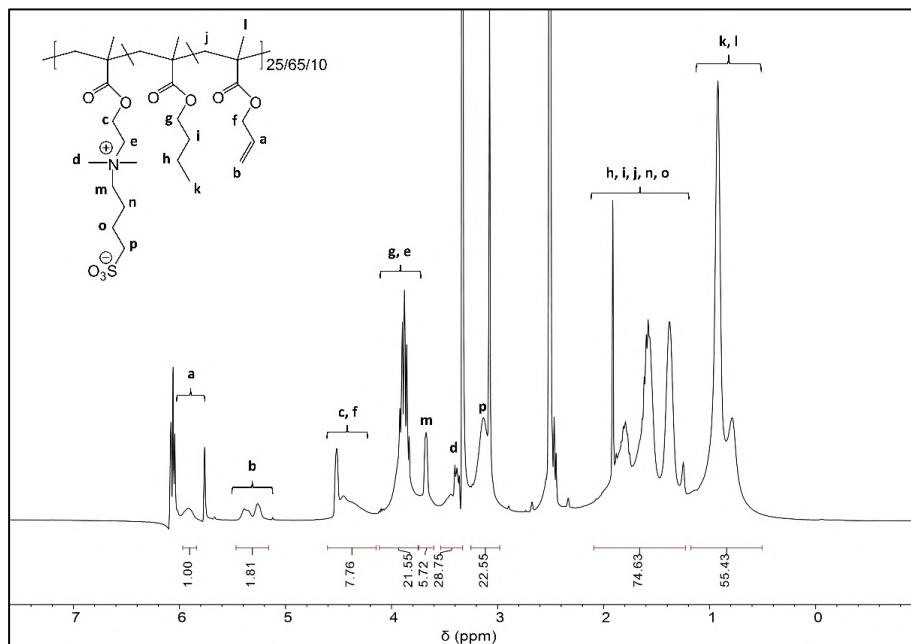
Figure S8: ^{1}H-NMR spectra (400 MHz, DMSO-d$_6$) zwitterionic polymer with ~10 mol. % AMA. δ 5.97-5.84 (b, 1.00H), 5.47-5.16 (b, 1.81H), 4.61-4.15 (b, 7.76H), 4.11-3.77 (b, 21.55H), 3.75-3.61 (b, 5.72H), 3.53-3.33 (b, 28.75H), 3.25-2.99 (b, 22.55H), 2.11-1.23 (b, 74.65H), 1.17- 0.51 (b, 55.43H).
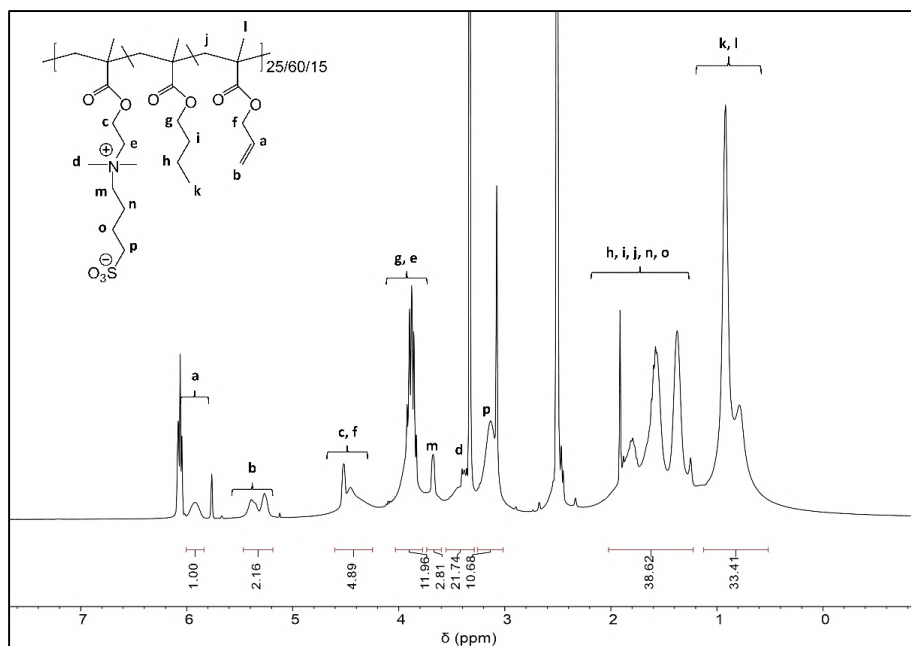
Figure S9: ¹H-NMR spectra (400 MHz, DMSO-d$_6$) zwitterionic polymer with ~15 mol. % AMA. δ 6.01-5.84 (b, 1.00H), 5.46-5.19 (b, 2.16H), 4.60-4.25 (b, 4.89H), 4.04-3.77 (b, 11.96H), 3.74-3.61 (b, 2.81H), 3.55-3.30 (b, 21.74H), 3.26-3.01 (b, 10.68H), 2.04-1.20 (b, 36.62H), 1.13- 0.51 (b, 33.61H)

S2: Ellipsometry data, modelling, and results

Coatings thicknesses were measured using a spectroscopic ellipsometer (J.A. Woollam, M-2000). To minimize the effects of ambient humidity hydrating the films, measurements of dry thickness were conducted with a dry-stream of nitrogen that flowed lightly over the samples. Analysis of the coatings was completed using CompleteEase, the instruments software, whereby a slab model was used to describe the coating. Here, a Si substrate layer, a 1 nm intermediate Si-SiO$_2$ layer, and a 100 nm SiO$_2$ layer were ordered below a Cauchy model (in the form of: $n(\lambda) = A + B/\lambda^2$).

Hydrated/swollen thicknesses of the coatings were measured using a 5 mL liquid cell set to 25 °C. Milli-Q water flowed onto the samples and left to equilibrate for at least 20 minutes before measurements were taken. Modeling the thicknesses was accomplished using the same Si, Si-SiO$_2$, and SiO$_2$ layers as above, and a two-component layer consisting of the dry polymer (with fitted A & B parameters from dry measurements) and water. Fitting according to the Bruggeman Effective Medium Approximation (BEMA) gave values of hydrated coating thickness and volume fraction of water.

Table S2-Table S4 display dry measurements on one of the coatings in the set measured. Corresponding hydrated measurements of those samples are shown in Table S5-S7. Averages and standard deviations of each set of coatings is shown in Figure 4 of the main manuscript, with labels of the averaged volume fraction of H$_2$O attached.

Coating	Fit Results	Optical Model	Ψ (Psi) Data & Model	Δ (Delta) Data & Model
Cat-L	MSE = 15.366 Thickness # 3 = 94.39 ± 0.051 nm A = 1.487 ± 0.00025900 B = 0.00671 ± 4.6051E-05	- Layer # 3 = Cauchy Thickness # 3 = 94.39 nm (fit) A = 1.487 (fit) B = 0.00671 (fit) C = 0.0000 + Urbach Absorption Parameters Layer # 2 = SIO2_JAW Thickness # 2 = 100.00 nm Layer # 1 = INTR_JAW Thickness # 1 = 1.00 nm Substrate = SI_JAW		
Cat-M	MSE = 16.643 Thickness # 3 = 112.45 ± 0.062 nm A = 1.490 ± 0.00029387 B = 0.00513 ± 4.4969E-05	- Layer # 3 = Cauchy Thickness # 3 = 112.45 nm (fit) A = 1.490 (fit) B = 0.00513 (fit) C = 0.0000 + Urbach Absorption Parameters Layer # 2 = SIO2_JAW Thickness # 2 = 100.00 nm Layer # 1 = INTR_JAW Thickness # 1 = 1.00 nm Substrate = SI_JAW		
Cat-H	MSE = 17.124 Thickness # 3 = 111.75 ± 0.063 nm A = 1.488 ± 0.00029854 B = 0.00426 ± 4.5187E-05	- Layer # 3 = Cauchy Thickness # 3 = 111.75 nm (fit) A = 1.488 (fit) B = 0.00426 (fit) C = 0.0000 + Urbach Absorption Parameters Layer # 2 = SIO2_JAW Thickness # 2 = 100.00 nm Layer # 1 = INTR_JAW Thickness # 1 = 1.00 nm Substrate = SI_JAW		

Table S2: Dry ellipsometry fit results, optical model, and data on cationic polyelectrolyte coatings with variable crosslink density

Coating	Fit Results	Optical Model	Ψ (Psi) Data & Model	Δ (Delta) Data & Model
An-L	MSE = 6.566 Thickness # 3 = 64.58 ± 0.022 nm A = 1.479 ± 0.00014453 B = 0.00482 ± 2.4140E-05	- Layer # 3 = Cauchy Thickness # 3 = **64.58 nm** (fit) A = **1.479** (fit) B = **0.00482** (fit) C = 0.0000 + **Urbach Absorption Parameters** Layer # 2 = SiO2_JAW Thickness # 2 = 100.00 nm Layer # 1 = INTR_JAW Thickness # 1 = 1.00 nm Substrate = Si_JAW		
An-M	MSE = 15.740 Thickness # 3 = 78.81 ± 0.112 nm A = 1.498 ± 0.00064792 B = 0.01128 ± 0.00013581	- Layer # 3 = Cauchy Thickness # 3 = **78.81 nm** (fit) A = **1.498** (fit) B = **0.01128** (fit) C = 0.0000 + **Urbach Absorption Parameters** Layer # 2 = SiO2_JAW Thickness # 2 = 100.00 nm Layer # 1 = INTR_JAW Thickness # 1 = 1.00 nm Substrate = Si_JAW		
An-H	MSE = 12.300 Thickness # 3 = 91.14 ± 0.040 nm A = 1.491 ± 0.00020969 B = 0.00603 ± 3.6964E-05	- Layer # 3 = Cauchy Thickness # 3 = **91.14 nm** (fit) A = **1.491** (fit) B = **0.00603** (fit) C = 0.0000 + **Urbach Absorption Parameters** Layer # 2 = SiO2_JAW Thickness # 2 = 100.00 nm Layer # 1 = INTR_JAW Thickness # 1 = 1.00 nm Substrate = Si_JAW		

Table S3:Dry ellipsometry fit results, optical model, and data on anionic polyelectrolyte coatings with variable crosslink density

Coating	Fit Results	Optical Model	Ψ (Psi) Data & Model	Δ (Delta) Data & Model
Zwitt-L	MSE = 28.974 Thickness # 3 = 86.80 ± 0.094 nm A = 1.484 ± 0.00050027 B = 0.00674 ± 9.3568E-05	- Layer # 3 = Cauchy Thickness # 3 = **86.80 nm** (fit) A = **1.484** (fit) B = **0.00674** (fit) C = 0.0000 + Urbach Absorption Parameters Layer # 2 = SIO2_JAW Thickness # 2 = 100.00 nm Layer # 1 = INTR_JAW Thickness # 1 = 1.00 nm Substrate = SI_JAW		
Zwitt-M	MSE = 18.668 Thickness # 3 = 98.09 ± 0.062 nm A = 1.489 ± 0.00031401 B = 0.00593 ± 5.2887E-05	- Layer # 3 = Cauchy Thickness # 3 = **98.09 nm** (fit) A = **1.489** (fit) B = **0.00593** (fit) C = 0.0000 + Urbach Absorption Parameters Layer # 2 = SIO2_JAW Thickness # 2 = 100.00 nm Layer # 1 = INTR_JAW Thickness # 1 = 1.00 nm Substrate = SI_JAW		
Zwitt-H	MSE = 25.052 Thickness # 3 = 97.41 ± 0.083 nm A = 1.494 ± 0.00042493 B = 0.00598 ± 7.1253E-05	- Layer # 3 = Cauchy Thickness # 3 = **97.41 nm** (fit) A = **1.494** (fit) B = **0.00598** (fit) C = 0.0000 + Urbach Absorption Parameters Layer # 2 = SIO2_JAW Thickness # 2 = 100.00 nm Layer # 1 = INTR_JAW Thickness # 1 = 1.00 nm Substrate = SI_JAW		

Table S4: Dry ellipsometry fit results, optical model, and data on zwitterionic polymer coatings with variable crosslink density.

Coating	Fit Results	Optical Model	Ψ (Psi) and Δ (Delta) Data & Model

Cat-L	MSE = 41.387
	Thickness # 3 = 228.95 ± 0.524 nm
	EMA % (Mat 2) = 58.7 ± 0.28
		Layer # 3 = EMA Thickness # 3 = **228.95 nm** (fit)
		  # of Constituents = 2
		  - Material 1 = Cauchy
		    A = 1.487 B = 0.00671 C = 0.0000
		    + Urbach Absorption Parameters
		  Material 2 = H2O
		  EMA % (Mat 2) = **58.7** (fit)
		  Depolarization = 0.333 Analysis Mode = Bruggeman
		Layer # 2 = SIO2_JAW Thickness # 2 = 100.00 nm
		Layer # 1 = INTR_JAW Thickness # 1 = 1.00 nm
		Substrate = SI_JAW	

Cat-M	MSE = 54.020
	Thickness # 3 = 198.24 ± 0.477 nm
	EMA % (Mat 2) = 43.9 ± 0.27
		Layer # 3 = EMA Thickness # 3 = **198.24 nm** (fit)
		  # of Constituents = 2
		  - Material 1 = Cauchy
		    A = 1.490 B = 0.00513 C = 0.0000
		    + Urbach Absorption Parameters
		  Material 2 = H2O
		  EMA % (Mat 2) = **43.9** (fit)
		  Depolarization = 0.333 Analysis Mode = Bruggeman
		Layer # 2 = SIO2_JAW Thickness # 2 = 100.00 nm
		Layer # 1 = INTR_JAW Thickness # 1 = 1.00 nm
		Substrate = SI_JAW	

Cat-H	MSE = 32.080
	Thickness # 3 = 148.72 ± 0.351 nm
	EMA % (Mat 2) = 28.6 ± 0.21
		Layer # 3 = EMA Thickness # 3 = **148.72 nm** (fit)
		  # of Constituents = 2
		  - Material 1 = Cauchy
		    A = 1.488 B = 0.00426 C = 0.0000
		    + Urbach Absorption Parameters
		  Material 2 = H2O
		  EMA % (Mat 2) = **28.6** (fit)
		  Depolarization = 0.333 Analysis Mode = Bruggeman
		Layer # 2 = SIO2_JAW Thickness # 2 = 100.00 nm
		Layer # 1 = INTR_JAW Thickness # 1 = 1.00 nm
		Substrate = SI_JAW	

Table S5: Hydrated ellipsometry results, fittings, and measurements of cationic polyelectrolyte coatings with varying crosslink density.

Coating	Fit Results	Optical Model	Ψ (Psi) and Δ (Delta) Data & Model

An-L	MSE = 29.344
	Thickness # 3 = 169.26 ± 0.231 nm
	EMA % (Mat 2) = 63.4 ± 0.19
		Layer # 3 = EMA Thickness # 3 = **169.26 nm** (fit)
		  # of Constituents = 2
		  - Material 1 = Cauchy
		    A = 1.479 B = 0.00482 C = 0.0000
		    + Urbach Absorption Parameters
		  Material 2 = H2O
		  EMA % (Mat 2) = **63.4** (fit)
		  Depolarization = 0.333 Analysis Mode = Bruggeman
		Layer # 2 = SIO2_JAW Thickness # 2 = 100.00 nm
		Layer # 1 = INTR_JAW Thickness # 1 = 1.00 nm
		Substrate = SI_JAW	

An-M	MSE = 33.718
	Thickness # 3 = 137.82 ± 0.390 nm
	EMA % (Mat 2) = 43.9 ± 0.25
		Layer # 3 = EMA Thickness # 3 = **137.82 nm** (fit)
		  # of Constituents = 2
		  - Material 1 = Cauchy
		    A = 1.498 B = 0.01128 C = 0.0000
		    + Urbach Absorption Parameters
		  Material 2 = H2O
		  EMA % (Mat 2) = **43.9** (fit)
		  Depolarization = 0.333 Analysis Mode = Bruggeman
		Layer # 2 = SIO2_JAW Thickness # 2 = 100.00 nm
		Layer # 1 = INTR_JAW Thickness # 1 = 1.00 nm
		Substrate = SI_JAW	

An-H	MSE = 36.212
	Thickness # 3 = 128.92 ± 0.377 nm
	EMA % (Mat 2) = 27.0 ± 0.31
		Layer # 3 = EMA Thickness # 3 = **128.92 nm** (fit)
		  # of Constituents = 2
		  - Material 1 = Cauchy
		    A = 1.491 B = 0.00603 C = 0.0000
		    + Urbach Absorption Parameters
		  Material 2 = H2O
		  EMA % (Mat 2) = **27.0** (fit)
		  Depolarization = 0.333 Analysis Mode = Bruggeman
		Layer # 2 = SIO2_JAW Thickness # 2 = 100.00 nm
		Layer # 1 = INTR_JAW Thickness # 1 = 1.00 nm
		Substrate = SI_JAW	

Table S6: Hydrated ellipsometry results, fittings, and measurements of anionic polyelectrolyte coatings with varying crosslink density.

Coating	Fit Results	Optical Model	Ψ (Psi) and Δ (Delta) Data & Model

Zwitt-L	MSE = 25.375
	Thickness # 3 = 114.31 ± 0.288 nm
	EMA % (Mat 2) = 26.1 ± 0.24
		- Layer # 3 = EMA Thickness # 3 = **114.31 nm** (fit)
		  # of Constituents = 2
		  - Material 1 = Cauchy
		    A = 1.484 B = 0.00674 C = 0.0000
		    + Urbach Absorption Parameters
		  Material 2 = H2O
		  EMA % (Mat 2) = **26.1** (fit)
		  Depolarization = 0.333 Analysis Mode = Bruggeman
		Layer # 2 = SIO2_JAW Thickness # 2 = 100.00 nm
		Layer # 1 = INTR_JAW Thickness # 1 = 1.00 nm
		Substrate = SI_JAW	

Zwitt-M	MSE = 25.264
	Thickness # 3 = 121.90 ± 0.263 nm
	EMA % (Mat 2) = 18.5 ± 0.23
		- Layer # 3 = EMA Thickness # 3 = **121.90 nm** (fit)
		  # of Constituents = 2
		  - Material 1 = Cauchy
		    A = 1.489 B = 0.00593 C = 0.0000
		    + Urbach Absorption Parameters
		  Material 2 = H2O
		  EMA % (Mat 2) = **18.5** (fit)
		  Depolarization = 0.333 Analysis Mode = Bruggeman
		Layer # 2 = SIO2_JAW Thickness # 2 = 100.00 nm
		Layer # 1 = INTR_JAW Thickness # 1 = 1.00 nm
		Substrate = SI_JAW	

Zwitt-H	MSE = 23.149
	Thickness # 3 = 107.74 ± 0.246 nm
	EMA % (Mat 2) = 11.8 ± 0.18
		- Layer # 3 = EMA Thickness # 3 = **107.74 nm** (fit)
		  # of Constituents = 2
		  - Material 1 = Cauchy
		    A = 1.494 B = 0.00598 C = 0.0000
		    + Urbach Absorption Parameters
		  Material 2 = H2O
		  EMA % (Mat 2) = **11.8** (fit)
		  Depolarization = 0.333 Analysis Mode = Bruggeman
		Layer # 2 = SIO2_JAW Thickness # 2 = 100.00 nm
		Layer # 1 = INTR_JAW Thickness # 1 = 1.00 nm
		Substrate = SI_JAW	

Table S7: Hydrated ellipsometry results, fittings, and measurements of zwitterionic polymer coatings with varying crosslink density.
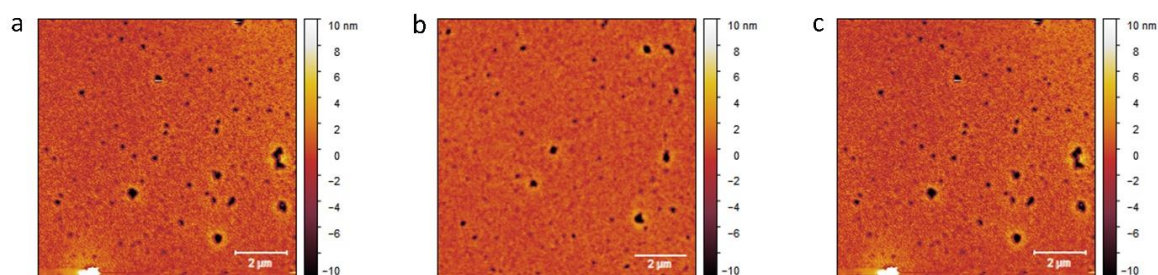
S3: AFM images of polymer coatings

Figure S10: AFM images of cationic polyelectrolyte coatings with (a) low (b) medium and (c) high crosslink density.
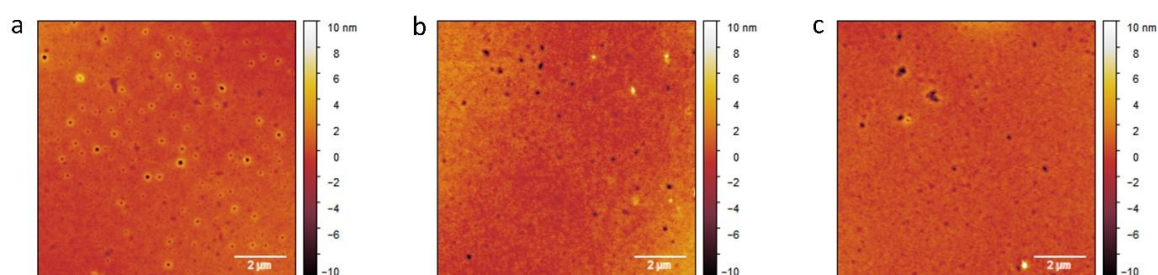

Figure S11:AFM images of anionic polyelectrolyte coatings with (a) low (b) medium and (c) high crosslink density.
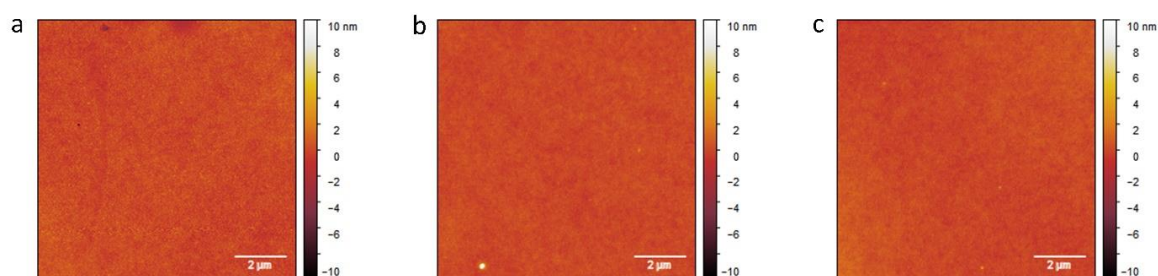
Figure 12: AFM images of zwitterionic polymer coatings with (a) low (b) medium and (c) high crosslink density.

S4: Freezing point depression in concentrated charged polymer solutions

Melting onset temperatures ($T_{m\ onset}$) was measured by DSC of concentrated aqueous charged polymer solutions of with mass fractions ranging from 0.09 – 0.8. As freezing point depression is often plotted and compared at various concentrations, usually molality, plots of melting onset temperature vs. polymer concentration (mol/kg) were prepared, as seen in Figure 5 in the main manuscript. In order to convert from mass fraction of water to molality, it is first necessary to know the molar mass of the polymer (here we assume targeted fractions and degree of polymerization), using Eq. S1 Following this, polymer molality in each sample can be calculated from the corresponding mass fraction through Eq. S2.

For the estimation of the phase transition temperature of the hydration water in each polymer coating, it was necessary to know the polymer concentration in a swollen polymer film. As volume fractions were derived from ellipsometry, corresponding mass fractions could be calculated using density of each component (water and the polymers). The density of bulk 'medium crosslink density' polymers was measured as in our previous manuscript. Here, the density of any dry polymer synthesized was approximate by adding a known mass of polymer to a precisely known volume a non-solvent (hexanes). After equilibrating for one week, the mass and volume of the combined mixture was recorded, and the volume of the polymer could be approximated. Dividing the dry polymer mass over the volume of the polymer gave the density of each polymer: $\rho_{Cat-M} = 1.071$ g/mL, $\rho_{Cat-M} = 1.128$ g/mL, $\rho_{Cat-M} = 1.031$ g/mL.

Following approximations of polymer density, the mass fraction of water in the polymer coating could be determined by Eq. S3. These values were then substituted into Eq. S4, to determine the polymer concentration (molality) in the coating. The molality of the polymer in the coating was then plotted, as seen in drop-lines in Figure 5 in the main manuscript, allowing the for estimation of phase transition temperature of the hydration water in the coatings, values of which are listed in Table S8.

Coating	Polymer concentration in coating (molality)	Estimate of phase transition temperature of coating hydration water (°C)
Cat-L	0.02541	-7.6
Cat-M	0.04767	-13.1
Cat-H	0.09304	-20.8
An-L	0.02133	-7.4
An-M	0.04561	-13.0
An-H	0.10069	-28.2
Zwitt-L	0.08246	-9.5
Zwitt-M	0.12560	-13.5
Zwitt-H	0.21195	-28.3

Table S8: Estimations of phase transition temperature of hydration water in various coating.

$$Molar\ mass\ Polymer\ (M_{polymer}) = \sum_{i=1}^{N} M_i \cdot D_p \cdot x_i$$

Eq. S1

Here, M_i for each monomer is without the counterion, 172.25 g/mol (METAC), 206.32 g/mol (SPMAK), 293.38 g/mol (SBMA) 142.20 g/mol (n-BMA), and 126.15 g/mol (AMA). D_p, the degree of polymerization, is 200, the targeted value.

$$Polymer\ molality = \frac{m_{polymer}}{M_{polymer}} \Big/ m_{H_2O\ total}$$

Eq. S2

$m_{polymer}$ is in units of grams, $M_{polymer}$ is in g/mol, and $m_{H_2O\ total}$ is in kg/mol.

$$w_{H_2O} = \frac{\left(\varphi_{H_2O} \cdot \rho_{H_2O}\right)}{\left(\left(\varphi_{H_2O} \cdot \rho_{H_2O}\right) + \left(1 - \varphi_{H_2O}\right) \cdot \rho_{polymer}\right)}$$

Eq. S3

ρ_{H_2O} is 0.997 g/mL, and $\rho_{polymer}$ is 1.071 g/mL

$$Polymer\ molality_{coating} = \frac{\left(\frac{\left(1 - w_{H_2O}\right)}{1000}\right) \Big/ M_{polymer}}{\left(\frac{w_{H_2O}}{1 \cdot 10^6}\right)}$$

Eq. S4

S5: Correlation of observed jump in ice adhesion strength to estimated phase transition temperature

Figure 6 in the main manuscript was produced comparing the estimations of phase transition temperature (in Table S8 above) to the observed jump in ice adhesion strength. Here, based on the temperature dependent ice adhesion data, values were listed at a specific temperature, or in-between two temperatures, depending on the magnitude of the increase in ice adhesion strength. For example, the sudden increase in ice adhesion strength seen in Cat-L, seemingly occurs between -5 °C and -10 °C, and is therefore defined at -10.0 °C. Meanwhile the increase in ice adhesion strength occurs approximately at -15 °C for Cat-M and is therefore defined at that value. Table S9 below lists the temperature of the observed jump in ice adhesion strength as plotted in Figure 6.

Coating	Temperature of observed jump in ice adhesion strength (°C)
Cat-L	-7.5
Cat-M	-15
Cat-H	-17.5
An-L	-7.5
An-M	-15
An-H	-25
Zwitt-L	-12.5
Zwitt-M	-17.5
Zwitt-H	-22.5

Table S9: Temperature of observed jump in ice adhesion strength.

S6: DSC data and analysis towards fraction of "non-freezable" water

In addition to quantifying the freezing point depression of aqueous charged polymer solutions, DSC also gave information regarding the fractions of freezable and "non-freezable" water in each polymer sample. As detailed in our previous investigation, the masses of freezable and "non-freezable" water could be gleamed from the melting enthalpy using Equation S5 and S6, respectively. "Non-freezable" water mass was then converted to a mass fraction, with regards to total water in the sample (Equation S7), or the mass of polymer in the sample (Equation S8).

Values in Table S19 describe the fraction of different types of water in each polymer coating. The conversion of volume fraction of water to mass fraction was accomplished using the density of the polymer, after which Equation SX was used to determine the mass of water in the polymer coating. From this, fractions of "non-freezable" and freezable water in the polymer coating could be establish using Equations S10 and S11, respectively. Finally, Equation S12 was used to quantity the mass fraction of "non-freezable" water in the total hydration water in the coating. simplifying to Equation S8.

Eq. S5
$$m_{H_2O\ freezable} = \Delta H_f \Big/ 334\ mJ/mg$$

Eq. S6
$$m_{H_2O\ "non-freezable"} = m_{H_2O\ total} - m_{H_2O\ freezable}$$

Eq. S7
$$\frac{m_{H_2O\ "non\text{-}freezable"}}{mg\ H_2O} = \frac{m_{H_2O\ "non\text{-}freezable"}}{m_{H_2O}\ total}$$

Eq. S8
$$\frac{m_{H_2O\ "non-freezable"}}{mg\ polymer} = \frac{m_{H_2O\ "non-freezable"}}{m_{polymer}}$$

Eq. S9
$$\frac{m_{H_2O}}{mg\ polymer\ coating} = \frac{w_{H_2O}}{1 - w_{H_2O}}$$

Eq. S10 $$\frac{m_{H_2O \text{ "non-freezable"}}}{mg \text{ polymer coating}} = \frac{m_{H_2O \text{ "non-freezable"}}}{mg \text{ polymer}} \cdot \frac{m_{H_2O}}{mg \text{ polymer coating}}$$

Eq. S11 $$\frac{m_{H_2O \text{ freezable}}}{mg \text{ polymer coating}} = \frac{m_{H_2O}}{mg \text{ polymer coating}} - \frac{m_{H_2O \text{ "non-freezable"}}}{mg \text{ polymer coating}}$$

Eq. S12 $$\left(\frac{m_{H_2O \text{ non-freezable}}}{m_{H_2O \text{ in coating}}}\right) = \frac{\left(\frac{m_{H_2O \text{ "non-freezable"}}}{mg \text{ coating}}\right)}{\left[\left(\frac{m_{H_2O \text{ "non-freezable"}}}{mg \text{ coating}}\right) + \left(\frac{m_{H_2O \text{ freezable}}}{mg \text{ coating}}\right)\right]} = \frac{m_{H_2O \text{ "non-freezable"}}}{m_{H_2O \text{ total}}}$$

w_{H_2O}	Mass Polymer Cat-L (mg)	Mass H$_2$O (mg)	ΔH_f (mJ)	$m_{H_2O\,freezable}$ (mg)	$m_{H_2O\,nonfreezable}$ (mg)	$\dfrac{m_{H_2O\,\text{"non-freezable"}}}{mg\ H_2O}$	$\dfrac{m_{H_2O\,nonfreezable}}{mg\ polymer}$
0.09	21.71	2.17	-	-	-	-	-
0.17	15.44	3.09	-	-	-	-	-
0.23	16.23	4.87	499.84	1.497	3.372	0.693	0.208
0.33	14.00	7.00	1207.08	3.614	3.386	0.484	0.242
0.43	13.95	10.46	2119.74	6.347	4.116	0.393	0.295
0.5	8.80	8.80	2212.32	6.624	2.176	0.247	0.247
0.6	8.31	12.47	3429.95	10.27	2.196	0.176	0.264
0.67	7.23	14.46	4151.47	12.43	2.030	0.140	0.281
0.8	5.99	23.96	7433.59	22.26	1.704	0.071	0.284
Averages							0.260 ± 0.030

Table S10: Assessment of water states by DSC in samples of Cat-L and water.

w_{H_2O}	Mass Polymer Cat-M (mg)	Mass H$_2$O (mg)	ΔH_f (mJ)	$m_{H_2O\,freezable}$ (mg)	$m_{H_2O\,nonfreezable}$ (mg)	$\dfrac{m_{H_2O\,\text{"non-freezable"}}}{mg\ H_2O}$	$\dfrac{m_{H_2O\,nonfreezable}}{mg\ polymer}$
0.09	18.54	1.85	-	-	-	-	-
0.17	16.04	3.21	-	-	-	-	-
0.23	15.63	4.69	385.5	1.154	3.535	0.7539	0.226
0.33	12.60	6.30	1188	3.557	2.743	0.4354	0.218
0.43	13.43	10.07	2315	6.932	3.141	0.3118	0.234
0.5	11.25	11.25	2864	8.576	2.674	0.2377	0.238
0.6	9.46	14.19	4032	12.07	2.117	0.1492	0.224
0.67	8.38	16.76	4860	14.55	2.210	0.1319	0.264
0.8	4.24	16.96	5200	15.57	1.390	0.0820	0.328
Averages							0.247 ± 0.042

Table S11: Assessment of water states by DSC in samples of Cat-M and water.

w_{H_2O}	Mass Polymer Cat-H (mg)	Mass H$_2$O (mg)	ΔH_f (mJ)	$m_{H_2O\,freezable}$ (mg)	$m_{H_2O\,nonfreezable}$ (mg)	$\dfrac{m_{H_2O\,freezable}}{mg\ polymer}$	$\dfrac{m_{H_2O\,nonfreezable}}{mg\ polymer}$
0.09	18.54	1.85	-	-	-	-	-
0.17	16.04	3.21	-	-	-	-	-
0.23	15.63	4.69	530.37	1.588	2.417	0.6035	0.181
0.33	12.60	6.30	1261.13	3.776	3.249	0.4625	0.231
0.43	13.43	10.07	2004.81	6.002	2.833	0.3206	0.240
0.5	11.25	11.25	2734.76	8.188	3.122	0.2760	0.276
0.6	9.46	14.19	4059.90	12.16	1.885	0.1342	0.201
0.67	8.38	16.76	5328.40	15.95	2.587	0.1395	0.279
0.8	4.24	16.96	8722.35	26.11	1.965	0.0700	0.280
Averages							0.241 ± 0.040

Table S12: : Assessment of water states by DSC in samples of Cat-H and water.

w_{H_2O}	Mass Polymer An-L (mg)	Mass H$_2$O (mg)	ΔH_f (mJ)	$m_{H_2O\ freezable}$ (mg)	$m_{H_2O\ nonfreezable}$ (mg)	$\dfrac{m_{H_2O\ \text{"non-freezable"}}}{mg\ H_2O}$	$\dfrac{m_{H_2O\ nonfreezable}}{mg\ polymer}$
0.09	19.59	1.96	-	-	-	-	-
0.17	15.64	3.13	-	-	-	-	-
0.23	13.76	4.13	648.26	1.941	2.187	0.530	0.159
0.33	12.3	6.15	1221.76	3.658	2.492	0.405	0.203
0.43	9.26	6.95	1766.35	5.288	1.657	0.239	0.179
0.5	9.63	9.63	2526.91	7.566	2.064	0.214	0.214
0.6	7.38	11.07	3193.70	9.56	1.508	0.136	0.204
0.67	5.53	11.06	3258.28	9.76	1.305	0.118	0.236
0.8	3.74	14.96	4689.96	14.04	0.918	0.061	0.246
Averages							0.206 ± 0.030

Table S13: Assessment of water states by DSC in samples of An-L and water.

w_{H_2O}	Mass Polymer An-L (mg)	Mass H$_2$O (mg)	ΔH_f (mJ)	$m_{H_2O\ freezable}$ (mg)	$m_{H_2O\ nonfreezable}$ (mg)	$\dfrac{m_{H_2O\ \text{"non-freezable"}}}{mg\ H_2O}$	$\dfrac{m_{H_2O\ nonfreezable}}{mg\ polymer}$
0.09	22.9	2.29	-	-	-	-	-
0.17	23.17	4.63	-	-	-		-
0.23	15.23	4.57	434.19	1.300	3.269	0.715	0.215
0.33	19.07	9.54	1687.12	5.051	4.484	0.470	0.235
0.43	14.49	10.87	2571.25	7.698	3.169	0.292	0.219
0.5	12.56	12.56	3381.15	10.123	2.437	0.194	0.194
0.6	8.88	13.32	3822.84	11.45	1.874	0.141	0.211
0.67	9.2	18.40	5428.92	16.25	2.146	0.117	0.233
0.8	5.53	22.12	6959.51	20.84	1.283	0.058	0.232
Averages							0.220 ± 0.015

Table S14: Assessment of water states by DSC in samples of An-M and water.

w_{H_2O}	Mass Polymer An-L (mg)	Mass H$_2$O (mg)	ΔH_f (mJ)	$m_{H_2O\ freezable}$ (mg)	$m_{H_2O\ nonfreezable}$ (mg)	$\dfrac{m_{H_2O\ \text{"non-freezable"}}}{mg\ H_2O}$	$\dfrac{m_{H_2O\ nonfreezable}}{mg\ polymer}$
0.09	22.08	2.21	-	-	-	-	-
0.17	19.83	3.97	-	-	-	-	-
0.23	16.43	4.93	450.03	1.347	3.582	0.727	0.218
0.33	15.7	7.85	1198.46	3.588	4.262	0.543	0.271
0.43	14.88	11.16	2613.11	7.824	3.336	0.299	0.224
0.5	11.17	11.17	2837.85	8.497	2.673	0.239	0.239
0.6	6.39	9.59	2707.76	8.11	1.478	0.154	0.231
0.67	7.65	15.30	4456.89	13.34	1.956	0.128	0.256
0.8	5.94	23.76	7404.21	22.17	1.592	0.067	0.268
Averages							0.244 ± 0.021

Table S15: Assessment of water states by DSC in samples of An-H and water.

w_{H_2O}	Mass Polymer Zwitt-L (mg)	Mass H$_2$O (mg)	ΔH_f (mJ)	$m_{H_2O\ freezable}$ (mg)	$m_{H_2O\ nonfreezable}$ (mg)	$\dfrac{m_{H_2O\ "non\text{-}freezable"}}{mg\ H_2O}$	$\dfrac{m_{H_2O\ nonfreezable}}{mg\ polymer}$
0.09	15.31	1.53	-	-	-	-	-
0.17	12.42	2.48	-	-	-	-	-
0.23	10.54	3.16	149.76	0.448	2.714	0.858	0.257
0.33	10.18	5.09	466.04	1.395	3.695	0.726	0.363
0.43	8.01	6.01	990.34	2.965	3.042	0.506	0.380
0.5	9.6	9.60	1950.72	5.840	3.760	0.392	0.392
0.6	9.44	14.16	3502.24	10.49	3.674	0.260	0.389
0.67	7.57	15.14	4051.46	12.13	3.010	0.199	0.398
0.8	5.97	23.88	7193.85	21.54	2.342	0.098me	0.392
Averages							0.367 ± 0.050

Table S16: Assessment of water states by DSC in samples of Zwitt-L and water.

w_{H_2O}	Mass Polymer Zwitt-M (mg)	Mass H$_2$O (mg)	ΔH_f (mJ)	$m_{H_2O\ freezable}$ (mg)	$m_{H_2O\ nonfreezable}$ (mg)	$\dfrac{m_{H_2O\ "non\text{-}freezable"}}{mg\ H_2O}$	$\dfrac{m_{H_2O\ nonfreezable}}{mg\ polymer}$
0.09	14.56	1.46	-	-	-	-	-
0.17	11.58	2.32	-	-	-	-	-
0.23	11.52	3.46	117.01	0.350	3.106	0.899	0.270
0.33	9.65	4.83	581.46	1.741	3.084	0.639	0.320
0.43	11.43	8.57	1461.18	4.375	4.198	0.490	0.367
0.5	9.73	9.73	1969.35	5.896	3.834	0.394	0.394
0.6	10.5	15.75	3806.25	11.40	4.354	0.276	0.415
0.67	6.68	13.36	3523.03	10.55	2.812	0.210	0.421
0.8	3.58	14.32	4270.94	12.79	1.533	0.107	0.428
Averages							0.373 ± 0.059

Table S17: Assessment of water states by DSC in samples of Zwitt-M and water.

w_{H_2O}	Mass Polymer Zwitt-H (mg)	Mass H$_2$O (mg)	ΔH_f (mJ)	$m_{H_2O\ freezable}$ (mg)	$m_{H_2O\ nonfreezable}$ (mg)	$\dfrac{m_{H_2O\ "non\text{-}freezable"}}{mg\ H_2O}$	$\dfrac{m_{H_2O\ nonfreezable}}{mg\ polymer}$
0.09	12.75	1.28	-	-	-	-	-
0.17	11.47	2.29	-	-	-	-	-
0.23	13.48	4.04	290.72	0.870	3.174	0.785	0.235
0.33	9.52	4.76	539.93	1.617	3.143	0.660	0.330
0.43	10.11	7.58	1164.70	3.487	4.095	0.540	0.405
0.5	9.24	9.24	1800.88	5.392	3.848	0.416	0.416
0.6	7.36	11.04	2588.88	7.75	3.289	0.298	0.447
0.67	5.37	10.74	2811.20	8.42	2.323	0.216	0.433
0.8	4.6	18.40	5517.70	16.52	1.880	0.102	0.409
Averages							0.382 ± 0.075

Table S18: Assessment of water states by DSC in samples of Zwitt-H and water.

Coating	Volume Fraction H$_2$O $(\varphi_{H_2O})^a$	Mass Fraction H$_2$O $(w_{H_2O})^b$	$\left(\dfrac{m_{H_2O}}{mg\ coating}\right)^c$	$\left(\dfrac{m_{H_2O\,non-freezable}}{m_{polymer}}\right)^d$	$\left(\dfrac{m_{H_2O\,non-freezable}}{mg\ coating}\right)^e$	$\left(\dfrac{m_{H_2O\,freezable}}{mg\ coating}\right)^f$	$\left(\dfrac{m_{H_2O\,non-freezable}}{m_{H_2O\,in\,coating}}\right)^g$
Cat-L	0.586	0.569	1.321	0.260 ± 0.030	0.343 ± 0.040	0.978 ± 0.040	0.260 ± 0.030
Cat-M	0.432	0.414	0.707	0.247 ± 0.042	0.175 ± 0.030	0.532 ± 0.030	0.247 ± 0.042
Cat-H	0.282	0.267	0.365	0.241 ± 0.040	0.088 ± 0.015	0.277 ± 0.015	0.241 ± 0.040
An-L	0.627	0.598	1.487	0.206 ± 0.030	0.306 ± 0.045	1.181 ± 0.045	0.206 ± 0.030
An-M	0.442	0.411	0.699	0.220 ± 0.015	0.154 ± 0.011	0.546 ± 0.011	0.220 ± 0.015
An-H	0.265	0.241	0.318	0.244 ± 0.021	0.078 ± 0.016	0.241 ± 0.016	0.244 ± 0.021
Zwitt-L	0.259	0.253	0.339	0.367 ± 0.050	0.124 ± 0.054	0.214 ± 0.054	0.367 ± 0.050
Zwitt-M	0.188	0.183	0.223	0.373 ± 0.059	0.083 ± 0.099	0.140 ± 0.099	0.373 ± 0.059
Zwitt-H	0.121	0.117	0.133	0.382 ± 0.075	0.051 ± 0.117	0.082 ± 0.117	0.382 ± 0.075

Table S19: Combination of DSC and ellipsometry measurements in order to describe the amounts of various states of water in the coatings. [a]Determined by ellipsometry measurements SI Section S2. [b]Conversion of volume fraction to mass fraction with each component's density (Eq. S3). [c]Calculated by Eq S5. [d]Averaged "non-freezable" water capacities for each polymer. [e]Product of "non-freezable" water capacity and mass of water in the polymer coating (Eq. S6). [f]Remaining water in polymer coating is assumed to be freezable (Eq. S7). [g]Fraction of "non-freezable" hydration water (Eq. S8).